Solvation dynamics in liquids and glasses

Lazonder, Kees; Wiersma, D. A.

Solvation Dynamics in Liquids and Glasses

Paranimfen:
  Drs. A. J. ten Hagen
  Drs. ing. T. J. van Zalen
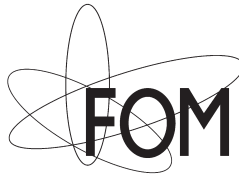
Cover photo by Michel Emde & Kees Lazonder

RIJKSUNIVERSITEIT GRONINGEN

Solvation Dynamics in Liquids and Glasses

Proefschrift

ter verkrijging van het doctoraat in de
Wiskunde en Natuurwetenschappen
aan de Rijksuniversiteit Groningen
op gezag van de
Rector Magnificus, dr. F. Zwarts,
in het openbaar te verdedigen op
vrijdag 6 oktober 2006
om 16.15 uur

door

Cornelis Lazonder

geboren op 25 januari 1969
te Leek

Promotor:
    Prof. dr. D. A. Wiersma

Copromotor:
    Dr. M. S. Pshenichnikov

Beoordelingscommissie:
    Prof. dr. K. Duppen
    Prof. dr. J. Knoester
    Prof. dr. S. Völker

Table of contents

Voorwoord

Promoveren kan ik iedereen aanraden. En van alle redenen die ik kan aanvoeren om deze stelling te onderbouwen is de mix van de collega's die je treft en het plezier dat je met hen hebt, niet de minste. Tijdens mijn promotieonderzoek zijn collega's gekomen en gegaan, en het zou ondoenlijk om ze hier allemaal met naam en toenaam op te sommen. Bovendien zou ik ze daarmee te kort doen. Ik heb aan iedereen goede herinneringen. Van alle werkomgevingen die ik ken, is de wetenschappelijke wereld één van de meest collegiale, diverse en vriendelijke die ik ken. Dit is een gegeven dat door de meeste mensen die zich al lang in deze wereld begeven vaak uit het oog verloren wordt, en dat tegelijkertijd door buitenstaanders zelden wordt opgemerkt.

Een aantal mensen was zo belangrijk voor de totstandkoming van dit werk dat ik hen hier wel bij naam noem. Mijn promotor, Douwe Wiersma, wil ik natuurlijk in de eerste plaats bedanken voor het feit dat hij me deze kans geboden heeft. Maar ook voor zijn niet aflatende enthousiasme en vertrouwen in een succesvolle afronding van dit project. Dit geldt ook voor mijn copromotor, Maxim Pshenichnikov, die mij dagelijks begeleidde vanaf het moment dat ik van het picoseconde naar het femtoseconde werk overstapte. Hij overzag mijn metingen en nam me mee naar conferenties. Zonder zijn vele ideeën, heldere uitleg, en inspirerende peptalks was die succesvolle afronding zonder meer uitgebleven. Voor het picoseconde werk ben ik dank verschuldigd aan Koos Duppen, die mij geholpen heeft bij het publiceren van de resultaten daarvan. Ik zal de borrels in de Paddepoelbar missen. Essentieel was ook de hulp van Ben Hesp bij het opzetten en draaiende houden van mijn apparatuur en goede humeur. Wat dat laatste betreft, kon ik ook niet zonder de hulp van Foppe de Haan. Hij hielp bovendien bij de data acquisitie, data analyse en de aansturing van de setup. Ook wil ik mijn leescommissie en proefleesteam bedanken voor al het nuttige commentaar.

Mijn ouders wil ik hier zeker noemen. Hun opvoeding en hun ondersteuning legden de basis voor dit proefschrift. Tot slot, maar zéker niet in de laatste plaats, bedank ik Iris voor haar voortdurende steun, vertrouwen en liefde. Ik ben dankbaar dat ze zoveel geduld met me gehad heeft. Nu dit project erop zit kijk ik samen met haar reikhalzend uit naar het volgende grote avontuur.

Het is uiteindelijk de grote groep mensen die ik heb leren kennen in en rond het lab in Groningen, die samen van de laatste jaren een geweldige periode hebben gemaakt. Ik ben blij dat het erop zit, maar ik zal altijd met veel plezier aan iedereen terug denken. Vandaar dat ik op de volgende pagina ruimte laat voor een persoonlijk woord voor al die collega's, huisgenoten, teamgenoten, kennissen, familie en vrienden die ik hier nog niet genoemd heb.

Chapter 1

Introduction to Glasses

Even though glasses are utilized everywhere and anywhere in our daily lives, our understanding of these materials is limited. Glasses form together with liquids, polymers and various organic materials the class called soft condensed matter. This class of materials is set apart to emphasize its inherent lack of regularity. This regularity is the defining trait of the other class of condensed matter: crystalline solids. The inherent randomness of glasses affects all characteristics of these amorphous solids. This thesis discusses the limits in which two theoretical approaches that are commonly used to describe dynamics in amorphous condensed matter, in particular the glass phase, are valid. In this chapter a first description of glasses and the glass transition is given. Some issues concerning amorphous solids are discussed and two common myths are dispelled. The dynamical aspects of glasses that are especially the focus of this work are introduced together with a short introduction to the optical techniques that are used to study these facets. The chapter concludes with an outline of this thesis.

1.1 Why Are Amorphous Solids Interesting?

Amorphous solids and glasses are not exactly the same; there is a subtle difference between the two. Amorphous solids are characterized by a lack of long-range translational order on the microscopic level. The atoms or molecules that make up these substances are randomly packed together. Long range order is typical for crystals. Glasses also lack this regularity and at the same time can be prepared by cooling down a liquid fast enough below the glass

transition temperature, contrary to amorphous materials [1-3]. Therefore, glasses are amorphous solids exhibiting a glass transition. This distinction is largely historical and rooted in the fact that more methods than the rapid cooling of a liquid exist to prepare an amorphous solid. The greater part of this work deals with true glasses, although all the aspects focused on are relevant to amorphous solids as well, despite the difference. Therefore, the terms glass and amorphous solid are used as synonyms in this work, together with the alternative terms vitreous solid and non-crystalline solid.

Other types of materials in the class of soft condensed matter are liquid crystals, proteins, colloids, polymer solutions and melts, foams and gels [4]. These materials by and large consist of organic molecules that interact weakly; as a result, thermal fluctuations, external fields, and boundary effects strongly influence their structure and properties. They have complex structural and dynamical properties that are in-between those of crystals and fluids.

Before describing glasses in greater depth and explaining what typifies a glass transition, a clarification of why glasses are an interesting research topic to begin with, is in order. For starters, glasses are omnipresent in daily life. From 'high tech' computer memory elements, solar cells and optic fibers to the 'low-tech' application of many metal alloys, plastics and of course windowpanes, all these applications rely on glass-specific qualities and crystalline materials can in most cases not replace the used glass components [5,6].

Ever since Assyrians and Egyptians made the first glass beakers four and a half thousand years ago, this reliance on the properties specific to glasses has been crucial [7,8]. For example, the Phoenicians were the first to manufacture transparent glass and were able to create an export-oriented glassmaking industry using the quartz-rich sands of the Lebanese coasts [9]. The key feature of the oxide glasses that was exploited in these cases is that glasses soften slowly with increasing temperature, instead of having a discrete melting temperature as crystals do. This typical behavior of glass near the glass transition temperature obviously allows for easy processing of the raw material into any desired shape. It makes it possible to produce flat windowpanes. Furthermore, these windows could be produced with relatively high optical quality without having to bother with problems associated with crystals such as polycrystallinity or anisotropic optical properties.

The latter means that the optical properties of a glass pane do not depend on the orientation of the window with respect to the direction of the light traveling through the glass. This isotropic optical nature of glasses is worth mentioning, since it is a direct result of the lack of translational long-range order, as are other macroscopic properties such as the low thermal conductivity. The optical traits of these silicate glasses are these days exploited in state of the art optical fibers. Their transparency is remarkable, optical attenuation in the near

infrared regime can be as low as 0.1 decibel per kilometer, allowing light pulses to travel over tens of kilometers without losing too much intensity.

Even though the oxide glasses from which our windows are made are probably the first that spring to mind when one is asked about glasses, nowadays by far the most common types of amorphous materials are plastics. Polymeric solids are organic glasses and are easy and cheap to produce on a massive scale, are light, can have high mechanical strength. Again, many of these properties stem from the amorphous nature of these substances.

It is hard to overestimate the pervasiveness of amorphous solids in the modern world. Yet despite all this, these materials do not get the respect and attention of scientists one would expect and thus the fundamental knowledge of glasses is limited. Textbooks on solid-state physics illustrate this best, e.g. the book used for advanced undergraduate courses at the natural sciences faculty of Groningen University spends a mere 17 pages of a total of 646 pages on amorphous materials. The other 629 pages are spent on the physics of crystals [10]. It is worth noting, however, that most of the discussed features of crystals are caused by imperfections in the crystalline structure, i.e. by some limited randomness. Even so, every course on solid-state physics begins with a discussion of crystal lattices and periodicity, as if translational order is an essential requirement for solidity.

The result of the focus on crystals and periodicity is that many people do not even acknowledge that glasses are solids at all. Many scientists and science students will answer when asked about the solidity of amorphous materials that glasses are in fact very viscous liquids. They might even continue to illustrate this statement by recounting the legend of antique windowpanes that are thicker at the bottom than at the top due to the minute enduring flow of the material over the years. However, this story has been refuted for a long time already [11-14]. Although some antique windowpanes might be thicker at the bottom, there is no statistical evidence that the ticker part is always at the lower side of the window. Variations in thickness are simply due to the manufacturing process at the time of production. Glasses are not liquids. They do not flow when subjected to moderate forces and react to the impact of force with elastic deformation and are therefore solids [1,6,15].

Although the powerful tools that aid the solid-state scientist are mostly based on the translational periodicity and long-range order of crystals, this does not justify the situation as described above. The absence in amorphous solids of a well-defined **k**-space, Brillouin zones, Bloch functions, and electronic band structures etc., limits the use of symmetry and group theory principles for the descriptions of the vitreous state to a very large extent. However imperative periodicity is for these mathematical tools, it is important to realize that the key properties of a large class of solids do not stem from long-range order and therefore this order is dispensable for a comprehensive description of these features.

Summarizing the points made above: the abundance of applications of amorphous solids in every day life and the general lack of understanding of amorphous materials calls for further research in this field.

1.2 Preparation of Glasses

Now that it is established that glasses are solids and presuming that we know what solids are –a solid is a material whose shear viscosity exceeds $10^{14.6}$ poise [1]– the description of a glass can be explored in further detail.

The result of a *gedanken*-experiment often used to illustrate phase transitions is depicted in the volume *vs.* temperature graph in Figure 1.1 [taken from ref. 15]. Starting out at the high temperature side of the diagram, it shows the volume reduction of a vapor of some sort of molecules as it is cooled down. The volume shrinks quickly until the boiling temperature T_b is reached and the gas condenses as a liquid. The volume then slowly reduces further until the melting temperature T_f is reached, as described by the liquid's thermal expansion coefficient. At this point, two possible pathways exist. Depending on the cooling rate, the liquid can either freeze into a solid at this temperature, resulting in a sudden drop-off of the volume, or the liquid can be cooled to a so-called "super-cooled" state. In the former case,
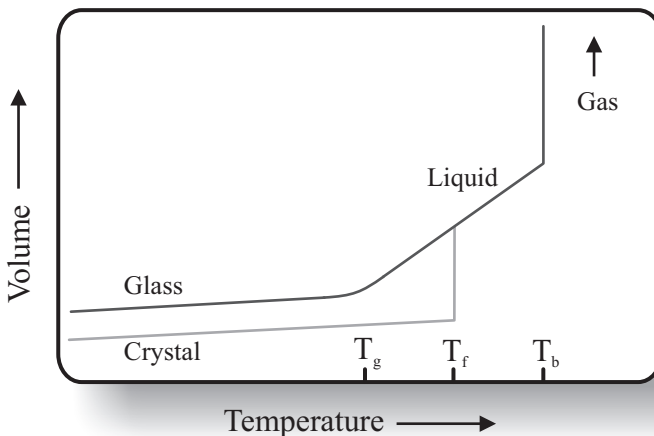
Figure 1.1. Cooling down from the boiling point T_b, a typical substance can take two possible pathways to the solid state. At the freezing point T_f the liquid can either crystallize or subsist in a super-cooled state until the glass transition temperature T_g is reached. Adapted from reference [15] .

the slope of the diagram at temperatures below the melting point is set by the thermal expansion coefficient of the crystal. The melting point itself is characterized in the volume-temperature plot by a discontinuous change in volume; this is a sudden reduction for most liquids. Other thermodynamic observables show similar discontinuities.

If the cooling rate is high enough, the liquid can alternatively be cooled to a super-cooled state. In this state, the properties of the substance are still those of a liquid. When the temperature is lowered further, its volume will keep decreasing continuously, although its temperature is lower than the melting point. At some point the cooling will result in a drastic increase in the viscosity of the super-cooled liquid. This is where the glass transition temperature T_g is reached. Below this temperature the substance is in the glass state and the thermal expansion rate is smaller then that of the liquid.

The first point to notice is that this transition is not accompanied by a sudden volume drop-off, but instead the liquid transforms rather continuously into a solid. The phase transition occurs without exhibiting a discontinuous reduction of the volume. The second noteworthy point is that this transition happens at a narrow temperature interval instead of one well-defined temperature.

The result of both scenarios is a liquid-to-solid transition whereby the cooling rate determines the pathway. The first scenario results in a well-ordered crystalline solid, the second in an amorphous solid, i.e. a solid with no long-range regularity. Until rather recently it was thought that not all liquids could be cooled fast enough to produce a glass [16]. With the development of experimental techniques that allow cooling rates well over 10^6 K s^{-1} [17], it is now generally believed that all condensates can be prepared as a glass, even simple metal melts, with the exception of exotic fluids as liquid Helium [18,19].

So, strictly speaking, the often-used term "glass-forming liquids" is without meaning since glasses can be produced from all liquids. The term will be used in this work, however, to identify those liquids that form glasses at relatively low cooling rates already. This is particularly true for liquids that have a value of the ratio of boiling temperature to freezing temperature that is larger than 2.0 [3]. For these materials typical quenching rates of 10^{-5} to 10^{-1} K s^{-1} will suffice in order to prepare the glass-state [20].

1.3 The Glass Transition

The question remains of course how the properties of a material, once the freezing point is passed with a high enough quenching rate, can suddenly change so drastically without a major structural rearrangement on a molecular level. A Nobel laureate calls this "the deepest and most interesting unsolved problem in solid-state theory" [P.W. Anderson in ref. 21].

The liquid-to-glass transition is an example of a second-order phase transition. This means that over the transition, derivative functions of the chemical potential, such as volume, entropy, enthalpy and heat capacity change continuously with temperature as they do not do in a first-order phase transition. Actually, the term second-order phase transition is somewhat misleading in the case of the glass transition since the second-order derivative of the free energy is not even discontinuous. The changes of the slope of the first-order derivative are not sharp, but are diffuse instead. Differential calorimetric scans for example, nowadays used to determine the glass transition temperature of glass-forming liquids, show specific heat changes occurring on a small temperature interval. Consequently, the classification of phase transitions is better done in terms of first-order phase transitions involving a latent heat and continuous phase transitions with no associated latent heat [22].

This is illustrated by Figure 1.2.b, which shows the specific heat that can be measured in a characteristic differential calorimetric scan of a glass-forming liquid as typically used in this work. Such a scan measures the amount of heat absorbed and released to induce a temperature change in a certain quantity of the substance. The specific heat at constant pressure is defined as $C_p(T) \equiv (dQ/dT)_p = T(\partial S/\partial T)_p$. The top curve of the glass shows the heat extracted to cool the sample down and the bottom glass curve shows the heat absorbed by the sample to warm up.

The precise temperature at which the liquid-to-glass transition occurs depends somewhat on the cooling rate. This can be understood when one realizes that upon cooling, at some point particle motion becomes so slow that a time-independent state can no longer be reached. The system's particles can no longer sample enough configurations to reach a time independent equilibrium. In other words, the system reaches a non-ergodic state, since the precise state is dependent on the thermal history of the sample. The molecules will become so slow-moving that the system will be structurally trapped in a certain random configuration. For different cooling rates this will happen at different temperatures, hence the small variation in glass transition temperatures. Typically, changing the cooling rate by an order of magnitude, changes the glass temperature by a few Kelvin.

This emphasizes the kinetic characteristics of the glass transition. It is clear that in Figure 1.2.b the peaks associated with the glass transition display some hysteresis. More generally: the variations in the cooling or annealing history of a glass result in different $C_p(T)$ signatures. All this has hampered the definition of what constitutes a glass transition, or a consistent definition of the glass transition temperature, let alone any reasonably complete explanation of the phenomenon [18,19,23]. All current theories concentrate on the ergodicity-breaking aspect of the transition; the focus is on the kinetic events that lead to the thermodynamic change of state.

The thermodynamic aspects of the transition can be illustrated by observing the change in entropy of a super-cooled liquid, cooled down from the freezing point to the glass temperature, in comparison with that of the corresponding crystal at the same temperature. The
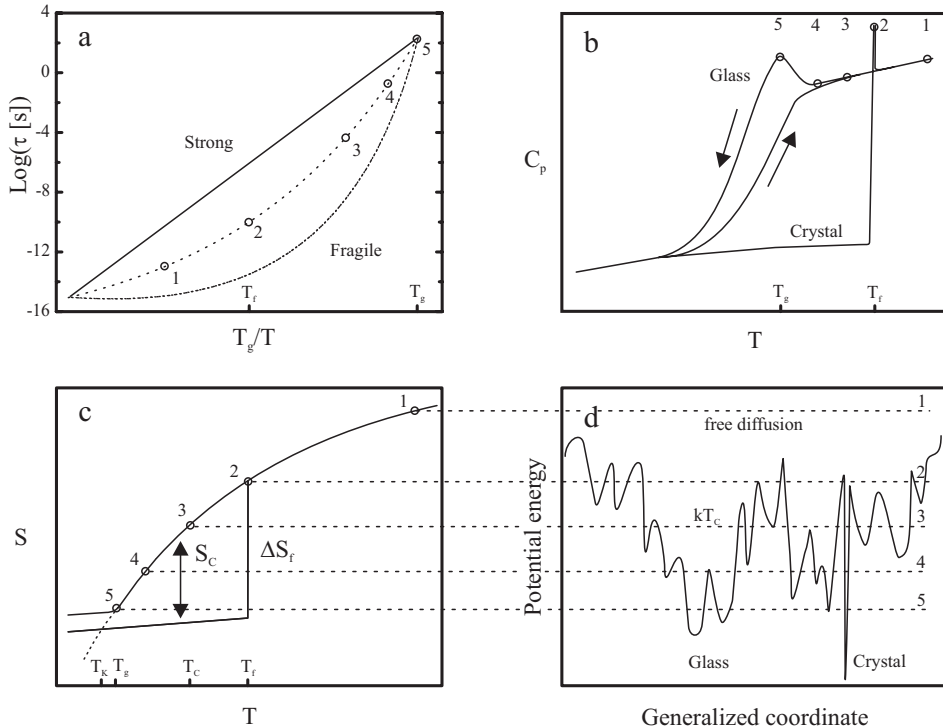
Figure 1.2. A graphical representation of the most important concepts in glass dynamics. (a) An Arrhenius plot, scaled on the glass transition temperature T_g, showing 'strong' liquids with an ideal Arrhenius behaviour and 'fragile' liquids with strongly diverging relaxation times. (see section 2.1) (b) The specific heat C_p of a substance vs. temperature. The temperature signature of the glass shows some hysteresis. (c) An entropy plot illustrating the Kauzmann temperature T_K and the configurational excess entropy S_C used in the Adam-Gibbs approach. (d) A 1D representation of the potential energy landscape, where the system can be cooled down from a state where particles can diffuse freely through the system (1), past the freezing point T_f (2), to below the cross-over temperature T_C (3) where diffusion is hampered by the barriers in the landscape (4) until the glass transition temperature is reached (5). Adapted from references [30] and [37].

values of the entropy of both states are plotted in Figure 1.2.c. The entropy of the super-cooled liquid will decrease more rapidly and will approach the entropy of the crystal because the specific heat of the liquid is larger than that of the crystal. The temperature at which the entropies of both phases would be equal is called the Kauzmann temperature T_K. The entropy of the super-cooled liquid would even reach a negative value at a finite temperature if the temperature was lowered below this point. Since the existence of an amorphous phase with lower entropy than the well-ordered crystalline phase is unphysical, a pronounced change in the specific heat has to occur before this temperature is reached and this change is, of course, the glass transition.

The glass transition is therefore an entropy crisis, or rather an event to avoid such a crisis. The imminence of this entropy crisis is called the Kauzmann paradox [24]. It sets a lower limit on the glass temperature, independent of the cooling rate and it shows the underlying thermodynamic basis of the transition [25,26].

1.4 Glass Theory

Although the nature of the glass transition is still not completely understood, significant advances have been made in this field in recent times [23]. An overview of the approaches used for describing glass dynamics is presented in this chapter by dividing the subject in three major categories. These categories are based on the temperature region that they cover: (i) the high temperature regime of super-cooled liquids well above the glass transition, (ii) the region of the transition itself and (iii) the low temperature regime well below the glass transition.

In the high temperature regime well above the glass temperature, upon cooling, the liquid becomes viscous but is always ergodic; its properties have no history dependence. The dynamics of the system in this region are described by means of a model based on molecular collisions. At the highest temperatures the system is expected to respond on perturbations with relaxation times that depend exponentially on temperature, i.e. with a normal Arrhenius-type dependence. This changes however, when the temperature is lowered further. Dielectric relaxation, viscosity, diffusion and other functions connected to molecular mobility need to be described within another framework in this region, since the observables show deviations from an Arrhenius-type temperature dependence. Many approaches exist, but the most popular one is the Vogel-Fulcher approach that is briefly outlined in the next chapter [27,28]. Furthermore, besides the temperature dependence of the relaxation rates, the relaxation functions themselves become non-exponential with time in this regime, which is an indication of the existence of distributions of relaxation regimes in the liquid.

The most difficult region to comprehend is that of the actual transition, at somewhat lower temperatures. Not only does the history of the studied material influence the observables of interest, also the timescale of the perturbation and the characteristic time scale of the measurement itself influence these observables. The common methods for describing relaxation dynamics such as the VF approach are no longer practical since they can only be effectively applied over limited temperature intervals and timescales. The widespread assumption is that the non-exponential relaxation processes with respect to temperature and time are strongly influenced by the underlying potential energy landscape.

1.5 The Landscape Paradigm

This is also typical of the state of affairs well below the glass transition. In this region the system is best described by means of a potential energy landscape spanned by all the degrees of freedom it has. Landscape paradigms are commonly used to describe the qualitative behavior of complex systems [29]. In the case of amorphous materials, the shape of the landscape in the vicinity of its configurational state and particularly the height of surrounding barriers and ridges determine the amount of configurational space the system can explore. Evidence is mounting [30,31] that the onset of non-exponential relaxation corresponds to a well defined cross-over temperature T_C, well above the glass temperature, below which the system can no longer freely explore all of the configurational space but instead is confined to deep basins in the landscape. At lower temperatures the system gets trapped in the lowest accessible basin.

The concept of a crossover temperature is appealing since it connects the landscape approach to mode-coupling theory (MCT), a kinetic description of glass dynamics that has been extensively used [32-35]. MCT is formulated in terms of nonlinear coupling between density fluctuation modes and although it does not use any aspects of the potential energy landscape approach, it predicts a critical temperature well above the glass transition temperature below which the dynamical properties of the glass diverge. It has been suggested that this critical temperature and the crossover temperature are reflections of the same change in thermodynamic state of the material [18].

This is quantified in the Adam-Gibbs description [36] of viscous liquids that states that the time scale for viscous liquid relaxation is related to the excess entropy of the liquid over the corresponding crystal as indicated in the Kauzmann paradox mentioned earlier. This excess entropy S_C represents the accessible configurational states in the landscape basins with an amorphous packing ground state. When this entropy is evaluated as the entropy generated above the Kauzmann temperature T_K the VF-equation can be recovered, thus

providing a connection between the kinetic and landscape descriptions of glass dynamics, as is illustrated in Figure 1.2.c and d.

The lowest temperature regime is non-ergodic as well, but here the system at least shows a behavior that is essentially reversible with respect to a temperature change that stays within this region. The temperature signature of any relaxation processes around the glass transition temperature will reflect that of the activated type. Activated relaxation is a term commonly used in the literature on super-cooled liquids [37]. It refers to relaxation that is characterized by episodic particle motions as the system jumps from one configurational basin to another by overcoming energy barriers. This type of relaxation sets in at the cross-over temperature and is completely dominant below the glass transition temperature.

The development of an approach that encompasses these three regions remains a major challenge. No clear picture of how this will come about is emerging at this time. All descriptions have only limited applicability. The most promising approach to universal account of glass dynamics appears to be the MCT in combination with the Adam-Gibbs approach.

However, landscape-type approaches are ultimately the only complete method for dealing with many-body disordered systems, since all degrees of freedom are inherently incorporated. This abundance of degrees of freedom also sets the challenge in quantification of this approach to be able to predict the values of thermodynamic and kinetic observables. The crucial step is formulating a real space model that captures the essential features of the collective system [30,31,38].

One such model is the so-called two-level system model. It is used at the lowest temperatures, below ± 4 K, where the system is trapped in the bottom of a single basin and vibrational and translational motion is frozen out. At these temperatures the relevant features of the energy landscape are represented by an ensemble of nearly degenerate double potential wells, the two-level systems (TLS's). The potential double wells couple to the remains of the phonon bath at these temperatures and can change state from one potential well to the other by means of tunneling. These flips represent the left over relaxation processes in the system and result in a description of the glass dynamics at low temperatures in terms of a randomly distributed ensemble of spin Hamiltonians.

This model was first introduced independently by Phillips [39,40] and Anderson [2,22] in 1972. It has been successfully applied to explain various properties that seem to be universal in glasses. An examples is the specific heat C_p that obeys the Debye T^3 law in crystals but depends approximately in a linear fashion on temperature in disordered materials [41,42]. Similarly, the thermal conductivity depends quadratically on temperature in amorphous solids in contrast with the cubic dependence found in crystals. These glass specific

temperature dependencies can be described well within the TLS model, as are sound propagation properties as well as dielectric response properties at these temperatures [1,43].

The TLS theory has also been applied to explain so-called optical line broadening experiments, yielding similar successes [44,45]. These types of experiments are central to this work and therefore the TLS approach to describe glass dynamics is used as a starting point here to explore glass dynamics. The theory is examined in detail in the next chapter, and the underlying assumptions, together with the most obvious problems, are examined.

At slightly higher temperatures the specific heat of glasses still deviates from a Debye dependence, showing a universal broad maximum in C_p/T^3 vs. T plots around 10 K [41,42]. This feature is attributed to an excess in the vibrational density of states $g(\nu)$ of glasses over the crystalline Debye behavior, leading to a maximum in the $g(\nu)/\nu$ curve, which is known as the boson peak, and can be observed in Raman and inelastic neutron scattering experiments [46]. The precise nature of these low-frequency vibrations is still a matter of debate [47].

All these theoretical approaches, albeit with their applicability to limited temperature regimes, demonstrate that the problems in describing the reactions of glasses to certain perturbations are all interconnected. The similarities in responses for different perturbations in a glass and the similarities of those responses among a wide variety of glasses do seem to warrant the search for a universal theory of glass dynamics.

Many approaches other than the ones mentioned here exist. For example the Tool-Narayanaswamy-Moynihan and Kovacs-Aklonis-Hutchinson-Ramos (TNM-KAHR) model used by glass manufacturers to estimate residual stress in annealed glass goes unmentioned here since it only relates to specific aspects of glass dynamics [48-51]. Many other complex systems exist that show dynamics that can be described with glass-related methods such as frustrated spin glasses, neural networks and stock markets. No attention is given to protein dynamics or protein folding and related fields either. All these subjects do however illustrate the opportunities still offered for fundamental and applied research in this field.

1.6 What Is in This Thesis?

In this work glass dynamics are studied with optical line narrowing techniques. When a dye molecule is dissolved in an amorphous solvent its absorption spectrum is broad and featureless. This is because each individual chromophore is surrounded by a different configuration of solvent molecules. This causes small differences in the resonance frequencies of the dye molecules, hence the so-called inhomogeneously broadened absorption line shapes. Relaxation dynamics can change the environment of the chromophores with time, thus creating

time depending changes in the resonances frequencies. This is called spectral diffusion. If the evolution of these frequencies is followed over time, information on the timescales of relaxation of the solvent is uncovered. This information can be harvested when the broadening of a small subset of chromophores with identical resonance frequencies is followed over time as illustrated in Figure 1.3.

Optical line narrowing techniques such as hole-burning and photon echoes do exactly this, and the latter technique is the main tool of investigation in this work. In the former, the hole burning experiment, the selection of the subset is made with the use of a narrow band laser tuned to some frequency in the inhomogeneous absorption band. The chromophores that absorb at this frequency are either temporarily stored in an excited electronic state or permanently photochemically bleached. The initial width of the chromophore subset can then be measured by measuring the resulting dent in the absorption band.

The narrowest possible selection is called the homogeneous line width. The line shape of the subset will then broaden with time at rates that are equivalent to the relaxation rates of solvent molecules in the vicinity of the chromophores. At some point all memory of the initial subset will be erased and it will have the same shape as the overall inhomogeneous absorption profile. Information on the glass dynamics is therefore gathered from the particular characteristic timescales of the broadening function.

In the photon echo technique used in this work the sample is interrogated with short laser pulses. In a nutshell, two pulses are used to create a complex pattern in frequency space – both in the ground and the optically excited state – from which a third pulse is scattered. After the first pulse coherently excites chromophores with a resonance frequency within the
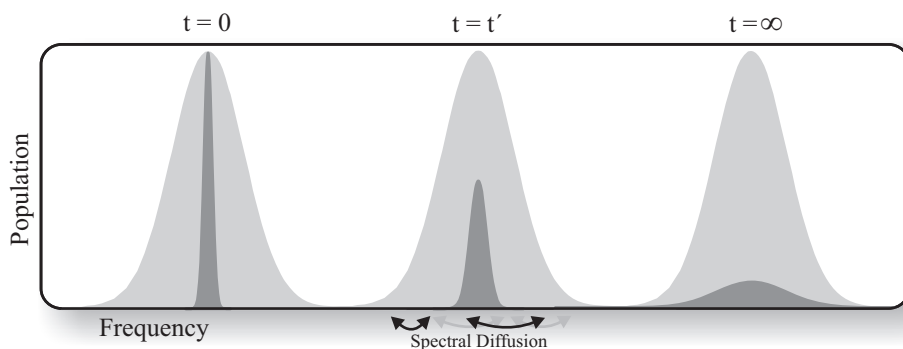
Figure 1.3. A schematic representation of spectral diffusion due to random walks of chromophore resonance frequencies. The homogeneous line shape selected at $t = 0$ slowly broadens with time to eventually reflect the shape of the inhomogeneous line shape of the absorption spectrum.

spectral bandwidth of the pulse, these chromophores are left to dephase, i.e. to loose their relative coherence due to frequency offsets, during the 'coherence time' τ. The amount of dephasing is then stored in the above pattern by the second pulse. The third pulse is scat-
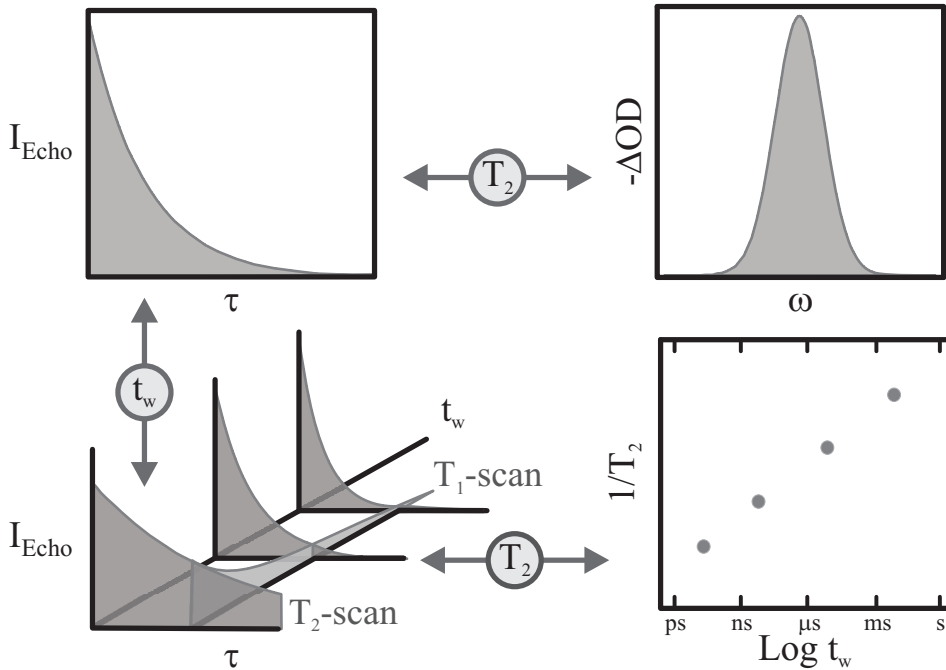
Figure 1.4. The relationship between a hole burning experiment and a photon echo experiment and between the population and coherence dimension of photon echo experiments. Top left: when the coherence time τ is scanned, a T_2-scan, the echo signal decays with a decay rate that is set by the dephasing time T_2. The larger T_2 is the quicker the echo signals decays. Top right: On the same footing, the larger T_2, the wider the line width that is measured in a hole burning experiment. This width is the same as the homogeneous line width as depicted in Figure 1.3. Bottom left: Therefore, when the waiting t_w is increased, the dephasing time effectively increases as well due to spectral diffusion, and faster decay rates are measured in T_2-scans. Bottom right: From the decay rates, T_2 can be deduced for each t_w and a line broadening plot can be constructed.
When the waiting time t_w is scanned for a fixed coherence time τ, another echo intensity decay is measured. In this case the decay rate is set by the population relaxation time T_1, and it is called a T_1-scan or longitudinal echo decay.

tered after a usually much longer 'waiting time' t_w, and the measured signal is the time delayed scattered light as a function τ and t_w. Varying the coherence time for a fixed waiting time will yield a signal with a decay rate proportional to the smallest selectable width $1/(\pi T_2)$ of the subset of chromophores for the time period spanned by the sum of the coherence time and the waiting time. This coherence dimension of the echo experiment is illustrated in Figure 1.4. The magnitude and times scales of bath dynamics are usually expressed in a time-correlation function that conveys the loss of coherence over time.

The complex character of the pattern stored by the first two pulses actually enables the retrieval of more information than only correlation times of bath dynamics. Also the precise nature of the interaction between chromophore and bath, in case the excitation of a chromophore actually induces bath dynamics, can be investigated as well. And finally, Figure 1.4 also shows that varying the waiting time for a fixed coherence time will yield a decay rate that is proportional to the population lifetime T_1 of the excitation involved. This is the longitudinal population dimension of the echo.

All this makes the photon echo technique a very powerful tool for investigating bath dynamics. An advantage is e.g. that it eliminates the time resolution limitations in hole burning caused by the time periods needed for burning the hole and between burning the hole and measuring the initial hole width. By setting the time period between the creation of the pattern and the scattering of the third pulse to zero and by carefully choosing the temporal and spectral properties of the pulses the ultimate time resolution associated with the optical transition can be achieved. For in depth reviews of these techniques and other methods in non-linear spectroscopy the reader is referred to one of the many textbooks on this subject [52-55] and Chapter 3 of this thesis.

First, in Chapter 2 a concise review on glass and viscous liquid dynamics is given, with emphasis on those aspects that are relevant to the experiments described in later chapters. It reviews the aspects of glass dynamical theories mentioned in this introduction in further detail. Special focus is on TLS theory and the current issues regarding its interpretation.

The third chapter then introduces the theory of the non-linear optical techniques used in this work. Special attention is given to recent developments in the description of photon echo experiments and the consequences of a particular description of bath dynamics in the outcomes of the experiments. A brief overview is given of the theoretical aspects of non-linear optics that are relevant to this work.

The experimental procedures are detailed in Chapter 4. Special attention is given to a subtle and previously overlooked experimental artefact due to heating effects in the photon echo experiments. Energy dumped by chromophores relaxing from some excited state can induce delayed heating effects in nearby molecules and thus influence the outcome of echo

experiments. This has consequences for the interpretation of previously found features of dynamics in amorphous materials.

The coherence dimension of the photon echo is explored in Chapter 5. The time dependence of the homogeneous line width of Zn-porphin in deuterated ethanol glass at 1.8 K is measured by stimulated photon echo. The observed spectral dynamics is interpreted in terms of the standard two-level system model and by using a commonly used modified version of it. The necessity of modified TLS parameter distributions is discussed. After correcting for time-dependent local heating, the time dependent behaviour of the effective homogenous line width suggests the existence of excess optical dephasing on a short time scale. This effect is attributed to spectral diffusion induced by the change of electronic state of the chromophore. This phenomenon is not captured in existing theoretical models, which assume the probe molecule to be just a spectator of glass dynamics. Also any non-exponentiality of echo traces is quantified and explained within this framework.

Another trait of the photon echo technique is the possibility to explore the population dynamics of a chromophore in addition to its dephasing characteristics. This longitudinal dimension of photon echoes is also discussed in Chapter 5. The anomalous intensity loss is inspected in the light spectral diffusion of chromophore resonance frequencies out of the excitation band width.

In order to study glass formation and temperature solvent dynamics in the temperature regions between the cryogenic temperatures of the above chapter and room temperature enhanced time resolution is needed. Modern day all solid state Ti:Sapphire lasers provide this resolution. Chapter 6 deals with the effects of temperature on photon echoes generated with femtosecond light pulses.

At room temperature the model used to describe chromophore-bath dynamics is the multi-mode Brownian oscillator (MBO) model. It models the interactions between the system and the surroundings in terms of harmonic oscillators. This model makes it possible to accurately describe the outcome of various optical experiments at various temperatures with one relatively small group of model parameters. By varying the temperature over a large interval the validity of the approximations made in this model were put to the test and common interpretations could be looked into. For instance, the manner in which the modes that were used to described the fastest part of the dephasing were usually modelled needed to be changed to be able to accommodate temperature variations.

Furthermore, in Chapter 6 it is demonstrated that time-resolving the echo signal by mixing the echo signal with a fourth local oscillator pulse yields more information regarding the dephasing of the coherently excited chromophores. This so called heterodyne detected photon echo signal is more sensitive to fast coherence decay than the usually employed echo peak shift. The latter is a time integrated measure that is thought to accurately resem-

ble the loss of coherence over time. It is shown however that the heterodyne detected echo is more sensitive to the short time coherence loss.

Finally in Chapter 7 the same heterodyne detected photon echo data as presented in Chapter 6 is shown in a different representation. After Fourier transforming the data along two time axes, the time between the first two pulses and the time between the last two pulses, the so-called 2D correlation spectrum is recovered. The precise ins and outs of this operation are outlined in this chapter. It is then demonstrated that this frequency domain representation gives clear and easy to understand information on the precise amount of coherence loss in the system. A brand new method for quantifying this coherence loss is given. It is concluded that representing time resolved photon echo data in the frequency domain is easy to achieve and is advantageous for the both the qualitative and quantitative interpretation of the results.

Chapter 2

Theory of Liquid and Glass Dynamics

An outline is given of the approaches used to describe the response of an amorphous medium, in this case either a liquid or a glass, to some perturbation. The various approaches of describing glass dynamics in terms of macroscopic observables are given in a short historic overview. The newer methods that originate from microscopic considerations, are also mentioned before a more extensive review is given of the so-called two-level system model that is used to describe glass dynamics at temperatures below 4 K. The model implies a large number of low energy solvent excitations that are represented as two level systems. These entities can quantum mechanically tunnel between their two states on a broad distributions of time scales and as a result account for a number of thermodynamical, acoustic and optical properties that are characteristic of glasses. The experimental results at low temperatures in this thesis are interpreted by means of this model. At higher temperatures in the liquid phase more abstract models are used to describe the coupling of an optical system to a heat bath. Two approaches for this case that are specifically used in spectroscopy are mentioned at the end of this chapter.

2.1 Introduction

This work is concerned with the time-dependent properties of materials in the condensed phase in general and the glass phase in particular. Dynamics in the condensed phases are

studied by measuring the response of a substance to a certain perturbation. There are a number of excitations and corresponding relaxation phenomena that are useful in this respect. In the viscous liquid domain the most important observables used to characterize the dynamics are kinetic transport properties and configurational relaxation times [37,56]. The transport properties include the viscosity η, the diffusivity D and the conductivity [57], and the relaxation times concern mainly the dielectric relaxation time τ_D [58-60], but also longitudinal and shear mechanical relaxation [61,62], nuclear electron spin relaxation [63,64], enthalpy relaxation [65] and more.

A configurational relaxation time will be related to translational and rotational diffusion and the diffusion is in turn related to the viscosity. A first order approach to kinetic theory in liquids is the well-known Arrhenius law. It explains the temperature dependence of reactions rates and molecular mobility in terms of collisions frequencies and activation energy E_a. Molecular self-diffusion can be expressed as a hopping process, involving a diffusion barrier E_{diff}:

$$D(T) = A\exp\left[-E_{diff}/kT\right].$$
(2.1)

The Stokes–Einstein formula gives the relation between the self-diffusion coefficient D and the viscosity η:

$$D(\eta) = \frac{kT}{6\pi\eta r},$$
(2.2)

where r is the effective molecular radius of the substance. Similarly the self-diffusion can also be related to the rotational reorientation time using the Debye–Einstein relation. The classic text book picture is that the activation energy or diffusion barrier can be determined by plotting the logarithm of the diffusivity or viscosity against $1/T$. In ideal liquids the pre-exponential factor A is considered constant over large temperature intervals and the temperature dependence of the diffusion constant viscosity ratio is usually ignored [37,57].

The concern with these properties is that in viscous liquids approaching the glass transition the temperature dependence can show strong deviations from Arrhenius behavior. This is illustrated by Figure 1.2.a. Some liquids show little deviation from Arrhenius-type behavior [3] and are customarily classified as "strong liquids". These liquids typically show little difference between the liquid and crystal heat capacities. On the other end of the scale, "fragile liquids" show large deviations of Arrhenius-type behavior and have liquid heat capacities that are significantly larger than the corresponding crystal heat capacities [20], in other words liquids that have a relatively high Kauzmann temperature.

In absence of a complete description of glass formation a plethora of equations is used to fit experimental temperature dependence of relaxation data. From these the Vogel-Fulcher equation is the most common and serves as an example here [27,28]. When related to the viscosity it reads:

$$\eta(T) = \eta_0 \exp\left[\frac{B}{T - T_0}\right], \tag{2.3}$$

where η_0 and B are constants and the divergence temperature T_0 is an attempt to relate the viscosity to a universal, history independent, glass temperature.

A very simple model of the glass transition that actually does predict the VF law is the free volume model of Turnbull and Cohen [66]. Although this model implies simple and unrealistic assumptions – it was conceived as a hard spheres model [67] – it is widely used, especially in polymer science [15]. It states that diffusion takes place when molecules jump to excess free volume that is present in the bulk material. Every so often stochastic rearrangements open up voids large enough to allow a diffusive step. In the model these rearrangements are based on the Stokes-Einstein relation and on the notion that free volume is freely redistributed so that Boltzmann statistics apply. The amount of the excess free volume V_f is temperature dependent as the liquids become denser at lower temperatures:

$$V_f = V_{vg} + \alpha_v(T - T_0). \tag{2.4}$$

Here V_{vg} is the excess free volume at T_0, and α_v is related to the difference in glass and liquid expansion coefficients. It can then be shown that

$$\eta(T) \propto \exp\left[\frac{kV_0}{V_f}\right], \tag{2.5}$$

and the VF law follows. Therefore, when the excess free volume is squeezed out of the bulk the viscosity diverges, i.e. the glass transition occurs. This approach can be, and was [68-70], refined and here it serves as an illustration of the typical features of models that describe the glass transition from a perspective of liquid dynamics and kinetics. In this representation the glass transition occurs as a 'maneuverability crisis'.

The VF equation works reasonably well in strong liquids, although it can by no means be fitted to the temperature dependent relaxation times in all types of liquids at all temperatures. In fragile liquids other approaches are necessary if the data need to be fitted with the same parameters over a wide time and temperature range. The types of liquids that are the subject of this work are simple molecular liquids, and tend to be fragile. Neither this VF equation nor any other three-parameter approach can fit the data spanning a large number of orders of magnitude in these liquids. Only close to the glass transition and in the high temperature limit the curvature of an Arrhenius plot is smaller.

Over limited temperature ranges it is quite successful however in describing the response to rather different types of perturbations with the same parameters. Apparently a strong coupling exists between different relaxation modes of a viscous liquid. Exceptions to this tendency of glasses to exhibit universal temperature dependence for relaxation times for all sorts of responses are substances that contain more than one type of particle, as can be the

case in polymers. For instance, the small particle motions can then get decoupled from the motions of the larger species. Another example is the carefully studied glass of salol that has a mixture of types of interactions between molecules. Both hydrogen bonds and Van der Waals interactions are present, and will cause a system of this type to respond with different relaxation times in different temperature regimes.

But if the interactions between molecules of the material have a consistent nature the VF equation can yield physically meaningful parameters over appreciable time ranges when the transport and thermodynamic relaxation times are examined. The pre-exponent is associated with quasi lattice vibration periods that set the time between successive attempts at crossing some rearrangement barrier or diffusive step. The divergence temperature T_0 is for a large number of substances almost equal to the independently measured Kauzmann temperature T_K and is usually about 10 to 50 K lower than T_g [58-60,71,72].

However, at this time, with no broadly accepted theory of glass dynamics present, one should be careful to interpret these results from viscous liquid relaxation data as universal glass constants. Many interpretation difficulties remain, e.g. macroscopic properties as viscosity reflect the average of relaxation times in a material whereas a measured dielectric relaxation time is usually the most probable relaxation time [37]. Only if the distribution of relaxation times does not vary with temperature, the temperature dependence of the two types of measurements will be equal.

The configurational confinement concept is also present in another early attempt at describing the glass transition. Using the excess entropy, as defined in Chapter 1 with regard to the Kauzmann paradox (see Figure 1.2.c), as the starting point, a third model for the glass transition that is mentioned here is the configurational entropy model by Adam and Gibbs [36]. It describes relaxation as rearrangements within cooperative regions. The size and scale of these regions increases slowly with decreasing temperature until the Kauzmann temperature is reached. Theoretical results then relate the configurational entropy S_C to relaxation times and the viscosity

$$\eta(T) = \eta_0 \exp\left[\frac{C}{TS_C}\right], \tag{2.6}$$

where the configurational entropy follows from the excess heat capacity:

$$S_C = \int_{T_K}^{T} \frac{\Delta C_p(T)}{T} dT . \tag{2.7}$$

When the temperature dependence of the excess heat capacity is assumed to be hyperbolic, the VF law of equation (2.3) is consequently recovered. This provides a connection between the Kauzmann temperature and the divergence temperature.

Notwithstanding this connection and some successes in linking various dynamical properties of a range of glass formers using equation (2.6) [73] it is not entirely clear what rearrangements within cooperative regions exactly are. Evidence seems to point in a direction that links these cooperative regions with basins in the potential energy landscape [31,74]. This landscape is a $3N+1$ dimensional representation of the system, where N represents all the degrees of freedom of the system. In the glass state the system resides in a local minimum of this hyper dimensional space and can only explore a small part of it that depends on the temperature and the height of the surrounding barriers.

In this approach the diverging relaxation times and the vanishing entropy difference between super-cooled liquid and the crystal are linked to the particular properties of the potential energy surface. Any property that is dependent on the availability of configurational states at a certain temperature will show anomalies as T_K is approached.

2.2 Relaxation Dynamics

Apart from the Arrhenius-type exponential dependence of macroscopic observables and relaxation times on temperature, another point of interest in the study of glass dynamics is the decay of a relaxation function with time itself. In order to be able to define an unambiguous relaxation time τ this function must be exponential. This is however rarely the case in viscous liquids and glasses. The decays are usually characterized by distributions of relaxation times as indicated above. A very economical form of describing non-exponential decays is the Kohlrausch function [75], also called a stretched exponential:

$$f(t) = \exp[-t/\tau]^{\beta} \text{ with } 0 < \beta \leq 1. \tag{2.8}$$

It has a stretch parameter β and a relaxation time τ and describes relaxation occurrences in glasses rather well. As can be expected, in the high temperature - high fluidity range the stretch parameter approaches unity and at temperatures closer to T_g the deviations from exponentiality become more pronounced. This departure of exponentiality seems to coincide with the departure from Arrhenius behavior of the relaxation times with respect to temperature. This coincidence is called the time–temperature superposition (TTS) and is predicted by mode coupling theory, which is introduced in the this section, for some special cases. No general explanation yet exists though and the TTS is still under close scrutiny [76]. A correlation between the temperature dependence of the stretch parameter and viscosity for example has not been found yet.

Exponential or not, when investigating relaxation times of super-cooled liquids from the freezing temperature T_f to the glass transition temperature T_g, increases of up to 14 dec-

ades in the relaxation times are found, without the occurrence of major structural changes. To be able to describe this super-cooled regime a model that starts from configurational-confinement concepts as well is gaining acceptance at this moment. It is called mode coupling theory (MCT) [32-34]. It states that nonlinear feedback mechanisms on a microscopic level become so important with decreasing temperatures that they lead to a structural arrest of the substance's constituent particles. The plausibility of the physical assumptions that are the basis of this approach is not completely clear yet, and the VF equation does not follow from this model. It assumes that density fluctuations exist in the viscous liquid or glass, which can be represented as damped density waves or modes. From the decay of the density-density correlation function it can then be demonstrated that various modes are coupled. In short, the decay of the correlation function is related to the self-diffusion coefficient and thus to the viscosity. But since a correspondence between the density-density correlation function and a stress-stress correlation is reasonable as well, and this latter correlation function also sets the viscosity through the exact Kubo formula, a feedback loop is created. This results in a closed nonlinear equation for the viscosity that for finite values of the involved parameters in turn yields a divergence for the relaxation time of density fluctuations. Consequently the viscosity diverges as a power law at what can be explained as an ideal glass temperature.

Although the MCT is not unanimously accepted in the field of glass dynamics – the divergence temperature predicted by MCT is usually well above the experimental glass temperature – it is very successful in predicting the initial slowing down of relaxation times in the high temperature regime well above the glass transition. This initial slowing down, that is corroborated by molecular dynamics simulations, is associated with a high temperature cross-over temperature T_C, below which the molecules can no longer diffuse freely through the system but are somehow confined in a local environment. It is believed by many that the MCT is especially helpful in understanding the early stages of how a free liquid system gets trapped in a single of the many potential energy basins of the potential energy landscape, but is less helpful for describing the intricacies of this configurational space and how the system accesses minima in the energy landscape (*cp*. Figure 1.2).

Above the crossover temperature T_C no localized modes exists in the system, and it will be free to sample the complete configurational space. Below that temperature the first effects of the landscape are felt by the system and activated jumps are necessary to progress from one basin to another. The density of the available states determines the fragility of the liquid. The change from the high temperature free liquid regime to the temperature regime described by collective modes within local configurations is described by MCT (see Figure 1.2.d). On the other side of the glass transition, the substance is trapped in a local minimum

and the system can explore larger parts of the energy landscape only by annealing just below T_G, to find other nearby local minima and lower its entropy in this way.

2.3 Dynamics in the Energy Landscape Regime

If the temperature is lowered to well below the glass transition, all translational motion disappears. Kinetic descriptions of the remaining dynamics are therefore not the obvious choice and a potential energy landscape description is called for. Not withstanding the fact that the number of dimensions of this potential energy hyper landscape is overwhelming, it is ultimately the only complete description for disordered many-body systems. The use of this approach relies on formulating models that capture its essential features for describing the particular problem at hand.

Nevertheless, in this temperature regime the glass phase presents the opportunity of studying particular aspects of the liquid phase. The combination of the comparable structural disorder and the contrasting structural dynamics, allows for the identification of the various inertial and translational contributions solvent dynamics in both phases.

Not only can all translation solvent motion be frozen out below the glass temperature, by cooling further down to cryogenic temperatures below 3 K, all other relaxation channels than those described by the tunnelling two-level system (TLS) model are blocked as well. At these temperatures the thermodynamic properties of glasses differ significantly from those of crystalline materials. The temperature dependence of the specific heat, the thermal conductivity and also the sound velocity are the classic examples of such "anomalous" behaviour [41,77]. Nevertheless there is great simularity in these properties for many different glasses and therefore it was thought that this universal behaviour must arise from their intrinsic disorder. More than 25 years ago the standard two-level system (TLS) model was proposed to explain the anomalies [2,39]. It is based on the assumption that collective structural rearrangement, by means of tunnelling of a local conformational state into another, is the main relaxation mechanism in glasses. These conformational states are represented by two nearly degenerate potential wells, the two-level systems.

The TLS model has been quite successful in the description of the anomalous low-temperature properties of glasses. It also predicts that these properties are time dependent, which has indeed been shown to be the case [78,79]. This time dependence has been attributed to the existence of a broad distribution of rates in the glass at which the tunnelling processes occur. The optical properties of a chromophore dissolved in a glass are dependent on dynamical processes in the direct vicinity of the chromophore. Therefore, these optical properties will also be time dependent. A number of optical techniques have been employed

to explore the dynamics of the chromophores on different time scales and thus probe the distribution of rates of tunnelling processes. Most notably hole burning, photon echo and single molecule spectroscopy have been employed to probe glass dynamics on a range of time scales spanning up to 18 orders of magnitude. This allows for the investigation of the particular nature of the TLS's. These so called optical line narrowing experiments provide a pivotal test for the adequacy of the TLS model in describing glass dynamics.

2.3.1 The TLS-Model

The properties of a cold molecular glass that are discussed here are governed by its multi-dimensional potential hypersurface [40]. This is the potential energy surface spanned by all the degrees of freedom of all the molecules that constitute the glass. The TLS model stipulates that the relevant features of this energy landscape at low temperatures are nearly degenerate double-well potentials. The glass can suitably be described as a random array of these two level systems (the TLS's) [2,39]. The TLS's represent a number of atoms or molecules within the glassy structure that can reside in either of two configurational states. Transitions between the two states of a TLS can occur by phonon-assisted tunnelling. The natural disorder of the glass is represented by distributions of the characteristic features of the double-well potentials.

A TLS is a convenient representation of low-level excitations in the glass potential energy surface since it can be described by a simple spin-boson Hamiltonian with a basis set of two localized wave functions:

$$\mathbf{H}_{TLS} = \varepsilon \mathbf{S}_z - \Delta \mathbf{S}_x = \frac{1}{2} \begin{pmatrix} \varepsilon & -\Delta \\ -\Delta & -\varepsilon \end{pmatrix}. \tag{2.9}$$

Here $\mathbf{S}_z = \frac{1}{2}(|R\rangle\langle R| - |L\rangle\langle L|)$ and $\mathbf{S}_x = \frac{1}{2}(|R\rangle\langle L| + |L\rangle\langle R|)$ are Pauli operators. Therefore a double well potential is characterized by an asymmetry ε and a tunnelling matrix element Δ as is shown in Figure 2.1. In fact, the tunnelling matrix element, or the overlap between the two states can be evaluated exactly for harmonic potentials, and depends exponentially on the barrier height V:

$$\Delta = \hbar E_0 \exp\left[\frac{-2md^2V}{\hbar^2} \right]^{\frac{1}{2}}, \tag{2.10}$$

where E_0 is the eigen frequency of one of the states, d the well separation and m the tunnelling particle mass. However only Δ and ε are regarded as parameters in this model and from them the energy gap between the two eigenstates $|1\rangle$ and $|2\rangle$ can be calculated. These eigenstates of the TLS Hamiltonian are
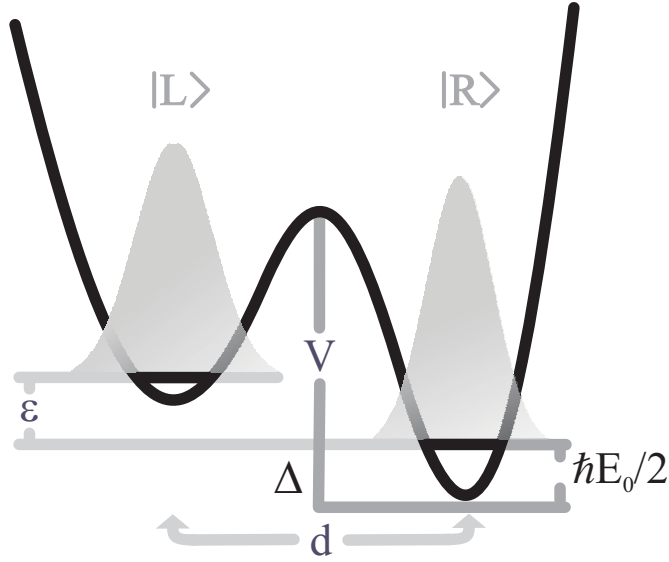
Figure 2.1. Left: A Two Level System with energy splitting ε and a tunnelling matrix element Δ that is set by the barrier height as $\Delta \propto \exp(-d^2 V)$.

$$\begin{aligned} |1\rangle &= \cos\varphi |L\rangle + \sin\varphi |R\rangle \\ |2\rangle &= -\sin\varphi |L\rangle + \cos\varphi |R\rangle. \end{aligned} \qquad (2.11)$$

Here $\tan(2\varphi) = \Delta/\varepsilon$. The energy gap of the eigenvalues of these states is

$$E = \sqrt{\varepsilon^2 + \Delta^2} \ . \qquad (2.12)$$

The two main parameters are considered to be uncorrelated and distributed with featureless probability functions. In the original standard model these probability functions have the following form:

$$P(\varepsilon) \sim constant \qquad |\varepsilon| < \varepsilon_{max} \qquad (2.13)$$

$$P(\Delta) \sim \frac{1}{\Delta} \qquad \Delta_{min} < \Delta < \Delta_{max} \ . \qquad (2.14)$$

The probability distribution function of equation (2.13) is chosen as simple as possible since there is no *a priori* theoretical reason to assume any particular form. This reflects the true random nature of an amorphous material. The potential energy hypersurface of the glass is frozen in at the glass temperature T_g . Thus the extreme values of the energy differences ε between two configurational states are on the order of plus and minus kT_g . The glass temperatures [16] of all molecular glasses studied here and elsewhere are at least 100 K. The experiments are done at temperatures around 1 K and therefore in this temperature

region the distribution $P(\varepsilon)$ is considered very broad, since $\varepsilon_{max} \gg kT$, and is set constant. The same applies for the maximum of the distribution function of the tunnelling matrix element. The minimum value of this function is also chosen so that it does not contribute to the outcome of the calculation by associating it with a value that corresponds to a flipping rate that is much slower than can be measured with the longest experimental time scale available.

This standard tunnelling model successfully predicts a number of thermodynamical and acoustic properties of glasses at low temperatures [41,42,80-86]. Not surprisingly it has also been used for the interpretation of optical experiments on glasses [87-100]. As explained earlier, when a chromophore is dissolved in a glass matrix, its resonance frequency is dependent on its local environment. This leads to optical spectra at low temperatures that are strongly inhomogeneously broadened. This is clearly due to the disordered nature of the glass that allows for much more variety of local structures near chromophores than is the case in a crystal. As will be shown below, the distributions of ε and Δ lead to a very broad distribution of flipping rates of TLS's. In fact, TLS's change from one of the two states to the other on time scales varying from picoseconds to hundreds of years. This distribution of relaxation rates represents the dynamical processes in the glass. Its shape is modelled by the choice of the distribution of TLS parameters in equations (2.13) and (2.14). Thus by probing the distribution of TLS flipping rates, the validity of these choices can be verified.

When a flipping TLS couples to a chromophore, the optical resonance frequency of the chromophore becomes a time dependent property. Since the chromophores couple to a number of different TLS's, their resonance frequencies perform a random walk through frequency space.

The result is that the optical line width of a subset of chromophores with indistinguishable resonance frequencies, as introduced in the first chapter, is now dependent on the time scale t_w of the particular selection experiment [95,96,101,102]. The time scale of the experiment is the time between selecting the set of chromophores and the determination of the optical line width of the set. When t_w is increased, TLS's with slower relaxation rates can also contribute to the line broadening. Consequently this waiting time dependence can be used to probe the very broad distribution of TLS relaxation rates.

2.3.2 Modifications to the Standard Model

Since its introduction and application to optical experiments, numerous studies have indicated that the TLS model in its initial form cannot account for the distribution of relaxation rates needed to give an explanation for the experimental results. Already at the time of the

first optical experiments on amorphous solids [92,97,103] several modifications of the standard tunnelling model were proposed to still be able to explain the results in a universal way. This usually involves modifying the forms of the TLS parameter distributions of equations (2.13) and (2.14). Notably, Silbey *et al.* [87,91] proposed the distributions:

$$P(\varepsilon) = \frac{1+\mu}{\varepsilon_{max}^{1+\mu}} \times \begin{cases} \varepsilon^{\mu} & \text{for } 0 \leq \varepsilon \leq \varepsilon_{max} \\ 0 & \text{otherwise,} \end{cases} \tag{2.15}$$

$$P(\Delta) = \begin{cases} \dfrac{\nu}{\Delta_{max}^{\nu} - \Delta_{min}^{\nu}} \times \dfrac{1}{\Delta^{1-\nu}} & \text{for } \Delta_{min} \leq \Delta \leq \Delta_{max} \text{ and } \nu > 0 \\[2mm] \dfrac{1}{\ln[J_{min}/J_{max}]} & \text{for } \Delta_{min} \leq \Delta \leq \Delta_{max} \text{ and } \nu = 0 \\[2mm] 0 & \text{otherwise.} \end{cases} \tag{2.16}$$

This time, normalization factors are included [104]. Note that for $\nu \rightarrow 0$ the normalization factor of the distribution becomes $1/\ln[\Delta_{max}/\Delta_{min}]$. The extremes of the probability distributions remain the same, i.e. $\varepsilon_{max} \gg kT$, since TLS's with a large energy splitting will have a very slow flipping rate and will therefore not contribute to any dephasing. Positive and negative asymmetries are equally probable and including negative values will only lead to renormalization of the distribution, and therefore the minimum value is set to zero.

The second distribution function, following the same line of reasoning, is based on the Wentzel-Kramers-Brillouin description of the tunnelling matrix element [105]. Since a limited spread in the elements constituting the exponential term, as shown in equation (2.10), already result in a large range of real and positive values for Δ, the upper cut-off in this model is again assumed to be $\Delta_{max} \gg kT$. The minimum value of the tunnelling matrix element is chosen such that $\Delta_{min} \ll (2ckTt_w^{max})^{-\frac{1}{2}}$, where t_w^{max} is the longest experimental time scale possible [84].

The dimensionless parameters μ and ν are fitting parameters for any experimental observations that cannot be covered by the original form of the model. It was estimated [87,106] that for most glasses $\mu \approx 0.3$ to explain the characteristic temperature dependence of optical line widths in glasses [43]. From numerical experiments on glasses [107-110] and to explain short time scale non-exponential echo decays [87] it was guessed that ν is on the order of $0.0 \sim 0.2$.

Since the standard TLS model emerges as a special case of the model proposed by Silbey *et al.*, we will use the latter throughout the remainder of this thesis even though there is no particular *a priori* reason to expect that the distribution of the thermally accessible local minima in the potential energy landscape has any features.

2.3.3 TLS–Phonon Coupling; Phonon Assisted Tunnelling

The TLS's are flipped from one state to another by the phonon bath. This is called phonon assisted tunnelling. The usual approach is to consider one-phonon processes only [111]. Suppose TLS's that weakly couple to the phonon bath; then a single TLS–phonon interaction Hamiltonian is put as

$$\mathbf{H}_{TLS-phonon} = \varepsilon \mathbf{S}_z - \Delta \mathbf{S}_x + \sum_q b_q b_q^\dagger \omega_q + \sum_q g_q \left(b_q + b_{-q}^\dagger \right) \cdot \mathbf{S}_z \ . \tag{2.17}$$

Here the index q labels all the phonon modes of the system with angular frequency ω_q, additionally b_q and $b_q^\dagger$ are the respective annihilation and creation operators of that mode and g_q is its TLS strain field coupling constant.

The relaxation rate, the sum of the rate constants for upward (w_1) and downward (w_2) tunnelling, follows from Fermi's golden rule, by fulfilling the detailed balance condition for thermal equilibrium:

$$\frac{w_1}{w_2} = \exp\left[-\frac{E}{k_B T} \right] . \tag{2.18}$$

At a finite temperature well below the Debye temperature, the direct absorption or emission of a single phonon will then lead to a total relaxation rate *R:*

$$R = w_1 + w_2 = c\Delta^2 E \coth\left[\frac{E}{2k_B T} \right], \tag{2.19}$$

where c is set by the sound velocity v_s in the glass and its deformation potential parameter γ, that depends on the TLS-coupling to longitudinal and transverse elastic waves, and the mass-density ρ_m of the glass [81,84]:

$$c = \frac{\gamma^2}{v_s^5} \frac{1}{2\pi\hbar^4 \rho_m} \ . \tag{2.20}$$

These parameters are known quantities for a large number of glasses from acoustical experiments.

The spread in the parameters ε and Δ lead to a very broad distribution [86,88,112-114] of TLS relaxation rates. This function is best expressed in terms of the relaxation rate R and the energy splitting E. By summing over all the relevant values of ε and Δ, as given in equations (2.15) and (2.16), the distribution of relaxation rates is found to be [87,91]

$$P(R,E) = P_0 \frac{E^{\mu+\nu}}{R^{1-\nu/2} \left(1 - R/R_{max} \right)^{1/2(1-\mu)}} , \tag{2.21}$$

where $R_{max} = cE^3 \coth\left(E/2kT \right)$ is the fastest tunnelling rate for a TLS with a energy level difference E. The slowest possible flipping rate becomes:
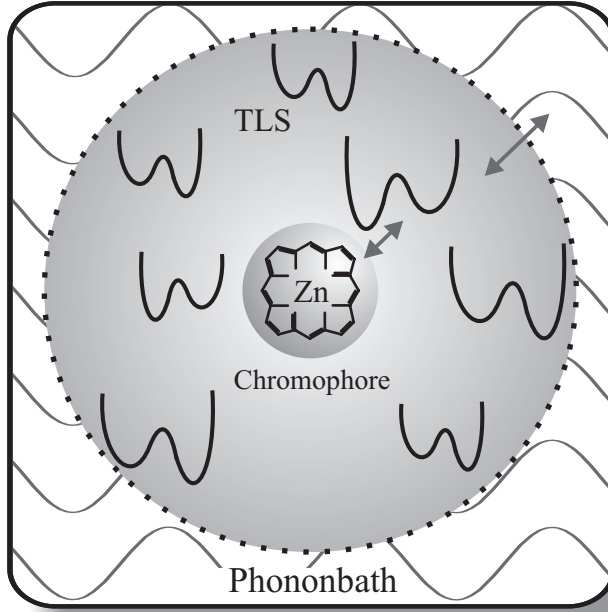
Figure 2.2. Chromophores couple to TLS's that are flipped by the phonon bath.

$$R_{\min} = c\Delta_{\min}^2 E \coth\left[E/2kT\right].$$
(2.22)

Note that in the case that $R \ll R_{\max}$ and $\mu = \nu = 0$, this yields a hyperbolic distribution of flipping rates:

$$P(R) \sim 1/R.$$
(2.23)

Finally the normalization constant is defined as:

$$P_0 = \frac{\nu(1+\mu)}{\varepsilon_{\max}^{1+\mu}\left(\Delta_{\max}^{\nu} - \Delta_{\min}^{\nu}\right)} \overset{\nu \to 0}{=} \frac{1+\mu}{\varepsilon_{\max}^{1+\mu} \ln\left[\Delta_{\max}/\Delta_{\min}\right]}.$$
(2.24)

Using the distribution $P(E,R)$, the consequences of spectral diffusion for the echo signal can be calculated in the framework of a non-linear spectroscopy formalism.

2.3.4 TLS–TLS Coupling

Interactions between TLS's are likely to occur. When the bath shifts from one conformational state into another at one place, this is likely to inflict a strain field at the site of an-

other TLS. In fact, such coupling is believed to determine the pure dephasing rate in acoustic phonon echo experiments [80,94,112]. However, the energy splitting of a TLS coupled to a chromophore caused by another TLS will probably be small compared to the TLS asymmetry itself and will therefore be insignificant to the fluctuations caused in the energy levels of the chromophore. The TLS are treated as evolving independently in optical spectroscopy and therefore the TLS jumps are assumed to be uncorrelated. Studies on linearly coupled TLS's coupled to a phonon bath have confirmed the validity of this approach [115].

2.3.5 TLS–Chromophore Coupling; Spectral Diffusion

The time dependence of the resonance frequencies of chromophores that couple to TLS's for some distribution $P(E,R)$, was first deduced by Black and Halperin [112] following the work of Klauder and Anderson [116] on spectral diffusion in magnetic resonance experiments and was later extended to the optical domain [99,100,106]. The TLS's are considered as elastic dipoles, so that flipping of the i-th TLS leads to a variation $\delta \vec{e}_i$ of the strain field $\vec{e}_i$:

$$\delta \vec{e}_i = \frac{\varepsilon_i}{E_i} \cdot \frac{\bar{\bar{T}}_i}{\mathbf{r}^3} .$$
(2.25)

The tensor $\bar{\bar{T}}_i$ depends on the deformation potential parameter γ from equation (2.20) and on the orientation of the TLS with respect to the chromophore. This deformation potential tensor can be combined with some electronic–elastic coupling parameter into a TLS–chromophore coupling constant Ω to express the frequency shift of the j-th probe molecule as

$$\delta \omega_{ij} = \frac{3\sqrt{3}}{4} \pi \Omega \frac{\varepsilon_i}{E_i} \frac{\left(1 - 3\cos^2 \theta_i\right)}{r_{ij}^3} .$$
(2.26)

The TLS–chromophore distance is r_{ij} and θ_i is the relative orientation. The relative orientation is random, so averaging over this parameter distribution would only renormalize the coupling constant by using

$$\int_{-1}^{1} \left|1 - 3\cos^2 \theta\right| d\cos\theta = \frac{8}{3\sqrt{3}} .$$
(2.27)

In the sudden jump model [116] it is assumed that this shift is immediate and can be represented by stochastic variable $h(t)$ that is a telegraph function representing the random flipping of a TLS [84,89,100,102,117]:

$$\omega_j(t) = \omega_0 + \sum_i \delta \omega_{ij} h_i(t) .$$
(2.28)

The final step in finding an expression for the spectral diffusion lies in averaging over the distributions over the relevant parameters influencing the frequency offset. In order to perform this average the TLS's are supposed to be uniformly distributed over space with random orientation within a sphere of radius r_{max} :

$$P(r) = \begin{cases} \dfrac{3r^2}{r_{max}^3} & if \ r \leq r_{max} \\ 0 & if \ r > r_{max}. \end{cases} \tag{2.29}$$

The maximum radius is introduced to bring the normalization of the distribution about. This radius is taken to infinity at some point during the averaging.

Lately, Monte Carlo-type simulations on sets of chromophores coupled to randomly chosen sets of TLS's have led to questions concerning the validity of implicitly setting the lower cut-off of this distribution to zero [118,119]. The TLS's and chromophores are considered to be point dipoles and can be infinitely close. This is not necessarily a realistic situation, but at this time there is not enough evidence to warrant an overhaul of the theory at this point.

Finally it should be noted that it is thought that TLS's are only weakly coupled to the chromophores, i.e. that an excitation of a chromophore does not influence any TLS's. This leaves only the distributions of equations (2.15) and (2.16) and their respective cut offs as parameters for the interpretation of the echo experiments. It will be shown that if the choices for the cut offs are made as mentioned, they will not affect this interpretation, leaving only the specifics of the TLS internal parameter distributions as an explanation for time and temperature dependence of the experimental results.

2.4 Liquid Dynamics

In the above the interactions of the chromophores with the molecules of the solvent is outlined for the case of cold molecular glasses. Solvation dynamics, however, is a field that concerns all condensed phases at all temperatures. Particularly the influence of liquids at room temperature on solutes is the focus of many studies. This is caused by the influence of solvation dynamics on chemical reactivity. Chemical reactions that take place at room temperature in a liquid solvent, are of course very common, as e.g. almost all biological reactions take place under these circumstances. Understanding the role of the solvent in such processes is therefore an important part of understanding these reaction. For instance, in a particular chemical reaction, the dynamically evolving solvent shells can provide the energy to surmount reaction barriers or create reaction paths that otherwise would have been

blocked and thus influencing the outcome of the reaction [120]. Especially reactions that involve some sort of charge transfer are particularly influenced by the surroundings.

As with glasses, in this work solvation is studied without an actual reaction happening. By monitoring the effects of the solvent on a dissolved chromophore after excitation, just as with glasses, detailed information about solvent effects on the microscopic state of the solute can be retrieved. The model used in room temperature experiments, differs from that used in experiments on cold glasses in that it can incorporate a bath response to a change in state of the chromophore.

The most straightforward way to illustrate this response is to consider the time resolved fluorescence spectrum of an excited chromophore and the associated Stokes shift. The Stokes shift clearly indicates the reorganization of the surroundings of the optical transition either by intramolecular or intermolecular relaxation. Hence, time resolved fluorescence spectroscopy is often used to study solvation dynamics. In these studies the aim is to connect the reorganization energy, the relaxation times and also inhomogeneous widths of the spectra with solvent motions as studied through statistical thermodynamic theory and computer simulations [121-124].

As an example, suppose the following Hamiltonian characterizes an optical system:

$$\mathbf{H}_{e,g} = \mathbf{H}^0_{e,g} + \mathbf{H}_{bath} + \mathbf{V}_{e,g-bath} \,, \tag{2.30}$$

where the energy difference between the excited state e and the ground state g in the unperturbed gas phase sets the resonance frequency $\hbar\omega_{eg} = \mathbf{H}^0_e - \mathbf{H}^0_g$. The solvent Hamiltonian is $\mathbf{H}_{bath}$ and the system-bath coupling potential is expressed through $\mathbf{V}_{g-bath} = \mathbf{V}_{g-bath} + \Delta E$. These latter interactions cause a fluctuation of the energy gap that is the point of interest here:

$$\overline{\hbar\omega}(t) = \mathbf{H}_e(t) - \mathbf{H}_g(t) = \hbar\omega_{eg} + \overline{\Delta E}(t). \tag{2.31}$$

The time dependent fluorescence Stokes shift is therefore expressed as a normalized response function of this fluctuating energy gap:

$$S(t) = \frac{\overline{\hbar\omega}(t) - \overline{\hbar\omega}(\infty)}{\overline{\hbar\omega}(0) - \overline{\hbar\omega}(\infty)} = \frac{\overline{\Delta E}(t) - \overline{\Delta E}(\infty)}{\overline{\Delta E}(0) - \overline{\Delta E}(\infty)} \,. \tag{2.32}$$

The overbar indicates an average. Thus the dynamics are dominated by the average solvent excited state interaction $\overline{\Delta E}(t)$ [123,124]. Within the linear response approximation, valid for small fluctuations relative to the energy gap, this response function is expressed as a normalized time correlation function [125]. The energy gap right after excitation of a chromophore i is characterized by an ensemble averaged quasi-equilibrium offset $\langle\Delta E\rangle$ due to the charge redistribution in the excited state and the fluctuating contributions of the solvent [121]:

$$\Delta E_i(t) = \langle\Delta E\rangle - \delta E_i \,. \tag{2.33}$$

The average correlation between $\delta E(t)$ and $\delta E(0)$ is described by the time correlation function

$$C(t) = \left\langle \delta \mathrm{E}(t) \delta \mathrm{E}(0) \right\rangle .$$ (2.34)

Whereas at short times the correlation function has a finite value $\lim_{t \to 0} C(t) = \left\langle \delta E(0)^2 \right\rangle$, at long times this function vanishes: $\lim_{t \to \infty} C(t) = 0$. This correlation decay is the regression of microscopic fluctuations in Onsager's theorem, which relates the correlation function to the evolution of a macroscopic relaxation of an observable $\overline{\Delta E}(t)$ in an initial state not far from equilibrium, towards the equilibrium value $\left\langle \Delta E \right\rangle$ [126,127]. Using the classical fluctuation dissipation relation this theorem yields an expression relating the fluorescence Stokes shift to the correlation function:

$$S(t) = \frac{\overline{\Delta E}(t) - \left\langle \Delta E \right\rangle}{\overline{\Delta E}(0) - \left\langle \Delta E \right\rangle} = \frac{\left\langle \delta E(t) \delta E(0) \right\rangle}{\left\langle \delta E(0)^2 \right\rangle} .$$ (2.35)

This shows that even without choosing a particular model for the system-bath interactions the optical response in a time resolved fluorescence experiment can be defined in terms of a normalized autocorrelation function of the energy gap using very general arguments. The echo experiments described in this work are also described in terms of the same two-time correlation functions of the energy gap

$$M(t_1, t_2) = \frac{\left\langle \delta\omega(t_2) \delta\omega(t_1) \right\rangle}{\left\langle \delta\omega(t_1)^2 \right\rangle} .$$ (2.36)

Various models can be applied for relating the correlation function to the physical processes of bath dynamics. To relate optical experiments at room temperature to molecular dynamics studies in liquids the instantaneous normal mode analysis is often used. This method, suggested some time ago, emphasizes the significance of the shape of the potential energy surface explored in liquids. The instantaneous normal mode approach treats the liquid in effect as a set of bilinearly-coupled harmonic oscillators. It uses the eigenvectors (normal modes) and eigenvalues of the Hessian matrix (the second derivatives of the potential energy) to provide a snapshot of the multidimensional landscape in the neighbourhood of an equilibrium phase space point [128-133]. The oscillators and their frequencies are determined by taking an ''instantaneous'' representation of a liquid by calculating and diagonalizing the Hessian matrix with respect to the coordinates of the bath.

The phonon-based harmonic mode models are well established descriptions for solvation dynamics in the high–temperature high–fluidity regime. At the other end of the temperature scale the chromophore – solvent interaction in low temperature glasses is also extensively studied as described in the previous section. In the intermediate regime no dominant approach exists. At temperatures just above the regime where the TLS-model applies the tem-

perature dependence of optical line shapes is usually described with additional chromo-phore–phonon coupling terms [134-136].

There have been numerous attempts to describe glass dynamics at even higher tempera-tures in conjunction with the high temperature harmonic mode models [38,137-139]. This usually involves harmonic modes about some local minimum in the potential energy sur-face until a thermal fluctuation causes a barrier crossing event [140].

Another theoretical approach used in this respect is the earlier mentioned mode-coupling theory, since it quantitatively predicts the time evolution of the correlation function and the dependence on temperature of characteristic correlation times [141]. The temperature re-gion in which MCT is able to make predictions for the long time dynamics is limited to weakly super-cooled states. So, unfortunately, the analysis of optical experiments with these models outside this temperature range is not well established at this time [142-144].

So far no dominant self-consistent approach for describing the complete intermediate temperature regime has emerged. Therefore, for the time being, only the two heuristic mod-els that are most often used in non-linear optics at room temperature will be briefly intro-duced here.

2.4.1 The Stochastic Model

Many methods exist to model the influence of a heat bath on the electronic state of the chromophores. In the above TLS model the influence of the heat bath was modelled by ran-dom changes of the eigen-frequency of the chromophores by weakly coupled TLS-flips. The implicit step therefore, is a division of the Hamiltonian of a total system in a part that is precisely calculated, the optical transition in this case, and a part that lumps together all other degrees of freedom together as a random process.

In room temperature solvent dynamics a similar division is made, but then quite often the bath fluctuations are treated as an abstract stochastic process [55,145-147]. It appears in the description only as a probability distribution of the random frequency walks and a cor-relation time of the fluctuations. This then requires no specific knowledge of the physical properties of the bath. Depending on the choice of distribution and timescale of the fluctua-tions an expression can be derived for the evolution of the electronic state of the chromo-phores. A choice often made, for convenience, is the Kubo random oscillator. That model treats the stochastic fluctuations as a Gauss-Markov process [125]. This choice is not based on any physical knowledge of the solvent other than that it causes random frequency fluc-tuations and that it is weakly coupled to the solute, and therefore this approach is usually referred to as the stochastic model.

In this case the electronic states of system are projected on a collective solvent coordinate $\mathbf{Q}$, which means that the system – bath interaction is spread out over numerous solvent degrees of freedom. Therefore fluctuations of the energy gap are characterized by Gaussian statistics and can be represented by an effective harmonic representation even though the underlying microscopic modes of the solvent might be very anharmonic.

So a typical Hamiltonian for a chromophore approximated as an optical two level system with system coordinate $\mathbf{Q}_S$ would look like:

$$\begin{aligned}
\hat{\mathbf{H}}_{tot} &= |g\rangle\Big[\hat{\mathbf{H}}_g(\mathbf{Q}_S) + \hbar\,\delta\omega_g(t)\Big]\langle g| + |e\rangle\Big[\hat{\mathbf{H}}_e(\mathbf{Q}_S) + \hbar\omega_{eg} + \hbar\,\delta\omega_e(t)\Big]\langle e| \\
&= |g\rangle\hat{\mathbf{H}}_g(\mathbf{Q}_S)\langle g| + |e\rangle\Big[\hat{\mathbf{H}}_e(\mathbf{Q}_S) + \hbar\omega_{eg} + \hbar\,\delta\omega(t)\Big]\langle e|.
\end{aligned} \tag{2.37}$$

This very simple Hamiltonian only considers the adiabatic eigen states of the optical system through $\hat{\mathbf{H}}(\mathbf{Q}_S)$ with an energy difference $\hbar\omega_{eg}$ and ignores any interaction with these modes other than a modulation of this energy gap $\hbar\delta\omega(t)$.

2.4.2 The MBO Model

If one wishes to include strong interaction between bath and system, it makes of course sense to only consider a few relevant bath modes explicitly in the Hamiltonian instead of all possible bath modes. In the multimode Brownian oscillator (MBO) model this is done by coupling the adiabatic eigenstates of the optical system linearly to a limited number of nuclear harmonic oscillator modes. These modes can then either depend on the nuclear state of the system or also couple to the system in precise the same way as a Gauss-Markov heat bath would [55,147].

At room temperature the MBO model is successfully used to describe the solvent dynamics in the liquid phase [145,148]. It has been tested at lower temperatures as well [149-151]. In this model the system is again described as a two level Hamiltonian, but now coupled to a number of harmonic oscillators that describe the nuclear coordinates $\mathbf{Q}_B$ of the bath.

$$\hat{\mathbf{H}}_{tot} = |g\rangle\Big[\hat{\mathbf{H}}_g(\mathbf{Q}_S) + \hat{\mathbf{h}}_g(\mathbf{Q}_S, \mathbf{Q}_B)\Big]\langle g| + |e\rangle\Big[\hat{\mathbf{H}}_e(\mathbf{Q}_S) + \hat{\mathbf{h}}_e(\mathbf{Q}_S, \mathbf{Q}_B)\Big]\langle e|. \tag{2.38}$$

For convenience the system modes are described as two linearly displaced harmonic potentials:

$$\hat{\mathbf{H}}_{e,g} = \frac{P^2}{2m} + \frac{m\omega_0^2}{2}\big(Q + D_{g,e}\big)^2. \tag{2.39}$$

The system with momentum P, coordinate Q, mass m, frequency ω_0 and displacement D ($D_g \equiv 0$) couples to a number of N harmonic modes

$$\hat{\mathbf{h}}\left(\mathbf{Q}_S,\mathbf{Q}_B\right) = \sum_{i=1}^{N} \frac{p_i}{2m_i} + \frac{m_i\omega_i^2}{2}\left(q_i + \frac{c_i Q}{m_i\omega_i}\right)^2 , \qquad (2.40)$$

that in turn have momentum, coordinate, mass, frequency and also a coupling constant c_i. These modes all result in a damping of the harmonic oscillator that is usually taken to be independent of its frequency

$$\gamma_i\left(\omega\right) = \frac{c_i^2}{2m_i\omega_i^2}\delta\left(\omega - \omega_i\right) \approx \gamma_i . \qquad (2.41)$$

Moreover since the two potentials of the harmonic chromophore are linearly displaced, any change in its coordinates will result in an energy fluctuation that depends on the displacement. In this idealized case, all the solvent dynamics can be related to a correlation function of the energy gap through the spectral density of states. In the Brownian oscillator model it is simply supposed to consist of a number of harmonic modes:

$$C\left(\omega\right) = \sum_i^N C_i\left(\omega\right) = \frac{2}{\pi}\sum_i^N \frac{\lambda_i\omega_i^2\gamma_i\omega}{\left(\omega_i^2 - \omega^2\right) + \omega^2\gamma_i^2} . \qquad (2.42)$$

The amount of reorganization of the bath upon a change of state of the system and fluctuations of the systems energy gap can be straightforwardly related to correlation functions that directly depend on this spectral density. Although, as later will be shown, this approach offers a very complete description of solvent dynamics studied through optical experiments, it sheds as little light on the physical processes that cause frequency fluctuations as the previous model.

A defining point of the MBO model is that it treats the system as two identical harmonic potentials that couple linearly to the harmonic bath modes. The coupling term $\hat{\mathbf{h}}\left(\mathbf{Q}_S,\mathbf{Q}_B\right)$ in the Hamiltonian of equation (2.38) is expressed using a cumulant expansion that is cut off after the linear term. At room temperature when the bath is fluctuating fast and with nearly identical potential energy surfaces of the system's ground and excited state, this is a reasonable approximation. In the case that the ground and excited state propagate differently in time or when the fluctuations are slower, so that the fluctuation dissipation theorem does not hold, however, higher order coupling terms might need to be considered. Unfortunately, addressing the effects of quadratic coupling of even higher order coupling terms on the general outcome of optical experiments is not trivial. Some of the characteristics and effects of these terms will be discussed in Chapter 6 in order to clarify the temperature dependence of the ultrafast initial decay of the optical polarization.

Chapter 3

The Photon Echo Technique

A structure is outlined for the description of nonlinear optical techniques in general and photon echo experiments in particular. The traditional terms in which photon echo results are discussed, are introduced. The effects of various representations of the heat bath on the expressions for the photon echo signals, are established.

3.1 Introduction

In recent years significant advances have been made on the theoretical description of four wave mixing experiments [52,55]. In essence, the theories report on the evolution of the electronic states of a system that is in contact with a bath, while it interacts with a number of externally applied electromagnetic fields. The system includes those degrees of freedom that interact with the radiation fields applied in the experiment. The bath covers all other degrees of freedom. Depending on the number of degrees of freedom of the bath that interact with the system, and the amount of symmetry these modes contain, one chooses an appropriate method of incorporating the system-bath interactions in the description of the experiment. In baths that consist of condensed matter, which are the subject of this study, it is obviously impossible to use a full quantum mechanical description of the bath, due to the vast number of bath states and their random and asymmetric nature. Also, the number of degrees of freedom of the modes that interact with the optical fields, is very large in these experiments. Therefore one has to resort to an ensemble-averaged description of the evolution of the system that is classical with respect to the system-bath interaction.

This chapter will introduce the details of the photon echo technique, through the formalism developed by Mukamel and Loring [55,152,153]. Also some concepts that follow from the more traditional Maxwell-Bloch approach, that can be helpful when discussing the experimental results, will be introduced [154]. Then the effects of system-bath interactions on optical experiments will be introduced in a context that applies to glasses and in one that applies to liquids. The focus will be on those aspects of these approaches that are under scrutiny in the following chapters. More detailed accounts of these descriptions can be found elsewhere and references are given in the appropriate sections of this chapter.

Various other non-linear optical techniques can be used to study solvent dynamics as well. In ultrafast spectroscopy, especially photon echo spectroscopy is often used to study solvent dynamics efficiently, but this is by no means the only technique. For example, the optical Kerr effect, fluorescence upconversion and various coherent Raman scattering experiments can be used [53,54].

3.2 Non-Linear Polarization and Wave Equation

The photon echo experiment is an example of non-linear spectroscopy in general and of the four-wave mixing technique in particular. In non-linear spectroscopy the optical response of the sample depends on the incident optical fields in a non-linear manner. The material of the sample interacts with these fields and this interaction results in a polarization. The polarization can be expanded in powers of the applied fields, in order to quantify any non-linearity in a perturbative manner [155-157]:

$$
\begin{aligned}
\tilde{P}(t) &= \chi^{(1)} \tilde{E}_{appl}(\mathbf{r},t) + \chi^{(2)} \tilde{E}_{appl}^2(\mathbf{r},t) + \chi^{(3)} \tilde{E}_{appl}^3(\mathbf{r},t) + \cdots \\
&\equiv \tilde{P}^{(1)}(\mathbf{r},t) + \tilde{P}^{(2)}(\mathbf{r},t) + \tilde{P}^{(3)}(\mathbf{r},t) + \cdots
\end{aligned}
\tag{3.1}
$$

Here $\chi^{(n)}$ is the n-th order susceptibility tensor associated with the n-th order polarization $P^{(n)}(\mathbf{r},t)$. The induced polarization in turn acts as a source for the optical response $E_s(t)$ of the sample. It contains all the information needed for the interpretation of a spectroscopic experiment.

This expansion of the polarization implies that the incident radiation fields are weak, relative to the internal electric fields due to the system's atomic electrons and nuclei. Furthermore, the fields are treated as classical Maxwell fields, but the relevant optical modes of the system are treated quantum mechanically. The first assumption assures that the propagation of the new response field in non-linear media with refractive index n is in turn governed by the Maxwell equations [52-55,157]. In isotropic source free media, as used in this work, the wave equation is

$$\nabla \times \nabla \times \tilde{E}\left(\mathbf{r},t\right) + \frac{n^2}{c^2}\frac{\partial^2 \tilde{E}\left(\mathbf{r},t\right)}{\partial t^2} = \frac{-4\pi}{c^2}\frac{\partial^2 \tilde{P}\left(\mathbf{r},t\right)}{\partial t^2} \ . \tag{3.2}$$

Four wave mixing implies three incident fields with wave vector $\mathbf{k}_n$, that are e.g. quasi-monochromatic linearly polarized plane waves

$$\tilde{E}\left(\mathbf{r},t\right) = \sum_{n=1}^{3} E_n\left(t\right)\exp\left[i\left(\mathbf{k}_n \cdot \mathbf{r} - \omega_n t\right)\right] + c.c. \ , \tag{3.3}$$

that induce a polarization $\tilde{P}\left(\mathbf{r},t\right)$ which in turn gives rise to a plane wave signal $\tilde{E}_s\left(\mathbf{r},t\right)$. When it is assumed that the signal has a field amplitude $E_s\left(t\right)$ that varies slowly compared to the carrier frequency ω_s, the wave equation can be simplified to a first order form when it is transformed to a frame moving at the speed of light c [158]. The solution for the generated signal in a sample of thickness L, will be like

$$E_s\left(L,t\right) = \frac{2\pi i \omega_s L}{n\left(\omega_s\right)c} P\left(t\right)\mathrm{sinc}\left[\Delta\mathbf{k} \cdot L/2\right]\exp\left[i\Delta\mathbf{k} \cdot L/2\right]. \tag{3.4}$$

This introduces the phase matching condition, which states that in order to have any detectable signal, the wave vector mismatch $\Delta\mathbf{k}$ must be small. In fact, the condition

$$\Delta\mathbf{k} \equiv \mathbf{k}_s - \sum_{n}\mathbf{k}_n << \frac{\pi}{L} \tag{3.5}$$

must be met.

The even order terms in equation (3.1) vanish in random isotropic materials and centrosymmetric crystals, since changing the sign of the applied fields results in a change of sign of the induced polarization, while at the same time this polarization should not be dependent on direction in these materials. Therefore the lowest order nonlinear polarization is $P^{(3)}$ and it acts as the source for the photon echo signals discussed in this work. The third order polarization can be expressed as a convolution of the three incident fields and some nonlinear system response function $R^{(3)}$ [159]:

$$P^{(3)}\left(\mathbf{r},t\right) = \int_0^{\infty}dt_3\int_0^{\infty}dt_2\int_0^{\infty}dt_1\ R^{(3)}\left(t_3,t_2,t_1\right)E_1\left(\mathbf{r},t-t_3\right)E_2\left(\mathbf{r},t-t_3-t_2\right)E_3\left(\mathbf{r},t-t_3-t_2-t_1\right). \tag{3.6}$$

Here $R^{(3)}$ is used to track all contributions to the signal by the solute molecules. In this work these chromophores are modelled as two level systems. The third order response function is determined by the dependence of the nonlinear susceptibility on the material parameters as the transition dipole moments and electronic energy levels of the chromophores and is therefore influenced by all nuclear and electronic motions and relaxation processes of the system.

3.3 The Density Matrix

Photon echo experiments rely on the sensitivity of the resonance frequency of dissolved chromophores to their surroundings. This sensitivity is clearly manifested by the broad featureless absorption spectra of dissolved chromophores. By charting the time-resolved correlation function of optical transitions upon ultra short excitation, detailed insight into the dynamics of the solvent can be obtained.

Thus, to be able to assess the optical response from a particular sample, not only information about the applied excitation fields is needed, but also knowledge about the electronic state of the system. If one wishes to examine how a large number of electronic states interact with a field, an approach using the Schrödinger equation becomes unwieldy because one would have to solve the probability amplitudes of each state. In such a case the density matrix formalism can be used to describe the system in a statistical sense [52,105,154].

A wave function ψ can be constructed from a superposition of a complete set of the time independent eigenfunctions $u_n(\mathbf{r})$ of the system,

$$\psi_s(\mathbf{r},t) = \sum_n C_n^s(t) u_n(\mathbf{r}),$$

(3.7)

or shorthand:

$$|\psi\rangle = \sum_n C_n |n\rangle.$$

(3.8)

The expansion coefficient $C_n^s(t)$ is the probability that a system in state s is in state n at time t.

The density matrix is defined as an ensemble average, indicated by the overbar, over all possible states s that have a classical probability $p(s)$, of all the combinations of energy eigenstates expansion coefficients of the system

$$\rho_{nm} = \sum_s p(s) C_m^{s*} C_n^s = \overline{C_m^* C_n}.$$

(3.9)

The indices n and m run over the energy eigenstates. The density matrix is the sum of all the outer product matrices of the basis set, weighted with the proper probabilities.

$$\rho(t) = \sum_{n,m} \rho_{nm} |n\rangle\langle m|,$$

(3.10)

So, the density matrix can be thought of as an operator acting on the Hilbert space of a system. The averaged expectation value of an operator is calculated by taking the trace of the product of the density matrix and the operator. The diagonal elements ρ_{nn} give the probability that the system is in an energy eigenstate $|n\rangle$. The off-diagonal elements ρ_{nm}, on the other hand, give the likelihood that the system is in a coherent superposition of eigenstates $|n\rangle$ and $|m\rangle$, and are called coherences.

E.g. the ensemble averaged expectation value of the induced dipole moment is:

$$\overline{\langle \boldsymbol{\mu} \rangle} = \text{tr}\left[\hat{\rho}(t)\hat{\boldsymbol{\mu}} \right],$$ (3.11)

where $\hat{\rho}(t)$ and $\hat{\boldsymbol{\mu}}$ stand for the operators associated with the density matrix and the transition dipole $\boldsymbol{\mu}_{nm}$ respectively.

The density matrix evolves according to the Liouville-Von Neumann equation [105]:

$$\frac{\partial \rho}{\partial t} = -\frac{-i}{\hbar}\left[\hat{\mathbf{H}}, \hat{\rho} \right] \equiv -\frac{i}{\hbar}\mathscr{L}\rho .$$ (3.12)

Here, for compactness, the Liouville operator $\mathscr{L}$ is introduced. The density matrix elements can be rearranged in the matrix notation as follows:

$$\frac{d\rho_{jk}}{dt} = \frac{-i}{\hbar}\sum_m \left[\mathbf{H}_{jm}\rho_{mk} - \rho_{jm}\mathbf{H}_{mk} \right] = \frac{-i}{\hbar}\sum_{m,n} \mathscr{L}_{jk,mn}\rho_{mn} .$$ (3.13)

This shows that the Liouville operator $\mathscr{L}$ is a $N^2 \times N^2$ matrix, a vector in Liouville space, and it is also called a super operator. The vector space is introduced here to represent the density matrix in a similar manner as the wave function that is expanded in a complete basis set $\left\{ |n\rangle \right\}$ in Hilbert space. Thus, similarly as in equation (3.7), in Liouville space, a set of $n \times n$ matrices $|j\rangle\langle k|$ is introduced, with j rows and k columns. When these matrices are denoted as $|jk\rangle\rangle$, the density matrix, cp. equation (3.10), can be represented in this Liouville double bracket notation as [160]:

$$|\rho\rangle\rangle = \sum_{j,k} \rho_{jk} |jk\rangle\rangle .$$ (3.14)

Since the equations (3.8) and (3.14) are analogous, the latter equation facilitates the use of all methods and techniques that are applicable in Hilbert space. Therefore, operator $\mathscr{A}$ in Liouville space, called a super operator, can be defined as a superposition of all the Liouville space vector outer products:

$$\mathscr{A} = \sum_{\substack{j,k \\ m,n}} |jk\rangle\langle jk| \mathscr{A}_{jk,mn} |mn\rangle\langle mn|,$$ (3.15)

with the matrix elements $\mathscr{A}_{jk,mn} = \langle\langle jk | \mathscr{A} | mn\rangle\rangle$.

The advantage of a density matrix type description is that also effects that cannot realistically be included in the Hamiltonian can contribute to the equation of motion for the matrix elements, e.g.:

$$\left(\frac{d\rho_{nm}}{dt} \right) = \frac{-i}{\hbar}\left[\left(\hat{\mathbf{H}}_0 + \hat{\mathbf{V}} \right), \hat{\rho}(t) \right]_{nm} + \left(\frac{d\hat{\rho}_{nm}}{dt} \right)_{relaxation}.$$ (3.16)

In this particular case the Hamiltonian consists of a part that describes the unperturbed system $\hat{H}_0$, for which the basis functions $u_n(\mathbf{r})$ are energy eigenfunctions to the time-independent Schrödinger equation. In matrix notation this is:

$$\hat{\mathbf{H}}_{0,nm} = E_n \, \delta_{nm} .$$ (3.17)

The commutator of the unperturbed Hamiltonian and the density matrix operator can be written in terms of the transition frequency ω_{nm} :

$$\frac{-i}{\hbar}\left[\hat{\mathbf{H}}_0,\hat{\rho}\right]_{nm} = \frac{-i}{\hbar}\left(E_n\rho_{nm} - E_m\rho_{nm}\right) = -i\omega_{nm}\rho_{nm} \,. \tag{3.18}$$

The other part of the Hamiltonian $\hat{V}$ contains the interaction of the system with the externally applied electromagnetic fields. It is usually assumed, in terms of the dipole approximation, to be of the form

$$\hat{V}\left(\mathbf{r},t\right) = -\hat{\boldsymbol{\mu}}\cdot\tilde{E}\left(\mathbf{r},t\right)\,. \tag{3.19}$$

The last term on the right hand side of equation (3.16) contains any relaxation mechanism due to interactions that cannot be included in the Hamiltonian and that can change the state of the system, such as population relaxation or other phenomenological damping terms.

This method of partitioning the Hamiltonian into pieces that interact with the bath or the system degrees of freedom, that are relevant for the expectation value of the operator in question, has the obvious advantage that one only has to trace over a small subset of states. This reduced density matrix however, does not allow for investigating the time dependence of this expectation value for the case it is governed by both the system and the bath states, and a correlation exists between system and bath.

3.4 The Maxwell-Bloch Approach

For example, in the case of a sample doped with chromophores that can be approximated as a two-level system with an excited state $|e\rangle$ and a ground state $|g\rangle$, the equations of motion for the individual elements of the density matrix become [154,161]:

$$\begin{aligned}
\left(\frac{d\rho_{eg}}{dt}\right) &= -i\omega_{eg}\rho_{eg} + \frac{i}{\hbar}V_{eg}\left(\rho_{gg}-\rho_{ee}\right) - \frac{1}{T_2}\rho_{eg} \\
\left(\frac{d\rho_{ee}}{dt}\right) &= -\frac{i}{\hbar}\left(V_{eg}\rho_{ge}-\rho_{eg}V_{ge}\right) - \frac{1}{T_1}\left(\rho_{ee}-\rho_{ee}^{eq}\right).
\end{aligned} \tag{3.20}$$

The other two elements evolve in a similar manner. The two relaxation mechanism that are incorporated in a phenomenological way, are population relaxation with characteristic time T_1, representing the decay of population from the excited state to the ground state, and dephasing time T_2, representing elastic processes that lead to decaying coherences $\rho_{eg} = \rho_{ge}^*$. The diagonal elements can all contain population in thermal equilibrium but since in optical systems $\hbar\omega_{eg} \gg kT$, spontaneous upward transitions do not occur, hence $\rho_{ee}^{eq} = 0$. Therefore one relaxation time T_1 characterizes the population decay. The dephasing time T_2 is associated with the homogeneous line width $1/2\pi T_2$.

Now, in order to follow the time development of the individual elements of the density matrix when perturbed by a field at some frequency, it is actually convenient to change from the Schrödinger picture above to the interaction picture, i.e. transforming to a frame rotating at the optical frequency, $\sigma_{eg} = \rho_{eg} e^{i\omega t}$. After this transformation any term oscillating at twice the optical frequency is dropped, following the rotating wave approximation (RWA) [52,154].

With a near resonant steady state optical field $\tilde{E}(\mathbf{r},t) = E_0 e^{-i(\omega t - \mathbf{k}\cdot\mathbf{r} - \varphi)} + c.c.$ switched on, the equations of motion of the two elements described above become:

$$
\begin{aligned}
\left(\frac{d\sigma_{eg}}{dt}\right) &= \frac{i\Omega}{2}\left(\sigma_{gg} - \sigma_{ee}\right)\exp\left[i\left(\mathbf{k}\cdot\mathbf{r} - \varphi\right)\right] - \frac{1}{T_2}\sigma_{eg} - i\Delta\sigma_{eg} \\
\left(\frac{d\sigma_{ee}}{dt}\right) &= \frac{i\Omega}{2}\left(\sigma_{ge}\exp\left[i\left(\mathbf{k}\cdot\mathbf{r} - \varphi\right)\right] - \sigma_{eg}\exp\left[-i\left(\mathbf{k}\cdot\mathbf{r} - \varphi\right)\right]\right) - \frac{1}{T_1}\sigma_{ee},
\end{aligned}
\tag{3.21}
$$

with the Rabi frequency $\hbar\Omega = \mathbf{\mu}\cdot E_0$ and detuning $\Delta = \omega - \omega_{eg}$.

In the Bloch approach now, the formal solution to equation (3.12) or (3.13) is, by integrating, stated straightforwardly as

$$
\sigma(t) = \exp\left[\frac{-i}{\hbar}\mathscr{L}t\right]\sigma(0) \equiv \mathscr{U}(t)\sigma(0).
\tag{3.22}
$$

The time evolution operator $\mathscr{U}(t)$ can then be expressed as a matrix as well and the individual elements can be solved for the case that the field is switched on and for the case it is switched off. The polarization of the system can after that be determined by propagating the system's states over the times that the field is switched on or off during the particular pulsed experiment.

By combining the real and imaginary parts of the four matrix elements in a three-dimensional vector, the Bloch vector, this time evolution can be represented in a graphical manner. The effect of an optical pulse on the system is subsequently characterized by the angle θ by which it rotates this vector along one of its axis, the so-called pulse area. The total time evolution of the density matrix after a sequence of pulses is calculated by multiplying the corresponding matrices, and the total polarization is found by taking the trace of the dipole operator times the density matrix. This so-called Maxwell-Bloch approach is used in NMR and optical experiments in crystals. The minutiae of this model are not important here, since a more general method is used in this work. It is mentioned since it introduces the terminology of homogeneous and inhomogeneous line widths and shows the phenomenological background of the terms.

In optically doped crystals the optical centres exhibit very fast motions around an equilibrium static position that determine the homogeneous line width. The equilibrium positions however often have a completely static offset due to crystal imperfections and strain,

thus contributing to a broader inhomogeneous line width. In this case a very clear-cut separation of times scales exists, validating the distinction between homogeneous and inhomogeneous widths. If an ensemble of optical two-level systems is inhomogeneously broadened, one has to integrate the polarization, as determined for some homogeneous line width $1/2\pi T_2^{hom}$ over the distribution of resonance frequencies, determined by the inhomogeneous line width $1/2\pi T_2^{inhom}$, in order to calculate the complete system response [154].

In glasses and liquids, with dynamics occurring on all possible time-scales, a clear separation of time scales cannot be made. Even though the interpretation of photon echo experiments in terms of homogeneous and inhomogeneous line widths is then flawed, it is still common practice to characterize the dynamics of solute and bath in these terms, and as such these will therefore also be used throughout this thesis. The usual method for describing dephasing in a system with a broad distribution of time scales on which dynamics occur, is to resort to the definition of an *effective* homogeneous line width.

The traditional homogeneous line width consists of a lifetime contribution $1/2\pi T_1$ and a part due to "pure dephasing" $1/2\pi T_2^*$, reflecting the short time dynamics in a system with a clear separation of time scales:

$$\frac{1}{T_2^{hom}} = \frac{1}{2T_1} + \frac{1}{T_2^*} \ . \tag{3.23}$$

In all other systems only the fluctuations of the resonance frequency on a time scale shorter than the experimental timescale will contribute to the homogeneous line width. Then, by definition, the shortest possible experimental time scale will set the homogeneous line width.

When the experimental time scale is lengthened to a time t, the *effective* homogeneous line width $1/2\pi T_2^{eff}$ is measured. The *effective* pure dephasing rate is rendered after subtracting the lifetime contribution from the effective homogeneous line width:

$$\frac{1}{T_2^{eff}}(t) = \frac{1}{2T_1} + \frac{1}{T_2^*} + \frac{1}{T_2^{SD}}(t) \ . \tag{3.24}$$

Note that only fluctuations occurring on time scales slower than T_2^* but faster than t contribute to the term $1/T_2^{SD}(t)$, that indicates the dephasing due to spectral diffusion (SD). This is the average offset caused by the drift of the resonance frequency due to bath dynamics. Nevertheless, the nature of the processes causing this drift is identical to the nature of those that contribute to the pure dephasing term $1/T_2^*$.

The inhomogeneous line width is then the effective homogeneous line width at a time much longer than the time on which the slowest dynamics in the system occur. At this time $t = \infty$ a chromophore will have sampled all possible resonance frequencies, leading to the broadest possible line width. In ergodic systems with a sufficiently large number of two
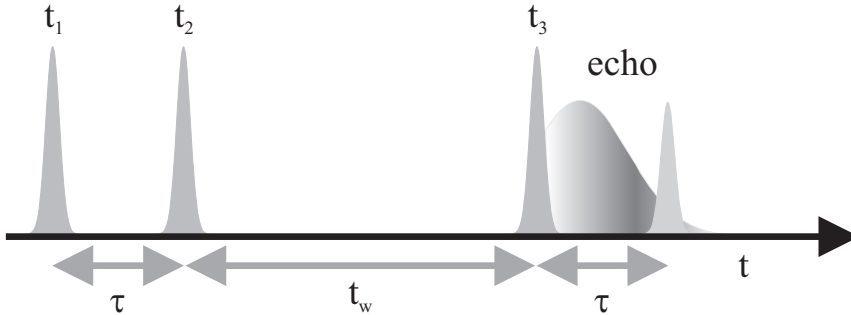
Figure 3.1. The pulse sequence in a three pulse stimulated echo experiment. Two types of echo signals are indicated, one peaking at $t = 2\tau + t_w$, indicating the typical signal in a situation where the Bloch equations readily apply and a signal peaking at earlier times indicating system-bath dynamics with a strong non-Markovian character (see text).

level systems interacting with the field, this should equal the width of the inhomogeneously broadened absorption spectrum.

Even though the time scale separation problem is repaired in this manner, the problem with describing correlated system–bath dynamics still stands and another method is needed to adequately describe the system response when such dynamics are significant.

3.4.1 Photon Echoes in the Bloch Model

In this work the photon echo technique is used to chart the bath dynamics. Examining the time evolution of the off-diagonal elements of the density matrix does this. The coherences attain a phase by coherent excitation of the ensemble of modes interacting with the field, and this phase relation is subsequently washed out by the bath fluctuations at the dephasing rate.

In a three pulse stimulated photon echo (3PE) experiment both the optical dephasing time as well as the population relaxation time can be measured, using a three-pulse grating scattering configuration. The first pulse coherently excites the optical transition of the chromophores. After a time interval τ, the second pulse interacts with the freely propagating system, which gives rise to a population distribution between ground and excited state, which depends on the position of the chromophores in the inhomogeneously broadened line [52-54,154].
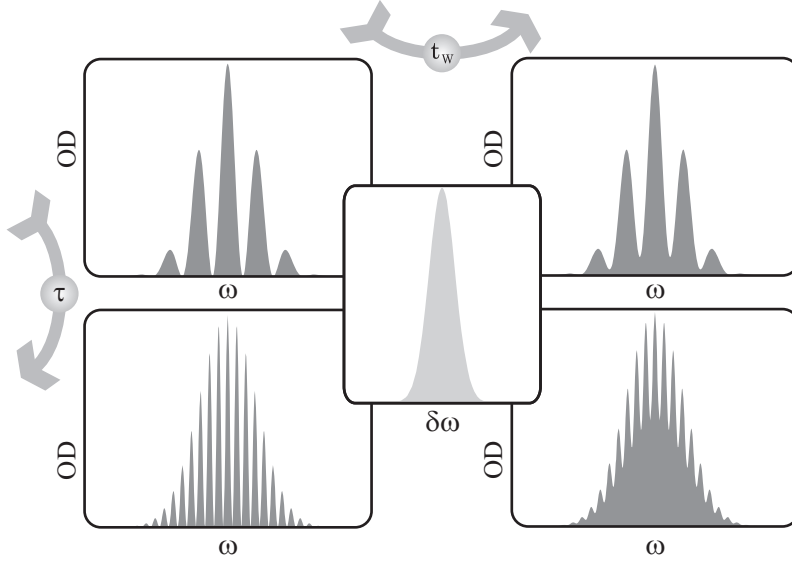
Figure 3.2. Grating scattering in frequency space. The first two pulses create a frequency grating in the ground and excited state, which gets washed out by spectral diffusion.

Using the Bloch formalism, this distribution can be easily visualized. Using the first two pulses of the sequence shown in Figure 3.1, the multiplication of propagator matrices with the field switched on and off that give $\sigma(t)$ (cp. equation (3.21)) is:

$$\sigma(t) = \mathscr{U}^{off}(t)\mathscr{U}^{on}(\theta_2)\mathscr{U}^{off}(\tau)\mathscr{U}^{on}(\theta_1)\sigma(0). \tag{3.25}$$

Now suppose that both pulses have a $\theta = \frac{1}{2}\pi$ pulse area and have wave vector $\mathbf{k}_{12}$ and phase differences φ_{12}. In this case, right after both excitations when $t \approx \tau$, the distributions of the two populations are:

$$\sigma_{ee}(\tau) = \tfrac{1}{2}\left(1 - \exp\left[-\frac{\tau}{T_2}\right]\cos\left[\Delta\tau - \mathbf{k}_{12}\cdot\mathbf{r} + \varphi_{12}\right]\right)$$
$$\sigma_{gg}(\tau) = 1 - \sigma_{ee}(\tau). \tag{3.26}$$

This implies a modulation of the population in the excitation band width due to the detuning factor Δ. This population grating in frequency-space entails a frequency modulated transmission spectrum of the sample as depicted in Figure 3.2. The spacing of the grating in the ground and excited state of the chromophores is inversely proportional to the pulse separation τ.

After a waiting time t_w a third pulse is scattered from these gratings, resulting in an echo at a time τ after the last pulse. Spectral diffusion washes out the gratings during the waiting time t_w and consequently decreases the echo amplitude. In Figure 3.2 the SD is shown as a convolution of the frequency grating with a Gaussian, representing the average frequency excursion distribution of the chromophores. The longer τ is, the finer the grating is and the easier it is washed away, leading to a faster effective dephasing time.

3.5 Perturbative Approach to Four Wave Mixing

A perturbative description of the induced polarization is needed for the formulation of the non-linear optical response function in terms of multi-time correlation functions of the resonance frequencies of chromophores. These correlation functions can be connected to bath dynamics by various methods, depending on the nature of the system under study, without having to resort to phenomenological constants. Furthermore it is possible, if necessary, to include the effects of correlated dynamics in the description by choosing the appropriate reduced Hamiltonian.

The density matrix generates the ensemble averaged time evolution of the quantum states, as is described by the Liouville equation (3.12) and (3.13), just as the time evolution of a wave function is described by the time dependent Schrödinger equation. So when we revisit the formal solution introduced in equation (3.22) through integration of the Liouville equation given some initial state $\rho(t_0)$, the state at any subsequent time can be obtained when the Hamiltonian is time-independent [152,153,162]:

$$| \rho(t) \rangle\rangle = \exp\left[-\frac{i}{\hbar} \mathscr{L}(t-t_0) \right] | \rho(t_0) \rangle\rangle \equiv \mathscr{U}(t,t_0) | \rho(t_0) \rangle\rangle . \tag{3.27}$$

The time evolution operator on the right hand side is called the Liouville space propagator and can be defined by the usual series. For time dependent Hamiltonians, this operator is formulated with a time ordered exponential:

$$\mathscr{U}(t,t_0) = 1 + \sum_{n=1}^{\infty} \left(\frac{-i}{\hbar} \right)^n \int_{t_0}^{t} d\tau_n \int_{t_0}^{\tau_n} d\tau_{n-1} \cdots \int_{t_0}^{\tau_2} d\tau_1 \mathscr{L}(\tau_n) \mathscr{L}(\tau_{n-1}) \cdots \mathscr{L}(\tau_1) . \tag{3.28}$$

Note the changes in the integration limits of the series with respect to a normal Taylor expansion, so only terms with the proper time ordering contribute to the result.

By it self, this expansion is not very useful, since the time evolution operator encompasses the entire Hamiltonian. In spectroscopy, usually only the parts of the Hamiltonian that describe the interaction with the applied fields are treated perturbatively and the remainder is treated exactly. This is in fact the interaction picture that was already used in the

Bloch approach [161]. On the condition that the respective parts of the Hamiltonian are well chosen, it can make the expansion hold for long times even when truncated at low order. When the Hamiltonian is split into a system part and a time dependent part that interacts with the fields, the Liouville equation becomes

$$\frac{d\rho}{dt} = -\frac{i}{\hbar}\mathscr{L}\rho - \frac{i}{\hbar}\mathscr{L}_{\text{int}}(t)\rho .$$

(3.29)

It is then easily shown that the expansion of the time evolution operator can be expressed in a terms of a time evolution operator that signifies the system part of the previous equation and a time ordered exponential referring to the interaction with the fields:

$$\mathscr{U}(t,t_0) = \mathscr{U}_0(t,t_0) + \sum_{n=1}^{\infty}\left(\frac{-i}{\hbar}\right)^n \int_{t_0}^{t}d\tau_n \int_{t_0}^{\tau_n}d\tau_{n-1}\cdots\int_{t_0}^{\tau_2}d\tau_1 \times$$

$$\mathscr{U}_0(t,\tau_n)\mathscr{L}(\tau_n)\mathscr{U}_0(\tau_n,\tau_{n-1})\mathscr{L}(\tau_{n-1})\cdots\mathscr{U}_0(\tau_2,\tau_1)\mathscr{L}(\tau_1)\mathscr{U}_0(\tau_1,t_0).$$

(3.30)

This means that in the *n*-th order the system interacts n times through $\mathscr{L}_{\text{int}}$ with $\hat{H}_{\text{int}}$ at times τ_1 to τ_n. At other times, before, after and in between, it freely propagates through the time operator $\mathscr{U}_0(t,t')$ that refers to the Liouville operator of the system part. It is possible to rewrite the integrals in this equation and equation (3.28) in terms of an ordinary, not time-ordered, exponential series by applying a cumulant expansion, commonly truncated in the second order. Although often used in time resolved spectroscopy, one has to take caution in using these expansions, since little is known about the convergence of the perturbation series [55,153,163,164].

The optical polarization is the observable of interest. Since it acts as a source for the radiation field, full knowledge of the polarization is what is needed for the interpretation of any experiment. The density matrix can be used to calculate the optical polarization of a sample, subject to incident light pulses. The polarization is given by the expectation value of the dipole operator:

$$P(\mathbf{r},t) = \text{tr}[\hat{\mathbf{V}},\hat{\rho}(t)] = \langle\langle\mathbf{V}\,|\,\rho(t)\rangle\rangle .$$

(3.31)

In order to work out the third order response function of equation (3.6), the density matrix too has to be expanded in powers of the applied fields, as in equation (3.1):

$$P^{(n)}(\mathbf{r},t) = \langle\langle\mathbf{V}\,|\,\rho^{(n)}(t)\rangle\rangle .$$

(3.32)

The *n*-th order contribution of $\rho(t)$ is then calculated by means of the appropriate term of the above Liouville space propagator. The first higher order term that is non-vanishing in random isotropic media is the third order contribution $P^{(3)}$, and is the source of the signal field of the experiments discussed here.

The interaction part of equation (3.29) is, within the dipole approximation described by the time-independent Liouville space dipole operator $\mathscr{V}$:

$$\mathscr{L}_{\text{int}}(t) = -E(t)\mathscr{V} .$$

(3.33)

Furthermore, when t_0 is taken to minus infinity, in order that $\rho(-\infty)$ is the system in thermal equilibrium at $t = -\infty$, and three fields interact at times $t \geq \tau_3 \geq \tau_2 \geq \tau_1$, the third order of the polarization can then established from equation (3.30) and (3.32) as the convolution of the fields in equation (3.6):

$$P^{(3)}(\mathbf{r},t) = \sum_{\lambda,\mu,\nu} \int_0^\infty dt_3 \int_0^\infty dt_2 \int_0^\infty dt_1 \ R^{(3)}(t_3,t_2,t_1,t) E_\lambda(\mathbf{r},t-t_3)$$
$$\times E_\mu(\mathbf{r},t-t_3-t_2) E_\nu(\mathbf{r},t-t_3-t_2-t_1), \tag{3.34}$$

with a non linear response that is then in sourceless isotropic media:

$$R^{(3)}(t_3,t_2,t_1,t) = \left(\frac{i}{\hbar}\right)^3 \langle\langle \mathbf{V} \,|\, \mathscr{G}(t_3)\mathscr{V}\,\mathscr{G}(t_2)\mathscr{V}\,\mathscr{G}(t_1)\mathscr{V} \,|\, \rho(-\infty)\rangle\rangle. \tag{3.35}$$

The sum designates the possible time permutation of the three incident fields. Note here that $\mathscr{G}(t)$ stems from the time operator $\mathscr{U}_0(t,t')$ of the material part of equation (3.29):

$$\mathscr{G}(t) = \theta(t)\exp\left[-\frac{i}{\hbar}\mathscr{L}t\right]. \tag{3.36}$$

It uses the Heavyside step function $\theta(t)$ to ensure that the system only evolves through this operator after the corresponding field has been applied. A change of time variables is made,

$$t_1 \equiv \tau_2 - \tau_1, \quad t_2 \equiv \tau_3 - \tau_2, \quad t_3 \equiv t - \tau_3. \tag{3.37}$$

Also the fact is used that at equilibrium $\rho(t_0)$ the density matrix, of course, does not evolve when only subject to the material part of the Hamiltonian with no fields:

$$G(\tau_1 - t_0)\rho(t_0) = \rho(t_0). \tag{3.38}$$

The expression for $R^{(3)}$ in equation (3.35) is very general. It is valid for all third order type experiments in isotropic media constituted of point dipoles, and since pulse orders can be interchanged, the time periods $t_{1,2,3}$ are not necessarily the same as the coherence time τ and waiting time t_w indicated in Figure 3.1. This expression can be implemented for systems of arbitrary size in case the optical response is non-local in nature, or can straightforwardly be converted into momentum ($\mathbf{k}$) space if needed.

Now suppose that the modes of the systems that interact with the applied fields, and that are therefore explicitly considered, are optical two level systems with ground state $|g\rangle$ and excited state $|e\rangle$, with a lifetime $\gamma_{g\,\text{or}\,e}$, and an energy difference $\hbar\omega_{eg}$. When these systems are excited at near resonance as in the previous section, a change to the rotating frame $\sigma_{nm} = \rho_{nm}e^{i\omega_{nm}t}$ is appropriate. This would yield in the matrix notation:

$$R^{(3)}\left(t_3, t_2, t_1, t\right) = \left(\frac{1}{i\hbar}\right)^4 \langle\langle \mathbf{V} \mid \sigma\left(t_1 + t_2 + t_3\right)\rangle\rangle$$

$$= \left(\frac{i}{\hbar}\right)^3 \langle\langle \mathbf{V} \mid \sum_{\substack{k,l,m, \\ n,o,p}}^{g \text{ or } e} \mathscr{G}_{kl}\left(t_3\right)\mathscr{V}_{kl,mn}\mathscr{G}_{mn}\left(t_2\right)\mathscr{V}_{mn,op}\mathscr{G}_{op}\left(t_1\right)\mathscr{V}_{op,gg} \mid \sigma\left(-\infty\right)\rangle\rangle \times$$

$$\exp\left[-it_3\left(\omega_{kl} - i\frac{\gamma_k + \gamma_l}{2}\right) - it_2\left(\omega_{mn} - i\frac{\gamma_m + \gamma_n}{2}\right) - it_1\left(\omega_{op} - i\frac{\gamma_o + \gamma_p}{2}\right)\right].$$

(3.39)

Since Liouville operators are commutators and as such can act on both the bra and the ket side of $\sigma(t)$, this results in 8 possible pathways to evaluate equation (3.35) or (3.39). In a time resolved experiment these eight terms are valid for each permutation of the three applied fields, yielding 48 terms to be considered for a complete description of a third order experiment. However, not all terms need to be taken into account when evaluating the signal of a particular experiment. Depending on the type of experiment and the characteristics of the system only a limited number of pathways will actually contribute to the measured signal.

3.5.1 Photon Echoes

The perturbative approach allows for a richer description of the dynamics, but it also involves the evaluation off all 48 Liouville pathways contributing to equations (3.35) and (3.39). An instructive graphical way to keep track of the various contributions to the signal field, is by using the double-sided Feynman diagrams as depicted in Figure 3.3 [52,55,165]. These Feynman diagrams are specific for the stimulated echo experiment (3PE) on an ensemble of chromophores that are two-level systems. Time in these diagrams flows from the bottom to the top. Those diagrams are selected that describe an ensemble that initially is in the ground state $|g\rangle\langle g|$, since optical systems are in the ground state at equilibrium, and those that also end in a population state. Furthermore, the pathways that describe the system when it goes through a period in which it evolves as a coherent superposition of states $|g\rangle\langle e|$ between the first two interactions, and through another coherence period between the last and the signal, contribute to the echo signal. All other diagrams, e.g. those that end in a coherent super position, can be neglected. Diagrams with interactions that lead to the absorption of a photon, indicated by the incoming wavy arrow, while not simultaneously causing a transition from the ground to the excited state, or *vice versa* diagrams with emissions that do not cause a return to the ground state will yield highly oscillatory fields and can be neglected by implying the rotating wave approximation. Finally, when also symmet-
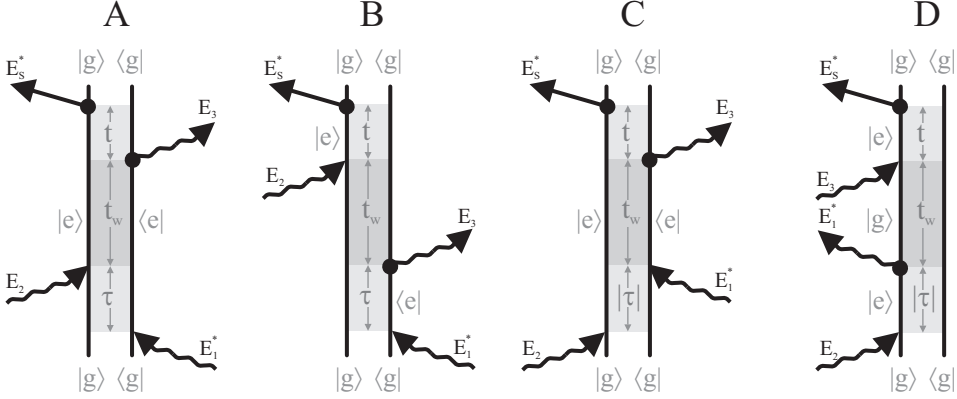
Figure 3.3. Double sided Feynman diagrams, representing the 3PSE signal in the $\mathbf{k}_3 + \mathbf{k}_2 - \mathbf{k}_1$ *direction. Diagrams A and B represent the pathways leading to an echo signal and C and D depict the virtual echo pathways.*

ric pathways are combined, the total number of diagrams contributing to the 3PE signal in a two-level system is reduced to four. From these, the third-order polarization in the direction $\mathbf{k}_S = \mathbf{k}_3 + \mathbf{k}_2 - \mathbf{k}_1$ can be calculated.

In the first two diagrams in Figure 3.3, the system evolves through two different coherent superpositions: first a dephasing period $|g\rangle\langle e|$ during t_1 and later a rephasing period $|e\rangle\langle g|$ during t_3. These diagrams represent the actual echo signal. The latter two diagrams play a role for overlapping pulses or negative delays τ, when the pulse characterized by amplitude E_2 arrives before the E_1 pulse. In this case the system goes through two dephasing periods and no rephasing occurs. The signal E_S in the $\mathbf{k}_S$ direction is then called the virtual echo and does not reflect the homogeneous line width.

To be totally inclusive, the diagrams that represent the case that the E_3 pulse arrives before the E_2 pulse should also be included. These respective diagrams can be found by exchanging the proper indices in Figure 3.3, but are neglected for the time being. Implicitly, the transition dipole moment is set to fixed value μ_{eg} in accordance with the Condon approximation. This states that the optical transition probability can be calculated at a fixed nuclear position, because the electronic transition occurs on a time scale short compared to nuclear motions. The final expression for the 3PE is then, in case all pulses have the same excitation frequency ω:

$$P^{(3)}\left(t,\tau,t_w t_1,t_2,t_3\right) = \left(\frac{\mu_{eg}}{i\hbar}\right)^4 \int\limits_0^\infty dt_3 \int\limits_0^\infty dt_2 \int\limits_0^\infty dt_1$$

$$\times\left(\left\{R_A\left(t_3,t_2,t_1\right)\exp\left[-\frac{1}{2T_1}\left(t_3+2t_2+t_1\right)\right]+R_B\left(t_3,t_2,t_1\right)\exp\left[-\frac{1}{2T_1}\left(t_3+t_1\right)\right]\right\}\right.$$

$$\exp\left[-i\left(\omega_{eg}-\omega\right)\left(t_3-t_1\right)\right]E_3\left(t-\tau-t_w-t_3\right)E_2\left(t-\tau-t_3-t_2\right)E_1^*\left(t-t_3-t_2-t_1\right) \qquad (3.40)$$

$$+\left\{R_C\left(t_3,t_2,t_1\right)\exp\left[-\frac{1}{2T_1}\left(t_3+2t_2+t_1\right)\right]+R_D\left(t_3,t_2,t_1\right)\exp\left[-\frac{1}{2T_1}\left(t_3+t_1\right)\right]\right\}\times$$

$$\left.\exp\left[-i\left(\omega_{eg}-\omega\right)\left(t_3+t_1\right)\right]E_3\left(t-\tau-t_w-t_3\right)E_1^*\left(t-t_3-t_2\right)E_2\left(t-\tau-t_3-t_2-t_1\right)\right).$$

It is assumed here that the lifetime of the excited state here is $\gamma = 1/T_1$. The population relaxation terms and coherent phase conjugation terms $\exp\left[-i\left(\omega_{eg}-\omega\right)\right]$ can be found by applying the terms of equation (3.39) according to the diagrams. The R-terms are the nonlinear response terms that describe the actual time evolution of the elements of the density matrix according to the pathway represented by the corresponding Feynman diagrams:

$$\begin{aligned}
R_A(t_3,t_2,t_1) &= \left\langle \mathscr{G}_{eg}\mathscr{G}_{ee}\mathscr{G}_{ge} \left| \sigma(-\infty)\right\rangle\right. \\
R_B(t_3,t_2,t_1) &= \left\langle \mathscr{G}_{eg}\mathscr{G}_{gg}\mathscr{G}_{ge} \left| \sigma(-\infty)\right\rangle\right. \\
R_C(t_3,t_2,t_1) &= \left\langle \mathscr{G}_{eg}\mathscr{G}_{ee}\mathscr{G}_{eg} \left| \sigma(-\infty)\right\rangle\right. \\
R_D(t_3,t_2,t_1) &= \left\langle \mathscr{G}_{eg}\mathscr{G}_{gg}\mathscr{G}_{eg} \left| \sigma(-\infty)\right\rangle\right.
\end{aligned} \qquad (3.41)$$

So, now the Liouville space propagation of the reduced density matrix has to be considered.

Before considering methods for doing this, it is worthwhile pointing out that the multi-dimensional space, spanned by the pulse timings in $P^{(3)}\left(t,\tau,t_w,t_1,t_2,t_3\right)$, contains all information about the time evolution of the ensemble of the systems with an optical transition. By varying the pulse timings in various ways, cross-sections can be made of this space and particular aspects of this time evolution can be assessed. At the same time, different experimental techniques will yield different projections of the polarization. Time integrated echo experiments observe $\int \left|P^{(3)}(t)\right| dt$ for instance, while heterodyne detected echoes, where an additional field is mixed with the signal field, have the potential to observe $P^{(3)}(t)$ directly, and with time resolved spectral interferometry, the Fourier transform $P^{(3)}(\omega)$ can be detected.

3.6 Random Frequency Fluctuations

The point of introducing the above FWM formalism was to be able to describe dephasing caused by frequency fluctuations on varying times scales and including strong system bath interactions. To start with the former point, in the Bloch model the system can only be described correctly when it is subject to very fast frequency fluctuations or when the systems have a static resonance frequency offset (see section 3.4). In both cases the state of the system is only determined by the present and its evolution is not in any way influenced by the past, i.e. it has no phase memory. When in a stochastic process the distant past is irrelevant given the knowledge of the recent past, it is called a Markovian process. The two limits above are called the fast and the slow modulation limit [125,145,166,167].

In liquids and glasses the dynamics of the dye molecule dictated by the timescale of the optical experiment and the evolution of the bath through stochastic processes are on the same time scales and therefore an approach is necessary to describe non-Markovian solvent dynamics in these systems. A number of approaches exist and some of them will be briefly outlined here.

When an ensemble of optical two level systems couples to the stochastic motions of a bath, this leads to a time dependent random modulation of the resonance frequency of the these systems that can be introduced as:

$$\omega_{eg}(t) = \omega_{eg}(0) + \delta\omega_{eg}(t) \tag{3.42}$$

The time evolution of the off-diagonal elements of the density matrix, introduced in equation (3.16) can then be written for a system that interacted with a short pulse at time $t = 0$, and when the bath dynamics are independent of the state of the system:

$$\rho_{eg}(t) = \rho_{eg}(0)\left\langle \exp\left[-\frac{i}{\hbar}\int_0^t d\tau\left(\hat{\mathbf{H}}_{ee}(\tau) - \hat{\mathbf{H}}_{gg}(\tau)\right)\right]\right\rangle$$

$$= \rho_{eg}(0)\exp\left[-i\omega_{eg}(0)t\right]\left\langle \exp\left[-i\int_0^t d\tau\,\delta\omega_{eg}(\tau)\right]\right\rangle. \tag{3.43}$$

The angular brackets indicate averaging over the random history of all the degrees of freedom of the system and the bath. Depending on the knowledge of the nature of the fluctuations, a method for the way this averaging is performed is chosen.

This particular manner of propagating the density matrix can be used in the above expression of the third order polarization. For instance, the nonlinear response function corresponding to Feynman diagram A of Figure 3.3 becomes, when population relaxation through the diagonal element of the density matrix is ignored for the moment,

$$R_A\left(t_3,t_2,t_1\right) = \left\langle \exp\left[-i\int_0^{t_1} dt\ \delta\omega_{ge}\left(t\right) - i\int_{t_1}^{t_1+t_2} dt\ \delta\omega_{ee}\left(t\right) - i\int_{t_1+t_2}^{t_1+t_2+t_3} dt\ \delta\omega_{eg}\left(t\right) \right] \right\rangle. \tag{3.44}$$

Here the brackets denote averaging of the baths history again. The other three response functions can be expressed in the same way. Now by taking $\delta\omega \equiv \delta\omega_{ge} = -\delta\omega_{eg}$ and also $\delta\omega_{gg} = \delta\omega_{ee} = 0$ the total expression for all the diagrams can be simplified. Even more so for experiments where the time periods between the pulses are long compared to the pulse length so that these can be considered as delta pulses, $E_i\left(t\right) = E_i\delta\left(t\right)$, and the diagrams C and D can be ignored. This is the case in all the picosecond experiments in this work and it reduces the phase relaxation part of the nonlinear response function to a term describing the dephasing during the period between the first to pulses and a rephasing period between the last pulse and the echo signal. So the total expression for the optical polarization with also taking the population lifetime of the excited state into account as was already done explicitly in equation (3.40), becomes:

$$P^{(3)}\left(\tau,t_w,t\right) = \left(\frac{\mu_{eg}}{i\hbar}\right)^4 E_1^* E_2 E_3 \exp\left[i\left(\omega-\omega_{eg}\right)\left(t-\tau\right) - \frac{1}{2T_1}\left(t+\tau\right) \right]$$
$$\times \left(R_{stoch}\left(\tau,t_w,t\right) \exp\left[-\frac{t_w}{T_1} \right] + R_{stoch}\left(\tau,t_w,t\right) \right). \tag{3.45}$$

Note also that due to the constraints on pulse duration and the precise sequence, the switch to the coherence time variable and waiting time variable could be made again. The two remaining nonlinear response terms are equal in this stochastic approach:

$$R_{stoch}\left(\tau,t_w,t\right) = \left\langle \exp\left[-i\int_0^{\tau} dt\ \delta\omega\left(t\right) + i\int_{\tau+t_w}^{\tau+t_w+t} dt\ \delta\omega\left(t\right) \right] \right\rangle. \tag{3.46}$$

The stochastic averaging over all possible frequency fluctuations $\delta\omega$ indicated by the brackets, can be performed in various ways. The method of choice depends on the knowledge of the physics of the fluctuations. In the TLS-model the averaging is traditionally performed with use of Laplace transformation techniques. Under the assumption of weakly coupled independent TLS's, the average of the argument of the exponent in equation (3.46) can be taken instead of the full expression. This method is outlined in section 3.9.

3.6.1 Stochastic Model for Solvent Dynamics

In another approach, when the fluctuations are random with frequency offsets probabilities that can be described by a time independent, i.e. stationary, normal distribution, the expo-

nential term can be expanded into a Taylor series. In solvent dynamics, the central limit theorem applies, which is to say that the effect of the motions of all individual solvent molecules on a chromophore is thought of as a sum of many independent identically distributed random variables, and is therefore normally distributed. Expanding this into the power series yields [145,166,167]:

$$\left\langle \exp\left[-i\int_0^\tau dt\,\delta\omega(t)\right]\right\rangle = \sum_{n=0}^{\infty} \frac{-i^n}{n!} \int_0^\tau\int_0^\tau\ldots\int_0^\tau \left\langle \delta\omega(t_1)\,\delta\omega(t_2)\ldots\delta\omega(t_n)\right\rangle dt_1 dt_2 \ldots dt_n \,. \tag{3.47}$$

Using the properties of the stationary Gaussian fluctuation process, all odd terms can be dropped. In addition, the order of the two times $t_{1,2}$ in a two-time correlation function $\left\langle \delta\omega(t_1)\,\delta\omega(t_2)\right\rangle$ is not important in this case, and higher order correlation functions can therefore be rearranged as a sum of two-time correlation functions. Performing all the sums of the series results in a much simpler expression with just a single two-time correlation function that has to be averaged over:

$$\left\langle \exp\left[-i\int_0^\tau dt\,\delta\omega(t)\right]\right\rangle = \exp\left[-\frac{1}{2}\int_0^\tau\int_0^\tau \left\langle \delta\omega(t_1)\,\delta\omega(t_2)\right\rangle dt_1 dt_2\right]. \tag{3.48}$$

The averaging can be performed within the resulting integrals. When the frequency fluctuations are both Gaussian, i.e. normally distributed, and Markovian, i.e. future probabilities are determined by their most recent values, this correlation function is an exponential.

$$\left\langle \delta\omega(t_1)\,\delta\omega(t_2)\right\rangle = \Delta^2 \exp\left[-\Lambda|t_1-t_2|\right]. \tag{3.49}$$

Consequently the integration can be performed:

$$\left\langle \exp\left[-i\int_0^\tau dt\,\delta\omega(t)\right]\right\rangle = \exp\left[-g(\tau)\right], \tag{3.50}$$

with the line shape function $g(t)$ defined as:

$$g(t) = \frac{\Delta^2}{\Lambda^2}\left(\exp[-\Lambda t] + \Lambda t - 1\right). \tag{3.51}$$

Here, Δ is the standard deviation of the frequency fluctuations distribution and Λ is the inverse of the correlation time τ_c of the fluctuations. Typically, in evaluating experiments more than one Gauss-Markov process is used to describe the experimental results, e.g. by using a process with a fast and one with a long correlation time:

$$g(t) = g_{fast}(t) + g_{slow}(t). \tag{3.52}$$

In the case of averaging over multiple double integrals, as in equation (3.44), the Taylor expansion and the subsequent re-summing result, in a slightly more complicated sum of double integrals than in equation (3.48). Nevertheless, by using the same type of line shape functions, and by again taking $\delta\omega \equiv \delta\omega_{ge} = -\delta\omega_{eg}$ and $\delta\omega_{gg} = \delta\omega_{ee} = 0$, the R-terms of the

nonlinear response functions of diagram A and B, and diagram C and D respectively, can be rewritten as:

$$R_{A,B}^{stoch} = \exp\left[-g(t_3)+g(t_2)-g(t_1)-g(t_2+t_1)-g(t_3+t_2)+g(t_3+t_2+t_1)\right]$$
$$R_{C,D}^{stoch} = \exp\left[-g(t_3)-g(t_2)-g(t_1)+g(t_2+t_1)+g(t_3+t_2)-g(t_3+t_2+t_1)\right].$$
(3.53)

The above is not only valid for the Gauss-Markov line broadening process of equation (3.51). Other correlation functions can be used, however, the Taylor expansion holds only for normally distributed frequency fluctuations. For non-Gaussian processes a cumulant expansion of the integral is needed to achieve the same result. The only requirement then is that only stochastic processes govern the resonance frequency excursions, in other words, the fluctuations are random and independent of the state of the system. Only the optical degrees of freedom are taken explicitly into account in the Hamiltonian used in equation (3.43). This is similar to the Hamiltonian used in the Bloch model in section 3.4. Therefore, correlated system-bath dynamics cannot be described in this approach.

The two timescales characterizing the Bloch model emerge as limiting cases in the stochastic model. The inhomogeneous broadening limit, when the experimental timescale τ of equation (3.50) is much shorter than the correlation time τ_c of the fluctuations, the relaxation function has a Gaussian character. In the opposite homogeneous broadening case the relaxation function is an exponential. The absorption line shape is proportional to a Fourier transform of equation (3.48) and therefore time integrated:

$$I_{abs}(\omega) \propto \text{Re}\left[\int_0^\infty dt \exp\left[i(\omega-\omega_{eg})t\right]\exp\left[-g(t)\right]\right].$$
(3.54)

Now, when $\Delta \gg \Lambda$, the slow modulation limit applies and the absorption line shape will have a predominantly inhomogeneous character, with a Gaussian shape and a line width $1/2\pi T_2^{inhom} \propto 2\Delta\sqrt{2\ln 2}$. Similarly, when $\Delta \ll \Lambda$, the line shape will have mainly a homogeneously broadened character and a Lorentzian shape with a width $1/2\pi T_2^{hom} \propto 2\Delta^2/\Lambda$. This is called the fast modulation limit. In the regime between these two limits, when $\Delta \approx \Lambda$, the solvent dynamics are non-Markovian.

3.6.2 The multi-mode Brownian oscillator model

With the problem of non-Markovian dynamics tackled, the final and most general approach would also need to include strong system-bath coupling, in order to model an eventual response of the bath to a change in the system electronic state, as outlined in section 2.4.2. In order to be able to do this, in this last section describing the FWM formalism with respect

to photon echoes, a harmonic normal mode model will be briefly introduced. This MBO model is often applied in describing liquid dynamics [55,145-147,166,167].

Since the evolution of the bath states in this model also depends on the system evolution, the correlation function of the line broadening function, as also used in the above

$$\left\langle \exp\left[-i\int_0^\tau dt\, \delta\omega(t)\right]\right\rangle = \exp\left[-g(t)\right], \tag{3.55}$$

becomes a complex quantity:

$$g(t) = \Delta^2 \int_0^t d\tau_1 \int_0^{\tau_1} d\tau_2\, M'(\tau_2) - i\lambda \int_0^t d\tau \left[1 - M''(\tau)\right]. \tag{3.56}$$

This broadening function is made up of the two system-bath correlation functions, $M'(t)$ and $M''(t)$, and two static parameters, λ and Δ. The former is the reorganization energy due to the relaxation of the bath upon a change of state of the system. The latter is the root mean square of amplitude of the frequency fluctuations. Both the correlation functions are connected to the spectral density of states $C(\omega)$ in this way:

$$M'(t) = \frac{1}{\Delta^2} \int_0^\infty d\omega \frac{C(\omega)}{\omega} \coth\left[\frac{\hbar\omega}{2k_B T}\right] \cos[\omega t], \tag{3.57}$$

$$M''(t) = \frac{1}{\lambda} \int_0^\infty d\omega \frac{C(\omega)}{\omega} \cos[\omega t]. \tag{3.58}$$

Since the spectral density is supposed to be temperature independent when dealing with harmonic potentials, population changes in this spectral density of states, represented through the hyperbolic cotangent term, introduce the temperature dependence expected in the MBO-model. Although these relations are introduced here with the Hamiltonian of section 2.4.2 in mind, they are in fact very general and obtained by invoking a cumulant expansion on the left hand side of equation (3.55). In this case, with the complex line broadening function, the nonlinear response functions of equation (3.41) become:

$$\begin{aligned}
R_A &= \exp\left[-g^*(t_3) + g(t_2) - g^*(t_1) - g^*(t_2+t_1) - g(t_3+t_2) + g^*(t_3+t_2+t_1)\right] \\
R_B &= \exp\left[-g(t_3) + g^*(t_2) - g^*(t_1) - g^*(t_2+t_1) - g^*(t_3+t_2) + g^*(t_3+t_2+t_1)\right] \\
R_C &= \exp\left[-g^*(t_3) - g^*(t_2) - g(t_1) + g(t_2+t_1) + g^*(t_3+t_2) - g(t_3+t_2+t_1)\right] \\
R_D &= \exp\left[-g(t_3) - g(t_2) - g(t_1) + g(t_2+t_1) + g(t_3+t_2) - g(t_3+t_2+t_1)\right].
\end{aligned} \tag{3.59}$$

This again shows that the results obtained for the stochastic model can be recovered when the line shape function is real.

When calculating the third-order optical polarisation for a given set of pulses, a combination of several harmonic oscillators can be used to make up the spectral density. These

modes can have different characteristics depending on their damping factors, amplitudes etc. The resulting spectral density is simply the sum of the various modes:

$$C(\omega) = \sum_i C_i(\omega) = \frac{2}{\pi} \sum_i \frac{\lambda_i \omega_i^2 \omega \gamma_i}{\left(\omega_i^2 - \omega^2\right) + \omega^2 \gamma_i^2} \; . \tag{3.60}$$

At room temperature the experiments with femtosecond pulses, that were used to map out the spectral density, reveal three types of oscillators that are needed to accurately describe the signal. First of all, prominent 'quantum beats' in the echo signals are indicative of intramolecular vibrational dynamics that can be described by underdamped Brownian oscillator (UBO) modes ($\gamma_i \ll \omega_i$). In this case the correlation functions become:

$$M'(t) = M''(t) = \exp\left[\frac{-\gamma_i t}{2}\right] \left(\cos[\Omega_i t] + \frac{\gamma_i}{2\Omega_i} \sin[\Omega_i t] \right), \tag{3.61}$$

with

$$\Omega_i = \sqrt{\omega_i - \left(\frac{\gamma_i}{2}\right)^2} \; . \tag{3.62}$$

Performing the integrations in equation (3.56) gives the associated line broadening function:

$$
\begin{aligned}
g(t) = \frac{\Delta_i^2}{\omega_i} &\left(\exp\left[\frac{-\gamma_i t}{2}\right] \left\{ \frac{-\gamma_i}{2} \frac{\sin[\Omega_i t]}{\Omega_i} \left(3 - \left(\frac{\gamma_i}{\omega_i}\right)^2 \right) - \cos[\Omega_i t] \left(1 - \left(\frac{\gamma_i}{\omega_i}\right)^2 \right) \right\} + \gamma_i t - 3 \right) \\
&+ \frac{i\lambda_i}{\omega_i^2} \left(\exp\left[\frac{-\gamma_i t}{2}\right] \left\{ \frac{\sin[\Omega_i t]}{\Omega_i} \left(\omega_i^2 - 2\left(\frac{\gamma_i}{2}\right)^2 \right) - \gamma_i \cos[\Omega_i t] \right\} - \omega_i^2 t + \gamma_i \right).
\end{aligned}
\tag{3.63}
$$

The associated coupling strength parameters are interrelated through:

$$\Delta_i^2 = \int_0^\infty C(\omega) \coth\left[\frac{\hbar\omega}{2k_B T}\right] = \lambda_i \omega_j \coth\left[\frac{\hbar\omega_j}{2k_B T}\right]. \tag{3.64}$$

These modes are dependent on the type of chromophores used and nearly independent of the type of solvent that is used, and therefore their intramolecular character is broadly acknowledged.

Secondly, an ultrafast decay is found for all solutes in all solvents on the time scale of 6 ~ 60 fs. This decay is usually in part attributed to a free induction type decay due to impulsive excitation of the vibronic manifold, as known from the theory of radiationless processes. Since this decay occurs almost on the same timescale as the resolution of the femtosecond experiments, it is often not included in MBO analysis, also because at the shortest timescales the analysis of correlation function through echo signals is complicated. This decay is also considered to be an intramolecular effect. The fastest of the solvent modes

decays on a timescale of about 50 ~ 100 fs. Therefore the remaining part of the ultrafast decay is often linked to inertial solvent motions that happen when the first shell of solvent molecules reacts to the change in the electronic state of the chromophores. Both these fast decays can be modelled using a temperature independent Gaussian distribution of un-damped ($\gamma_i = 0$) oscillators (GSD):

$$C(\omega) = \frac{2\lambda_i \omega}{\sqrt{2\pi} \ \omega_0} \exp\left[\frac{-\omega^2}{2\omega_0^2}\right].$$
(3.65)

This contribution to the spectral density is often used in the analyses to relate the ul-trafast decay to the solvation frequency (ω_0) that is found in molecular dynamics simula-tions of solvent dynamics. In several studies, it was noted that the time scale of the inertial solvent response is similar for different solvents and that the precise spectral shape of the contribution is not vital when describing the data. In polymers e.g. a decay on a similar timescale is often described using a single strongly damped oscillator. The correlation func-tion that describes the imaginary part of the line broadening functions, is, in the case of a GSD:

$$M''(t) = \exp\left[\frac{-\omega_0^2 t^2}{2}\right].$$
(3.66)

No analytic expression exists for $M'(t)$ and the line broadening function can only be cal-culated by numerically evaluating the spectral density in this case.

Thirdly and finally, the correlation function typically decays on a number of times scales, varying from ±100 fs to over 200 ps depending on the solvent. These modes are generally associated with diffusion like solvent motion and are expressed as several strongly over-damped ($\gamma_i \gg \omega_i$) oscillators:

$$C_i(\omega) = \frac{2\lambda_i \Lambda_i \omega}{\pi\left(\Lambda_i^2 + \omega^2\right)},$$
(3.67)

where $\Lambda_i = \omega_i^2 / \gamma_i$. The strongly overdamped Brownian oscillator (SOBO) is very useful for understanding solvent dynamics because when the high temperature limit (HTL) ap-plies, $\hbar\Lambda_i / k_B T << 1$, it yields a simple inverse correlation time of the system-bath fluctua-tions:

$$M'(t) = M''(t) = \exp\left[-\Lambda_i t\right].$$
(3.68)

The line broadening function associated with the SOBO is similar to the broadening in the stochastic model as the correlation functions are like their stochastic counterpart in equation (3.51):

$$g(t) = \left(\frac{\Delta_i}{\Lambda_i}\right)^2 \left(\exp\left[-\Lambda_i t\right] + \Lambda_i t - 1\right) + i\frac{\lambda_i}{\Lambda_i}\left(1 - \exp\left[-\Lambda_i t\right] - \Lambda_i t\right).$$
(3.69)

Furthermore, in the HTL, the relation between the two normalization constants becomes:

$$\Delta_i^2 = \frac{2k_B T \lambda_i}{\hbar} \qquad (3.70)$$

This type of oscillator is often used to describe spectral diffusion type of effects. It is important that for temperatures lower than room temperature, the validity of the high temperature limit is checked. Two or three of these SOBO oscillators are often needed to adequately model the correlation function in echo experiments. The correlation times of these modes are strongly solvent dependent. In addition, a number of solvents also show some residual static inhomogeneity that is usually modelled with a SOBO oscillator with a correlation time that is much longer than the longest experimental timescale.

So, usually, only the part of the spectral density that is covered by the last group of BO's and one of the fast GSD modes is considered to describe pure solvent dynamics. The similarities of this part of the spectral density with the pure solvent spectral densities probed by Raman experiments and especially optical Kerr effect (OKE) experiments are striking, although there is no proven theoretical correspondence between the echo and the neat solvent experiments. Due to the abstract nature of this type of model for solvent dynamics, one learns little about the precise origins of this part of the correlation function, although the evidence seems to suggest collision induced phase relaxation. Therefore, temperature dependent measurements should be instructive in further identifying the underlying processes.

3.7 Echo Peak Shift

The last chapters of this thesis deal with echo experiments at temperatures as high as room temperature, using femtosecond pulses. The echo signal is measured by a slow detector that records the time integrated intensity of the signal field, and is therefore proportional to time integrated the square of the induced third order polarization:

$$I_{(2,3)PE}\left(t_w, \tau\right) \propto \int \left|P^{(3)}\left(t, t_w, \tau\right)\right|^2 dt . \qquad (3.71)$$

Even though for time integrated echoes on samples with very short dephasing times, equations (3.45) and (3.46) still hold, ignoring contributions due to overlapping pulses is not possible under these experimental conditions because the differences between dephasing times, free induction decays, the pulse delay times and the pulse lengths are much smaller. Instead, the full expression of equation (3.40) needs to be evaluated.

Since the objective of the experiment is to resolve the system-bath correlation function, the analysis of all τ dependent echo experiments for all different waiting times t_w with the parameters of this expression can prove quite time consuming. Fortunately, it was demon-

strated [168-173] that the plot of the shift from zero time of the time integrated echo signal maximum, as a function of t_w, is surprisingly similar to the system-bath correlation function.

This shift of the time integrated echo signal with respect zero time ($\tau = 0$) is called the echo peak shift (EPS). Figure 4.14.a illustrates this shift by indicating the time difference between the maxima of the integrated stimulated echo signal in the two signal directions. The echo at negative delays is measured in the direction where the virtual echo is found at positive delays; in this case pulse 1 and 2 are effectively interchanged. Figure 3.4 illustrates the principle for a simple simulated correlation function. At short waiting times, the signal is Bloch echo like, reflecting the inhomogeneous broadened character of the transition, while at long waiting times the signal is similar to a free induction decay due to the dominating homogeneous qualities of the dynamics at these timescales.

Ignoring contributions to the polarization at negative pulse delays and assuming delta
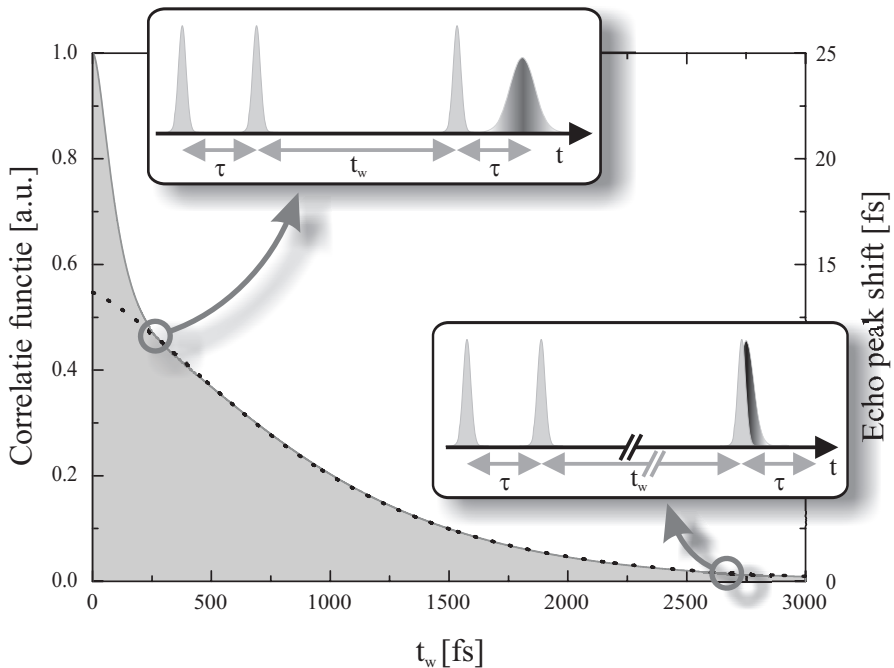

Figure 3.4. The echo peak shift (dotted line) as fitted to a simulated correlation function (grey curve) as indicated in equation (3.74). The EPS function fits the correlation function well, except at short times. The insets illustrate the pulse sequence and the evolution of the echo signal with t_w.

pulses, $E(t) \approx \delta(t)$, equation (3.40) can be simplified, and equation (3.71) becomes

$$I_{(2,3)PE}(t_w, \tau) \propto \exp\left[\frac{-2t_w}{T_1}\right]\cos^2\left[\operatorname{Im}\left[g(t_w) + g(t) - g(t + t_w)\right]\right]\times$$

$$\exp\left[-2\operatorname{Re}\left[g(\tau) - g(t_w) + g(t) + g(\tau + t_w) + g(t_w + t) - g(\tau + t_w + t)\right]\right].$$

(3.72)

To evaluate the above expression with respect to the peak shift as a function of τ the zero-crossing point has to be found:

$$\frac{\partial I_{2,3(PE)}(\tau, t_w)}{\partial t} = 0 .$$

(3.73)

This zero-crossing point can be found analytically by making certain assumptions: the correlation function is supposed to exist of a fast and a slow part in this derivation – as was done in the stochastic approach, cp. with equation (3.52) –,

$$M'(t) = (1 - a)M'_{fast}(t) + aM'_{slow}(t),$$

(3.74)

and the fast part is supposed to have completely decayed at time t_w while the slow part is constant on the time scale of both τ and t_w. As will be discussed later, this is a physical situation that can be reasonably expected. For both parts a critically damped Brownian oscillator is chosen:

$$M'_{f,s}(t) = \Delta^2_{f,s}\exp\left[-\Lambda_{f,s}t\right].$$

(3.75)

When the above assumptions are met, by using a Taylor expansion around t_w of the remaining terms of the expression of the integrated echo signal, one yields for the waiting time dependence of position of the echo-peak $I_{max}(t_w)$ [148,170,171]:

$$aM'_{slow}(t_w) = \frac{\Delta\sqrt{\pi}I_{max}(t_w)}{1 + 2\Delta^2 I^2_{max}(t_w)} .$$

(3.76)

This shows that the echo peak shift is mainly influenced by the slow part of the correlation function and the static offsets of chromophores. Δ can be guessed from the inhomogeneous width of the absorption spectrum. Note that short time EPS signals have to be analyzed with care because of these premises. There are other expressions suggested in the literature to express the coincidence of the correlation function and the EPS signal, which are not equal to (3.76), but similar with respect to the dynamical part of the expression [172,173].

Also correlation functions that exhibit richer dynamics such as rephasing vibrational modes can be included in EPS analysis. Vibrational modes need to be evaluated with care but since these have an intramolecular nature, the analysis of these modes will be introduced when needed.

3.8 Heterodyne Detected Echoes

More information about the correlation function can be retrieved when the transient echo signal is mixed with a fourth pulse. In this case, not the echo intensity is the observable, but the echo amplitude. The signal is proportional to:

$$A_{HDPE}(t) = -2\,\mathrm{Im}\left[\int_{-\infty}^{\infty} E_{LO}^*(t-t') \times P^{(3)}(\mathbf{k}_S, t)\exp\left[i\psi_{LO} + i(\omega_{LO} - \omega)t\right]dt \right]. \tag{3.77}$$

$E_{LO}(t)$ is the field of the local oscillator, the fourth pulse, that has a phase shift relative to the induced polarization ψ_{LO}. This pulse can be used to increase the signal strength with respect to any signal not mixed with the local oscillator or any other homodyne background scattering. The experiment, called heterodyne detected photon echo (HDPE), has the further advantage that it can selectively yield information on both the real and the imaginary part of the optical response functions. Consider the mixed signal in the limit of delta pulses and when by implying large inhomogeneous broadening so that only the rephasing Feynman diagrams need to be included (see Figure 3.3 and equation (3.40) and (3.41)). The previous expression can then be rewritten as [174-176]:

$$A_{HDPE}(\tau, t_w, t) = 2\,\mathrm{Re}\left[\left(R_1(\tau, t_w, t) + R_2(\tau, t_w, t)\right) \times \exp\left[\psi_{LO}\right] \right]$$

$$= \begin{cases} 2\,\mathrm{Re}\left[R_1(\tau, t_w, t) + R_2(\tau, t_w, t) \right] & \text{when } \psi_{LO} = 0 \\[2mm] -2\,\mathrm{Im}\left[R_1(\tau, t_w, t) + R_2(\tau, t_w, t) \right] & \text{when } \psi_{LO} = \dfrac{\pi}{2}. \end{cases} \tag{3.78}$$

Ergo, if the phase of the local oscillator can be controlled with respect to the transient echo field, the complete complex character of the nonlinear response function can be charted.

Besides the fact that the amplitude of the echo instead of the intensity is measured, even without locking the phase of the local oscillator to the polarization, the gated character of the detection scheme ensures that it is sensitive to both the fast and the slow part of the correlation function. In the previous detection method, the signal was dominated only by the slower part instead.

To illustrate this, one has to realize that equation (3.77) shows that the local oscillator resolves the temporal echo shape; the resulting signal will have an envelope shaped like the convolution of the transient echo signal and the gate pulse over a carrier frequency that is set by the interference between the two contributions, see Figure 4.14.b for example. So, if delta pulses are assumed, the temporal envelope of the transient third order polarization is measured.

Suppose the system studied in such an experiment has a purely inhomogeneously broadened optical line shape, where all the transitions have a static Bloch model type offset, the resulting transient echo will always peak at the time $t_{34} = t_{12} = \tau = \tau'$. Scanning the time

between the first two pulses will delay the echo maximum with this coherence time τ. On the other hand, in a purely homogeneously broadened system no echo will occur and only a free induction decay type signal will be measured. This decay always peaks at the time of the third pulse $\tau' = 0$. In practice, the echo maximum will peak at some time in between, and a plot of the echo maximum versus coherence time at a certain waiting time can indicate whether the system is dominated by fast or slow dynamics at that particular time scale. These three scenarios are illustrated by Figure 3.5.

The correlation function is used in the simulation of the third intermediate situation has the same features as used in the illustration of the echo peak shift data. As in equation (3.74) it is a bimodal function with a slow and a fast part. In this case, two strongly overdamped oscillator in the high temperature limit were used:

$$M'_{f,s}(t) = \Delta_{f,s}^2 \exp\left[-\Lambda_{f,s}t\right] \tag{3.79}$$

When the maximum of the transient echo signal has to be found and the local oscillator is
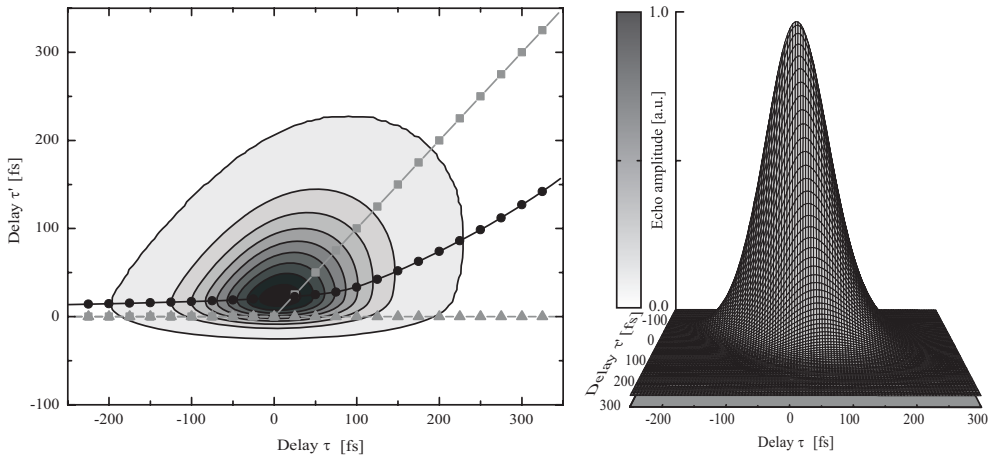
Figure 3.5. A simulation of the time resolved transient echo signal, as measured in a heterodyne detected echo experiment, for a bimodal correlation function (see text) and 10 fs excitation pulses. The left hand side representation shows the contour of the echo amplitude. The black circles indicate the transient echo maximum of a scan of the local oscillator pulse over the coherence time τ. The bimodal system is an intermediate between the two extremes of the Bloch model: a purely inhomogeneously broadened system, which would have echo maxima indicated by the squares, and a purely homogeneously broadened system that would have maxima indicated by the triangles. The right hand side panel shows another 3D representation of the time resolved echo amplitude.

treated as a gating delta pulse, the zero crossing point of the first differential of the polarization $\left| P\left(\tau, t_w, \tau' \right) \right|$ with respect tot the timing of the LO has to be found. The maximum is found at the time $t_{max} = \tau'$ for which holds [148,177]:

$$\left(1 - a \right) \int_0^{t_{max}} M'_{fast}\left(t \right) + a t_{max} - a M'_{slow}\left(t_w \right) \tau = 0 \,. \tag{3.80}$$

This shows that the transient signal at time $\tau \approx 0$ is dominated by the slow part of the correlation function,

$$\left. \frac{\partial t_{max}}{\partial \tau} \right|_{\tau \approx 0} = \frac{1-a}{a} \int_0^{t_{max}} M'_{fast}\left(t \right) \,, \tag{3.81}$$

and at longer times τ by the slower part of the correlation function as well,

$$\left. \frac{\partial t_{max}}{\partial \tau} \right|_{\tau \to \infty} = M'_{slow}\left(t_w \right) \,. \tag{3.82}$$

This gives then a and $M'_{slow}\left(t_w \right)$ for this type of correlation function. It is thought that the time, at which the change in slope separating these two regimes occurs, can be defined as

$$\tau_{br} = \frac{1-a}{a} \frac{\int_0^\infty M'_{fast}\left(t \right) dt}{M'_{slow}\left(t_w \right)} \,, \tag{3.83}$$

and that hence this point is indicative of the correlation time t_{fast} associated with the fast part of the correlation function:

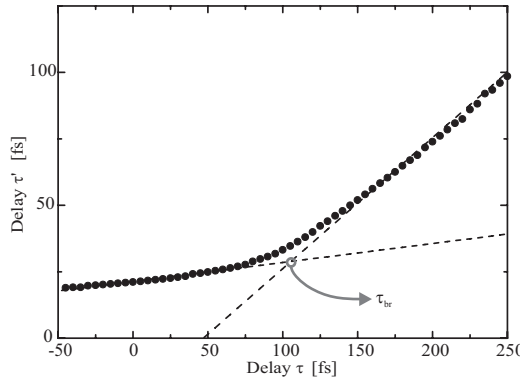*Figure 3.6. A detailed view of the transient echo maxima calculated for the bimodal correlation function in the last figure. Linear fits to the slope of the plot of the echo maximum in the regime $\tau \approx 0$ and $\tau \to \infty$ are shown as dashed lines.*

$$t_{fast} = \int\limits_0^\infty M'_{fast}(t) \, dt \, . \tag{3.84}$$

The simulations of which the results are displayed in Figure 3.5 are performed using the complete expression of equations (3.40) and (3.41), assuming Gaussian shaped pulses with a temporal width of 10 fs. The two equally weighed strongly overdamped oscillators had decay times $\Lambda_{fast} = 0.01 \text{ fs}^{-1}$ and $\Lambda_{slow} = 1 \times 10^{-5} \text{ fs}^{-1}$ and therefore the breakpoint is expected to be at $\tau_{br} \approx 101 \text{ fs}$. In fact a small offset occurs due to the finite pulse duration. This also causes the HDPE signal to peak at non-zero times when the coherence times are negative.

3.9 Stimulated Photon Echoes in the TLS Model

Chapter 5 deals with photon echo experiments in cold molecular glasses using relatively narrow band picosecond pulses that overlap with only a limited part of the chromophore absorption spectrum. At these temperatures, the dephasing times are so long that in the analysis using the above formalism any contributions due to overlapping pulses can be neglected. In section 3.6 it was shown that this simplifies the expression for the echo signal.

The waiting time can typically be varied from picoseconds to hundreds of milliseconds when the excited state population is stored in a long-lived triplet state of the chromophore during fluorescence [178]. Then, as long as the triplet state lives, the third pulse can still be scattered from the population grating in the ground state. This technique is called the long-lived stimulated photon echo. The two-pulse photon echo (2PE) is the same experiment in the limit $t_w = 0$. This is the experiment that determines the optical line width on the shortest possible time scale and hence the homogeneous line width. It can easily be shown [117,179,180] that the photon echo decay with respect to τ at a fixed t_w is equivalent to the Fourier transform of the hole shape in a hole burning (HB) experiment with a pump-probe delay t_w. In order to assess the amount of spectral diffusion, the intensity of this echo is measured as a function of τ for various t_w's. This is essentially the same experiment as the *gedanken* experiment introduced in the first chapter and Figure 1.3.

Slow integrating detectors measure the echo intensity and consequently the square of the third order polarization is detected, as presented in equation (3.71). Furthermore, according to equation (3.45), when assuming delta pulses, the time-integrated polarization can be expressed as:

$$P(\tau, t_w) \propto A(t_w) \left\langle \exp\left[-i\left(\int_0^\tau dt\, \omega(t) - \int_{t_w+\tau}^{t_w+2\tau} dt\, \omega(t) \right) \right] \right\rangle . \tag{3.85}$$

The brackets again indicate an average over all stochastic realizations. The term $A(\tau, t_w)$ incorporates any population relaxation during the waiting time. The dephasing terms and population relaxation terms can be separated here, because in these experiments the dephasing is typically much faster than the population decay rate. Since in this case typical waiting times can exceed the coherence times by far ($t_w \gg \tau$), in a chromophore with a non-radiatively coupled long-lived bottleneck state this term only depends on t_w and takes a slightly different form from the optical two-level system case:

$$A(t_w) = \exp\left[\frac{-t_w}{T_1} \right] + \frac{1}{2}\varphi_{ISC}\left(\exp\left[\frac{-t_w}{T_{triplet}} \right] - \exp\left[\frac{-t_w}{T_1} \right] \right) . \tag{3.86}$$

T_1 is the lifetime of the excited state, $T_{triplet}$ of the bottleneck state and φ_{ISC} is the intersystem-crossing yield.

Presuming the 2PE to decay exponentially, a premise to be discussed later, the homogeneous line width $1/2\pi T_2^{hom} \equiv 1/2\pi T_2^{2PE}$ is related to the echo intensity as follows [90,102,112]:

$$I(\tau) \propto \exp\left[-4\tau / T_2^{2PE} \right] . \tag{3.87}$$

The factor 4 stems from the 2 coherence periods and the intensity dependent detection.

Now the effects of spectral diffusion due to the flipping of TLS's in cold glasses on photon echo experiments can be evaluated. The TLS's and the distributions of TLS parameters were introduced in section 2.3.

The formalism used all through the literature on this subject originates from the description NMR spin echo experiments [116]. In spin resonance experiments, the resonance frequencies of spins that interact with the applied fields are influenced by flips of neighbouring spins. Spin-½ Hamiltonians are identical to the Hamiltonians of TLS's. Hu *et al*. have analytically solved the effect of ensembles of spins, with broad distributions of parameters, on NMR spin-echo decays [86,103,181]. These results were further developed when applied to the effects of TLS's on acoustic phonon-echo experiments, by Maynard, Rammal and Suchail [85,112]. Analogous to this approach, in the optical domain the results were also applied to fluorescence line narrowing experiment by Reinecke [97]. Huber *et al*. used the exact results of Hu and Walker to describe two-pulse photon echo results [98-100,182,183]. The method by Huber *et al*. was further extended to encompass other optical experiments as three-pulse photon echoes [106]. When a more general description of the echo response function along the lines of the theory described in the previous sections emerged, the method developed by Huber *et al*. was incorporated in this description by Fayer *et al*.

[88,89,95,96,114,117,179,180]. However, in essence, these results all stem from the exact solution of the averages over all TLS-parameter distributions by Hu and Walker [86,103], implemented for the case of dipolar coupling described by Maynard, Rammal and Suchail [85].

Finally, Silbey and co-workers reworked and extended these results with a more thorough evaluation of the stochastic averaging results [102], and the slightly modified TLS-parameter distributions (cp. section 2.3.2) [87,107].

3.9.1 Configurational and Stochastic Averaging

As mentioned earlier in section 2.3, any of a number of N_{chrom} chromophores dissolved in a glass can couple to a number of N_{TLS} TLS's. When this is the case, a flip of the i-th TLS will, following the so-called "sudden-jump" model [116] as described in section 2.3.5, cause an immediate shift in the j-th chromophore's resonance frequency $\omega_j(t)$:

$$\omega_j(t) = \omega_0 + \sum_i \delta\omega_{ij}\, h_i(t)\,. \tag{3.88}$$

The stochastic variable $h_i(t)$ represents the state of the corresponding TLS and can take random values of $+1$ and -1. The interaction between chromophore and TLS is when dipolar coupling is assumed between the chromophore and the TLS's, as given in Chapter 2, set by the particular parameters of the TLS:

$$\delta\omega_{ij} = \frac{3\sqrt{3}}{4}\,\pi\,\Omega\,\frac{\varepsilon_i}{E_i}\,\frac{\left(1 - 3\cos^2\theta_i\right)}{r_{ij}^3}\,. \tag{3.89}$$

It is these parameters that have to be averaged over, in particular the spatial distribution and the orientations of the double wells, the distribution of the relevant TLS asymmetry and tunnelling matrix elements, following the distributions described in Chapter 2 [85,86,112], and the stochastic histories.

Assuming spatially uniformly distributed non-interacting TLS's, this directly gives a nonlinear response term:

$$R^{\mathrm{TLS}}\left(\tau, t_w, \tau\right) = \frac{1}{N_{chrom}} \sum_{j=1}^{N_{chrom}} \left\langle \prod_{i=1}^{N_{TLS}} \exp\left[-i\left(\int_0^\tau dt\, \delta\omega_{ij}\, h_i(t) - \int_{t_w+\tau}^{t_w+2\tau} dt\, \delta\omega_{ij}\, h_i(t)\right)\right] \right\rangle. \tag{3.90}$$

For an infinite number of these statistically independent TLS's, the product of all these single TLS correlation functions can be rewritten as [98,182,183]:

$$R_j^{\text{TLS}}\left(\tau,t_w,\tau\right)=\exp\left[-N_{chrom}\left\langle 1-\exp\left[-i\delta\omega_j\left(\int_0^\tau dt\,h(t)-\int_{t_w+\tau}^{t_w+2\tau}dt\,h(t)\right)\right]\right\rangle\right],\qquad(3.91)$$

where a frequency shift $\delta\omega_j$ indicates the average frequency offset of a single chromophore. The spatial average over all chromophore environments under the assumption of evenly distributed and randomly oriented TLS's will yield when $r_{\max}\to\infty$ [181], see also equation (2.29),

$$R^{\text{TLS}}\left(\tau,t_w,\tau\right)=\exp\left[-\frac{4\pi^3}{3}\left\langle \delta\omega_{avg}\left(\int_0^\tau dt\,h(t)-\int_{t_w+\tau}^{t_w+2\tau}dt\,h(t)\right)\right\rangle\right].\qquad(3.92)$$

Here $\delta\omega_{avg}$ is an average frequency offset determined by the distribution functions of the tunnelling parameters, the interaction strength Ω and the density of TLS's, which is indicated by ρ_{TLS}:

$$\delta\omega_{avg}=\Omega\rho_{TLS}\frac{\varepsilon}{E}\,.\qquad(3.93)$$

Therefore, equation (3.92) now only involves averages over the tunnelling matrix elements, the TLS asymmetries and the history path of the flipping TLS's.

This averaging was accomplished exactly by Hu and Walker [86], and later in a more thorough fashion by Suarez and Silbey [102], by means of Laplace transform methods. The Laplace transform of the sum of the two integrals in equation (3.92) yields an expression involving the probability of a TLS jumping from the lower to the upper state w_1 and *vice versa* probability w_2:

$$\int_0^\infty d\tau\left\langle \int_0^\tau dt\,h(t)-\int_{t_w+\tau}^{t_w+2\tau}dt\,h(t)\right\rangle\exp[-\sigma\tau]=$$

$$\frac{2w_1w_2\left((\sigma+2w_1+2w_2)-\sigma\exp[-(w_1+w_2)t_w]\right)}{(w_1+w_2)^2\sqrt{(\sigma+2w_1+2w_2)(\sigma+2w_1)(\sigma+2w_2)\sigma^3}}.\qquad(3.94)$$

The flipping rate R of a TLS is the sum of these probabilities, and under the assumption of the initial probabilities to be those of a thermal equilibrium, i.e. $w_1/w_2=\exp[-E/k_BT]$, the inverse Laplace transformation of the solved history average gives after some rearranging:

$$R^{\text{TLS}}\left(\tau,t_w,\tau\right)=\exp\left[-\left\langle \mathscr{F}\left(R,\tau\right)+\mathscr{G}\left(R,\tau,t_w\right)\right\rangle\right].\qquad(3.95)$$

The average indicated by the brackets now only involves the internal TLS parameters Δ and ε. The line broadening function $\mathscr{F}\left(R,\tau\right)$ describes the 2PE decay and the function $\mathscr{G}\left(R,\tau,t_w\right)$ describes additional dephasing brought in by the non-zero waiting time t_w during a 3PE experiment. It is now convenient to represent the averaging over ε and Δ in terms of integrals over E and R, as was already done previously in the distribution func-

tion of equation (2.21). This yields an expression for the 2PE line broadening function with a further change of variables $x = R\tau$ and $z = E/k_B T$:

$$\mathscr{F}(R,\tau) = \frac{\pi^3}{3}\Omega P_0 \rho_{TLS} c^{-\nu/2} (k_B T)^{(1+\mu-\nu/2)} \tau^{(1-\nu/2)} \int\limits_{E_{min}/k_B T}^{E_{max}/k_B T} dz \; z^{(\mu-\nu/2)} \frac{\mathrm{sech}^2[z/2]}{\coth^{\nu/2}[z/2]}$$
$$\times \int\limits_{R'_{min}\tau}^{R'_{max}\tau} \frac{dx}{x^{2-\nu/2}} \left(1 - x/R'_{max}\tau\right)^{\mu/2} F\left(\tanh[z/2], x\right). \tag{3.96}$$

Similarly $\mathscr{G}(R,\tau,t_w)$ becomes:

$$\mathscr{G}(R,\tau,t_w) = \frac{\pi^3}{3}\Omega P_0 \rho_{TLS} c^{-\nu/2} (k_B T)^{(1+\mu-\nu/2)} \tau^{(1-\nu/2)} \int\limits_{E_{min}/k_B T}^{E_{max}/k_B T} dz \; z^{(\mu-\nu/2)} \frac{\mathrm{sech}^2[z/2]}{\coth^{\nu/2}[z/2]}$$
$$\times \int\limits_{R'_{min}\tau}^{R'_{max}\tau} \frac{dx}{x^{2-\nu/2}} \left(1 - x/R'_{max}\tau\right)^{\mu/2} G\left(\tanh[z/2], x\right) \tag{3.97}$$
$$\times \left(1 - \exp\left[-\frac{t_w x}{\tau}\right]\right).$$

The functions $F(\xi,x)$ and $G(\xi,x)$ involve modified zero and first order Bessel functions of the first kind $I_{0,1}[x]$, and can be evaluated numerically:

$$F(\xi,x) = 2\exp[-x]\int dx' \; I_0\left[(x-x')\xi\right] x'\left(I_0[x'] + I_1[x']\right)$$
$$G(\xi,x) = \frac{1}{2}\frac{\partial F(\xi,x)}{\partial x} = \exp[-x]\int dx' \; I_0\left[(x-x')\xi\right] I_0[x']. \tag{3.98}$$

Note that $\xi = \tanh[E/2k_B T] = (w_1 - w_2)/(w_1 + w_2)$ and the change of variables also sets $R'_{max} = c(k_B T)^3 z^3 \coth[z/2]$ and $R'_{min} = c\Delta^2_{min} k_B T z \coth[z/2]$ (compare section 2.3.2).

The first function, $\mathscr{F}(R,\tau,t_w)$, goes to zero at $R \gg 1/\tau$ and $R \ll 1/\tau$. This means that only TLS's that relax on the same timescale as the optical dephasing contribute to the 2PE-decay. An analysis of this function shows that in order to obtain a single exponential 2PE-decay, a hyperbolic distribution of flipping rates, $P(R) \propto 1/R$, is necessary [85]. The second function, $\mathscr{G}(R,\tau,t_w)$, behaves as a window function, being constant between $1/\tau < R < 1/t_w$ and zero elsewhere because of the last term. Only TLS's that flip on timescales that fall within this 'window' contribute to the 3PE-decay. This illustrates the potential of the 3PE to map out the distribution of flipping rates.

The above functions are normally evaluated by setting the maximum limits to the TLS parameter distributions, and therefore the upper limits of the integrals, to infinity and the lower limits to zero. Remembering that the 2PE amplitude is set by $P^{(3)}(\tau, t_w = 0) = \exp[-\tau/t_w]\exp[-\mathscr{F}(\tau)]$, and by setting $\nu = 0$ for the time being, since

this parameter was introduced explicitly to bring in non-exponential echo decays, the homogeneous line width can be calculated in the model by Silbey *et al.*:

$$\frac{1}{\pi T_2^{hom}} = \frac{\pi^2}{6} \Omega P_0 \rho_{TLS} K_\mu \left(k_B T \right)^{1+\mu} - \frac{1}{2\pi T_1} \tag{3.99}$$

Here, K_μ is a constant that can be evaluated numerically ($K_{\mu=0} = 7.32772$):

$$K_\mu = \int_0^\infty dz \, z^\mu \operatorname{sech}^2 \left[z/2 \right] \int_0^\infty dx \frac{F\left(\tanh\left[z/2 \right], x \right)}{x^2} . \tag{3.100}$$

In this approach, the 2PE and 3PE decays are expected to be exponential for $\nu = 0$, and nearly exponential otherwise. In addition, the photon echo decay time varies linearly with $\ln\left[t_w \right]$ for $\nu = 0$ [87,91] (and slower than logarithmic for larger values of ν):

$$\frac{1}{\pi T_2^{SD}} \left(t_w \right) = \frac{\pi^2}{6} \Omega P_0 \rho_{TLS} \left(k_B T \right)^{1+\mu} \left(L_\mu \ln\left[c \left(k_B T \right)^3 t_w \right] + M_\mu \right), \tag{3.101}$$

with numerical constants

$$L_\mu = \int_0^\infty dz \, z^\mu \operatorname{sech}^2 \left[z/2 \right], \tag{3.102}$$

and

$$M_\mu = \gamma L_\mu + \int_0^\infty dz \, z^\mu \operatorname{sech}^2 \left[z/2 \right] \ln\left[z^3 \coth\left(z/2 \right) \right], \tag{3.103}$$

that use Euler's constant γ. The derivation of these results is not trivial and the results are also disputed. The problems with the use and the validity of the methods involved will be discussed when the relevant experimental results are analyzed. For a thorough discussion of these problems the reader is referred to reference [104], which also contains a more extended review of the above.

To summarize the foregoing results: the line widths associated with the echo decays are expected to broaden logarithmically with the waiting time and show a power law dependence on temperature:

$$\frac{1}{2\pi T_2^{SD}} \propto T^{1+\mu-\nu/2} \ln\left[t_w \right]. \tag{3.104}$$

At the same time, the echo signal is expected to depend exponentially on the coherence time.

3.9.2 Echo Intensity Waiting Time Dependence

When the intensity dependence of the 3PE is explored as a function of waiting time instead of the coherence time, the population dynamics of the chromophore are probed. This longitudinal echo decay, for a fixed separation time between the first two pulses τ, can, however, also be derived from the coherence decay measurements. When the triplet state lifetime exceeds all others by far [90,178,184], the echo intensity it is predicted to be:

$$I_\tau\left(t_w\right) = I_0 \exp\left[-\frac{4\tau}{T_2^{eff}\left(t_w\right)}\right]\left(\exp\left[-\frac{t_w}{T_1}\right] + \frac{1}{2}\varphi_{ISC}\left(\exp\left[-\frac{t_w}{T_{triplet}}\right] - \exp\left[-\frac{t_w}{T_1}\right]\right)\right)^2. \qquad (3.105)$$

This equation presents the echo intensity relative to the intensity I_0 at a short waiting time t_w^0, with $t_w^0 \gg T_1$. $T_{triplet}$ is the triplet state life time and φ_{ISC} is the intersystem crossing yield.

This particular projection of the space spanned by the parameters of $P^{(3)}\left(\mathbf{k}_S, \tau, t_w, t\right)$ might not seem very valuable because it mainly contains information on T_1 population dynamics that can be retrieved by simpler means than an echo experiment. But there is some remaining T_2 dependence, and the experiment can therefore serve as a check on the results from the coherence dimension. And sure enough, in echo experiments on a deuterated ethanol glass and other glasses, Meijers *et al.* [90,185], and also Thorn Leeson *et al.* [45,184] for proteins, found a significantly smaller echo intensity from the microsecond region onwards to longer time scales than predicted by equation (3.105). This implies the existence of an additional population relaxation process. To establish the nature of this extra relaxation channel several mechanisms leading to an anomalous intensity loss have been proposed. Some of these will be discussed with the presentation of the longitudinal data in the experimental chapters.

Chapter 4

Methods and Experiments

The experimental techniques used in this work are introduced. Special attention is dedicated to some recently discovered heating artefacts in picosecond echo experiments. Methods for sample handling and data analysis are also discussed.

4.1 Introduction

All experiments described in this thesis share a number of key characteristics, since all experiments involve photon echoes. However, very different ways of optical pulse generation, sample preparation, signal detection and data collection were used in distinct experiments. For the most part these techniques have been described in great detail elsewhere, so in this chapter only an outline of the experimental techniques will be given. Only elements that are new or become important in later chapters are reviewed more thoroughly.

In a three-pulse photon echo experiment, three pulses are applied to a sample at discrete times in separate directions. Figure 4.1 illustrates the pulse sequence. The configuration depicted in this figure satisfies perfect phase matching [55,186], as introduced in section 3.2. Assuming weak fields and slowly varying pulse envelopes the intensity of the echo scattered from the frequency grating is proportional to:

$$I_{\text{echo}} \propto \text{sinc}\left(\left|\mathbf{k}_{\text{echo}} - \mathbf{k}_{\text{tot}}\right| \cdot L/2\right) \text{ with } \mathbf{k}_{\text{tot}} = \mathbf{k}_3 + \mathbf{k}_2 - \mathbf{k}_1 . \tag{4.1}$$

(Cp. with equations (3.4) and (3.5).) The sample thickness, L, is very large, and the echo is most intense when the difference between the total wave vector of the incident pulses, $\mathbf{k}_{\text{tot}}$, and the wave vector of the excited signal, $\mathbf{k}_{\text{echo}}$, is zero, i.e. perfect phase matching. When

the angles between the incident beams are small however, this sinc function varies only slowly with the precise configuration and therefore some freedom exists in choosing configurations in specific experiments.

The experiments in this thesis fall into two categories, those carried out using optical pulses of several picoseconds and on a low repetition rate with waiting times up to tens of milliseconds, and those conducted with broadband femtosecond laser pulses and high repetition rates. The setups that were used to generate these two types of pulses differ fundamentally and are described in the following two sections.

4.2 The Picosecond Laser Setup

In order to study dynamics of residual low-level excitations of chromophores in glasses at cryogenic temperatures relatively narrow band pulses are needed. In this way the long-lived photon echoes only probe these precise dynamics without other modes being exciting, in particular when tuned precisely to the zero-phonon transition of the chromophore. The narrow bandwidth does result in a lower time resolution due to Fourier-transformation limitations that limit pulse duration in these experiments to a minimum of several picoseconds.
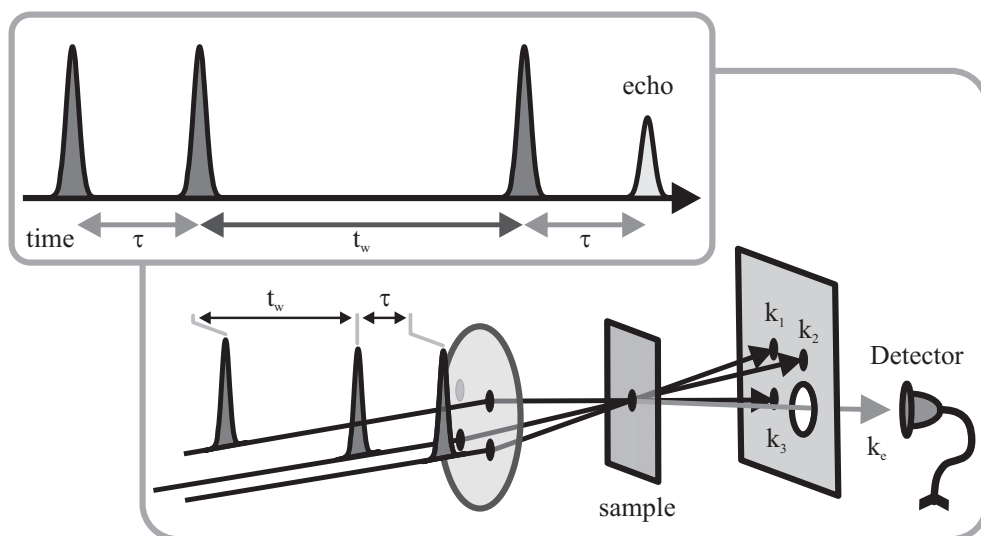
Figure 4.1. Overview of the timing and spatial configuration of the optical pulses in a three-pulse photon echo experiment.

The setup used to produce picosecond pulses is based on two synchronously pumped dye lasers and a three stage amplifier also based on liquid laser dyes. An overview of the setup is given in Figure 4.2. Both elements and the total setup have been described in detail before [44,158,187]. Dye lasers can be considered proven technology. Even today, with plenty of all solid state laser sources available and notwithstanding their poor pulse-to-pulse stability and low efficiency, dye lasers are still very effective tools for producing Fourier transform limited picosecond pulses because of their tunability and ease of operation.

4.2.1 The Dye-Lasers and Amplification Stages

An actively mode-locked Spectra Physics model 171 argon-ion laser synchronously
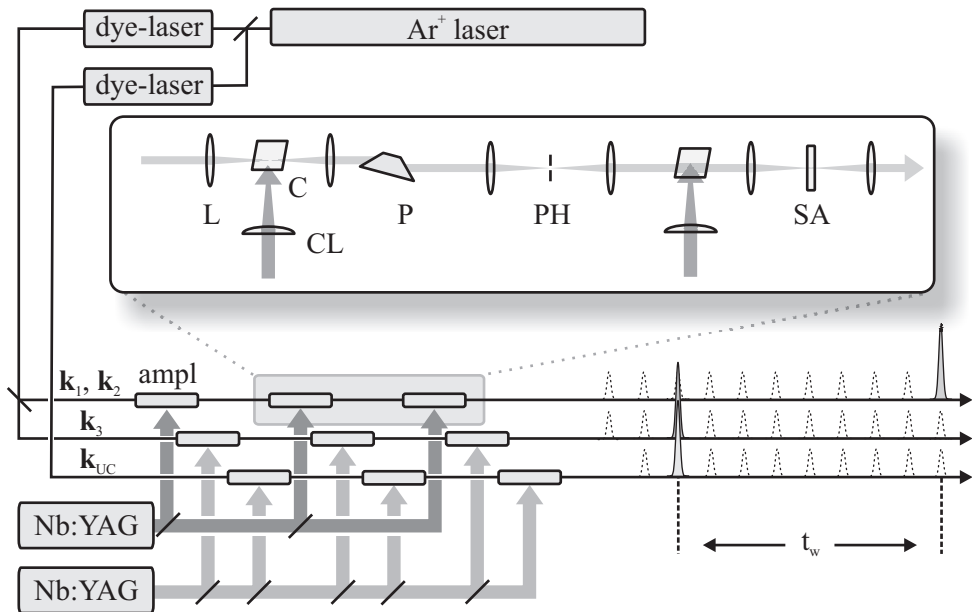
Figure 4.2. The picosecond dye-lasers with 3 lines of 3 amplification stages. The k-vector symbols at the beginning of each line denote the pulses that part generates. The insert gives a detailed view of the last two stages of each line. The first stage is identical to the second. L = lens, C = cuvet, CL = cylindrical lens, P = direct vision prism, PH = 100 μm pinhole, SA = saturable absorber. The pulses at the end of the amplification lines illustrate the principle of electronically generated delay.

pumped two Spectra Physics model 375 dye lasers with extended cavities [113,188], to match the pump laser's cavity at an 82 MHz repetition rate with ~800 mW in ~100 ps pulses. Using a two-plate Lyot filter 4 ps pulses with an 8 cm^{-1} spectral width were produced. Optimum pulse widths were achieved by tuning the dye laser cavities slightly, so that the intracavity round trip time of the pulses is slightly shorter than the repetition rate. Solutions of 2×10^{-3} M Rhodamine 6G in ethylene glycol were used as the laser dye [158]. If needed the cross-correlation of the pulses of both dye lasers could be continuously monitored using a home-build cross-correlator.

The output of the lasers was amplified in three home-build three-stage amplifier lines pumped by two Spectron SL401 Q-switched Nd:YAG lasers, in a typical experiment at a 10 Hz repetition rate, with 15 mJ pulses [189]. Consequently, in each line only one in eight million dye laser pulses was amplified and a saturable absorber at the end of the line filtered out the rest. The YAG-lasers were triggered by the radio frequency signal used for mode-locking the argon-ion laser. A combination of a frequency divider and two home-build electronic cable-delay timers was used to manipulate the timing between the two YAG-lasers with respect to each other and to the dye-laser pulse train. The timing between the amplified pulses in the respective amplifier lines could be varied from 0 to 0.1 s with steps of 12.5 ns, the time between two subsequent pulses in the dye laser pulse train. This delay was used to generate long waiting times t_w. Figure 4.2 illustrates the principle. In practice the maximum waiting time used was 56 ms.

In the first two amplification stages of each amplification line, the dye laser pulse was focused in a transversely pumped dye-cell. A direct vision prism and a spatial filter were used to filter out any spontaneous emitted light to avoid the occurrence of amplified spontaneous emission. No focusing was used in the third amplification stage and any spontaneous emitted light was filtered out with the saturable absorber. A detailed description of the layout and operation of the amplification stages is given in the theses of Hesselink [187] and Meijers [44]. Especially the choice of type of laser dye used and the precise concentration of the dye in the various stages for amplification of pulses with different wavelengths were critical factors and warranted some careful experimentation.

In order to reduce the pulse-to-pulse fluctuations of the amplified pulses, the amplifier stages were operated in a near-saturation regime with respect to the YAG pump pulses by adjusting the pump intensity [190]. At the same time the amplifier stages were fully depleted by the seeding dye-laser pulses through adjustment of the laser-dye concentration of the stage and by varying the position of the focus of the seed in the amplifier cells. Pulse-to-pulse fluctuations were considerable nonetheless, and usually amounted up to 15% of the total pulse intensity. Amplification of the wings of the pulses slightly increased the width to 6 ps. Pulse intensities up to 100 μJ could be achieved in this manner, although the setup

was seldom used to produce pulses stronger than 10 μJ. Due to time jitter between the up-conversion and excitation pulses cross-correlations yielded profiles that were slightly, ~ 1 ps, broader than the corresponding autocorrelation profiles, see Figure 4.3.

4.2.2 Signal Detection and Data Collection

The pulses were timed using the electronic delay for the waiting time t_w. Delay τ and the delay of the so-called upconversion pulse were timed by two home-build translation stages mounted with retro reflectors that were computer controlled and could be scanned over 1.5 ns with 0.1 ps precision. The beams were focused in the sample using a lens with a 160 mm focal length. The beam-configuration was identical to the configuration depicted in Figure 4.1.

The sample was mounted in an Oxford Instruments Variox helium bath optical cryostat, in which the sample was cooled to 1.5 K by flowing cold helium gas through the sample space. A temperature controller could be used to stabilize the sample at any temperature between 1.5 K and 300 K with 0.1 K precision.

Due to the bad optical quality of the samples, stray light was orders of magnitude stronger than the signal in the $\mathbf{k}_3 + \mathbf{k}_2 - \mathbf{k}_1$ direction and direct detection of the echo-signal was impossible. A number of measures were taken to counteract this.
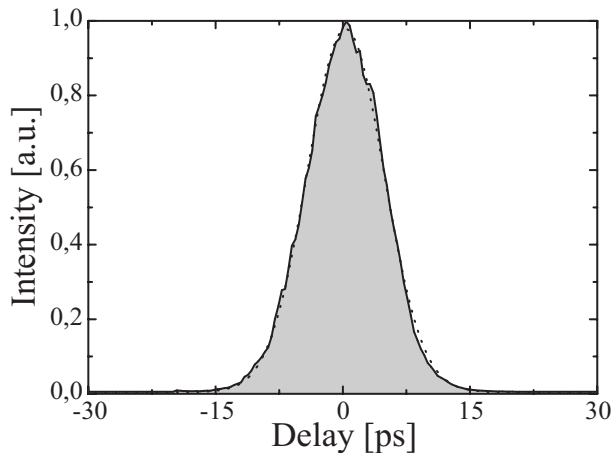

Figure 4.3. Cross-correlation of an amplified excitation pulse with an amplified up-conversion pulse. The dotted line is a fit of a Gaussian pulse profile to the data, FWHM 5.3 ps.

All light, except the light in the signal direction, was blocked using a diaphragm and a pick-up mirror. The remaining light was mixed with an upconversion pulse at the time $t_w + 2\tau$, when the Bloch echo occurs, in a 1 cm thick KDP-crystal. This upconversion pulse acted as both a spatial and a time gate for the echo signal, thus vastly improving the signal to noise ratio. The sum frequency of both fields was detected through a Scott UG11 filter and a Spex 1704 monochromator by an EMI 9816QB photomultiplier. Since the upconversion laser was tuned to a frequency that differed from the frequency of the excitation pulses, this detection scheme acted as a frequency gate as well and further suppressed stray light. Finally, the signal was measured by a boxcar integrator, digitized and automatically collected.

4.2.3 Sample Preparation and Handling

In order to perform photon echo experiments with a waiting time up to 0.1 s, a chromophore is needed that has an equally long excited state lifetime, in other words, the population lifetime needs to be long enough to make long waiting time experiments possible. On the other hand, if the chromophore has a lifetime longer than 0.1 s, either the repetition rate of the experiments has to be made impractically low or accumulation of excited state population may impede the experiment. Chromophores with a high intersystem crossing yield (ISC) to a long-lived triplet state, like Zn-porphyrines [191] suit the bill. The triplet state acts as a bottleneck for the excited state population to return to the ground state, thus allowing for long waiting time experiments on the ground state. Furthermore, the porphyrines are soluble in the liquids relevant for the studies described here and have resonance frequencies that match the capabilities of the laser system. In the experiments covered by this thesis, Zinc porphin (ZnP, see Figure 4.4), purchased from Porphyrin Products, was used without further purification. It has an excited state lifetime of ~ 3 ns in ethanol, the ISC is approximately 90% and the lifetime of the main triplet state is ~ 90 ms [192-196].

The glass forming potential of the host determined the choice of solvent. Not all liquids form glasses on rapid cooling. It has been found that liquids with a boiling to melting temperature ratio larger than 2 tend to be fragile and are generally good glass formers [37] (see section 2.1). In the picosecond experiments ethanol, with a glass temperature of 97 K, was the solvent of choice. In fact deuterated ethanol (EtOD) was employed as supplied (Janssen p.a.). The use of EtOD instead of normal ethanol, suppresses permanent hole burning, which is detrimental to photon echo measurements. During the experiments signatures of photochemical hole burning were observed, but no corrections were found to be necessary for the measurement of a single echo decay (ca. 20 min.). ZnP was dissolved in EtOD at

concentrations between 5×10^{-4} and 1×10^{-3} M . The solution was carefully degassed in a square cuvet ($10 \times 10 \times 1$ mm) and sealed before cooling down. The optical density of the samples at the excitation wavelength was 0.15 – 0.2 at 77 K.

Samples were precooled by plunging them into liquid nitrogen and then allowed to relax for 3 days at 77 K. Hereafter they were cooled to low temperatures in a helium bath cryostat. Prior to performing the experiments the samples were again allowed to relax for at least two hours at the experimental temperature. Because the cooling rate was higher than 6 K min^{-1} (T_g = 97 K) and the sample was kept below 90 K at all times a structural glass had formed. It so happens that both ethanol and deuterated ethanol can also be prepared as a stable orientational glass [197-200]. In this phase the molecules are arranged on an ordered lattice but with disordered orientations. Even though the structural glass was used for the experiments here, positional disorder is not essential for the manifestation of glasslike behavior.

The excitation wavelength was 567 nm, and pulse energies were varied from 400 nJ per pulse to 20 nJ per pulse using absorbing neutral optical density filters. Pulse energies were measured using a Molectron J3-02 pyrometer for the unattenuated pulses and a calibrated BPY photodiode for lower laser fluences.
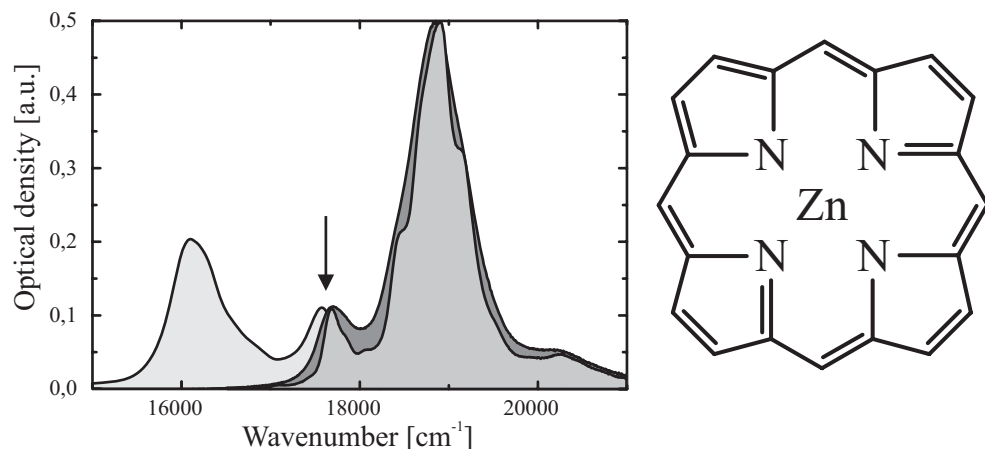
Figure 4.4. The absorption spectrum of zinc-porphin (right) at 300 K (dark grey), 77 K (grey) and the scaled emission spectrum at 300 K (light grey). The arrow indicates the excitation wavelength at 567 nm.

4.2.4 Data Processing

In order to study the physics behind the echo decays, high experimental accuracy had to be achieved. Great care was taken to eliminate any sources of noise as much as possible. The main source of experimental noise were the ~15% pulse-to-pulse fluctuations of the excitation and upconversion beams. Therefore, reducing these variations by optimizing the amplifier setup as described in section 4.2.1 was the first step in improving the signal to noise ratio.

Furthermore, by optimizing the dye laser pulse length and the width of the argon laser pulses the time jitter between the three amplifier lines could be reduced and this further improved the experimental resolution. Any remaining noise was filtered out by averaging over several (3 ~ 10) shots per data point and subsequently averaging every scan, lasting 5 to 10 minutes, 3 to 5 times. This resulted in scans as depicted in Figure 4.5.

In order to exclude any long-time drifts the complete series of scans was always performed in a random order with respect to the waiting times. Long-time trends were never observed in the data. Scans of different spots in the sample sometimes yielded small offsets
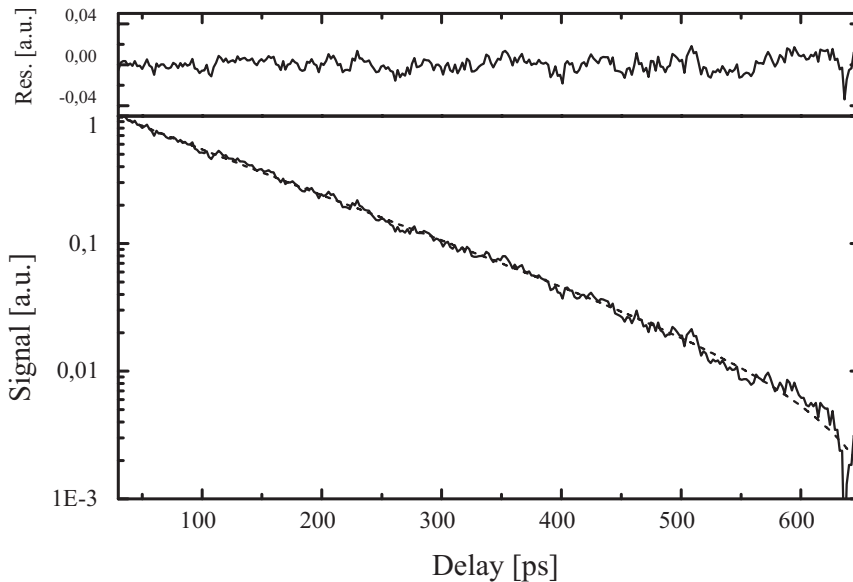
Figure 4.5. A typical picosecond echo trace. The dashed line is a fit of a stretched exponential decay to the data. The fit was performed assuming normal distributed proportional noise. The fitted value of the stretch parameter was 0.9 (see text). The top plot displays the residual noise.

of the exponential decay times, but the observed trends with respect to the waiting times were always the same. Occasionally, over periods of several hours, some bleaching or hole burning was detected, but never to the extent that it could influence a single scan of the coherence time or a scan of the waiting time for a fixed coherence period.

Since pulse-to-pulse fluctuations are the main source of noise, the data were fitted assuming normal distributed noise proportional to the signal intensity. Fitting the data with proportional normal noise, combined with the measured static instrumental background noise did not improve the results. The confidence limits of the resulting fit parameter values, was assessed by comparing the fits to a number of similar data sets, by comparing fits to a set of synthetic data sets created by a Monte Carlo simulation, or by comparing fits to data sets simulated by using a boot-strap method for generating synthetic data [201].

The echo traces retrieved in the picosecond experiments are not always exact exponential decays. This hampered the interpretation of the traces in terms of a single decay constant. In order to quantify this effect the decays were fitted to stretched exponentials

$$I_{PE}(\tau) \propto \exp\left[-\frac{\tau}{T_{\text{stretch}}}\right]^{\beta}. \tag{4.2}$$

For true stretched exponentials, which are often reported for relaxation phenomena in disordered systems [75,202,203], β is positive and less than 1. Here the stretch parameter was set as a free fitting parameter. For each data set of a full waiting time scan an optimal value for the stretch parameter was found and then set as a fixed parameter. All traces were fitted from the same starting point just beyond the width of the cross-correlation, ~ 30 ps, over a time span of ~ 4 times the decay constant of the specific trace. If non-exponentiality was not an issue in the experiment, all the data were force fitted to a single exponential decay. The physical cause and the ramifications of any non-exponentiality will be discussed in Chapter 5.

4.2.5 Line Broadening Due to Laser Heating

When all waiting time dependent dephasing times are collected in the above manner, the effective homogeneous line width can be plotted against the waiting time as is done in Figure 4.6. This graph presents the 3PE data for ZnP/EtOD at 1.8 K using a laser fluence of 400 nJ per pulse. These data essentially reproduce Meijers' experiments [44,90,185,204] at a slightly higher temperature. The plateau, as first observed by Meijers and Wiersma is more evident than before due to a higher signal-to-noise ratio in the experiments. These data suggest a gap in the glass dynamics at rates between 10^{-5} to 10^{-4} s^{-1}, and therefore,

measurements like those made by Meijers *et al.*, suggest that the hyperbolic distribution of relaxation rates of equation (2.21) exhibits a gap on these time scales.

Recently Zilker *et al.* [205] showed that sample heating, caused by radiationless decay of excited molecules into the lattice, can cause a waiting time dependent line broadening in 3PE experiments. Earlier, in the work of Meijers *et al.*, this option was not considered because it was argued that in 3PE experiments, only the molecules in the ground state are probed. The population in the excited singlet state decays on the time scale of the fluorescence lifetime into the lowest triplet state, thus leaving only the grating in the ground state to be probed. The fact that only unexcited molecules are involved in generation of the signal led to the conclusion that high laser fluences cannot create any *waiting time dependent* excess dephasing. This conclusion was further supported by the fact that in a 2PE study, where the excited state is probed as well, hardly any dependence on the laser fluence was found. Actually, the fact that only ground state chromophores are probed at waiting times longer than the fluorescence lifetime was considered a major advantage of the technique used.

However in experiments on PMMA at temperatures below 1 K, Zilker and Haarer meas-
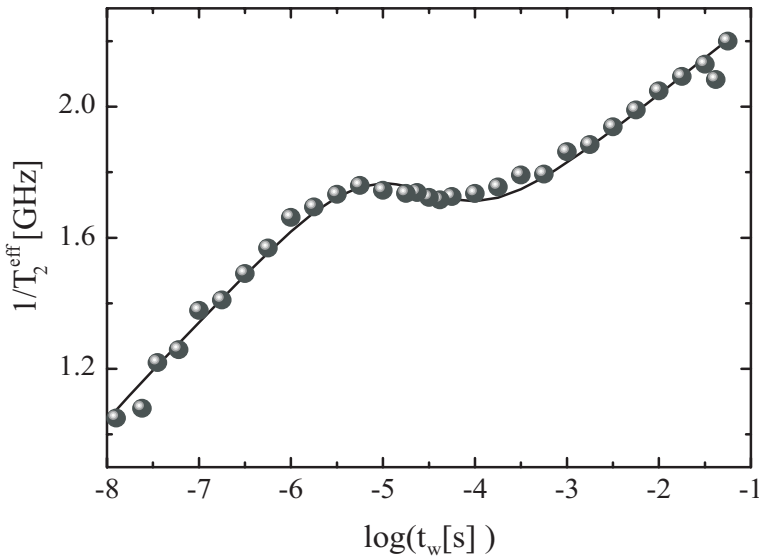

Figure 4.6. The effective homogeneous dephasing rate of ZnP in EtOD $1/T_{eff}$ as a function of the experimental waiting time at 1.8 K, reproduced from Meijers and Wiersma. The solid line is a fit through the data using equation (4.6) with $v \to 0$. The fit parameters are $\Delta T = 1.3 \ K$, $c = 4 \times 10^8$, $\Omega P_0 \rho_{TLS} = 53 \ MHz$.

ured a decrease in the effective homogeneous line width with increasing waiting time. This clearly indicated sample heating. It was subsequently shown [205,206] that dumping of the absorbed energy in combination with the small specific heat of glasses at low temperatures leads to a transient temperature rise in the focal volume. Zilker *et al.* [205] and Neu *et al.* [206] therefore suggested that the 'plateau' observed by Meijers *et al.* [44,90,185,204] was caused by heating, although Meijers and Wiersma used pulse energies of less than 100 nJ in their experiments.

4.2.5.1 Local Heat Dumping

The increase of the local temperature was estimated by calculating the energy released in the focal volume. Since in ZnP the intersystem crossing yield φ_{ISC} is about 95% and the energy difference of the $S_1 \rightarrow T_1$ transition is $\Delta E_{S_1 \rightarrow T_1} \approx 3700\ cm^{-1}$, which means that $\Delta E_{S_1 \rightarrow T_0} / \Delta E_{S_0 \rightarrow S_1} \approx 0.21$ when the excitation wavelength is 567 nm, [192,193,196], ca. 20% of the absorbed pulse energy E_{pulse} is transferred into heat during the decay of the singlet state. The rest of the absorbed pulse energy is transformed into heat during the decay of the long-lived triplet state.

The temperature rise was calculated using the following parameters as input. For the mass density ρ of EtOD glass $0.8 \times 10^3\ kg/m^3$ was taken. The focal volume was assumed to be a cylinder of size $V_{focal} = \pi a^2 L$, with spot radius $a \approx 50\ \mu m$ and depth of focus $L = 1\ mm$. For 100 nJ excitation pulses and an absorption A of 30% (O.D. 0.15) this would mean a typical heat release of $Q \approx 2\ mJ/g$ during the fluorescence lifetime of the ZnP chromophore resulting from the first two pulses, see equation (4.3). It was noted that Zilker *et al.* seem to have underestimated the heat dumped into the samples by an order of magnitude.

In a "worst-case scenario" when the heat release is much faster than the diffusion out of the focal volume this would cause a temperature increase given by the following relation:

$$\int_{T_{initial}}^{T_{final}} dT\, c(T) = Q = \frac{2\phi_{ISC} \Delta E_{S_1 \rightarrow T_1} A}{V_{focal}\, \rho\, \Delta E_{S_0 \rightarrow S_1}} E_{pulse}\ . \tag{4.3}$$

The specific heat of ethanol glass is known from $1.8\ K$ upwards [199] and is $c(T) = 4.4\, T\, \mu J/gK^2 + 18.2\, T^3\, \mu J/gK^4$. It can then be calculated that for a start temperature $T_{initial}$ of 1.8 K the estimated local temperature rise, $\Delta T_{est} = T_{final} - T_{initial}$, can amount to $\cong 1.7\ K$ for the experimental conditions mentioned above.

4.2.5.2 Heat Diffusion

The released heat will eventually spread through the sample. Zilker *et al.* solved the heat diffusion equation to yield a time dependent local temperature $T(\mathbf{r}.t)$ [207]:

$$\frac{\partial T(\mathbf{r},t)}{\partial t} - D\nabla^2 T(\mathbf{r},t) = 0 , \qquad (4.4)$$

where the diffusion constant is set by the heat conductivity κ, the specific heat c and the mass density ρ, as $D = \kappa/\rho c$.

Since the phonon relaxation times are much shorter than the diffusion times in the glass it was reasonable to assume that the phonons are in quasi-thermal equilibrium within the focal volume. The transient temperature could then be approximated by the spatial average over the focal volume. The dominant diffusion process is heat flow out of the focus in the radial direction over a time scale $\tau_a = a^2 \rho c/\kappa$. Heat flow along the longitudinal direction of the focal volume is much slower since $L \gg a$, and heat flow out of the sample into the Helium bath is even slower.

Furthermore it is reasonable to assume that the chromophores heat the focal volume to a temperature T_{final} after the fluorescence lifetime T_1, since $T_1 \ll \tau_a$. With the above simplifications, and when the specific heat and the thermal conductivity are treated as constants, the transient temperature could be calculated from the diffusion equation, assuming diffusion in an infinite cylindrical medium and with a temperature profile approximated by
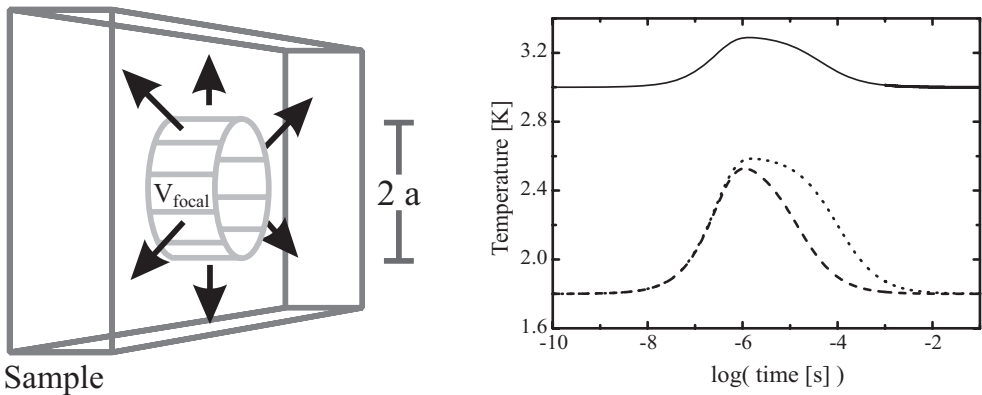

Figure 4.7. Left: A sketch of heat diffusion out of the focal volume. Right: An estimate of the transient temperature profile in the focal volume according to equation (4.5), with $T_{initial}$, T_{final} and τ_a respectively. 3 K, 3.3 K and 14 ms (solid line), 1.8 K, 2.6 K and 1 ms (dashed line), 1.8 K, 2.6 K and 100 ms (dotted line), with $T_1 = 2.7$ ns in each case.

the Gaussian laser intensity profile:

$$T(t) = T_{\text{initial}} + (T_{\text{final}} - T_{\text{initial}}) \left\{ \frac{1}{1 + t/\tau_a} - \exp\left[-\frac{t}{T_1}\right] \right\}. \tag{4.5}$$

This transient temperature profile could then be substituted into the derivation of equation (3.101). The transient temperature of the focal volume is plotted, for some reasonable parameter values in Figure 4.7.

However a full evaluation of the averaging over all stochastic history paths of the TLS's with a transient temperature profile is complicated and not necessary to get a good approximate idea of the effects of sample heating. Neu *et al.* [206] showed that following the formalism of Black and Halperin [112] the number of TLS's that flipped an odd number of times during the experiment can be counted using a simple master equation approach. The one-phonon flipping rate can be deduced if it is assumed that at $t_w = 0$ and temperature T_{start} the TLS's are in thermal equilibrium and that phonons are at quasi-equilibrium at all transient temperatures. From this the effective homogeneous line width then became, with $\mu = 0$ for the time being:

$$\frac{1}{\pi T_2^{\text{eff}}}(t_w) = \frac{\pi^2}{6} \Omega P_0 \rho_{TLS} \left(k_B T_{\text{initial}}\right)^{1+\mu-\nu/2} \left(K_{\mu,\nu} + f_{\mu,\nu}\left(t_w, R_{\max}\left[T(t_w)\right]\right)\right), \tag{4.6}$$

where the lifetime contribution is omitted and with

$$f_\nu\left(t_w, R_{\max}\left[T(t_w)\right]\right) = \frac{\displaystyle\int_0^\infty dz \left(1 - \left(t_w R_{\max}\left[T(t_w), z\right]\right)\right)^{\frac{\nu}{2}} \left(1 - \tanh(x)\tanh\left(\frac{zT_{\text{initial}}}{T(t_w)}\right)\right)}{\displaystyle\int dz\, z^\nu \operatorname{sech}(z)}, \tag{4.7}$$

and

$$R_{\max}\left[T(t_w), z\right] = c T_{\text{initial}}^3 z^3 \coth\left(\frac{zT_{\text{initial}}}{T(t_w)}\right). \tag{4.8}$$

In this model for heat diffusion, for values of ν between 0 and 0.3 and for the pulse energies used in our experiment, the echo decay depends proportionally on the incident pulse energy within the experimental resolution.

The experiment of Figure 4.6 could be analyzed along these lines. A pulse energy of ± 400 nJ leads, in the worst-case scenario described by equation (4.3), to an estimated temperature increase in the sample of $\Delta T_{\text{est}} = T_{\text{final}} - T_{\text{initial}} \approx 3.1$ K. This estimate could then be compared to the temperature rise as deduced from the dephasing data. The solid line in Figure 4.6 is a fit of the data using equation (4.6). The excellent fit obtained confirmed the suggestion of Zilker and Neu that sample heating is the cause of the observed plateau. In this fit, the temperature rise ΔT_{fit}, the time constant for the heat diffusion process τ_a, the TLS-

85

phonon coupling constant c, and $\Omega P_0 \rho_{TLS}$ were used as fitting parameters. The fit implied, with ν fixed in the limit of $\nu \to 0$, a temperature rise of $\Delta T_{\text{fit}} \approx 1.3$ K. This is a reasonable value compared to the worst-case temperature estimate ΔT_{est} and it is therefore an important result since it negates any timescale specific dynamics and consequent residual structural regularity in an ethanol glass.

The fixed value of ν used in this fit differs from the value found by Zilker *et al.*, who find the best fit for $\nu = 0.15$. Fitting our data with ν as an adjustable parameter yields only a marginally better fit for $\nu \approx 0.001$ and $\Delta T_{\text{fit}} \approx 0.8$ K. Since setting ν to a higher fixed value only decreases the value of the fit parameter ΔT_{fit}, the comparison of the estimated value ΔT_{est} and the fitted value ΔT_{fit} suggested that $\nu = 0$ for this system.

Actually, if Zilker et al. had not underestimated the amount of heat released in their experiments, their guesses for T_{final} would have been substantially higher, for example $\Delta T_{\text{est}} = T_{\text{final}} - T_{\text{initial}} \approx 0.9$ K instead of 0.2 K for $T_{\text{initial}} = 1.5$ K and $\Delta T_{\text{est}} = 1.5$ K instead of 0.5 K for $T_{\text{initial}} = 0.75$ K. This had implications when they compared these estimated values ΔT_{est} to the values of ΔT_{fit} deduced from fitting the dephasing rate data. Based on their estimates the data were fitted with $\nu \neq 0$ because this decreased the value ΔT_{fit} to the value of ΔT_{est}. Furthermore, it shows that it is of paramount importance to have artefact free and accurate data to be able to discuss the more subtle aspects of the physics behind the dephasing data. These aspects will be discussed in Chapter 5.

Finally, the diffusion time is found to be $\tau_a = 23$ μs in case $\nu \to 0$, and $\tau_a = 30$ μs for the case $\nu \approx 0.001$. Though, so far, the heat conductivity κ, that can be calculated from
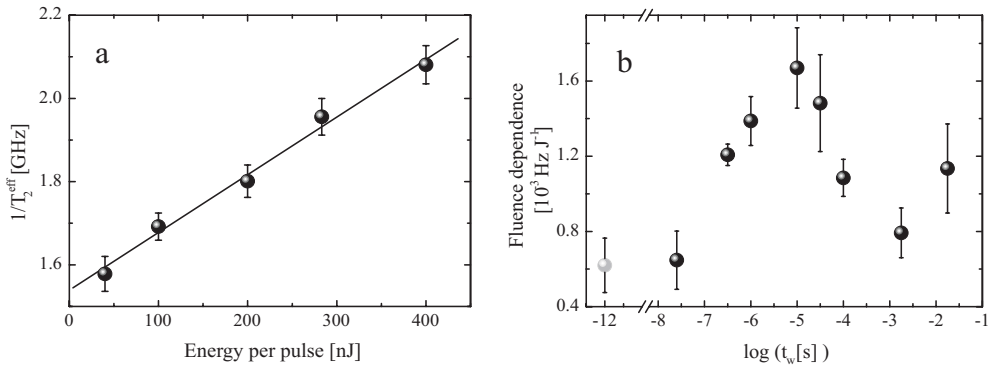
Figure 4.8. a) Dependence of the 3PE decay on the energy of the excitation pulses for an experimental waiting time of 1 μs. The solid line is linear extrapolation to zero laser fluence. b) The dependence of the echo decays on the energy of the excitation pulses for the 3PE (dark grey) and 2PE (light grey) experiment.
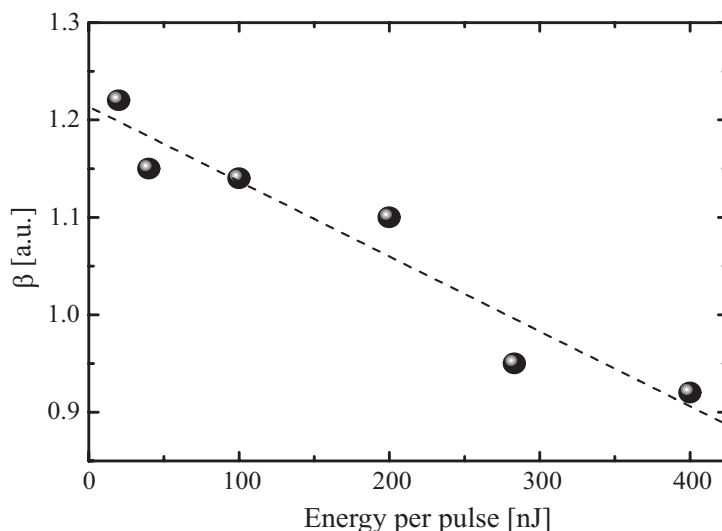
Figure 4.9. The non-exponentiality, quantified by stretch parameter β, as it varies with laser pulse intensity. The dashed is a linear fit to the data. Note that the echo decays do not extrapolate to perfect exponential decays for zero laser fluence.

τ_a, has never been reported for ethanol glass, comparison to other molecular glasses [208-210] indicates that the values found for τ_a are of the right order of magnitude.

4.2.5.3 Zero Fluence Extrapolation

The above model was further tested by performing the same picosecond 3PE experiments, but with echo decays extrapolated to zero fluence. Indeed, the echo decays show dependence on pulse intensity. On attenuation, measured effective line width decreases proportionally with the decreasing pulse energy, as is depicted in Figure 4.8 for 3PE decays with a waiting time of a microsecond. The effective pure dephasing rate was then extrapolated to zero pulse energy.

A complicating factor in this extrapolation is the fact that for both the 2PE and the 3PE at short waiting times ($t_w < 0.1\,\mu s$), the temporal shape of the echo decay changes with the laser fluence. As was mentioned above, this can impede comparison of the fitting results and therefore the decays were fitted to stretched exponentials. The stretch parameter β did not extrapolate to 1 for zero laser fluence; instead it varied from 1.2 at low fluence to 0.9 at high excitation pulse energies for 2PE decays of ZnP in EtOD. A rise of the experimental

temperature leads to a further decrease of the stretch parameter ($\beta \approx 0.75$ is found at 8 K). This last observation is in good agreement with the 2PE results of Thorn Leeson *et al.* [45,184] on protein samples. They found a similar decrease of the stretch parameter of the 2PE decay with increasing temperature.

The dots in Figure 4.8.b show the fluence dependence of the effective dephasing rate. This fluence dependence is determined by the slope of the line fitted through the data points of the plot of the dephasing rate *vs.* laser fluence (see e.g. Figure 4.8.a) The increase of the fluence dependence due to sample heating up to a waiting time of 10 µs can easily be distinguished. Then, up to a waiting time of a millisecond, the fluence dependence decreases because the waiting time is sufficiently long for the heat to diffuse out of the focal volume. It seems that at longer time scales (> 1 ms) the fluence dependence increases again, probably due to decay of the triplet state, which leads to additional heat dumping into the lattice. The interpretation of non-exponential decays and zero fluence dephasing data in the framework of glass dynamics theories is further explored in Chapter 5.

4.2.5.4 Conclusion

The conclusion to be derived from these results is that optical excitation-induced heating can and does influence the waiting time dependence of the 3PE decays in doped organic glasses. This is due to the low specific heat of glasses at low temperatures, causing a significant increase of the temperature in the immediate surroundings of excited chromophores that undergo radiationless transitions. This local temperature jump quickly decays by heat diffusion. As a consequence, neighbouring chromophores in the ground state that are probed in the experiment undergo a transient rise in temperature. This results in a waiting time dependent contribution to the dephasing rate and causes a plateau in spectral diffusion as observed by Meijers and Wiersma.

4.3 The Femtosecond Setup

In order to investigate glass dynamics and liquid dynamics at temperatures higher than 25 K, a significantly higher temporal resolution is needed than can be supplied by the picosecond setup. At present, laser sources for femtosecond pulses are routinely available [211-217]. Especially all solid state mode-locked Ti:Sapphire lasers [218-221] are excellent sources of such short pulses (10 – 15 fs) with unsurpassed pulse-to-pulse stability, although with only a limited range of wavelengths available. The laser used for the work in this the-

sis is a cavity-dumped variation on the standard Ti:Sapphire oscillator [222], to achieve higher pulse intensities and a variable repetition rate. It has proven to be a very useful tool for modern femtosecond time-resolved non-linear spectroscopy.

4.3.1 The Cavity-Dumped Ti:Sapphire Laser

The laser used in the femtosecond experiments in this thesis is developed [148] and subsequently improved upon [223] in house. A schematic representation of the laser is given in Figure 4.10.

A Spectra Physics Millennia Nd:YVO4 laser pumped a 4 mm Ti:Sapphire crystal with an output power of 4.2 W. The pump beam was tilted to the p-polarization. The arm of the oscillator containing the two intracavity fused silica prisms was folded, and the other arm included the output-coupler and a 3 mm Harris acousto-optic modulator, i.e. the cavity dumper. This Bragg-cell was operated in a double-pass geometry with its folding mirrors in a confocal position and driven by a 5 W electronic driver from CAMAC systems.

The 2% transmitted light through the output-coupler was detected by a high-speed photodiode and was used to trigger the Bragg-cell driver and to monitor the laser performance. The spectrum of this light, the pulse-to-pulse stability and its intensity were continuously
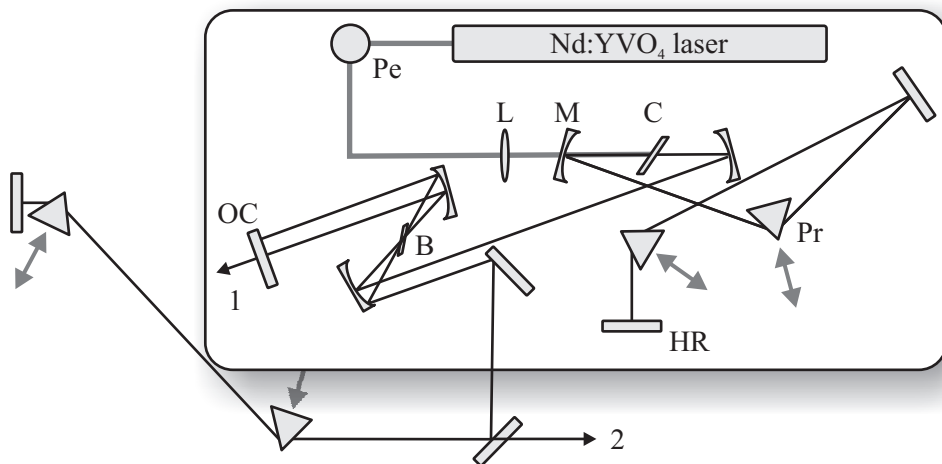
Figure 4.10. Overview of the cavity dumped laser. Pe = periscope, L = lens, M = focusing mirror, C = Ti:sapphire crystal, Pr = fused silica prism, HR = high reflector, B = Bragg-cell, OC = output coupler, 1 = 82 MHz output, 2 = cavity dumped output.

surveyed. In this way, by observing the pulse train traces, the dumping efficiency could be inspected. Dumping efficiencies up to 80%, with contrast ratios with preceding and succeeding pulses to over 10^3 were achieved.

In a typical experiment the laser produced 14 fs pulses of 40 nJ at a 10 kHz repetition rate, see Figure 4.11. The laser was operated in a soft-aperture mode-locking regime, by tuning the distance of the folding mirrors around the Ti:Sapphire crystal, to the inner edge of the second stability zone [224]. The oscillator was enclosed in a Perspex case to prevent instabilities caused by draft and acoustic noise.

4.3.2 Signal Detection, Data Collection and Samples

The pulses produced by the cavity-dumped laser were pre-compressed by double-passing the laser output through two fused-silica prisms to attain the shortest pulses in the sample. The excitation light was tilted to s-polarization and finally, to compensate for any divergence, reflected from a spherical mirror with a 2 m focal length.

Four pulses were used in the femtosecond echo experiments, three excitation pulses and a local oscillator pulse. The pulses were timed using 0.1 μm precision Newport delay
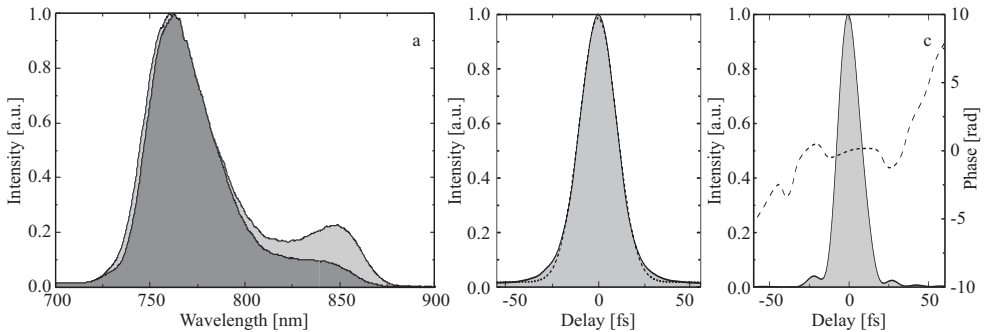
Figure 4.11. a) The spectrum of the 82 MHz laser output (light grey, comp. 1 in fig. 1.10) and of the cavity dumped pulse after precompression (dark grey, comp. 2 in fig. 1.10). b) The autocorrelation of the excitation pulses measured inside the cuvet mounted in the cryostat using a two-photon photodiode with the background subtracted. The dashed line is a Gaussian fit to the data, FWHM 24 fs. c) An estimate of the temporal profile of the phase (dashed line) and intensity of the pulses (grey shape) based on its spectrum and autocorrelation by means of a deconvolution algorithm, FWHM 14 fs.

stages and a fixed delay, properly aligned and subsequently focused in the sample using 125 mm focal length singlet lenses. The pulse train through the fixed delay was modulated using a mechanical chopper.

The sample was mounted in an Oxford Instruments Variox helium cryostat. The total amount of dispersive material in the optical path of each pulse was equalized using compensating plates. Higher order contributions to the dispersion by the optics and cryostat windows did lead to some slight broadening of the excitation pulses at the place of the sample, that could not be compensated for. The cross-correlation of all possible combina-
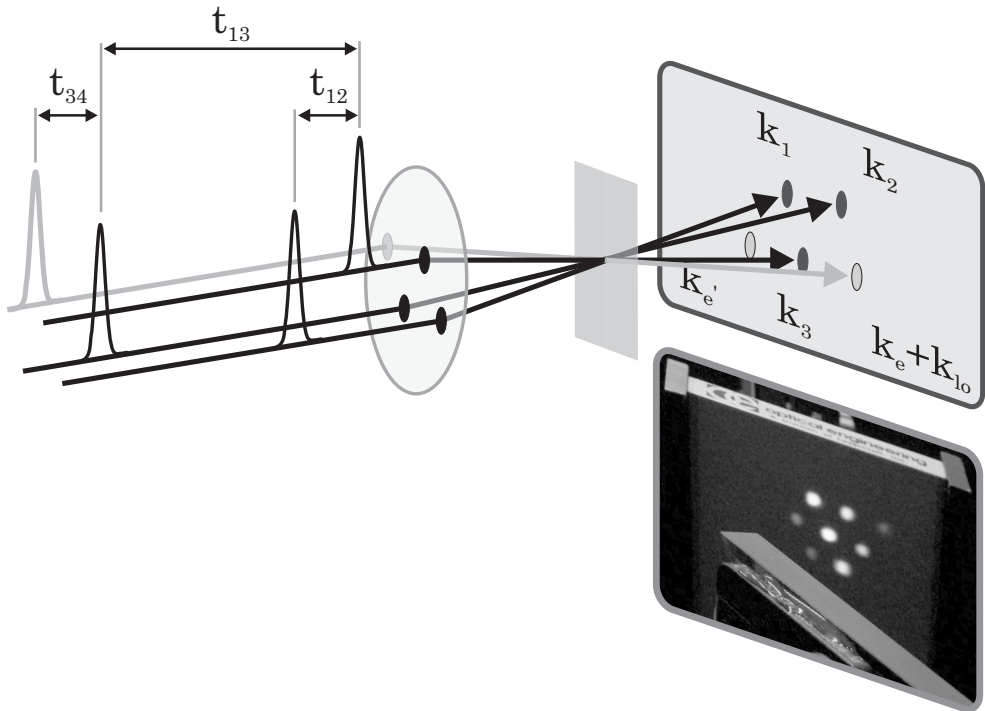
Figure 4.12. The configuration of the beams in the femtosecond experiments. On the right is a photo of the fluorescence caused by the frequency doubled excitation pulses reflecting of a surface, after passing though a BBO crystal at the same time ($t_{12} = t_{13} = 0$). The local oscillator pulse is not present in this picture. The two bright spots on the top line and the bright spot in the middle are caused by the excitation pulse trains themselves, the other spots are due to grating scattering, for example in the two echo directions. (The scattering in the directions on the right hand side is more visible here due to the orientation of the crystal.)

tions of pulses could be measured inside the cryostat by mounting a two-photon photodiode on the sample rod, or by using a 100 μm KDP crystal and subsequent detection of the sum frequency using a Scott UG 11 filter and a UV-sensitive Philips UV150 photomultiplier, see Figure 4.11.

The temperature in the cryostat could be varied to any temperature from 300 K to 1.7 K using either liquid nitrogen or liquid helium as a cooling agent. The temperature could be stabilized using an Oxford Instruments active temperature controller with a 0.1 K precision.

To make sure no sample heating effects would occur the excitation pulse intensity never exceeded 1 nJ, usually ~ 500 pJ, at the sample and the repetition rate was kept at 10 kHz. At these pulse energies an estimate as made in section 4.2.5.1 did not suggest that transient temperature effects played a role in these experiments. Notwithstanding the low pulse energies, at temperatures below 80 K and above the glass temperature (at 150 K, see below), where the heat capacity of the sample was small, some bleaching occurred over the time scale of several scans. In this case, the sample was moved within the cryostat to refresh the sample in the focal volume with each shot, to counteract this.

The beam configuration differed slightly from the box-geometry used in the picosecond experiments, to facilitate 3 pulse echo peak-shift (3PEPS) experiments (see Chapter 6). This configuration is shown in Figure 4.12, and is often used in echo peak-shift and related experiments.

As indicated in the drawing, in some experiments the field in one of the two signal directions was mixed with a fourth pulse, the local oscillator. Then, instead of a time integrated signal measured by a square-law detector in a homodyne echo experiment,
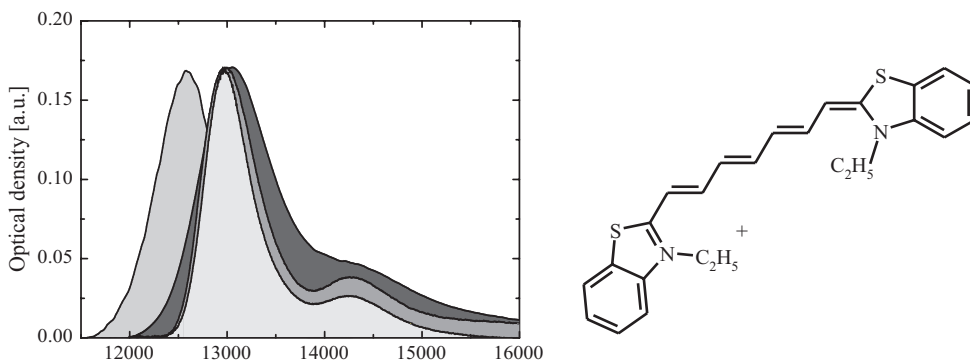
Figure 4.13. The absorption spectra of DTTCI (right) in a propanediol-ethanol mixture at 300 K (dark grey), 77 K (grey), 3 K (light grey) and its emission spectrum at 300 K. For comparison, the spectra are scaled with respect to the 3 K profile.

$$S_{\text{hom}}\left(t_0\right) \propto \int \left|P^{(3)}\left(t_0;\tau,t_w\right)\right|^2 dt , \qquad (4.9)$$

the heterodyne signal becomes proportional to the product of emitted echo field and the local oscillator field:

$$S_{\text{het}}\left(t_0\right) \propto \int_0^\infty \text{Re}\left[P^{(3)}\left(t_0;\tau,t_w\right) \times E_{\text{LO}}^*\left(t-t_0\right)\right]dt . \qquad (4.10)$$

Since $\left|E_{\text{LO}}\right| \gg \left|P^{(3)}\right|$, this greatly enhances the signal and facilitates detection even in situations with a lot of stray light present. The local oscillator field was a reflection taken from one of the compensating plates in the optical path of one of the excitation pulses, and was further attenuated by a factor of approximately two, using neutral density filters. Even though there is no *a priori* theoretical reason for the local oscillator field being weaker than the other excitation pulses, in practice best result were obtained with weaker pulses, depending on the optical quality of the sample.

Stray light was blocked using a mask and detecting at a 2 m distance via pick-up mirrors and occasionally via a spatial filter, further diminished its effect. The signal was detected by amplified slow photodiodes through two amplifiers locked into the chopping frequency.

Data collection and the control of the delay stages was computer controlled. Both homo-
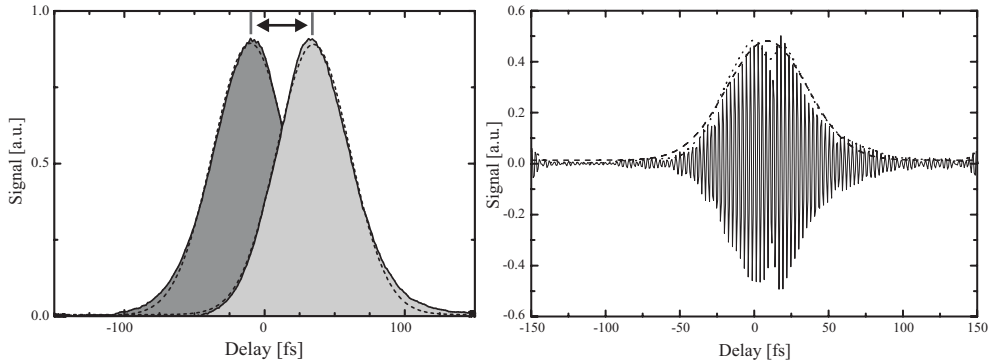
Figure 4.14. a) Typical echo peak-shift traces. The light grey trace is an echo signal as a function of the coherence time with the time between pulse 1 and 3 fixed, detected in the $\mathbf{k}_e$ direction. The dark grey trace is an echo with the time between pulse 2 and 3 fixed, detected in the $\mathbf{k}_{e'}$ direction. The dashed lines are Gaussian fits. b) Typical heterodyned echo data. The delay of the local oscillator is scanned and 0 fs coincides with the timing of the third pulse (pulse timing: $\tau = 10$ fs, $t_w = 210$ fs; sample: DTTCI solution in a propanediol – ethylene glycol mixture at 300 K). The dashed line is the Gaussian fit of the Fourier filtered data (dotted line).

dyne and heterodyne type experiments could be run in a completely automated manner without intervention of the experimentalist.

Solutions of 3,3'-diethylthiatricarbocyanine iodide (DTTCI, Lambda Physik) in a 1:1 volume mixture of ethanol and 1,2 propanediol with an optical density of ~ 0.15 at the absorption maximum at 77 K (see Figure 4.13) were used as sample material. The dye was chosen for its spectrum that matches the excitation spectrum, for its solubility, its photostability and for the experience that was already gathered using this dye in room temperature photon echo experiments. The solvent was chosen for the optical quality of the glasses it forms. The sample was mounted in a 1 mm quartz cuvet. After cooling down the sample was left to settle for at least an hour.

4.3.2.1 Data Collection

Typical traces, collected in the homodyne echo peak-shift experiment, when the coherence time was scanned, are depicted in Figure 4.14a. Specifically, the two traces represent the scan with the timing between the first and the second pulse fixed and the scan with the timing between the first and third pulse fixed. This yields an echo signal respectively in the $\mathbf{k}_{e'}$ and the $\mathbf{k}_e$ direction (see Figure 4.12).

The traces were fitted with a Gaussian profile to establish the position of the echo maximum. To allow at short waiting times for asymmetric profiles the traces were subsequently fitted with a third-order polynomial around the first guess of the maximum to pinpoint the maximum more precisely. The echo peak-shift is half of the distance between the maxima of the two traces and was plotted against the waiting time.

A standard heterodyned echo trace is shown in Figure 4.14b. To extract the actual echo profile the pump-probe background contribution was subtracted by fitting the data with a slowly varying polynomial and subsequent subtraction of this baseline. The carrier frequency component was removed from the signal using a Fourier filter. The resulting profile was fitted with a Gaussian in order to obtain the position of the maximum of the profile, its width, and height. In Figure 4.14 the raw data traces are shown together with the filtered trace as a function of the coherence time τ. All data in the above experiments were processed in an automated manner to treat each trace in an identical manner.

Chapter 5

Logarithmic Line Broadening and Optically Induced Dephasing

The time evolution of the homogeneous line width of Zinc-porphin (ZnP) in deuterated ethanol (EtOD) glass at 1 K is measured by means of stimulated photon echoes. The observed spectral dynamics are interpreted in terms of the standard two-level system (TLS) model and by using a commonly used modified version of it. The necessity of modified TLS parameter distributions is discussed. After correcting for time-dependent local heating, the time-dependent behaviour of the effective homogenous line width suggests the existence of excess optical dephasing on a short time scale. This effect is attributed to spectral diffusion induced by the change of electronic state of the chromophore. This phenomenon is not captured in the existing TLS models, which assume that the probe molecule is just a spectator of glass dynamics.

The intensity of the echo signal in this experiment is also evaluated. It shows an anomalous waiting time dependent decrease that can not be attributed to any known population relaxation. This evaluation is a follow-up on results from earlier studies on the population dimension of photon echoes. Also in those studies an inexplicable intensity loss was found consistently in a range of amorphous materials. Some possible causes of this intensity loss are excluded and an explanation is given within the framework of a general description of non-linear optics. The intensity loss is attributed to frequency drifts of the chromophores out of the frequency bandwidth of the excitation pulses.

5.1 Introduction

In Chapter 2 the description for cold molecular glasses, the TLS model, was introduced. It was demonstrated that optical experiments put the particular choices of the TLS parameter distributions to the test, by mapping out the time dependence of the effective homogenous line width. So-called optical line narrowing experiments, that do just this by removing in-homogeneous broadening, therefore provide a pivotal check for the adequacy of the TLS model in describing glass dynamics. However, the interpretation of chromophore dynamics in amorphous solids is frustrated by qualitative and quantitative discrepancies between the results rendered by different types of line narrowing techniques.

Thus, although separate results are in qualitative agreement with the TLS-model, the quantitative discrepancies between results rendered by different techniques indicated the need of further refinement of the TLS-model. Notwithstanding these problems, the concept of low-energy excitations being accountable for the properties of amorphous solids is well accepted. At the same time it is clear that experimental results have to be interpreted with great caution. Indeed, the optical dynamical properties can be influenced by various incon-spicuous experimental parameters. Examples are the cooling history of the sample, the par-ticular subset of chromophores selected in an experiment [225,226], and also, as was re-cently pointed out and discussed in Chapter 4, laser fluence [205,206].

In this chapter the boundaries of relevance and applicability of the TLS model are ex-plored and some shortcomings in this description of solvent bath dynamics are pointed out. It is shown that optically induced spectral diffusion, an effect unrelated to laser fluence, is of significant importance to the interpretation of all optical line-narrowing techniques. This finding points at the inadequacy of the currently used weak-coupling chromophore-TLS model for a complete description of glass dynamics.

A trait of the photon echo technique that is not often studied, is the possibility to assess the population dynamics of the chromophores in addition to the dephasing characteristics. When the intensity of the echo signal is measured as a function of the waiting time t_w for a fixed coherence time τ, the resulting echo intensity plot is proportional to the decay of the amplitude of the induced frequency grating instead of its spacing and acutance [52]. This amplitude decay is the result of depopulation of the excited state levels of the involved chromophores, and is therefore closely related to the time-resolved fluorescence and phos-phorescence decay.

In nuclear magnetic resonance (NMR) and spin-echo experiments this echo aspect is routinely exploited to gain information on various mechanisms that lead to the loss of popu-lation of coherently excited systems. This is not the case in studies that focus on optical spectral diffusion, especially since in the often used spectral hole-burning technique the

population dynamics are difficult to measure. In photon echo experiments however, the intensity of the three pulse photon echo (3PE) can serve as a test of the TLS model, complementary to the dephasing data. In this chapter the population dimension of the photon echo is explored and the subsequent results are presented.

5.2 Modifications of the TLS Model

As explained in Chapter 3, originally it was thought that the distribution of TLS parameters of the standard model would yield exponential echo decays, equivalent to Lorentzian hole shapes in a hole burning experiment. It was also predicted that the effective pure dephasing rate should be proportional to the temperature and the logarithm of the waiting time [85,86,88,89,96,112], as pointed out at the end of section 3.9.1:

$$\frac{1}{T_2^{eff}}(t_w) \propto T \ln[t_w].$$
(5.1)

However, not all experiments comply with this prediction. Experimentally a superlinear temperature dependence $\propto T^{1.3\pm0.1}$ was observed that seemed to be universal for organic glasses [43,91,227].

Furthermore, some experiments showed non-logarithmic line broadening due to spectral diffusion. For example, in a 3PE experiment on zinc-porphin in deuterated ethanol glass, Meijers *et al.*[44,90,185,204] observed broadening of the effective homogeneous line width for waiting times shorter than a microsecond and longer than a millisecond, but not in between.

In this case the lack of broadening was explained in an *ad hoc* manner by postulating a gap in the distribution of flipping rates. This, however, is in direct contradiction with the broad distribution of TLS relaxation rates that follows from the distributions of tunnel parameters in equations (2.13) and (2.14). Recently the so called "plateau" was attributed to transient heating effects, caused by energy released into the sample as a result of radiationless decay [205,206,228]. This mechanism, an experimental artefact, was already discussed in Chapter 4.

More examples of anomalous broadening have been reported. Non-logarithmic line broadening was found in experiments using a combination of so-called population hole burning and photophysical persistent hole burning. On time scales of milliseconds to seconds, a sharp increase in the line broadening was found for porphyrin molecules dissolved in polymethyl methacrylate (PMMA) [229,230]. This effect is found in addition to the normal logarithmic broadening encountered on all other time scales. Although the exact nature

of this additional line width increase is still obscure, the timing of the excess broadening suggests that it is connected to the excited state dynamics of the porphyrin chromophore.

Furthermore, for hole burning experiments at millikelvin temperatures on time scales longer than 10^4 s (3 h), a faster than logarithmic waiting time dependence was found in the same type of PMMA samples. These deviations from $\log(t_w)$ behaviour can be accounted for within the TLS model if non-equilibrium effects are considered [231]. If the time between cooling down the sample to the experimental temperature and the start of the experiment is of the same order or shorter than the waiting time, the TLS states that are probed are still far from equilibrium. This will lead to extra spectral diffusion at these temperatures, resulting in strongly non-logarithmic line broadening as the waiting time is changed.

Nevertheless, even if these non-equilibrium effects are carefully excluded from the experiment, a faster than logarithmic line broadening is still observed in PMMA on time scales exceeding 10^4 s [232-235]. There is an ongoing discussion in the literature whether this is best explained by assuming sets of interacting TLS's or by the assumption that the energy landscape of the PMMA glass shows a hierarchical organisation not unlike the potential energy surface of proteins [236].

The idea of strongly coupled TLS's implies an extra term in the distribution function $P(\Delta) = P_0\left(1/\Delta + \varepsilon/\Delta^2\right)$. This *"ad hoc Ansatz"* predicts a line width comprised of a $\log(t_w)$ and a $\sqrt{t_w}$ term. The assumption of a hierarchical energy landscape for polymers would lead to the conclusion that their disordered state would be fundamentally different from molecular glasses. In fact this would imply the existence of evenly distributed TLS's with low barriers in basins separated by high barriers. Tunnelling through these high barriers would imply conformational dynamics of polymer side chains.

Besides the super-linear temperature dependence and the non-logarithmic broadening, a final example of results not in compliance with the standard TLS-model are the reported non-exponential photon echo decays. However, the deviations of exponential behaviour are small and on the order of the experimental resolution [90,237]. Most notably, in two pulse photon echo (2PE) experiments on proteins, Thorn Leeson *et al*. found decays that could be best fitted with a stretched exponential [45]. The stretch parameter varied with temperature. Even though proteins exhibit different behaviour with respect to spectral diffusion than glasses, it is believed that the 2PE decay is governed by TLS dynamics.

Several modifications of the standard tunnelling model were proposed to be able to describe spectral diffusion in glasses in a universal way including all these deviations and after carefully correcting for possible heating artefacts, side chain dynamics etc. This usually involves modifying the forms of the TLS parameter distributions.

The most common adjustment to the standard TLS model has already been introduced. The equations (2.15) and (2.16) are adapted by means of the phenomenological parameters μ and ν. Silbey *et al.* first introduced both these parameters into TLS theory in a consistent manner and the resulting distributions are widely accepted throughout literature [87,91,99,100]. Because of this general acceptance and since the introduction of the new distributions offers a generalized version of the standard TLS model, these forms were used here from the start.

The dimensionless parameters μ and ν can be used as fitting parameters for the experimental observations. The phenomenological parameter μ was used to account especially for the superlinear temperature dependence found in glasses. In order to explain the above mentioned universal temperature dependence of $\propto T^{\pm 1.3}$ it was calculated that μ is typically 0.3 [87,99,100]. The effective line width behaves in this perspective as:

$$\frac{1}{\mathrm{T}_2^{eff}}\left(t_w\right) \propto T^{1+\mu-\nu/2}\,\frac{\nu}{2}\left(1-\left(R_{eff}\,t_w\right)^{-\nu/2}\right).$$

(5.2)

Here, R_{eff} is some effective average flipping rate.

The parameter ν was used to account for any non-logarithmic waiting time dependence of the optical line width and non-exponential echo decays. Moreover, numerical simulations, which were performed on a NiP model glass [107-110], showed a distribution of tunnelling parameters that could be best described by equation (2.16). It was estimated that for most glasses ν is 0.0 – 0.2.

5.2.1 Inconsistencies of the Model

On top of any modifications of the parameter distributions, the standard treatment of the optical response function in terms of the TLS model, as described in section 3.9, has also been closely examined for any inconsistencies. A recent evaluation of the averaging necessary to obtain the standard results by Geva and Skinner, showed that equations (3.99) and (3.101) are not entirely accurate [104]. After close inspection of all the approximations involved in the averaging over the TLS distribution functions, it was demonstrated that the upper limits of the integrals in equations (3.96) and (3.97) cannot be taken to infinity unconditionally. These equations express the TLS-model line broadening functions $\mathscr{F}\left(R,\tau\right)$ and $\mathscr{G}\left(R,\tau,t_w\right)$ averaged over the distributions over the TLS-parameters R and E. Taking the lower limits to zero and the upper to infinity led immediately to idealized behavior of the optical response described in equation (5.1).

For the 2PE, which evolves as $P\left(\tau\right) \propto A\left(t_w\right)\exp\left[-\mathscr{F}\left(\tau\right)\right]$, the problem lies with the upper limit of the x-integral of the function $\mathscr{F}\left(\tau\right)$: $R'_{max}\,\tau = c\left(k_B T\right)^3 z^3 \coth\left[z/2\right]\tau$. Close

inspection shows that only for $c(k_B T)^3 T_2 > 100$ this limit can be set to infinity. However, for the combinations of chromophores and organic or polymeric glasses used in this work, and for the combinations used in all other optical studies on dephasing due to TLS dynamics, this value varies between $2 < c(k_B T)^3 T_2 < 12$ [104]. Therefore, in a more exact approach, when analyzing 2PE results the complete expression including this limit has to be utilized:

$$\mathscr{F}(R,\tau) = \frac{\pi^3}{3} \Omega P_0 \rho_{TLS} c^{-v/2} (k_B T)^{(1+\mu-v/2)} \tau^{(1-v/2)} \int_0^\infty dz\ z^{(\mu-v/2)} \frac{\mathrm{sech}^2[z/2]}{\coth^{v/2}[z/2]}$$
$$\times \int_0^{R'_{max}\tau} \frac{dx}{x^{2-v/2}} \left(1 - \frac{x}{R'_{max}\tau}\right)^{\mu/2} F(\tanh[z/2],x). \tag{5.3}$$

The 3PE can be analyzed along the same lines. The x-integral of the line broadening function $\mathscr{G}(\tau,t_w)$ is simplified in the approach used in section 3.9 by setting $G(\tan[z/2],x) \simeq 1$. This is valid for small x only and hence implies that $c(k_B T)^3 T_2 < 0.1$ for $t_w \gg \tau$. It leads to equations (3.101) – (3.103) and is the approach used in most literature, even though it implies an assumption that is not valid and contradictory to the assumption implied in the analysis of the 2PE. Geva and Skinner offer a different approach to simplify the function $\mathscr{G}(\tau,t_w)$ that at least is consistent with the simplifications of $\mathscr{F}(\tau)$. However, they also indicate that it is better to use the same more exact approach by evaluating the whole integral when analyzing 3PE results:

$$\mathscr{G}(R,\tau,t_w) = \frac{\pi^3}{3} \Omega P_0 \rho_{TLS} c^{-v/2} (k_B T)^{(1+\mu-v/2)} \tau^{(1-v/2)} \int_0^\infty dz\ z^{(\mu-v/2)} \frac{\mathrm{sech}^2[z/2]}{\coth^{v/2}[z/2]}$$
$$\times \int_0^{R'_{max}\tau} \frac{dx}{x^{2-v/2}} \left(1 - \frac{x}{R'_{max}\tau}\right)^{\mu/2} G(\tanh[z/2],x) \left(1 - \exp\left[-\frac{t_w x}{\tau}\right]\right). \tag{5.4}$$

In this more exact method the temperature dependence of the effective homogeneous line width on the time scales of the experiments presented here is not proportional to $T^{(1+\mu-v/2)}$. Instead it is expected to be super-linear with an exponent significantly larger than $(1+\mu-v/2)$. In fact, the experimentally observed temperature dependence $T^{1.3\pm0.1}$ can theoretically be explained within the standard TLS model even when $\mu = v = 0$. Since the super-linear temperature dependence was the most important reason to introduce the μ-parameter in the first place, this raises the question whether the modifications of the distribution function are really necessary at all.

In the standard approach the parameter distributions of equations (2.15) and (2.16) only imply a stretched exponential echo decay in the case $v \neq 0$:

$$I_{2PE}(\tau) \propto \exp\left[\frac{-\tau}{T_2^v}\right]^{1-v/2}. \tag{5.5}$$

Note that since ν is small and positive and does not depend on temperature, modification of the parameter distribution cannot explain the observed behavior of the temporal shape of the 2PE decay as described in section 4.2.5.3.

Geva and Skinner also predicted slightly non-exponential 2PE decays starting out from these parameter distributions even in the case $\mu = \nu = 0$, without quantifying their results however [104]. For 3PE results they concluded that the deviation from an exponential decay is less pronounced and only observable for short waiting times ($t_w < 0.1\ \mu s$). They predicted that the shape of the echo decay is almost pure exponential for longer waiting times and also that higher temperatures ($T > 4\ K$) diminish the nonexponentiality. The mathematically more exact results do, with the two parameters set to zero, predict a linear dependence on $\log(t_w)$.

Since it was shown that the deviation from exponential behavior of the long waiting time photon echo decay is small and insignificant, for the analysis of experimental data presented in this chapter we will assume that this deviation is small enough to allow fitting with an exponential decay. This permits the definition of an effective pure dephasing rate $1/T_2^{eff}$ in all experiments. This can then allow for testing – by performing photon echo experiments on a doped ethanol glass – the necessity of introducing the parameter $\nu > 0$ for waiting times from picoseconds up to seconds.

With these two parameters set to zero, only two fitting parameters remain: the group of constants containing the TLS-density and TLS-chromophore coupling $\Omega P_0 \rho_{TLS}$, and the TLS-phonon coupling c. It is interesting to see how well the combination of temperature dependent and waiting time dependent photon echo results can be described by these two fitting parameters and how the values of the parameters compare to values of the same parameters found through thermodynamic and acoustic experiments.

5.3 The 3PE Results in the Coherence Dimension

The three pulse stimulated photon echo data, extrapolated to zero laser pulse intensity, for ZnP in EtOD are presented as circles in Figure 5.1. It is obvious that the plateau in the micro- to millisecond region reported earlier disappears at very low pulse intensities. Instead the photon echo decay time varies linearly with $\log(t_w)$, in line with the theoretical predictions. Additionally, the recovered waiting time dependence of the effective dephasing rate seems to point to the fact that the distribution of TLS parameters in EtOD is best described with $\nu \to 0$.

The solid line in Figure 5.1 is a linear fit through the 3PE dephasing data (solid circles). In the traditional TLS model, without the modified parameter distributions and with the

inconsistent averaging procedures, the slope of this line reflects the distribution of relaxation rates $P(R)$ of equation (2.21) for long waiting times ($t_w \gg \tau$) according to:

$$\frac{\partial\left(1/T_2^{eff}\right)}{\partial \log\left(t_w\right)} = R \cdot P(R) \equiv \omega. \tag{5.6}$$

This then allows for a consistency check using the 2PE, because that experiment also reflects the distribution of relaxation rates $P(R)$ within this framework. Since a linear fit through the 3PE data suggests that $\nu = 0$ and if we set $\mu = 0$ as before, $P(R)$ is hyperbolic (see equations (2.15) and (2.16)). In this approach the slope ω of the solid line in Figure 5.1 is only set by the first of the two fitting parameters:

$$\omega = \ln\left(10\right)\frac{\pi^3}{3}\Omega P_0 \rho_{TLS} kT. \tag{5.7}$$

The pure dephasing rate is then calculated as:

$$\frac{1}{T_2^*} = \Theta\frac{\pi^3}{3}\Omega P_0 \rho kT = \frac{\Theta}{\ln(10)}\omega, \tag{5.8}$$

with the well know numerical constant $\Theta = K_{\mu=0}/2 = 3.66$ (see equation (3.100)) [91]. From equation (5.8) we can calculate the predicted homogeneous line width $1/\pi T_2^{2PE}$ of ZnP in EtOD and this method was used in nearly all previous studies [44,45,184,185,228].

Since in section 5.2.1 it was shown that the above method is not exact for reasonable values of c and $\Omega P_0 \rho_{TLS}$, a more precise method for interpretation of the results is desirable. Nonetheless, the most straightforward indicator of the first fitting parameter $P_0^{ex} = \Omega P_0 \rho_{TLS}$ is still the waiting time dependence of the 3PE decays for $t_w \gg \tau$. The slope of the log-linear plot of the pure effective homogeneous line width *vs.* the waiting time is, assuming exponential decays, exclusively set by this parameter. Adjusting the TLS-phonon coupling parameter c does not affect the slope of this graph in any meaningful way.

5.3.1 The TLS Density in EtOD

Here we derive the P_0^{ex}-parameter by globally fitting the complete exact expression for the echo intensity on all zero-fluence data points that were uncovered:

$$I\left(t_w,\tau\right) = C\,A\left(t_w,\tau\right)^2 \exp\left[-2\mathscr{F}\left(\tau\right)\right]\exp\left[-2\mathscr{G}\left(t_w,\tau\right)\right] + baseline. \tag{5.9}$$

The constant C is an amplitude factor, the second factor is the term containing any population dynamics, see equation (3.86), and the baseline is added here to adjust for any offset of the slope of the 3PE line broadening data. The two line broadening functions were evaluated as the complete expressions in equations (5.3) and (5.4).

Equation (5.9) was used to calculate simulated echo data decays which were consequently fitted with single exponential decay functions to yield a synthetic line-broadening plot. The TLS-density parameter was then adjusted until the slope of the synthetic line-broadening function matched the line-broadening data extrapolated from experimental intensity dependent data. The influence of the TLS-phonon coupling constant on the slope of the line-broadening plot is negligible since $\nu = 0$, and was set to $ck_B^3 = 1.0 \times 10^9$ K^{-3}s^{-1}, a value that is typically reported in these type of experiments [104,238]. This leaves only the density parameter as a variable. Best fits were obtained for $P_0^{ex}k_B = (4.13 \pm 0.24) \times 10^6$ K^{-1}s^{-1} at $T = 1.7$ K.
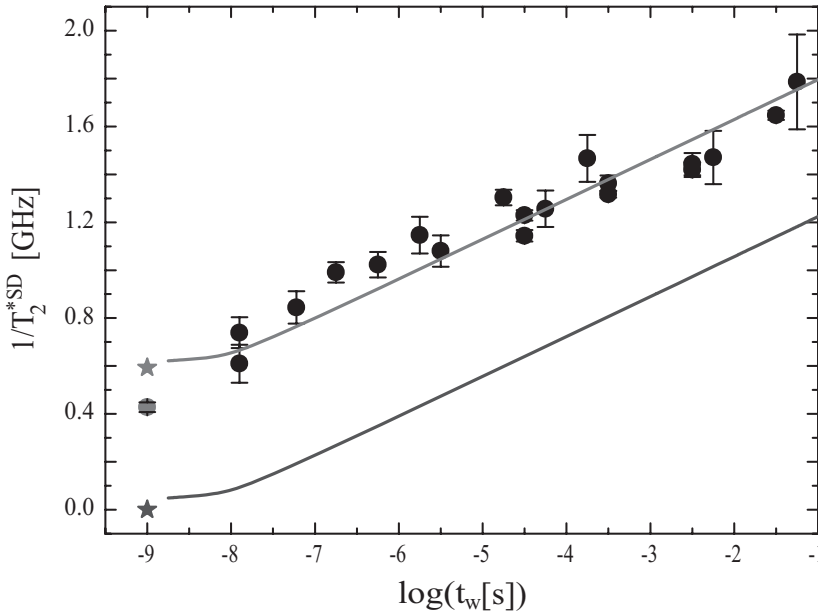
Figure 5.1 The effective pure homogeneous dephasing rate $1/T_2^{*eff}$ extrapolated to zero laser pulse intensity, as a function of waiting time t_w (●), and the pure homogeneous dephasing rate $1/T_2^*$ extrapolated from 2PE decays in a similar fashion (●). The position of the 2PE data on the x-axis is set by 2τ rather than by t_w. The dark gray line and star (★) depict the calculated echo decays using equation (5.10), with no optically induced dephasing term included, and with parameters $P_0^{ex}k_B = 4.13 \times 10^6$ K^{-1}s^{-1} and $ck^3 = 2 \times 10^8$ K^{-3}s^{-1}. The light gray line and star (★) show the same calculations using equation (5.12) with the optically induced dephasing set to $T_2^{extra} = 0.85$ ns.

This is reasonably on par with results obtained in other amorphous materials as PMMA at this temperature [239]. Obviously it is not possible to distinguish between a situation were a relatively small number of tunneling centers interact strongly with the chromophore and a situation were a large number of TLS's each only cause a small frequency shift. In other words, it is not possible to differentiate between a situation with a combination of a low TLS density ρ_{TLS} and a large TLS-chromophore coupling constant Ω, and a situation with a high TLS density and a small coupling constant.

5.3.2 TLS-Phonon Coupling in EtOD

The precise value of the TLS-phonon coupling constant c does not have a signature in the echo data that identifies its value just as clear as the slope of the 3PE data determines the TLS-density parameter. Its effect is most visible through non-exponential echo decays at short waiting times and through the temperature dependence of the 2PE decay when the distribution functions of the TLS parameters are not modified.

Figure 5.2 shows the non-exponentiality of the echo decays extrapolated to zero laser pulse intensities. It depicts the dependence of the stretch parameter β with waiting time, when the echo decays are fitted with stretched exponential decays (cp. with Figure 4.9 which shows the dependence of this parameter on laser fluence for the 2PE). It reveals a rather high value of $\beta = 1.23 \pm 0.02$ for the stretch parameter of the 2PE and true stretched exponentials with $\beta = 0.9 \pm 0.05$ for long waiting time data.

The largest deviations from exponential behavior are expected, as explained in section 5.2.1, when $0.1 < c(kT)^3 T_2 < 100$. Maximum deviation from exponential behavior is found in this case for $ck^3 = 2 \times 10^8$ K^{-3}s^{-1}. This corresponds to $c(kT)^3 T_2 \approx 2.7$ which is similar to values found in other glasses [104,238].

The TLS-phonon coupling constant can also be deduced from acoustic experiments at temperatures below 5 K. Some limited sound attenuation data from Brillouin scattering experiments on various forms of ethanol glass are published [240]. The above estimated value of ck^3 does comply within the experimental resolution of the reported value for the internal friction for reasonable values of the deformation potential parameter (see equation (2.20)). This parameter is not known for ethanol glass, but is reported for similar molecular glasses [238]. The Debye sound velocity and mass density of ethanol glass are known [199].

The solid line in Figure 5.2 shows the deviation of exponential behaviour for the measured value of $\Omega P_0 \rho_{TLS}$ and the estimated value of ck^3 applied to

$$I_{PE}(\tau, t_w) \propto A(\tau, t_w)^2 \exp\left[-2\mathscr{F}(\tau)\right]\exp\left[-2\mathscr{G}(\tau, t_w)\right]. \qquad (5.10)$$

Although the calculated data are in qualitative agreement with the extrapolated stretch parameters and seem to follow the experimental trend, the observed non-exponential echo decays cannot be completely reproduced quantitatively.

The same is true for the temperature dependent data. Figure 5.3 shows the dependence of the 2PE-dephasing rate on temperature in a log-log plot. The echo traces are taken at low laser pulse intensities, ± 40 nJ per pulse, but are not extrapolated to zero laser fluence. The echo decays are expected to depend on temperature in the following manner:

$$\frac{1}{T_2^*} = aT^\alpha + b\frac{\exp\left[-\Delta E/k_B T\right]}{1-\exp\left[-\Delta E/k_B T\right]}.$$

(5.11)

The first term on the right-hand side reflects the ideal linear dependence on temperature
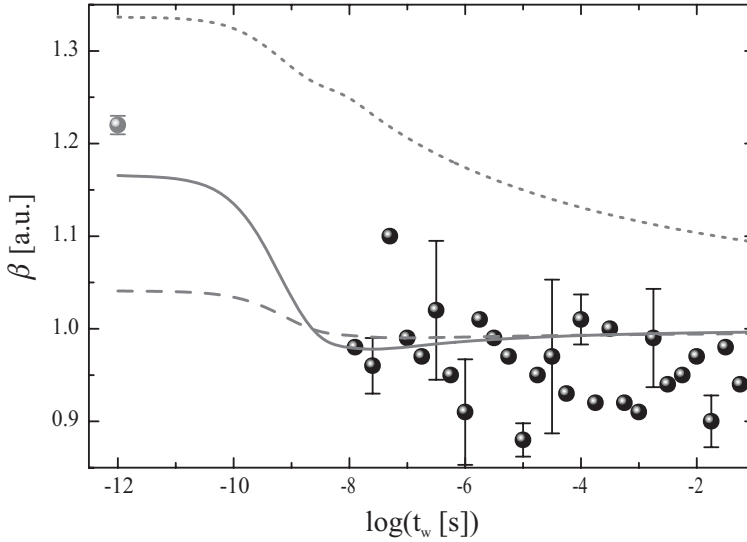
Figure 5.2. The change of the shape of the echo decay as a function of the waiting time. The experimental echo decays are fitted with a stretched exponential function yielding stretch parameters β for the 3PE decays ($\bullet$) and the 2PE ($\bullet$). The echo decays are extrapolated to zero laser fluence. The solid line is the dependence of the stretch parameter of fits to calculated echo decays on the waiting time using equation (5.10) with $P_0^{ex}k_B = 4.13\times 10^6$ $K^{-1}s^{-1}$ and $ck^3 = 2\times 10^8$ $K^{-3}s^{-1}$ and no additional short time dephasing. The dashed line is the result when equation (5.12) is used for the calculation of the echo decays with the same parameters and $T_2^{extra} = 0.85$ ns. The dotted line depicts the variation of β with waiting time when $P_{2PE}^{ex} = 2.42\times 10^7$ $K^{-1}s^{-1}$ and $P_0^{ex}k_B = 4.13\times 10^6$ $K^{-1}s^{-1}$ (see text).

predicted by the traditional implementation of the TLS theory as indicated in equation (5.1), adjusted with phenomenological parameter α to account for any super linear behavior which universally found in glasses [87].

In a typical organic glass the TLS induced temperature dependence of the dephasing follows a power law with $\alpha \approx 1.3$. At higher temperatures an exponentially activated process becomes important, modeled by the second term in equation (5.11). It is usually attributed to librational motions of the chromophore in the amorphous solvent and depends strongly on the type of solvent used [241]. For deuterated ethanol a value of $\Delta E = 21 \text{ cm}^{-1}$ was found, using various probes [204,242]. A value for the exponent $\alpha = 1.4 \pm 0.1$ is found, when the temperature dependent data is fitted with equation (5.11) using this activation energy. The fit is shown in Figure 5.2 as the solid line. Above $4-5$ K the contribution of the
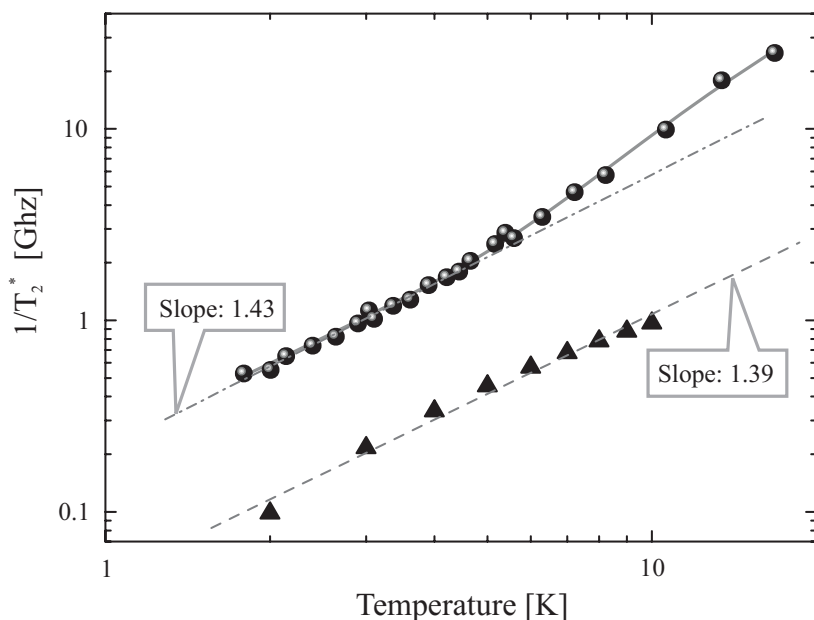
Figure 5.3. Log-log plot of the temperature dependence of the 2PE decay. The experimental data points (●) are fitted with equation (5.11) (solid grey line, see text for parameters) and with a straight line over the interval of 1 K to 5 K (dash-dotted line). The triangular data points (▲) show calculated 2PE traces, using equation (5.10) with $P_0^{ex} = 4.13 \times 10^6 \text{ K}^{-1} s^{-1}$ and $ck^3 = 2 \times 10^8 \text{ K}^{-3} s^{-1}$ and are linearly fitted (dashed line). This calculation does not include a term for excess optical dephasing a times shorter than a picosecond, hence the offset between the calculated and the experimental data points.

activated process starts to dominate.

The triangular data points in Figure 5.3 show the temperature dependent dephasing times by fitting single exponential decays to simulated echo traces using equation (5.10) with the parameters found above. Ignoring the large offset of the data, which is not influenced by the TLS-phonon coupling constant, for the moment it is clear that both sets show the same temperature response, up until where the activated contribution starts to dominate at 5 K. This is illustrated by the two straight lines fitted to both the experimental and simulated data sets which have similar slopes. The offset is caused by excess dephasing at timescales faster than a picosecond and is discussed in the next section.

The simulated data are force-fitted with a straight line, representing the superlinear temperature dependence. A closer look at these data points shows that the simulated points are not on a straight line. This indicates that a superlinear temperature dependence is not the correct description of the variation of the line width with temperature, although throughout literature this type of temperature dependence is always assumed, since it follows from the standard model as introduced in Chapter 3.

So, although the T_2^* temperature dependence and the non-exponential echo traces can be brought into qualitative agreement with the TLS-theory for reasonable values of the parameters, no unambiguous conclusion can be made about the shape of the distribution functions. More specifically, the experimental sensitivity to the TLS-phonon coupling is not high enough to accurately determine its value and allow for a precise prediction of the two trends. By using the μ and ν parameters of equations (2.15) and (2.16) the results can probably be brought into similar agreement for different values of ck^3. In the next section it is even demonstrated that also the other parameter distributions and assumptions, implicit in the expressions that lead to equation (5.10) can be altered to tweak the outcome of the predictions so that they match the experimental echo traces better.

5.4 Discussion of the 2PE and 3PE Results

Combining the values found for the parameters P_0^{ex} and ck^3 when predicting the full waiting time behaviour of the echo decay, reveals the biggest problem in uniting the echo decays with the TLS theory. The simulated data in Figure 5.1 show a large offset with the experimental data points. No reasonable value for these two fitting parameters or any subsequent modification of TLS parameter distributions can resolve this problem. It is unequivocally clear that the cause of this effect is beyond the framework of standard TLS theory. The conjecture to explain this effect proposed in section 5.4.1, is that it is due to opti-

cally induced spectral diffusion, meaning that optical excitation of the singlet state leads to fast tunneling of strongly coupled TLS systems.

5.4.1 Optically Induced Dephasing

Clearly there is a large discrepancy between the experimental and calculated value of the homogeneous line width of ZnP in EtOD at the shortest possible time scale, leading to an offset of the dephasing rate at longer waiting times. This implies that at this short time scale dephasing is much faster than predicted by the standard TLS model. In terms of the standard model, this means that the function $R \cdot P(R)$ of equation (5.6) is not flat, as assumed in the theory. Instead, at times shorter than $1/T_2^*$, the value of this function seems to be ± 3 times larger than at times longer than $1/T_2^*$.

The fast decay of the 2PE was also found by Meijers in other doped glasses, like toluene, triethylamine, and several polymers [44]. The 2PE and 3PE data of these materials could only be fitted by assuming a large value of the function $R \cdot P(R)$ of equation (5.6) at short waiting times. It points in the direction of excess dephasing on the shortest time scales, optical excitation of chromophores seems to induce line broadening as was suggested earlier [229,230,243].

It is impossible to distinguish between fast spectral diffusion that is intrinsic to the glass and spectral diffusion that is caused by the change of state of the chromophores. The TLS model by itself does not predict a larger distribution of flipping rates at the shortest waiting times. The latter scenario implies that the chromophores do not merely act as spectators, but can actually cause glass dynamics. These dynamics generate the excess spectral diffusion on the shortest time scale. This idea is in disagreement with the assumption of the chromophore only being a probe of glass dynamics.

If the TLS flipping is indeed caused by a change in dipole moment or distortion of the configuration of the solute, excess spectral diffusion is not only caused by optical excitations, but by any change in electronic state. So far, the most straightforward experimental method to explicitly demonstrate such interactions is to carefully compare 2PE results with 3PE data. In addition, comparisons of transient and persistent HB data by Müller *et al.* [229], and Khodykin *et al.* [230], show anomalous spectral diffusion in the time domain of the triplet state deactivation ($T_{triplet}$). This yields another clue that strong coupling between chromophores and the surrounding TLS's needs to be incorporated in the TLS model.

It may also be noted that this suggestion should come as no surprise, since strong coupling between chromophore and bath is often found in solvent dynamics [167], and can be observed in crystals as well. For instance, in photon-echo experiments on Tb^{3+} and Pr^{3+}

doped crystals, instantaneous spectral diffusion due to magnetic dipole interaction between the excited ions and the surrounding lattice was demonstrated [243-245].

The introduction of an extra dephasing term $1/T_2^{extra}$, can incorporate any coherence loss not caused by the background of flipping TLS's:

$$I_{PE}(\tau, t_w) \propto A(\tau, t_w)^2 \exp\left[-2\mathscr{F}(\tau)\right] \exp\left[-2\mathscr{G}(\tau, t_w)\right] \exp\left[-2\tau/T_2^{extra}\right]. \qquad (5.12)$$

The light gray line in Figure 5.1 and the dashed line in Figure 5.2 show the results of adding such a term with a value of $1/T_2^{extra} = 0.85$ ns.

Alternatively, one could argue that the excess dephasing is caused by additional TLS's flipping, introducing different values for P_0^{ex} in the functions $\mathscr{F}(\tau)$ and $\mathscr{G}(\tau)$ in equation (5.10). Setting $P_{2PE}^{ex} k_B = 2.42 \times 10^7$ K^{-1}s^{-1} for $\mathscr{F}(\tau)$ exactly reproduces the 3PE *vs.* waiting time data and the corresponding 2PE echo, the light gray line and in Figure 5.1. However, the difference between these two approaches can clearly be seen in the non-exponential character of the resulting echo decays as is demonstrated in Figure 5.2. In this graph the stretch parameter of the decays, resulting from former approach, equation (5.12), are indicated by the dashed line, and the stretch parameters of fits to the decays of the latter approach by the dotted line. Both approaches yield stretch parameters that deviate further from the experimental data points than those found for the original expression, but in opposite ways.

5.4.2 Adjusting the Parameter Distributions

Fitting all experimental results in a global manner with equation (5.10) is difficult because of the complexity of equations (5.3) and (5.4). To be able to evaluate the effects of adjusting TLS parameter distributions, or the effects of altering other implicit assumptions in this TLS model, another approach was suggested recently by Naumov and Vainer [246,247]. Because of the use of Monte Carlo techniques tt is computationally lighter to simulate a large number of randomly chosen TLS's interacting with a large number of chromophores. The time evolution of the ensemble of chromophores can be assessed straightforwardly since the chromophores are not interacting with each other and are only weakly coupled to mutually independent TLS's. So instead of averaging over the stochastic history of the whole ensemble, the non-linear response term of equation (3.90) can also be rewritten in terms of single-chromophore single-TLS correlation functions:

$$R^{TLS}(\tau, t_w, \tau) = \frac{1}{n_{chrom}} \sum_{i=1}^{n_{chrom}} \prod_{j=1}^{n_{TLS}} \phi_{ij}(\tau, t_w, \tau). \qquad (5.13)$$

The total number of chromophores in the experiment is n_{chrom} and n_{TLS} is the total number of TLS's interacting with each chromophore. Since all TLS's are independent, the above correlation functions can then be written as:

$$\phi_{ij}\left(\tau,t_w,\tau\right) = \left\langle \exp\left[-i\left(\int_0^\tau \delta\omega_{ij}\left(t\right)h_{ij}\left(t\right)dt - \int_{\tau+t_w}^{\tau+t_w+\tau} \delta\omega_{ij}\left(t\right)h_{ij}\left(t\right)dt\right)\right]\right\rangle_{stoch}, \qquad (5.14)$$

similar to the ensemble correlation functions in section 3.9.1.

This function was evaluated by Suarez and Silbey [102] and yields:

$$\phi\left(\tau,t_w\right) = 1 - \left\{F_1\left(\tau\right) + \left(1 - \exp\left[-2Rt_w\right]F_2\left(\tau\right)\right)\right\}, \qquad (5.15)$$

with

$$F_1\left(\tau\right) = 2R\int_0^\tau F_2\left(t\right)dt \quad \text{and} \quad F_2\left(\tau\right) = \frac{4\delta\omega^2}{R^2}w_1 w_2 \exp\left[-R\tau\right]\frac{\sin\left[Y^+\tau\right]}{Y^+}\frac{\sin\left(Y^-\tau\right)}{Y^-}, \qquad (5.16)$$

using $\left(Y^\pm\right)^2 = \delta\omega^2 - \left(R^2/4\right) \pm i\,\delta\omega\left(w_1 - w_2\right)$ and the same variables as in section 3.9.1. This means that w_1 is the probability of a TLS jumping from the lower to the upper state and w_2 is the probability of the opposite process. The functions $F_1\left(\tau\right)$ and $F_2\left(\tau\right)$ can now be expressed in terms of the parameters of each single TLS as shown in Appendix 5.7.

The parameters with distributions that can be tweaked are the TLS asymmetry ε_j, the tunnelling matrix element Δ_j, the TLS-chromophore distance r_j and also, as was suggested by single molecule experiments, the TLS-chromophore coupling constant Ω_j. Using the Monte Carlo like method for the simulation of echo decays outlined in the Appendix 5.7, the effects of any adjustments to these distributions can be examined.

In Figure 5.4.a, two echo decays calculated exactly with equations (5.3) and (5.4) are reproduced accurately with the above approach demonstrating the validity of the technique. In these calculations the distributions are not modified. The TLS-phonon coupling constant was set to the value found in section 5.3.2: $ck_B^3 = 2.0\times10^8$ K^{-3}s^{-1}. The value of the TLS-chromophore coupling constant is not known for the EtOD-ZnP combination but was set to $\Omega = 100$ GHz nm^{-3} in accordance with other host-solvent combinations [117,246-248]. The number of chromophores and upper cut-offs of the probability distributions, were chosen large enough not to influence the outcome of the simulations and small enough to compute these in a reasonable amount of time. The number of chromophores n_{chrom} was set to 500, and the maximum asymmetry ε_{max}, and tunnelling element Δ_{max} were set to a value much larger then $k_B T$, $\varepsilon_{max} = \Delta_{max} = 50\,k_B$K. The maximum distance was set as $r_{max} = 40$ nm. The lower cut-off of the tunnelling matrix element distributions was set to $\Delta_{min} = 10^{-8}\,k_B$K to ensure that $\Delta_{min} \ll \sqrt{2ck_B T t_w^{max}}$, where t_w^{max} is the longest waiting time used.

The exact calculations and the results of the Monte Carlo simulations are not scaled or adjusted to each other in any way. The number of TLS's used to interact with each chromo-

phore in the latter calculations can be related to the P_0^{ex} -parameter used in the exact evalua-tion by calculating the corresponding density: $\rho_0^{MC} = P_0^{ex}/\Omega P_0^{MC}$. Here P_0^{MC} follows from the above choices and equations (2.15) and (2.16). The number of TLS's is then calculated from the solvent shell set by r_{min} and r_{max} . The match between the exact results and the simulations is excellent as can be observed in Figure 5.4.a,b,c,d. The simulations with pa-
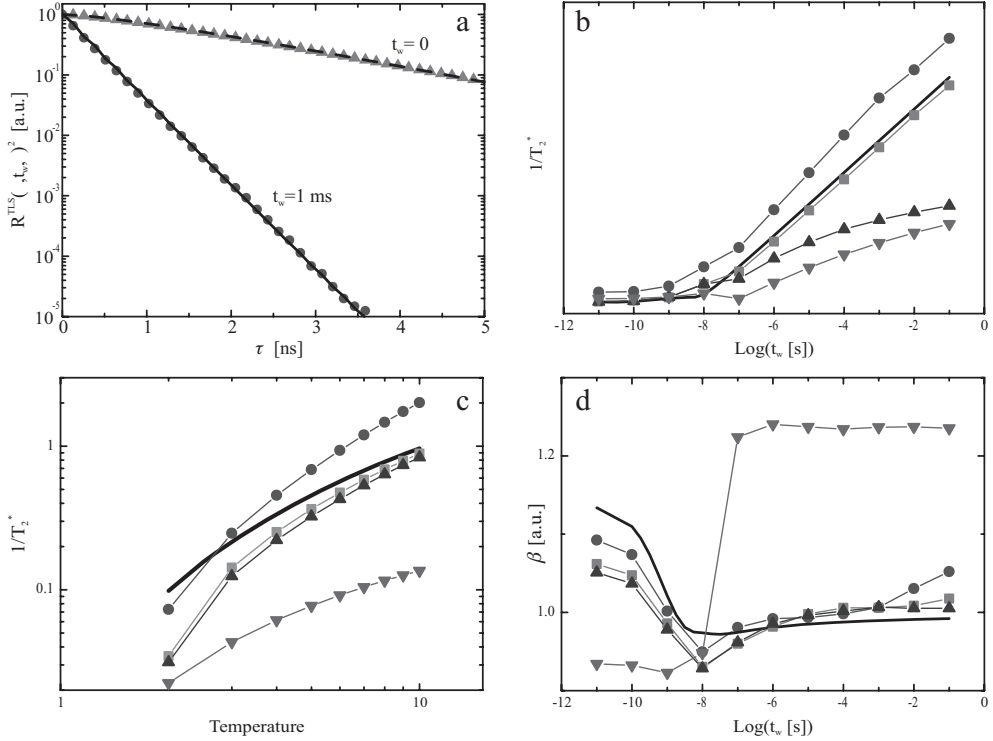
Figure 5.4. Monte Carlo simulations of echo experiments using adjusted parameter distributions. a) A reproduction of the 2PE decay and 3PE decay with a waiting time of 1 ms. The other graphs show the effect of adjusted distributions on the line broadening (b), the temperature dependence of the line width (c) and the nonexponential character of the decay through the stretch parameter β (d). In these three latter plots the squares (■) indicate the simulations with unadjusted parameters, the circles (●) simulations with $\mu = 0.3$, the upward pointing triangles (▲) simulations with $\nu = 0.2$ and the downward pointing triangles (▼) simulations with $r_{min} = 10\,nm$. The solid lines in all four plots indicate the exact results for unadjusted parameter distributions. See text for additional parameters.

rameter distributions that are not adjusted from the original propositions by Anderson [2] and Phillips [39], in other words with $\mu = \nu = r_{\min} = 0$ in equations (2.15) and (2.16), are compared to those with various modifications in the latter three plots. In these graphs the non-adjusted simulation results are shown as squares and the exact results are shown as a solid line.

Changing the TLS asymmetry distribution $P(\varepsilon)$ by setting $\mu > 0$, cp. equation (2.14), does not change the line broadening as a function of waiting time very much. Also the shape of the echo decays is not affected in any relevant way. It only strengthens the dependence of the line width on temperature, not surprising, since this was why the parameter was introduced to begin with [98,183,249]. However, since the temperature dependence of the dephasing already showed superlinear behaviour similar to the experimental results before the distribution was adjusted, setting $\mu > 0$ is not justified by the 2PE results.

Surprisingly, setting $\nu > 0$ in the tunnelling parameter distribution $P(\Delta)$, cp. equation (2.15), does not affect the deviation from exponential behaviour as much as expected. The predicted non-logarithmic waiting time dependence is discernable however and shows the same trend as originally thought [87,91]. Since no such non-logarithmic behaviour is observed experimentally, setting $\nu = 0$ seems to be the most appropriate choice.

Recently it was suggested that the spatial distribution of the TLS's $P(r)$, cp. Equation (2.29), might not be assumed as homogeneous as previously predicted [246,247]. However, setting a minimal chromophore-TLS distance, $r_{\min} > 0$, leads to very non-exponential echo decays at waiting times longer then 10 ns. This is not corroborated by the experimental results. The simulations also show non-logarithmic waiting time dependence and a stronger superlinear temperature dependence of the dephasing rate that cannot be accounted for.

Summarizing, there seems to be very little evidence that warrants the modifications of any of the parameter distributions in the original TLS model. The observed superlinear temperature dependence and non-logarithmic waiting time dependence of hole widths and dephasing rates can be explained with these distributions in an adequate manner by the more exact theory as given by Geva and Skinner [104].

5.5 The Longitudinal Echo Decay

When the population dynamics is probed by measuring the intensity dependence of the 3PE as a function of waiting time, the result is the so-called longitudinal echo decay. Although dominated by population relaxation terms, for a fixed and non-zero separation time τ between the first two pulses, the dephasing also influences this longitudinal plot, since spectral diffusion also reduces the echo intensity.
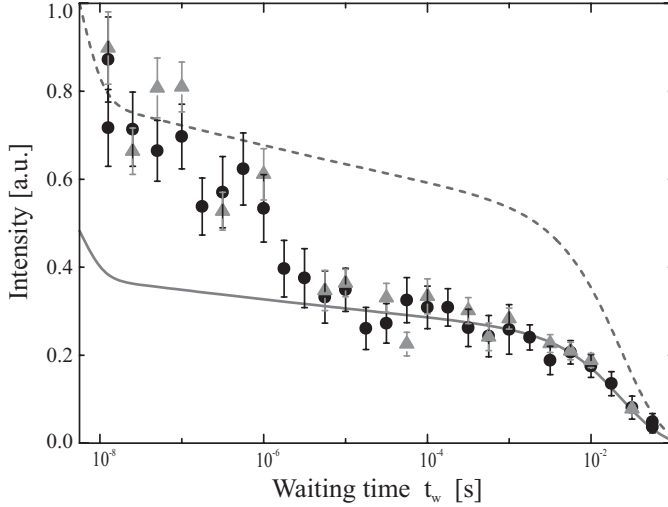
Figure 5.5. The intensity decay of the photon echo as a function of the waiting time with a fixed coherence time of $\tau = 100$ ps. The energy of the pulses is 400 nJ per pulse (●) and 50 nJ per pulse (▲). The dashed line and the solid line show the results of calculations of the intensity based on equations (5.10) and (5.17) using the parameters found in the measurements of the effective homogenous line widths: $P_0^{ex} k_B = 4.13 \times 10^6$ $K^{-1}s^{-1}$ and $ck_B^3 = 2.0 \times 10^8$ $K^{-3}s^{-3}$. The three data sets are scaled to their initial value at $t_w = 12.5$ ns, except for the solid line which is scaled to the long waiting time data. Calculations with induced fast dephasing as in equation (5.12) yield the same results.

As outlined in Chapter 2, when the triplet state lifetime exceeds all others by far, the echo intensity decay will be best described as [178]:

$$I_\tau\left(t_w\right) = I_0 \exp\left[\frac{-4\tau}{T_2^{eff}\left(t_w\right)}\right]\left(2\exp\left[\frac{-t_w}{T_1}\right] + \varphi_{ISC}\left(\exp\left[\frac{-t_w}{T_{triplet}}\right] - \exp\left[\frac{-t_w}{T_1}\right]\right)\right)^2. \qquad (5.17)$$

This shows that if the fluorescence and triplet lifetimes are known, the longitudinal echo decay can be derived from the coherence decay measurements. The echo intensity is scaled to the intensity I_0 at a short waiting time t_w^0, with $t_w^0 \gg T_1$. $T_{triplet}$ is the triplet state lifetime and $\varphi_{ISC} = 0.95$ is the intersystem crossing yield.

Typical results of a longitudinal photon echo experiment are presented in Figure 5.5, for echoes on Zinc-porphin in deuterated ethanol for a coherence time of 100 ps. At first sight the results are in accordance with what one would expect. A slowly decaying intensity due

113

to spectral diffusion during t_w up until the end of the bottleneck state lifetime $T_{triplet} = 53$ ms is followed by the a quick decrease of all remaining intensity. Note that the loss of nearly half of the signal intensity due to depletion of the excited singlet state during fluorescence and intersystem crossing – also not included in equation (5.17) – is not visible in this experiment since the singlet levels life time $T_1 = 2.7$ ns is much shorter than the first 3PE waiting time of 12.5 ns. Therefore all the intensity loss in this experiment is apparently due to refilling of the ground state from the bottleneck state and spectral diffusion.

Since porphyrines are well-studied chromophores [191], and all the relevant timescales are well know for ZnP [192,194,195], it is possible to quantitatively predict the longitudinal data by taking the waiting time dependent dephasing data from the previous chapter. The dotted line is such a prediction of the echo signal based on equation (5.17) and the calculated fit through the $T_2^{eff}(t_w)$ data of Figure 5.1 using equation (5.10). From the plot, it is immediately clear that the curve doesn't match up with the data. Obviously too much echo intensity is lost from short waiting times up until the microsecond time scale. The solid line in Figure 5.5 illustrates this best. It shows the same prediction for the echo intensity, but now scaled to the long waiting time data.

In other glasses and in proteins, a similar behavior of the longitudinal echo decay is found, although the specifics of the time scale and size of this effect vary. Especially in echo experiments on several simple molecular glasses Meijers *et al.* [44,90,185] and on proteins Thorn Leeson *et al.* [45,184], found the same significantly lower echo intensity from the microsecond region onwards to longer time scales than predicted by equation (5.17). They suggested that this indicates the existence of an additional population relaxation process.

5.5.1 Discussion of the Longitudinal Results

Two additional points have to be addressed before seeking to explain the anomalous intensity loss. In the first place, after extrapolation to zero laser fluence, the $T_2^{eff}(t_w)$ data no longer show a gap in the distribution of tunneling rates. The spectral diffusion makes therefore a larger contribution to the reduction of the calculated echo intensity. This reduces somewhat the discrepancy between the experiment and the calculated signal intensity reported in previous work [44,90,185,204], but it cannot account for the total difference in Figure 5.5.

In the second place, and on a related note, it was established in this work that sample heating has a profound effect on the dephasing rate in the coherence dimension of the echo. Therefore it can be expected that a similar effect can be found in the population dimension of the echo. It was speculated that sample heating might explain the discrepancy between

the 3PE intensity, as a function of waiting time and a prediction based on $T_2^{eff}(t_w)$ and the known population relaxation [205]. A quantitative inspection of equation (5.17) and equations (4.6) to (4.8), however, shows that the effect of sample heating on the data in the population dimension is too small to be experimentally detected. The intensity data of ZnP in EtOD, presented in Figure 5.5 for $\tau = 100$ ps, are in accordance with this conclusion, showing no significant dependence on the excitation pulse energy. The data are scaled with respect to the echo intensity for both excitation energies at $t_w^0 = 12.5$ ns and are taken at pulse energies of 400 nJ per pulse (circles) and 50 nJ per pulse (triangles). This spans an excitation energy range in which a considerable change in dephasing rate is found in the coherence dimension as is indicated by Figure 4.8 [228].

In the current TLS framework all this leaves only a completely new population relaxation mechanism as the explanation for the anomalous intensity loss. Given the fact that the population dynamics of ZnP is extensively studied by single photon counting on carefully degassed samples [44], it is unlikely that some, until now unknown, electronic level and accompanying relaxation channel is the cause of this discrepancy.

This leaves only the mismatch between the excitation spectrum of the third probing pulse with respect to the induced frequency grating, as a plausible alternative. The inhomogeneously broadened absorption spectrum of ZnP in a glass, is much broader than the excitation pulses used in the experiments. Nonetheless, drift of chromophores into and out off the excitation spectrum during the experiment is not commonly comprised in the traditional approach to probing spectral diffusion in glasses by means of photon echoes. Inspection of frequency ranges involved yields the following: the excitation bandwidth of the picosecond pulses was 8 cm^{-1}. These pulses were used to measure effective homogeneous line widths from 0.5 to 1.8 GHz, i.e. $0.02 - 0.06$ cm^{-1}, underneath an inhomogeneous absorption bandwidth of the $S_0 \rightarrow S_1$ transition of 230 cm^{-1}. So it is not likely that the constant background of frequency shifts of chromophores due to flipping TLS's causes the anomalous intensity loss.

In order to account for the effects, Meijers and Wiersma already introduced a special case of spectral diffusion by proposing the occurrence of 'large frequency jumps' [44,90,185]. They suggested that a subset of nearby TLS's is strongly coupled to the optical centers. These subsets need not to be the same for all chromophore surroundings. Flipping of the TLS's in these subsets induces large frequency jumps of the optical transition.

They argued that if these jumps were in the order of the exciting laser bandwidth this would lead to a decrease of the intensity of the 3PE in the population dimension, without affecting the intensity in the coherence dimension. Effectively this process can be considered as an extra population relaxation channel. However, these large frequency jumps cannot be optically induced, because if this would be the case, the induced jumps would lead to

permanent hole burning. This was checked for regularly during the experiment, and, as mentioned before, significant hole burning was never detected. But by themselves large frequency jumps are a possibility. In single molecule experiments such jumps are regularly observed. Chromophores studied by this technique often appear to temporarily shift into dark states as e.g. discussed by Moerner and Orrit and others [250,251]. The authors claim that such blinking and flickering effects would be almost unobservable and certainly misinterpreted in studies on large ensembles, because the various emitters contributing to the overall sum are generally uncorrelated: The mean value of the total emission would simply be smaller. However, in a time resolved fluorescence emission experiment, or even in the population dimension of the 3PE, such an effect would show up as an anomalous intensity loss.

5.6 Conclusions

When extrapolated to zero fluence the waiting time dependence of the 3PE decay shows a perfect logarithmic behavior on a time scale ranging from 10^{-8} to 10^{-1} s. Combined with recent theoretical results it seems not longer necessary to extend the standard TLS model by means of adjustable parameters like μ and ν for the distribution functions of equation (2.15) and (2.16). Both parameters can be set to zero.

The 2PE echo decays faster than is calculated from the waiting time behavior of the 3PE decays. It seems possible that this discrepancy is caused by excess spectral diffusion on short time scales due to optical excitation of the chromophores. This would imply strong coupling between TLS's and chromophores, which is not accounted for in the TLS model. It appears to be in agreement, however, with observations in hole burning and photon echoes on other glasses and chromophores. Since strong coupling between chromophore and bath seems to be commonplace in solvation dynamics theory, it seems necessary to account for this effect in a theoretical description of glass dynamics.

So far we discussed two different glass-dynamical processes, all with different intrinsic time scales. First there is the background process of flipping TLS's that cause spectral diffusion on all time scales, which is expressed by logarithmic line broadening. Secondly there is optically induced spectral diffusion, creating excess spectral diffusion at short time scales, and which is directly related to an optically induced change of electronic state.

The echo intensity loss in the population dimension of the 3PE experiment indicates that a substantial number of chromophores jump out of the laser spectral bandwidth on times scales faster than a microsecond. Note that local heating does not cause such an effect. The correctness of this scenario can be checked experimentally. If large frequency jumps are

indeed the cause of the anomalous echo intensity loss, the effect should be smaller when pulses with a larger spectral bandwidth are used. When the pulses overlap the complete absorption spectrum of the $S_0 \rightarrow S_1$ transition it should obviously completely disappear.

In single molecule experiments, the fact that different chromophores couple to different subsets of TLS's was clearly demonstrated. For instance, the fluorescence excitation line widths of a large number of single chromophores are distributed over an interval of up to three orders of magnitude [252-255]. Simulations of single chromophore line shapes confirm this wide variety of spectral widths [119,256-258]. It turns out that distributions of single molecule line shapes exist, together with distributions of the dependence on temperature and on waiting time of those line shapes . The average fluorescence excitation line width found in single molecule experiments is always larger than can be expected from 2PE experiments on the same samples [135,225,226].

The typical time scale of a single molecule experiment is often taken to be the time it takes to scan the line width of a molecule, typically tens of seconds. During this time the chromophore is driven through the excitation cycle many times. If optically induced dephasing is a factor to consider in these experiments, and the results presented here suggest it does, this changes the interpretation of these experiments considerably. In other words, if the chromophore's position in the potential energy landscape indeed alters every time it changes state, it explores a far larger region of the energy landscape than when it would otherwise.

In any case, the single molecule experiments unconditionally demonstrate that different chromophores couple to different subsets of TLS's. Thus it is likely that the coupling between some chromophores and their nearest TLS's exceeds the weak interaction limit. In fact it is found that a substantial part of the spectral jumps of individual molecules is photo induced [254,259,260].

5.7 Appendix: Monte Carlo Simulations

Naumov and Vainer [246,247] showed that the functions $F_1(\tau)$ and $F_2(\tau)$ of equation (5.16) can be transformed into forms that depend directly on the various TLS parameters. The 2PE decay only depends on $F_1(\tau)$, which can be written as:

$$F_1(\tau) = \frac{R\,\delta\omega^2\left(\Psi_1(\tau) - \Psi_2(\tau)\right)}{\left(Y_{re}^2 + Y_{im}^2\right)\cosh\left[E/2k_B T\right]}, \tag{5.18}$$

with

$$\Psi_1(\tau) = \frac{(-Y_{im} + R/2)\exp\left[-\tau(2Y_{im} + R)\right] + (Y_{im} + R/2)\exp\left[\tau(2Y_{im} - R)\right] - R}{4Y_{im}^2 + R^2},$$

$$\Psi_2(\tau) = \frac{\left(-2R\cos^2\left[\tau Y_{re}\right] + 2Y_{re}\sin\left[2\tau Y_{re}\right] + R\right)\exp\left[-R\tau\right] + R}{4Y_{re}^2 + R^2},$$

(5.19)

and,

$$Y_{re} = \mathrm{Re}[Y^\pm] = \sqrt{\tfrac{1}{2}\left(\delta\omega^2 - R^2/4 + \Theta\right)},$$

$$Y_{im} = \pm\,\mathrm{Im}[Y^\pm] = \sqrt{\tfrac{1}{2}\left(-\delta\omega^2 + R^2/4 + \Theta\right)} \text{ and finally}$$

$$\Theta = \sqrt{\left(\delta\omega^2 - R^2/4\right)^2 + \delta\omega^2 R^2 \tanh^2\left[E/2k_B T\right]}.$$

(5.20)

The other function becomes:

$$F_2(\tau) = \frac{\delta\omega^2}{\cosh^2\left[E/2k_B T\right]}\exp\left[-R\tau\right]\frac{\cosh\left[2Y_{im}\tau\right] - \cos\left[2Y_{re}\tau\right]}{2\left(Y_{re}^2 + Y_{im}^2\right)}$$

(5.21)

with

$$\left(Y^\pm\right)^2 = \delta\omega^2 - R^2/4 \pm i\,\delta\omega\left(w_1 - w_2\right),$$

(5.22)

using the variables from section 3.9.1.

The TLS parameters were randomly chosen according to the distributions introduced in Chapter 2. If $x_{rnd} \in [0,1]$ is some random number, the parameters of the j-th TLS can be chosen as:

$$\varepsilon_j = \left(\varepsilon_{max}^{1+\mu} x_{rnd}\right)^{\frac{1}{1+\mu}}$$

$$\Delta_j = \begin{cases} \Delta_{max}^{x_{rnd}}\Delta_{min}^{1-x_{rnd}} & \text{if } \nu = 0 \\ \left(\Delta_{min}^\nu + \Delta_{max}^\nu x_{rnd} - \Delta_{min}^{x_{rnd}} x_{rnd}\right)^{\frac{1}{\nu}} & \text{if } \nu \neq 0 \end{cases}$$

(5.23)

and

$$r_j = \left(r_{min}^3 + x_{rnd}\left(r_{max}^3 + r_{min}^3\right)\right)^{\frac{1}{3}}$$

$$o_j = \begin{cases} 1 & \text{if } x_{rnd} < 0.5 \\ -1 & \text{if } x_{rnd} \geq 0.5, \end{cases}$$

(5.24)

where o_j is the orientation parameter replacing the $\cos\theta_j$ term used in Chapter 2 and Chapter 3, since a simple distribution function is equally effective in this case.

The procedure for the simulation of echo decays consists of a threefold loop. Using the above equations $\varphi_{ij}(\tau)$ is calculated at a number of scan times τ and for a large number (n_{TLS}) of chromophores. The average number of TLS's interacting with some chromophore

can be estimated from the TLS density measured in single molecule experiments [256] and the volume of the shell surrounding each chromophore with inner radius r_{min} and outer radius r_{max}. A specific set of parameters is chosen for each TLS. In turn, the product of all the single-TLS single-chromophore correlation functions is calculated for a large number of chromophores n_{chrom}. The sum of all these correlation functions finally yields the echo decay function through equations (5.13) and (5.15).

Chapter 6

Liquid/Glass Solvent Dynamics: from 300 to 3 K

In this chapter the temperature dependence of the optical non-linear response of a dye dissolved in a glass-forming liquid is studied within the context of the multi-mode Brownian oscillator model. As the frequency – frequency time correlation function of a chromophore dissolved in a glass exhibits a femtosecond component at higher temperatures, femtosecond pulses are to be used in these experiments. The results of temperature-dependent echo-peakshift and heterodyned echo experiments in glass-forming liquids are discussed. Freezing out a large part of the bath fluctuations by varying the temperature from 300 K to 3 K allows for testing current solvation models.

6.1 Introduction

In the previous chapter solvation dynamics of glasses have been studied in the temperature realm of the two-level system (TLS) theory, were chromophores are supposed to couple to nearly degenerate double wells in the potential energy landscape. By charting the time-resolved correlation function of optical transitions upon ultrashort excitation, detailed insight into the dynamics of the solvent was obtained. However, at higher temperatures the TLS description of these dynamics becomes inadequate. Coupling of the chromophore to local phonon modes and other collective relaxation mechanisms becomes dominant as the temperature increases [94,117,134,180,242,261]. At room temperature, above the glass

transition for the solvents studied in this work, the description of the solvation dynamics usually follows the lines of the multi-mode Brownian oscillator (MBO) theory, as introduced in section 2.3. It models the chromophore – solvent interactions by assuming an electronic transition that is linearly coupled to a bath of harmonic oscillators.

The MBO model [55,146,147,152,153] which was successfully used to describe the solvent dynamics at room temperatures in the liquid phase, has also been tested at lower temperatures. All studies on temperature dependent solvation dynamics have been conducted in polymer hosts that form an amorphous solid already at room temperature. With respect to the bath dynamics, the polymer host can be considered as similar to a glass. However, no glass transition occurs in the temperature ranges that were studied, and experimentally, no major deviations from theoretical predictions for the linebroadening were reported.

Weiner *et al.* were the first to study the temperature dependence of the three pulse echo peakshift (3PEPS) in a glass host [168,169]. In the 3PEPS experiment, the offset of the waiting time between the second and the third pulse and/or the maximum of the time-integrated echo signal from zero delay is measured as a function of the temperature. A linear increase of ~30 fs of the echo peakshift was found with decreasing temperature when cooling a polymethyl methacrylate (PMMA) sample doped with cresyl violet from 290 K to 15 K. This was explained as a transition from homogeneous to inhomogeneous broadening due to smearing of the vibrational structure of individual dye molecules. Despite the clearly resolved peakshift in the low temperature scattering data, a pronounced echo tail, indicative of a long dephasing time T_2, was not observed. The waiting time measurements did not show any appreciable changes in the echo peak position which was interpreted as indication that spectral diffusion does not play a major role in the polymer matrix.

In a later study by Bardeen *et al.* [151,262] the two-pulse echo (2PE) and the three-pulse echo (3PE) response of two other dyes, Oxazine 4 and Styryl 7, dissolved in both PMMA and polyvinyl alcohol (PVA) were measured for temperatures from 30 K to 300 K. The echo decays in the case of the Styryl dye were too fast to be discussed in a meaningful way at any temperature. In the case of the Oxazine dye, the signal was interpreted as a combination of one dominant vibrational mode and a single exponential decay of the polarization. A linear dependence of the dephasing rate associated with this exponential decay with temperature was found. The authors note that this is consistent with linear coupling of the transition to the phonon bath when the high-temperature limit (i.e. $kT \gg \hbar\omega$) is valid for all phonons at all temperatures. This implies that the dephasing is caused by low frequency modes, that is, by those modes whose frequencies lie below $20\ \text{cm}^{-1}$. However, the dephasing time caused by these modes found in the echo decays is $\sim 50\ \text{fs}$, which corresponds to phonon frequencies in the range of $1000\ \text{cm}^{-1}$. Therefore, the system's frequency fluctuations appear to be Markovian when the correlation time is considered, and should thus be

described using high frequency modes. Hence, there exists an apparent incongruity between the linear temperature dependence of the dephasing rates and the Markovian character of the echo decays. The authors suggested that the linear coupling representation as implied by the MBO model is inadequate, and that quadratic or higher coupling terms need to be considered.

On the other hand, Nagasawa *et al.* [149,150,263] concluded that the MBO model should still be readily applicable to describe the optical dephasing of the infrared dyes IR144 and DTTCI dissolved in polyvinylformal (PVF) and PMMA down to temperatures of 30 K. Besides considering the 3PE signal and the absorption spectrum, they also studied the 3PEPS and transient grating scattering, which afforded a more detailed analysis of the temperature dependence of the modes involved in the optical dephasing process. The experiments revealed an initial decay of the peakshift that could be modeled by assuming fast dephasing of intramolecular vibrational wave packets and an inertial solvent response, followed by quantum beats originating from the prominent intramolecular modes of the dye. Nagasawa *et al.* found that in these glasses the inertial response was best modeled using a severely damped oscillator to allow for some undershoot in the peakshift data. At the same time they indicate that the precise characterization of this mode is limited by the resolution obtained in the analysis of the experimental data. Contrary to the experiments by Bardeen *et al.*, the detailed computer simulations showed that the peakshift signal and also the absorption and Raman spectra could be self-consistently reproduced at all temperatures, by assuming a fixed spectral density in terms of the MBO model.

Furthermore, according to the experiments by Nagasawa *et al.* the relatively weak coupling of DTTCI to its vibrational and bath modes results in a more prominent temperature dependence of the peakshift when compared with other dyes like IR 144. On the other hand the temperature dependence of the residual peakshift at long waiting times of the sample containing IR144 dissolved in PVF showed an unexpected maximum at temperatures around 100 K that, according to the authors, could not be accounted for within the framework of the harmonic bath model. However, later calculations by the same authors demonstrated that this feature originates solely from the effects of finite pulse widths, namely the temperature-dependent detuning between the laser and transition frequencies which was not initially taken into the consideration [150]. If these effects are included properly in the calculations, no major deviations from the MBO model are observed.

Optical dephasing of zinc-octaethylporphine in several glass forming liquids at temperature from 0.35 K to a maximum of 100 K was investigated by Vainer and Gruzdev *et al.* [134,261,264-267] using narrowband two-pulse and incoherent photon echoes. They were able to distinguish between a low temperature range, where dephasing mechanisms related to tunneling TLSs were dominant, and a higher temperature range where the dephasing was

best described by the coupling of the chromophore to one or two low frequency vibrational bath modes.

Almost all previously reported studies concentrated on polymer solvents that show no phase transition in the temperature range under consideration. Only the above mentioned narrowband studies by Vainer and Gruzdev *et al.* used a simple glass forming liquid and a wide temperature range, but also these studies were conducted at temperatures that were below the glass transition at all instances. The effect of a phase transition was not investigated.

In this chapter the temperature dependence of solvent dynamics in a glass forming host is studied using a number of femtosecond four-wave mixing (such as 3PE, 3PEPS and heterodyne detected photon echoes, HDPE) and steady-state spectroscopic techniques from room temperature down to the cryogenic regime. This temperature range includes a phase transition at 150 K where all diffusive solvent motion slows down to a completely static state of affairs. It is shown that the HDPE technique is far more sensitive to the changes of these parameters than the 3PEPS experiment is. In particular, the glass transition is hardly noticeable in the temperature dependent 3PEPS experiment at moderately long times, when it can be clearly seen in the temperature dependent HDPE data.

The ability of the MBO-model to accommodate temperature changes with a temperature independent spectral density (SD) is tested. It is found that it is not possible to account for the experimental results with a fixed SD even over relatively moderate temperature ranges. The parameters of the Brownian oscillator modes (BO's) that are used for describing the third-order optical response of the system at room temperature clearly exhibit temperature dependence, thus changing the SD of the system. The lack of diffusive motion below the glass transition does not exclude all dynamics at these temperatures, as the remaining intramolecular modes and some residual inertial solvent modes still cause coherence loss at short times. The temperature dependence of the MBO parameters matches largely the expected temperature dependence of the microscopical physical processes that underlie the modes in question. However the fastest mode that is frequently associated with dephasing of the vibronic manifolds does not depend on temperature in a way that is characteristic for the vibronic dephasing. Instead, this mode is attributed to quadratic or anharmonic coupling of pseudo-local phonon modes to the electronic transition, since its temperature dependence ties in with such or a similar mechanisms much better.

6.2 Experimental Results

An overview of the main experiments that are considered when obtaining the correlation function and SD is displayed in Figure 6.1. These plots are meant to give a concise outline of the effects of temperature on the outcome of the various experiments. The glass forming liquid of choice is a 1:1 volume mixture of ethanol and 1,2 propanediol (EtOH/PD) because this mixture yields glass samples of good optical quality upon rapid cooling. The infrared dye DTTCI was picked for its absorption spectrum that has an excellent overlap with the spectrum of the excitation pulses. It also has a low number of low-frequency vibrational modes relative to other laser dyes in the same frequency range.

The absorption spectrum of DTTCI in EtOH/PD in Figure 6.1.a shows the narrowing of the width of the spectrum with decreasing temperature. Where at 300 K the full width at half maximum (FWHM) of the spectrum is approximately 450 cm^{-1}, at 100 K this is reduced to $\cong 330 \text{ cm}^{-1}$ and at 3 K it is only $\cong 260 \text{ cm}^{-1}$. The spectrum also exhibits a small red-shift of $\cong 65 \text{ cm}^{-1}$ at the lower temperatures.

Typical time-integrated three pulse echo signals at various temperatures, from which the peakshift can be deduced, are shown in Figure 6.1.b. The increasing inhomogeneous character of the solvation dynamics with decreasing temperature is obvious from the echo signal. The signal becomes wider and more asymmetric and it peaks at a later time. Whereas at 300 K the echo is approximately 40 fs wide, at 3 K this has become $\cong 80 \text{ fs}$ at FWHM. The echo maximum shifts from nearly 9 fs at room temperature to over 22 fs at 3 K. Although the echo stretches to longer times at lower temperatures, the nanosecond decays observed in the experiments with picosecond pulses are not present here.

The peakshift measurements as a function of the waiting time reflect the above temperature dependence as illustrated by Figure 6.1.c. As the temperature drops, the dynamics become visibly slower, and correspondingly the peakshift increases. The signal is characterized by a fast inertial-like decay at short times that at first glance seems to be temperature independent. A region that is characterized by several recurrences of the peakshift follows this decay. These quantum beats, which are caused by the intramolecular vibrational motions of the chromophore, do not change their frequency substantially at lower temperature but seem to increase in amplitude while the damping of the vibrations seems to slow down. The long tail of the peakshift signal is an indication of the coupling of the chromophore to diffusional modes of the solvent. This part of the peakshift function shows the increased "inhomogeneous" portion of the correlation function with decreasing temperature by becoming nearly constant. This decreased slope of the 3PEPS function at times longer than 2 ps clearly indicates that the modes related to diffusional solvent motion are frozen out.

The effects of temperature on the vibrational dynamics are best observed in the longitudinal dimension of the homodyne echo traces as displayed in Figure 6.1.d. The quantum beats become more prominent at lower temperatures although little seems to change as soon as the glass temperature is passed ($T_g = 150$ K). Note that this lack of change below T_g is the first signature of the glass transition that is apparent from superficial inspection of the experimental data (*vide infra*). Fitting the traces with exponentially-damped cosine functions yields the relative amplitudes, frequencies and decays of the three main vibrational modes: 0.9, 150 cm^{-1}, 150 fs; 0.03, 380 cm^{-1}, 500 fs; and 0.07, 485 cm^{-1}, 700 fs, respectively. These values corroborate well with the previously published data [177,268-270], and will be rectified later while applying the full-scale modeling. As has been suggested earlier, the waiting time of 210 fs offers an outstanding opportunity to suppress the intramolecular vibrational contribution onto the experimental observables. First, at this time the most prominent 150 cm^{-1} mode is almost in its first recurrence (the period is ~ 220 fs). Second, by a coincidence the 485 cm^{-1} mode is in its third recurrence (the period ~ 70 fs). Third, the amplitude of the 380 cm^{-1} mode is negligibly small as compared to the other two and therefore its influence is minimized. We will use the 210 fs waiting time in a number of heterodyne-detected experiments to get rid of intramolecular vibrational involvement that masks greatly the true solvent dynamics.

Finally, the position of the maximum of the HDPE signal is displayed at two different temperatures in the Figures 6.1.e and 6.1.f. In the HDPE experiment, the echo field is heterodyned by a fourth pulse, the local oscillator [148]. By scanning the delay between the last two pulses (τ') for a set of fixed timings of the first two (τ), time resolved interferometric echo profiles are obtained. Here we focus mainly on the temporal echo amplitudes and therefore filter out the interferometric fringes by applying a Fourier-filter. For extracting information regarding the homogeneous *vs.* inhomogeneous contributions to the line broadening, the position of the echo maximum has proven to be very instructive [148]. For instance, in the framework of Bloch model, the echo maximum peaks at

$$\tau'_{max} = \tau - \frac{\left(T_2^{inhom}\right)^2}{T_2} \tag{6.1}$$

where T_2^{inhom} and T_2 are the inhomogeneous and homogeneous phase relaxation times, respectively. If the line broadening is perfectly static, the time resolved profile peaks at $\tau' = \tau$ at all times that $\tau > 0$. At the other extreme, a totally homogeneous system produces profiles that always peak at $\tau' = 0$ fs. In the more sophisticated models of solvent dynamics [55], a relation similar to equation (6.1) also holds although the interpretation of the relaxation times becomes somewhat different [148].
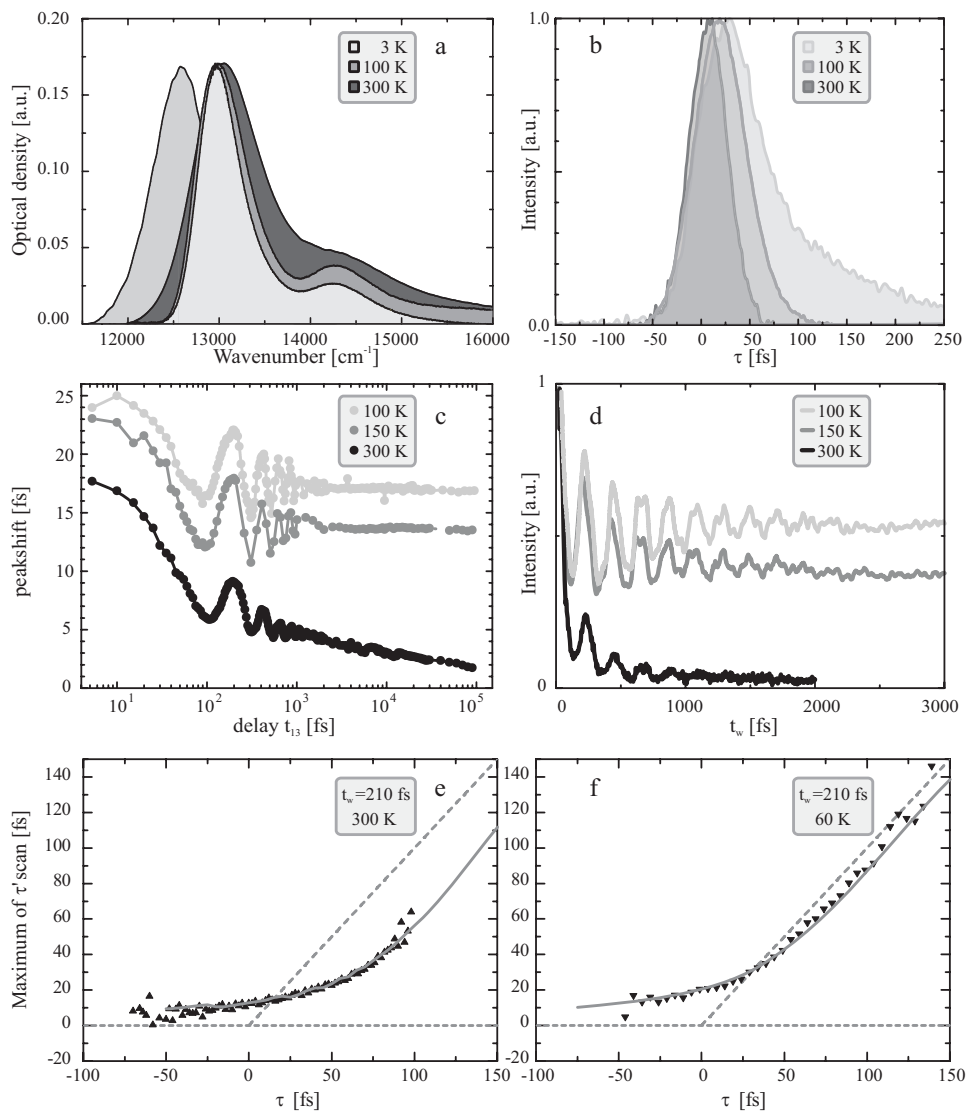
Figure 6.1. a) The absorption spectrum of DTTCI (right), and the fluorescence at 300 K (left). b) Time integrated 3PE scans for t_{13} = 210 fs . c) The 3PEPS signal. d) Longitudinal (t_w) 3PE scans with τ = 40 fs . e) and f) The position of the transient echo maxima as a function of t_w and τ (symbols) as compared to the full scale simulations of the positions of these maxima (line) at two temperatures. The transient echo is a scan of τ ' for these specific pulse timings.

From a fleeting glance at Figures 6.1.e and 6.1.f one could conclude that the plot of the time-resolved echo maximum position obeys equation (6.1) reasonably well. From this equation one infers that the estimated dephasing time at 60 K is $T_2 \cong 60$ fs as discussed in more detail in the next sections. Furthermore, if one compares the widths and heights of these traces it becomes evident that the transient echo signal broadens with decreasing temperature, and peaks at a later time. The former corresponds to the narrowing of the absorption spectra as the temperature lowers (Figure 6.1.a) while the latter indicates their increased inhomogeneity which can not be directly deduced from the spectra. By comparing projections (i.e. integration of profiles along the τ'-axis) of both plots onto the τ-axis, the lengthening of the integrated echo signal can also be seen which is in line with Figure 6.1.b.

6.2.1 Room Temperature Data

In this section, we outline the procedures according to which different experimental data sets were processed. As a starting point, the room temperature data are used, as much is known for the dye DTTCI dissolved in ethylene glycol from the work by de Boeij [148] where 8 modes were applied to describe the dynamics. The characteristic properties of the EtOH/PD mixture are very similar to those of ethylene glycol making this choice perfect for a reference. In the next section, temperature variations of the 8 modes parameters will be introduced to explain the temperature dependent data.

   All of the above experiments reflect particular aspects of the system-bath correlation function of the optical transition. For instance, the absorption and emission spectra are indicative of the overall static coupling strength parameter $\langle \Delta^2 \rangle$ and the total reorganization energy λ. The 2PE and 3PE signals are mostly susceptible to the slow parts of the correlation function. The longitudinal 3PE decay is especially useful to determine the low-frequency intramolecular modes. Alternatively, as explained in Chapter 4, the 3PEPS trace bears great resemblance to the overall correlation function, except for the shortest time-scales. This fast part of the correlation function is best determined through analysis of the time-resolved HDPE traces, as indicated above.

   Therefore, all the results from all these experiments at all temperatures have to be taken into account when simulating the temperature dependence of the solute–solvent correlation function in the framework of the MBO-model. The iterative numerical procedure that is needed to calculate the correlation function and the corresponding spectral density in this manner was described earlier for DTTCI in several solvents [148-150,177,268]. It involves the simultaneous fitting of all spectra, integrated echo traces and transient echo profiles with the results from the calculations. Improvements in computer technology and optimizations

of the algorithms used in the calculations have made it possible to perform these calculations on a small cluster of 10 ordinary off-the-shelf desktop PC's.

All the calculations of the transient third-order polarization $P^{(3)}(t)$ were performed using the three-fold integrals of the complete expressions of equations (3.40) and the non-linear response functions of equation (3.58). The actual carrier frequency and the finite pulse durations are taken into account and the measured spectral pulse profiles were used. Also, all possible pulse permutations were incorporated in the computations. After the polarization was determined, the simulated signals of the respective experiments were calculated using the appropriate expressions outlined in Chapter 3.

The contributions to the line broadening functions $g(t)$ were, depending on the nature of the mode under consideration, either evaluated directly whenever an exact expression of this function was available (see reference [145] and [148]) or through numerical integration

		Temperature:		300 K	250 K	150 K	100 K	3 K	MBO
Ultrafast mode	Gaussian decay (GCD)	$\Delta_0 = 850$ cm^{-1}	τ_0	20 fs	30 fs	80 fs	125 fs	315 fs	no
Intramolecular modes	Vibrational modes (UBO)	$\omega_1 = 150$ cm^{-1}	Δ_1	127 cm^{-1}	117 cm^{-1}	95 cm^{-1}	84 cm^{-1}	74 cm^{-1}	yes
		$\lambda_1 = 37$ cm^{-1}	γ_1^{-1}	150 fs	182 fs	317 fs	317 fs	317 fs	-
		$\omega_2 = 380$ cm^{-1}	Δ_2	43 cm^{-1}	41 cm^{-1}	37 cm^{-1}	37 cm^{-1}	36 cm^{-1}	yes
		$\lambda_2 = 3.5$ cm^{-1}	γ_2^{-1}	500 fs	600 fs	1 ps	1 ps	1 ps	-
		$\omega_3 = 485$ cm^{-1}	Δ_3	81 cm^{-1}	78 cm^{-1}	74 cm^{-1}	73 cm^{-1}	73 cm^{-1}	yes
		$\lambda_3 = 11$ cm^{-1}	γ_3^{-1}	670 fs	800 fs	1.3 ps	1.3 ps	1.3 ps	-
Solvent modes	Strongly overdamped modes (SOBO)	$\lambda_5 = 20$ cm^{-1}	Δ_5	91 cm^{-1}	83 cm^{-1}	65 cm^{-1}	65 cm^{-1}	65 cm^{-1}	yes[*]
			Λ_5^{-1}	0.5 ps	0.75 ps	>1 ns	>1 ns	>1 ns	-
		$\lambda_6 = 54$ cm^{-1}	Δ_6	150 cm^{-1}	137 cm^{-1}	106 cm^{-1}	106 cm^{-1}	106 cm^{-1}	yes[*]
			Λ_6^{-1}	2.5 ps	3.75 ps	>1 ns	>1 ns	>1 ns	-
		$\lambda_7 = 39$ cm^{-1}	Δ_7	128 cm^{-1}	116 cm^{-1}	90 cm^{-1}	90 cm^{-1}	90 cm^{-1}	yes[*]
			Λ_7^{-1}	100 ps	150 ps	>1 ns	>1 ns	>1 ns	-
		$\lambda_8 = 46$ cm^{-1}	Δ_8	139 cm^{-1}	126 cm^{-1}	98 cm^{-1}	98 cm^{-1}	98 cm^{-1}	yes[*]
			Λ_8^{-1}	>1 ns	>1 ns	>1 ns	>1 ns	>1 ns	-

Table 6.1. The temperature dependence of the fitting parameters of the harmonic modes used to simulate the optical response of DTTCI in EtOH/PD. The MBO-column indicates whether or not the temperature dependence of a particular parameter follows directly from the MBO-mode (see section 6.3 for discussion). * Only above the glass transition

of the corresponding part of the spectral density. To do this, equations (3.55),(3.57) and (3.58) can be rewritten as:

$$\text{Re}\left[g(t)\right] = \frac{1}{\pi}\int_0^\infty C(\omega)\coth\left[\frac{\hbar\omega}{2k_B T}\right]\frac{1-\cos[\omega t]}{\omega^2}d\omega \tag{6.2}$$

and

$$\text{Im}\left[g(t)\right] = -\lambda t + \frac{1}{\pi}\int_0^\infty \frac{C(\omega)}{\omega^2}\sin[\omega t]d\omega . \tag{6.3}$$

In this way the line broadening function can be evaluated by calculating only two single integrals. At room temperature the data were simulated with the set of oscillators outlined in the corresponding column of Table 6.1.

In earlier work [148] the fastest initial decay was modelled with a quasi-continuum of undamped bath modes with a Gaussian distribution of coupling strengths (GDS, see equation (3.65)). This distribution was thought to reflect the non-rephasing coherence decay resulting from the impulsive excitation of the vibronic manifold. The fastest solvent modes were also modelled by means of a Gaussian distribution of modes that reflected the inertial solvent response, i.e. the reaction of the molecules in the first solvent shell surrounding a chromophore to the change of its electronic state and therefore the dipole moment. The Gaussian character of this GDS profile is supported in liquids by molecular dynamics simu-
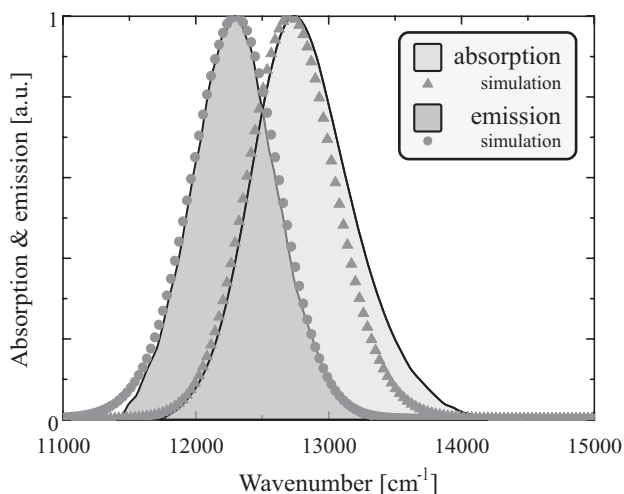

Figure 6.2. Absorption and emission spectra at 300K and the results of the corresponding simulations. The absorption due to ring modes at 14000 cm^{-1} has been subtracted from the overall spectrum (see text for details).

lations and optical response theory [121-124,129,271,272] and also by optical Kerr and Raman data on similar neat solvents [149,273-278]. In polymers it was suggested that this solvent response was best fitted by a critically damped oscillator [150].

For reasons that are discussed in the following sections and that follow from the temperature dependence of the ultrafast components of the correlation decay, both the fast intramolecular mode and the inertial solvent mode are modelled by a single decay of the correlation function, in the simulations performed here. This decay is taken to have a Gaussian shape centred at $t = 0$:

$$M(t) = \frac{\Delta_0^2}{\tau_0} \exp\left[\frac{-t^2}{\tau_0^2}\right].$$

(6.4)

This Gaussian correlation decay (GCD) is associated with the following expression for the corresponding spectral density $C(\omega)$:

$$C(\omega) = \frac{\Delta_0^2 \lambda \omega}{\sqrt{\pi}} \exp\left[\frac{-\omega^2 \tau_0^2}{4}\right].$$

(6.5)

The shape of the contribution of this mode to the overall SD is shown in Figure 6.14.b.

Besides these fast components to the correlation function, the optical transition of DTTCI is coupled to three distinct intramolecular vibrational modes modelled with under-
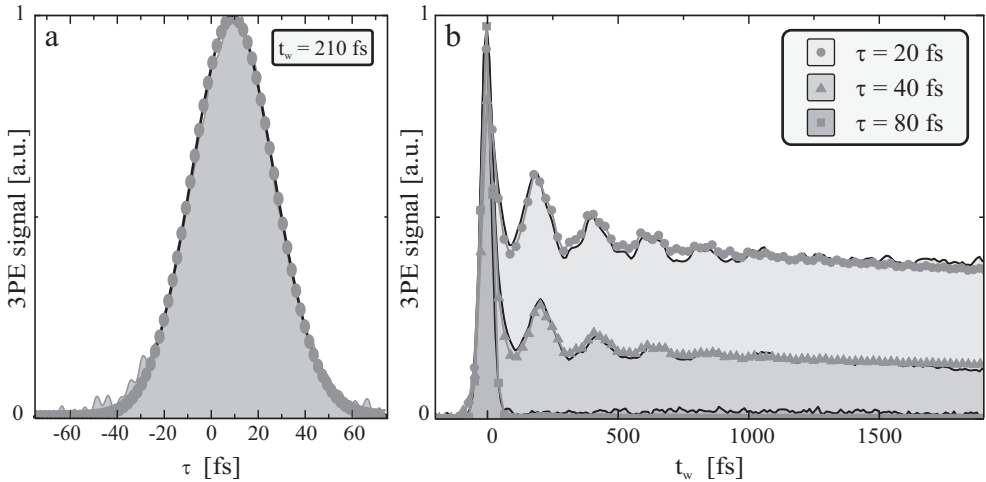

Figure 6.3. a) A typical 3PE trace as used in the determination of the 3PEPS at 300 K. The grey dots show the simulated echo trace. b) The longitudinal 3PE at three coherence times τ at room temperature. Again, grey black symbols show the simulations of these experiments.

damped Brownian oscillators (UBO's, see equation (3.63)). These modes model the peri-odical recurrences of the observed optical coherence.

After the ultrafast initial decay, and somewhat masked by the quantum beats due to the slow vibrational modes, solvent motions make the correlation function decay further on two picosecond time scales. This is in line with previous experiments, and this part of the decay is modelled by means of strongly overdamped Brownian oscillator (SOBO, see equation (3.69)). It is attributed to diffusional solvent motions. A final SOBO with a decay time set to infinity (≥ 1 ns) was used to model the residual inhomogeneity that was invariably found in the response of viscous liquids.

Figures 6.2 through 6.8 outline the results of simulations using the above parameters and expressions. It shows that the set of parameters from Table 6.1 can be used to describe all room temperature experiments adequately.

Figure 6.2 displays the emission and absorption spectra at room temperature. Note that the part of the DTTCI absorption spectrum that is due to excited modes of the conjugated rings of the dye has been largely subtracted to facilitate the comparison of the experimental and simulated data. This was done by fitting these modes on the blue side of 14000 cm^{-1} with a single Gaussian and subtracting the resulting fit

The calculated spectra fit the data very well, except for the small offset on the red side of the emission spectrum. This is more often observed in simulations of the linear spectra with the MBO-model. The limited number of modes explicitly considered in the model causes the vibronic coupling to be easily underestimated. In addition, the harmonic model does not
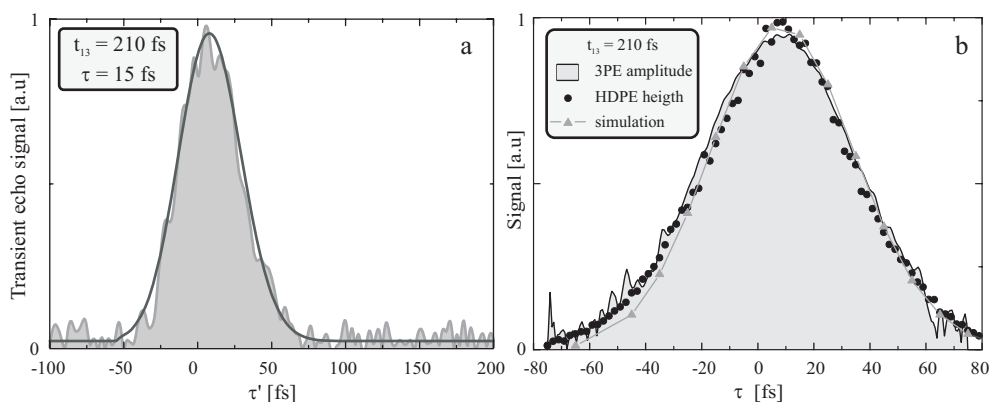

Figure 6.4.a) A typical filtered HDPE trace at room temperature and the correspond-ing simulated transient echo trace. b) A comparison of the amplitude of the 3PE with the height of HDPE traces and the transient echo simulations.
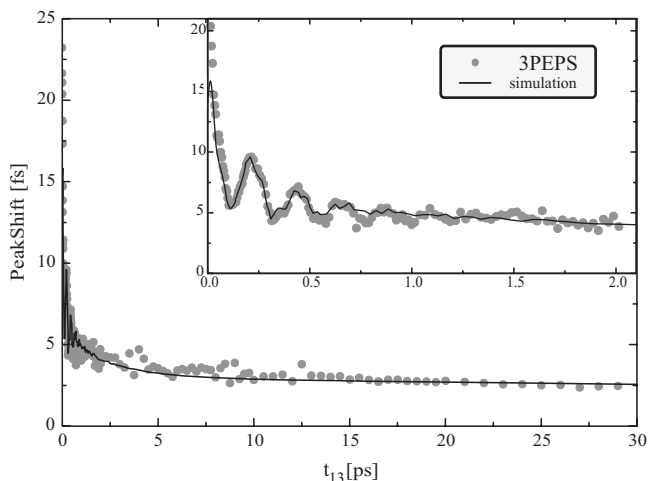
Figure 6.5. The 3PEPS signal of DTTCI in PD-EtOH at room temperature and the calculated peakshift trace. The insert shows the short waiting time data.

include any difference between the potential energy surfaces of the ground and excited state of DTTCI. This could be the case as suggested by the fact that emission and absorption are not perfect mirror images. If these surfaces are not identical, the energy gap is no longer linearly coupled to the generalized solvation coordinate, and quadratic coupling terms need to be considered as well. This leads to extra dephasing terms that should be taken into account. Possible anharmonicity of the potential energy surfaces is a related process that leads to the appearance of the nonlinear coupling. However, this is less likely to be important at room temperature because at this temperature the fast bath dynamics ensure the Gaussian statistics of the fluctuations of the energy gap. At temperatures below the glass transition the bath dynamics become far more static, and therefore the particle averaging of the solvent motions might be less effective. Then the Gaussian character of the statistics of the collective solvent coordinate is less probable

Besides reproducing the absorption and emission spectra, the same parameter set also reproduces the 3PE traces as shown in Figure 6.3. The simulations of longitudinal 3PE profiles show that the quantum beats that are modelled by the three UBO's, are reproduced perfectly. This is demonstrated in Figure 6.3.b. These same recurrences are also observable in the 3PEPS signal, demonstrated in Figure 6.5. The traces are reproduced as well in the calculations, except for the shortest waiting times, as was to be expected.

Next, the 3PE signal is time-resolved using a local-oscillator pulse in the HDPE experiment. A typical time-resolved trace and the corresponding prediction are shown in Figure

6.4.a. To demonstrate the comparative merits of these transient echo traces with the time-integrated 3PE signal, the maximum heights of the HDPE curves is plotted against the amplitude of the 3PE. Figure 6.4.b. shows that the square root of the time-integrated signal matches the heights of the transient echoes.

After having established the relation between the 3PEPS and the HDPE experiments, Figure 6.6 shows the full HDPE plots for several waiting times. Although it is possible to discern some increase in the homogeneous character of the time-resolved echo profile and coherence loss with increasing τ', these 2D plots are not very instructive when analyzing the correlation functions or the system – bath spectral density. The time-resolved echo at $t_w = 210$ fs has an ellipse shape, stretching to some extent along the $\tau' = \tau$ axis. The echo signal at $t_w = 100$ ps has a more circular shape, stretching more along the $\tau' = 0$ direction.

In order to quantify these findings, in Figure 6.7.a the same data as in the top left panel of Figure 6.6 is shown, but now with all τ'-traces are normalized. This illustrates the development of the position of the transient echo maximum along the τ-axis. In the subsequent panels of Figure 6.7 the position of the maximum of a fit of the transients with a Gaussian profile is plotted. These maxima are useful when interpreting the behaviour of the HDPE signal with varying waiting time and temperature.

The position of the maximum can be interpreted in terms of equation (6.1) as also outlined in Section 3.7. For the moment however, the positions of the maxima are only compared to those of the calculated transient echo traces in order to once more ascertain that the parameter set from Table 6.1 describes both the fast and slow parts of the correlation functions satisfactorily at room temperature. It is immediately clear form the five latter panels of Figure 6.7 that this is indeed the case; the calculations match the experimental data closely. Figure 6.8, that shows the variation of the maximum position with the waiting time for several coherence times, confirms this.

This shows that all experiments and data sets at this temperature can be reproduced with the parameter set of Table 6.1. At first sight an optimization space spanned by nearly 30 free parameters might seem rather excessive. However it is important to realize that not all these factors are free to take any value. The amplitude Δ_i of each mode is related the reorganization energy λ_i associated with that mode through the equations outlined in section 3.6.2.

Although adding more BO modes would of course improve the agreement between experiment and simulation, it is not possible to describe the data accurately with fewer oscillators. The fast initial 3PEPS decay shows clear evidence of two components, and the longitudinal echo traces necessitate the use of at least three UBO's. The diffusive solvent modes are determined by four SOBO's. Residual inhomogeneity and the 3PEPS decay at waiting times over 1 ps clearly show why the three slowest modes need to be considered.
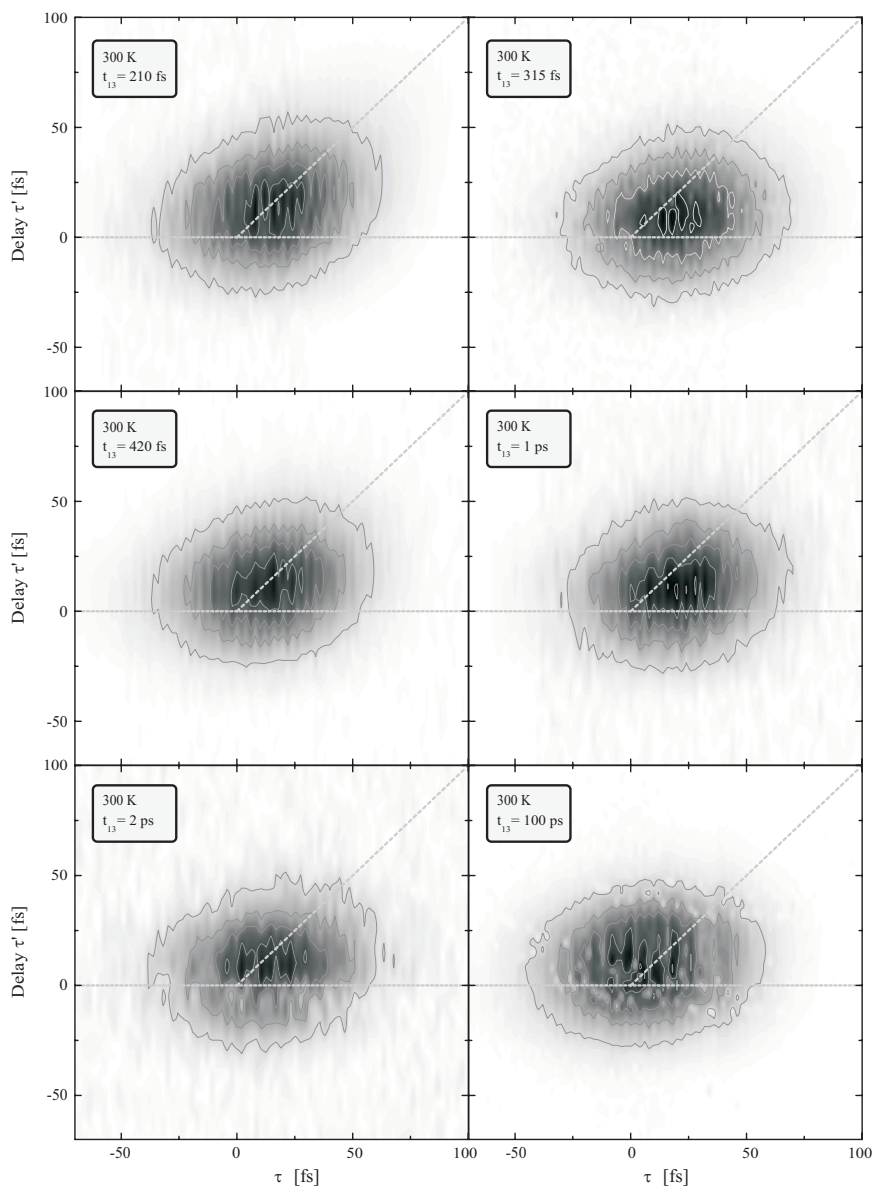
Figure 6.6. 2D representations of the HDPE scans at four different waiting times. The dashed lines are $t_{34} = 0\,fs$ and $t_{34} = \tau$ and indicate the position of the maxima of the transient echo traces in the case of perfect homogeneous and completely static line broadening respectively.
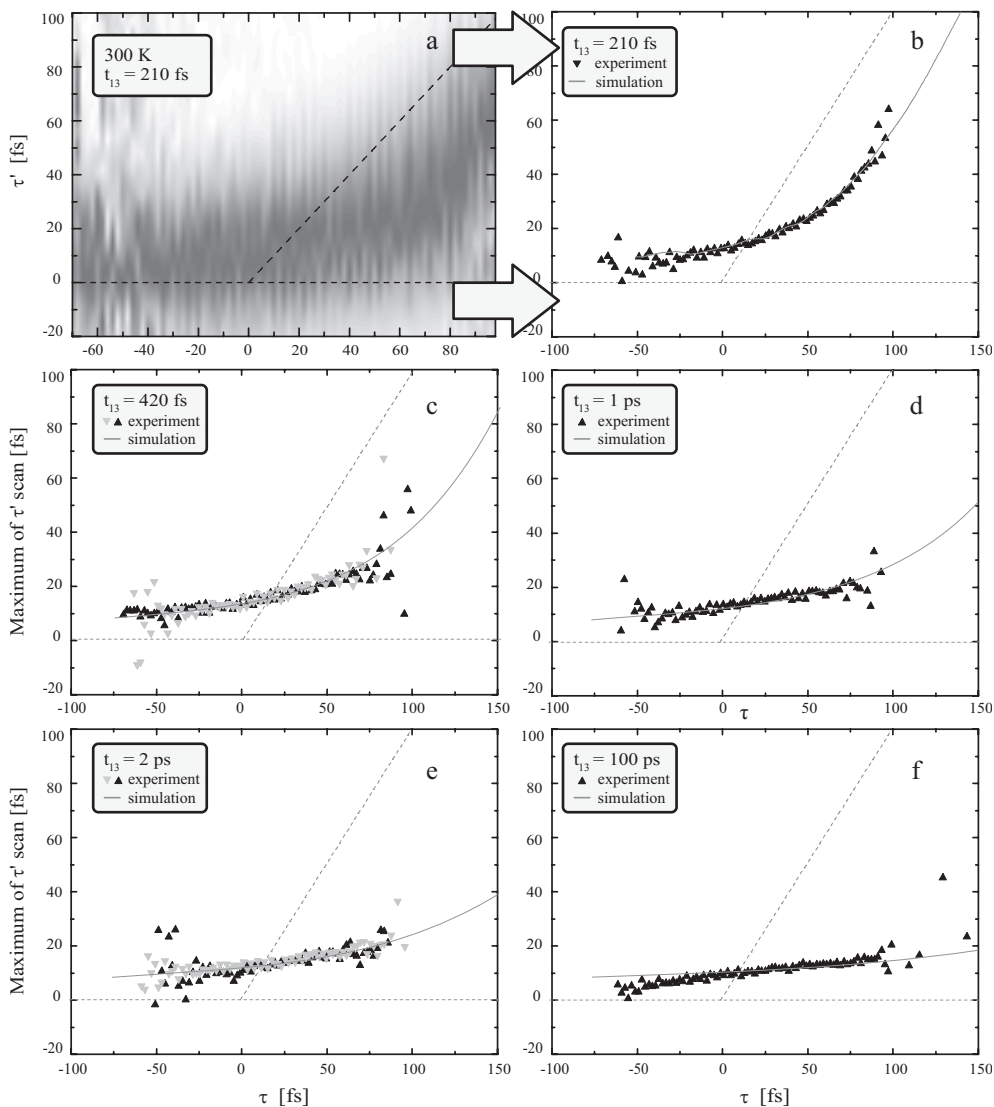
Figure 6.7.a) The HDPE plot as in Figure 6.6 with t_{13} = 210 fs and all traces along the t_{34} axis normalized. b) – f) The position of the maxima of the transient echo traces for several waiting times at room temperature (symbols) and the corresponding results of the calculations (lines).
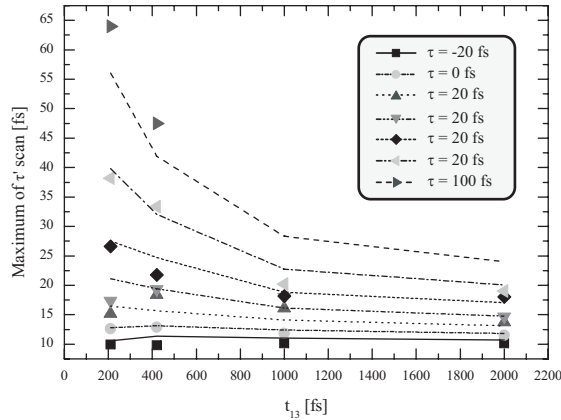
Figure 6.8. The dependence of the position of the maximum of the transient echo traces for several coherence times τ (symbols) and the corresponding theoretical predictions (lines).

The 500 fs mode is not as obvious since it is somewhat masked by the quantum beats due to the vibrational modes, but fits to the 3PEPS signal and longitudinal echo traces clearly improve when this mode is added to the simulations.

Now that the room temperature data are described adequately by the current set of BO's, it is time to verify how these oscillators can be used to described the data after a temperature change.

6.2.2 Temperature Dependent Data

The spectral density of states is the key quantity in modeling the system – bath interactions. In a first approach it is supposed not to be dependent on temperature. Even if one considers a temperature independent spectral density as a starting point for these calculations, some temperature effects still can be incorporated in the MBO-model through the Boltzmann term in equation (6.2). On the same footing the parameters of the different types of modes depend on temperature. For an UBO e.g. the amplitude of the oscillations can be calculated from the associated reorganization energy and the temperature as follows:

$$\Delta_i^2 = \lambda \, \omega_i \coth \left[\frac{\hbar \omega_i}{2 k_B T} \right]. \tag{6.6}$$

137

When the so-called high temperature limit (HTL) holds, i.e. when the frequency of the mode is low enough with respect to the temperature as in $\hbar\omega_i \ll 2k_B T$, this reduces to

$$\Delta_i^2 = \frac{2k_B T \lambda_i}{\hbar} \,. \tag{6.7}$$

This second expression for the amplitude of the frequency excursions is also valid for a SOBO in the HTL when the nuclear dynamics of the mode in question are slow compared to the magnitude of the fluctuations ($\Lambda_i \ll \Delta_i$). These temperature dependencies get expressed in the correlation functions $M'(t)$ and $M''(t)$ through the line broadening function $g(t)$, see equations (3.56), (3.57) and (3.58).

It should be noted that the modes included in the spectral distribution associated with the GCD cannot suit the HTL. At room temperature modes faster then $\sim 15\ \text{fs}$ do not satisfy this limit. At 30 K the HTL no longer holds for modes faster then ~150 fs and at 3 K even the quickest diffusional mode might not meet the constraints of the HTL.

Even if the 300 K parameter set is considered to describe a temperature independent spectral density, the model can accommodate temperature variations. However, it is not likely that the SD remains unchanged over the whole temperature range from 300 to 3 K, especially since this range includes a phase transition.

Close inspection of all the outcomes of all experiments at various temperatures, as sum-
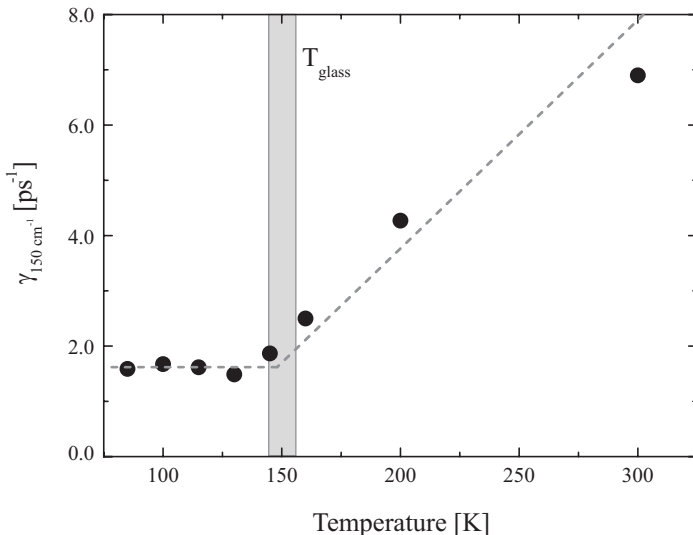
Figure 6.9. The temperature dependence of the damping of the 150 cm^{-1} vibrational mode of DTTCI in EtOH/Pd shows the effect of the glass transition (grey bar) on the vibrational mode.

marized in Figure 6.1, shows that the most apparent temperature dependent feature is the damping constant of the UBO's as seen in longitudinal echo decays and 3PEPS plots. When the longitudinal 3PE plots are fitted with the damping factors γ_i as free ranging parameters, the behavior of especially the damping of the 150 cm^{-1} mode shows a significant temperature dependence. This dependence is plotted in Figure 6.9. Below the glass transition temperature the slowing of the damping of this mode stops. In fact, this slowing of the damping of the intramolecular vibrational modes is the most straightforward observation of the glass transition upon inspection of the individual experiments.

However, for a proper analysis, evaluating all the experiments one by one will not do. What is needed, is a scenario that can explain all experiments within the confines of the MBO model. The above example does show it is not possible to describe all data with a completely temperature independent SD. Consequently, some additional temperature dependence of the SD needs to be incorporated in a model that makes physical sense, while varying as few BO parameters as little as possible.

In the following, the outcomes of several experiments are presented at several temperatures. In order to establish the need for a SD that depends on the temperature, some of these experiments are compared both to calculations that were based on a temperature independent SD and to calculations that include a SD that changes with temperature according to a single set scenario.
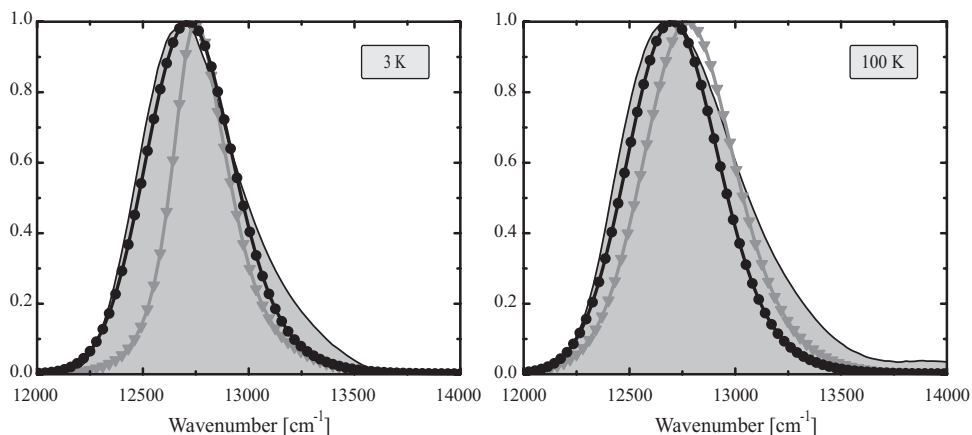
Figure 6.10. The absorption spectra of DTTCI in EtOH/PD at two different temperatures and the calculations of these spectra with the parameters in Table 6.1 (black circles). To emphasize the need for a temperature dependent SD to accurately simulate the data, the grey triangles indicate the absorption spectrum simulated with a temperature independent SD that was deduced from the room temperature data.

After having tried many possible scenarios, the data were successfully simulated with a spectral density that is still nearly temperature independent. The conjecture was a scheme in which all the intramolecular modes were supposed to show the temperature dependence through the relations within the MBO model as outlined above. Only the dissipation of vibrational energy into the surroundings is sensitive to the temperature. From Figure 6.9 the following relation was inferred:

$$\gamma_i = \begin{cases} \alpha\,\gamma_{room}\,\dfrac{T-T_g}{T_{room}-T_g} + \left(1-\alpha\right)\gamma_{room} & \text{for } T \ge T_g, \\[2mm] \left(1-\alpha\right)\gamma_{room} & \text{for } T < T_g. \end{cases} \qquad (6.8)$$

Here γ_{room} is the value of γ_i at room temperature T_{room} and $0 < \alpha < 1$. At the glass point the friction is typically halved with respect to room temperature ($\alpha \cong \frac{1}{2}$), and becomes temperature independent below T_g. It is reasonable to assume that when the bath dynamics slow down, the vibrational energy of the chromophore dissipates slower. However, the
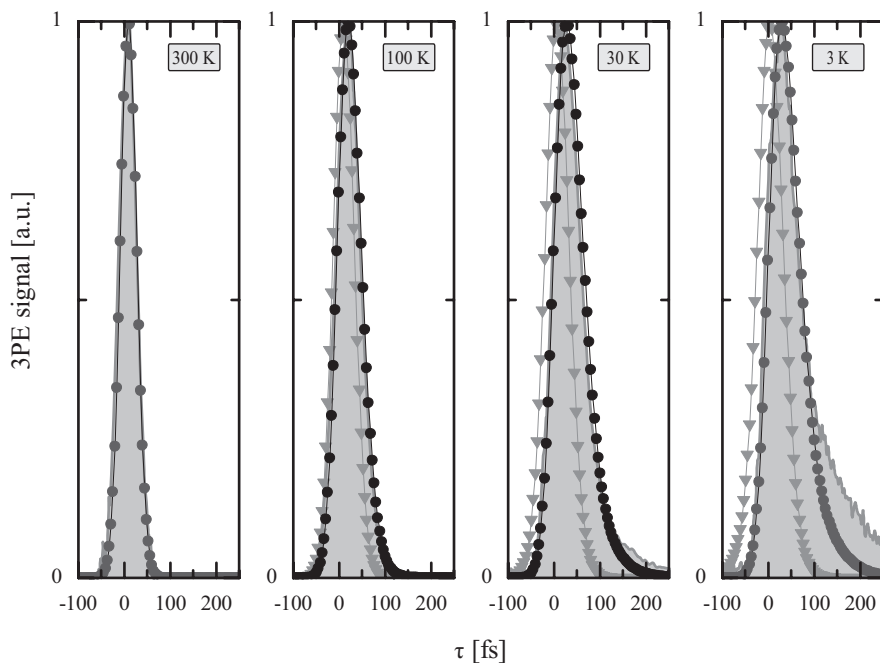
Figure 6.11. An example of typical 3PE traces at various temperatures. The waiting time for these traces is $t_{13} = 210\ fs$. The black circles indicate the simulations with a temperature dependent SD and the grey triangles simulations with a temperature independent SD.

choice for a linear temperature dependence and a damping factor below the glass transition that is half the room temperature value is made on phenomenological grounds.

At the same time, when considering the solvent modes, it makes sense to expect that all diffusion vanishes at the glass temperature. Therefore, a temperature dependence was introduced for SOBO's, that confirms with the freezing out of solvent diffusional modes. The strongly overdamped solvent modes were considered as contributing to the overall static inhomogeneity below the phase transition. The data were adequately described at all temperatures below T_g by setting the parameters of the *i*-th SOBO as follows: the correlation time Λ_i^{-1} was set to infinity (> 1 ns) and Δ_i^2 was set to its value at the glass temperature according to equation (6.7). Above the glass temperature Λ_j was set to linearly increase from zero to its value at room temperature:

$$\Lambda_i = \Lambda_{room} \frac{T - T_g}{T_{room} - T_g} .$$

(6.9)

This proposed behavior is inspired by the Vogel-Fulcher equation [27,28] describing non-Arrhenius relaxation in glass forming liquids, see equation (2.3). Here the divergence temperature in the argument of the exponent in equation (3.68) is set equal to the glass temperature. Δ_i^2 was set according to equation (6.7) above the glass point.

So far, this scenario is simple and physically appealing, since it only implies the slowing down of solvent modes and vibrational energy dissipation as the glass transition is approached. Unfortunately, it yields too little inhomogeneity which results in a peakshift that
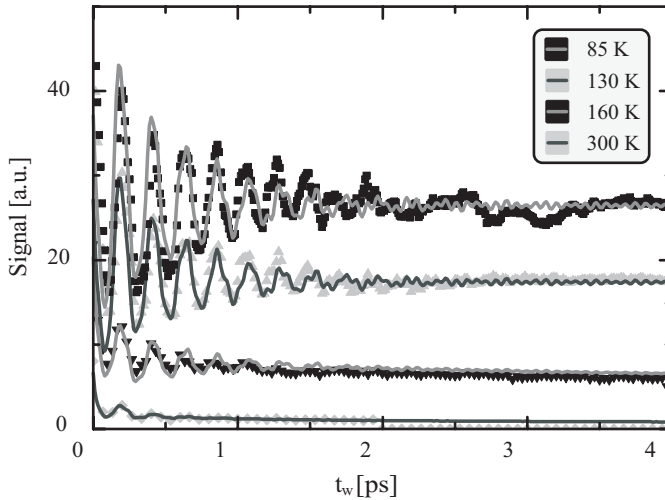
Figure 6.12. The longitudinal 3PE traces with $\tau = 40\,fs$ at several temperatures (symbols) and the corresponding calculations (lines) according to Table 6.1.

141

is too small at temperatures well below T_g. If the 3PEPS traces are calculated using the above scenario with a fast mode as in section 6.2.1., where the contribution of the fast mode only varies with temperature through the standard MBO relations as in equation (6.2) and (6.3), the traces do not match the experimental data. In this case the simulated data differ from the experimental data with an off-set that is constant at all but the fastest waiting times for a set temperature. For instance, Figure 6.14.a shows the difference between the calculated 3PEPS using the parameter temperature variation as introduced above and the experimental 3PEPS data at several waiting times as a function of temperature. The parameters of the fast mode were set to match the data at room temperature. Clearly an off-set exists between the calculated peak-shift and its experimental value which is virtually identical at all waiting times and which varies nearly linearly with temperature. This indicates that the fast MBO-modes must also vary with temperature.

De Boeij *et al.* used two Gaussian distributions of spectral modes (GSD) to describe the ultrafast part of the correlation decay [148,171,268]. If the parameters that are used to describe these distributions are taken to be temperature independent the data, of course, cannot be accounted for. As indicated, in this case the 3PE traces peak to early and the simulated data have an excessive homogeneous character. Of course this can be fixed by making the parameters of these two GSD's that de Boeij *et al.* used temperature dependent. In such a way the influence of the ultrafast part of the simulated correlation decay can be decreased at lower temperatures. Unfortunately, doing so will yield 3PE decays with unrealistically long tails, or in other words simulated echo decays that stretch to far longer times than the experimental data. Fitting both experiments with one parameter set seems impossible with
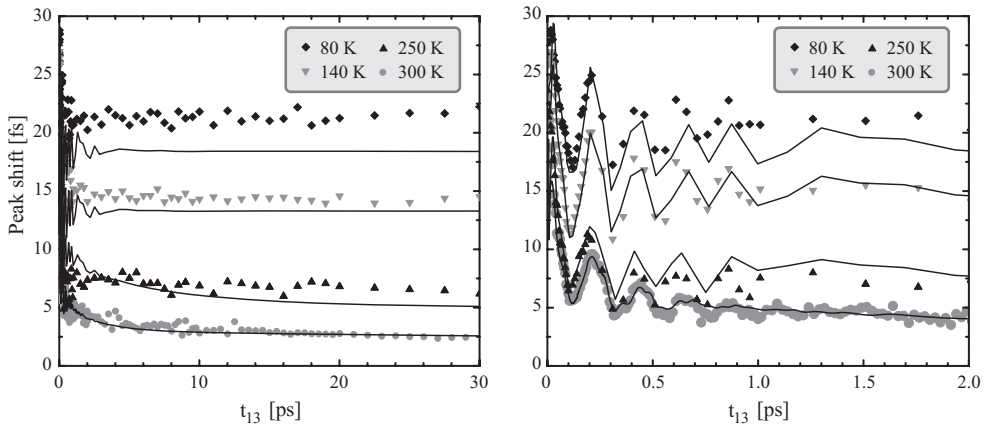
Figure 6.13. Temperature dependent 3PEPS data (symbols) and the corresponding simulations according to the scenario as outlined in the text (lines).

this GSD-type of ultrafast modes.

For this reason the Gaussian decay of the correlation function (GCD) was introduced in the previous section. This is the decay as described by equation (6.4). It differs only slightly from the GSD mode; the amplitude of the Gaussian correlation decay is divided by τ_0. By increasing the characteristic timescale τ_0 of this mode with decreasing temperature the ultrafast decay was slowed enough to let the simulated 3PE traces peak at a time that corresponds with the experimental 3PEPS data while at the same time it still had enough amplitude to yield realistic simulated 3PE data. Therefore both the solvent and the intramolecular GSD were replaced by this single GCD in the simulations.

The temperature dependence of the characteristic time of the GCD was chosen to be exponential. Since the 3PEPS does not vary linearly with the amplitude of this mode, a simple linear temperature dependence of τ_0 could not explain the experimental results in a satisfactorily manner. Other non-linear functional forms of this dependence can also be used. The exponential form was chosen for its simplicity only, and it yields a temperature dependence of τ_0 that goes as:

$$\tau_0 = \alpha_1 \exp\left[\frac{-T}{\alpha_0}\right].\tag{6.10}$$

The values of τ_0 that were used in the calculations are listed in Table 6.1 and are also
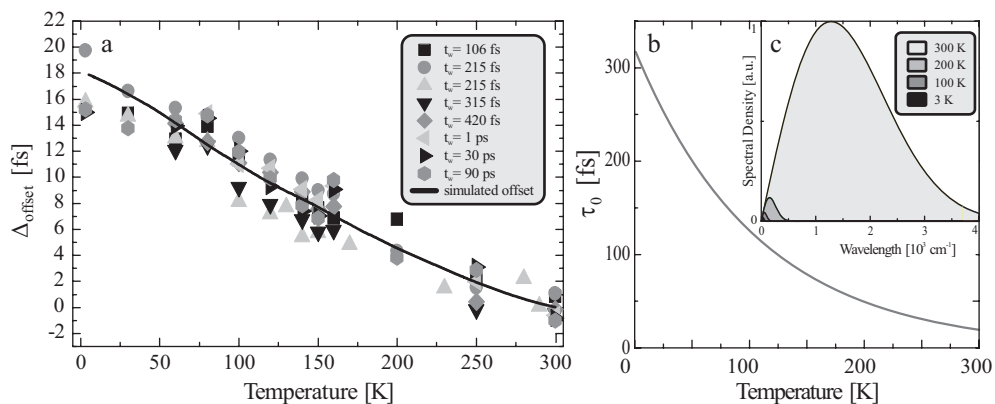
Figure 6.14. a) The difference between the experimental data at several waiting times and the simulated 3PEPS data without considering the temperature dependence of the fast GCD mode (symbols, see text). The solid line shows the difference between the simulation with and without this temperature dependence. b) The temperature dependence of the characteristic time τ_0 of the GCD mode used in this calculation. c) The spectral density associated with this temperature dependent GCD-mode.

shown in Figure 6.14.b. These values were obtained by setting $\alpha_0 = 107$ K and $\alpha_1 = 320$ fs. The amplitude Δ_0 of the mode was taken to be temperature independent. Since at all temperatures the characteristic times is still shorter than all the other modes this effectively means that the amplitude of the fast mode varies as $\propto \Delta^2 / \tau_0$. In principle, other parameterization functions, for instance, involving both parameters, could have been used as well. The difference between the simulated peak-shift data without the temperature dependence of this fast mode and with a fast mode that varies as in equation (6.10), is represented by the solid line in Figure 6.14.a. This shows that the chosen dependence for this mode is effective in eliminating the last remaining difference between the simulated 3PEPS traces and the experimental data.

The temperature dependence of this particular SD change is depicted in the inset of Figure 6.14. Although its temperature variations are not as physically appealing as those of the modes introduced earlier in this section, the overall behaviour does make perfect sense. With the temperature decrease, the SD of the bath fluctuations, in the first place, spans a narrower spectral region, and secondly, decreases in amplitude. As the fast intramolecular mode is usually associated with fast vibrational dephasing, both trends meet the intuitive expectations. However, the observed temperature dependence does not follow automatically from the MBO model, most probably, due to the breakdown of the assumption of lin-
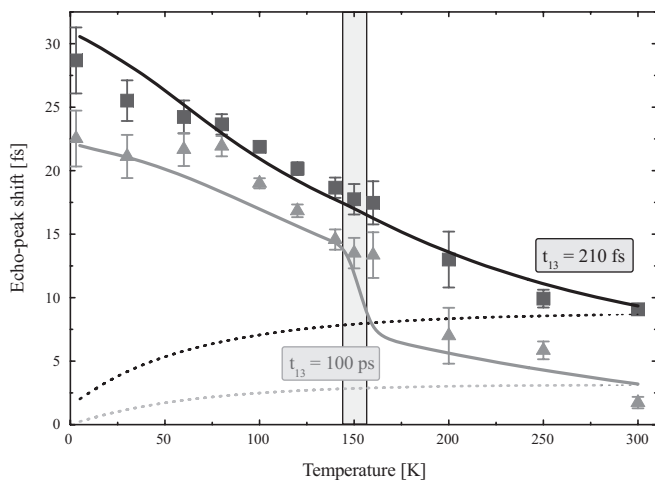
Figure 6.15. The temperature dependence of the echo peakshift at waiting times $t_{13} = 210$ fs (black) and $t_{13} = 100$ ps (grey). The glass temperature T_g is indicated by the grey bar. The solid lines are simulations of the experimental data using the scenario outlined in the text. The dotted lines are simulations of the 3PEPS experiment assuming a fixed, temperature independent, SD.

ear coupling to the vibronic manifold.

After this final tweak the scenario yields good results. Of course having more parameters vary more freely with temperature can improve the match between experimental results and the calculations, but this scenario is of all tested arrangements the simplest one that can describe the results adequately.

The first evidence of the ability of this scenario to describe the data is with the temperature dependence of the absorption spectra. This is presented in Figure 6.10. In all absorption spectra the ring modes with a 16000 cm^{-1} detuning were subtracted. This was done by fitting this part of the spectrum with a Gaussian profile and subtracting the resulting fit. The spectra can be accurately reproduced over the complete temperature range. All relevant parameters are also outlined in Table 6.1.

The 3PE echo profiles as reproduced similarly well at all waiting times and temperatures except for short waiting times ($<1 \text{ ps}$) at very low temperatures ($<5 \text{ K}$). Since at these times and temperatures the HTL no longer holds, the mismatch between experiment and simulation in the last panel of Figure 6.11, was to be expected. Otherwise the echo width and echo position are reproduced exactly. Also the longitudinal echo traces are reproduced, as demonstrated in Figure 6.12.

Especially the longitudinal echo traces reinforce the necessity of making the damping of the vibrational modes temperature dependent. The temperature dependence of the parameters that make up the UBO modes is characterized accurately. Close inspection shows that although there is some room for improvement of the fits, the data do not yield evidence enough for more complicated schemes than the one described in equation (6.8).

Figure 6.13 also shows the effectiveness of the proposed scenario. The 3PEPS data are reproduced reasonably well at the various temperatures. It shows evidence of the separation in the fast intramolecular modes not being sensitive to the glass transition and the diffusive solvent modes that are susceptible to this phase transition. Although at some temperatures the experimental asymptotic long time peakshift is not perfectly reproduced in the simulations, the trends of the values are replicated quite well. The mismatch between experiment and simulations is too small to warrant further refinement of the proposed temperature dependence.

The next plot perhaps best demonstrates this. Figure 6.15 plots the detailed temperature dependent data of the 3PEPS at two waiting times that correspond to the first vibrational recurrence at 210 fs and almost full relaxation at room temperature at 100 ps. The temperature dependence of these peaks shifts is correctly emulated by the simulations. The short time peakshift shows little evidence of a discontinuity at the phase transition. This is reasonable to expect, since the fast modes are not sensitive to this change in the bath dynamics, and the solvent modes are too slow to influence the peakshift at this waiting time.
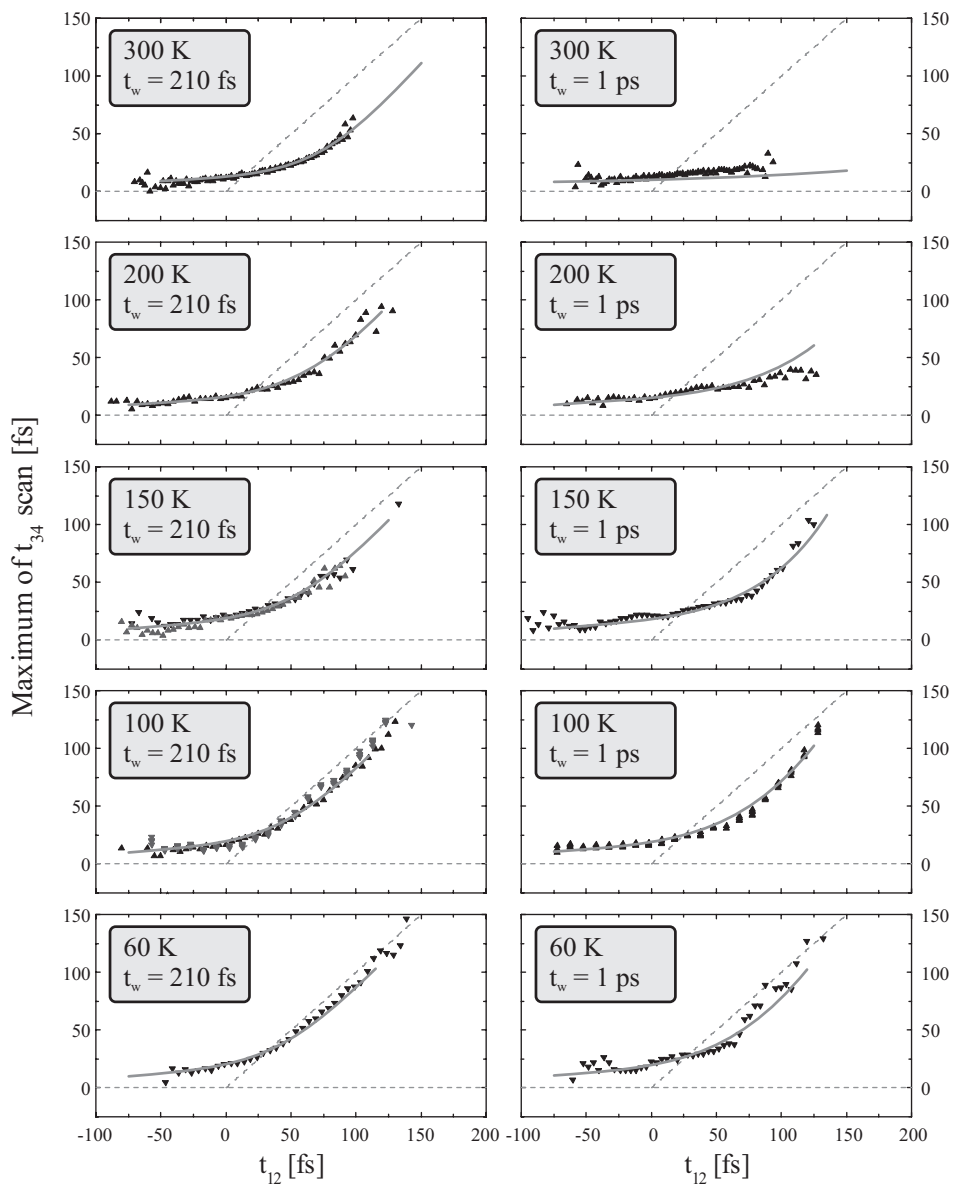
Figure 6.16. The maxima of transient echo traces at various temperatures and two waiting times (black and grey triangles) with the corresponding calculations (grey lines). The dotted lines are guides for the eye as in Figure 6.7.
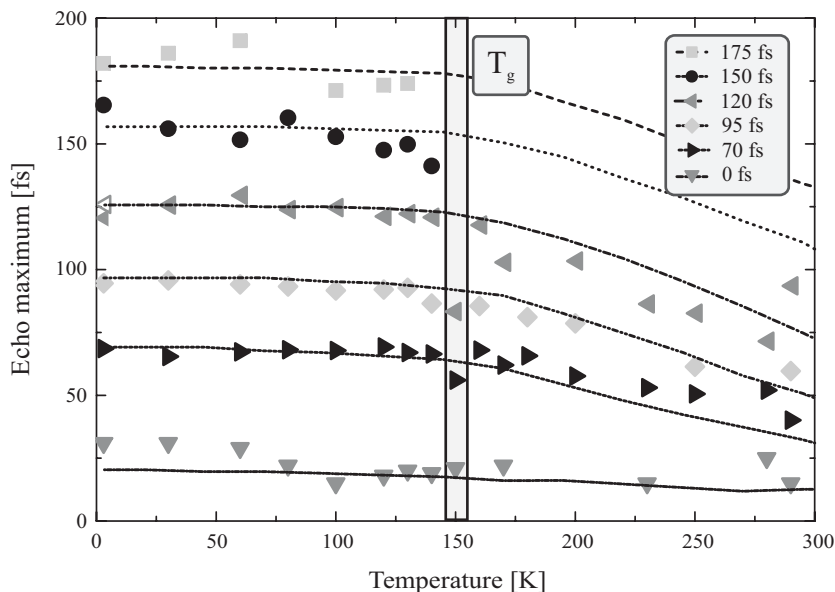
Figure 6.17. The position of the maximum of the time resolved echo profile at different coherence times τ as a function of temperature and the corresponding calculations. The waiting time was set at 210 fs.

 Only at long waiting times the glass to liquid transition is visible in the experimental 3PEPS results. At even lower temperatures, as the system becomes more inhomogeneous, the solvent relaxation nearly vanishes altogether. The offset between these two data sets at temperatures below the glass transition, therefore originates mainly from the vibrational relaxation of the 150 cm^{-1} intramolecular mode and the temperature dependent terms in equation (6.2).

Finally, the temperature dependence of the HDPE data is demonstrated in Figure 6.16. Comparing this figure with Figure 6.7 shows that the shape of the echo profiles is clearly changed with the temperature decrease. Actually, decreasing temperature and decreasing waiting time have a similar effect on the shape of the 2D plots, it makes them more asymmetric. This asymmetry is an indication of a more inhomogeneous character of the frequency fluctuations. As with the room temperature data, the maxima of the Gaussian fits to the transient echo traces are plotted as a function of the coherence time. These maxima positions of the maxima also compare well with the theoretical predictions based on the proposed scenario.

Figure 6.17 shows the temperature dependence of the maximum of several slices of these echo maximum profiles at different temperatures and at a waiting time of $t_w = 210 \text{ fs}$. It is immediately clear that the system grows to be more static at lower temperatures. From 300 K to the glass temperature at 150 K, the dynamics slow down in a linear fashion. Then, deceleration of the solvent dynamics seemingly comes to a halt around the glass temperature.

The glass transition is clearly discernable in the experimental HDPE data even at this waiting time, as opposed to the temperature dependent 3PEPS data. At longer coherence times at low temperatures the maxima are positioned at nearly the same delay as the corresponding coherence time, indicating a purely static and inhomogeneous character of the dephasing dynamics. The HDPE data are well reproduced by the proposed scenario for the temperature dependence of the BO parameters.

6.3 Discussion

The scenario for the temperature dependence of the spectral density discussed and investigated in the previous section can be used to successfully simulate the experimental data. The choices implemented in this scenario are made on phenomenological grounds. The feasibility and credibility of these grounds are discussed in further detail in this section.

Within the MBO model and still assuming a temperature independent shape of the spectral density, the amplitude of the frequency fluctuations Δ_i are assumed to depend on temperature while the associated reorganization energy λ_i is a constant instead of the other way around. The justification of this assumption lies in the fact that in the framework of the MBO model the reorganization energy is directly connected with the displacement d between the ground and excited state potential energy surfaces of the chromophores along the generalized solvent coordinate. Also, the absorption spectra exhibit some narrowing of their widths at lower temperatures which is consistent with decreasing of the frequency fluctuations. Finally, the argument that the Stokes shift (that is directly related to the reorganization energy) decreases with decreasing temperature, is refuted by noticing that the time scale at which the solvent reorganization occurs, at low temperatures becomes much longer than the excited-state lifetime. Therefore, the population relaxes long before the solvent has a chance to get reorganized.

The temperature dependence of BO parameters (i.e., reorganization energy λ_i, damping γ_i and frequency ω_i) is rarely discussed in current literature on harmonic oscillator solvent models. Gu *et al.* [279] remark, in their full quantum mechanical treatment of an electronic excitation linearly coupled to multiple passively damped harmonic oscillators, that in

a general approach the damping coefficient should be regarded as a function of temperature and frequency $\gamma_i = \gamma_i(T, \omega)$. They note that the specific temperature dependence is especially relevant if one considers the effects of a phase transition of the solvent. The ultimate cause of the damping of the UBO modes is the interaction of the optical system with the environmental solvent shells, and one would expect a large effect on the damping from the fluid viscosity. Therefore the authors conclude that the temperature dependence of γ_i is determined by the specific physical origin of the damping of the mode under consideration.

For these reasons in the last column of Table 6.1 the parameters that vary with temperature purely following equations (6.6) and (6.7) are indicated as following directly from the MBO model, whereas the temperature dependence of the damping parameters γ_i and Λ_i is not included in the model. This dependence was chosen in such a way that the simulations fit the experimental data.

The damping of the slow intramolecular modes discussed here, is determined by how quickly the vibrational energy dissipates into the surrounding solvent. In the absence of a solid theoretical framework the choice for linear variation of the damping of the under-damped oscillator with temperature follows readily from the experimental longitudinal 3PE data, as can be seen in Figure 6.12. The damping rates are relatively small, the decay rates of the oscillations are on the subpicosecond time scale. The slower relaxation processes, related to structural equilibration, should correlate well with the Stokes-Einstein equation that provides the relation between the self-diffusion coefficient D and the viscosity η:

$$D(\eta) = \frac{kT}{6\pi\eta r} \tag{6.11}$$

As pointed out in section 2.1, a similar relation exists for the rotational reorientation time, the Debye–Einstein relation. Therefore, as the diffusion coefficient decreases linearly with temperature, the microscopic structural relaxation times will increases in a similar fashion. It has been established [280,281] that this concept of evaluating hydrodynamic and thermodynamic functions of the solvent can be used to describe the solute oscillator – solvent coupling. The linear character of temperature dependence has been observed in Raman spectra of amorphous metal solids [282] and in IR pump-probe studies on the temperature dependent vibrational relaxation times of carbonyls solutes in various liquids [283,284]. Although this evidence is indirect, it indicates that the linear temperature dependence of the vibrational relaxation in the experiments presented here is reasonably realistic.

The temperature dependence of the inverse correlation time Λ_i of the strongly over-damped modes is established using the same concept of correlated temperature dependences of relaxation times. As it is reasonable to expect that all diffusive motion disappears at temperatures below the glass transition, this temperature is used as the divergence temperature in a Vogel-Fulcher description [27,28]. As outlined in section 2.1, this is a first-

order approach to model non-Arrhenius relaxation in glass forming liquids. Transient-dichroism experiments however, have demonstrated a similar correlation with viscosity and temperature [285-293].

The main experimental motivation for the linear temperature dependence of the inverse correlation time Λ_i of the solvent modes above the glass temperature was the temperature dependence of the HDPE traces, as displayed in Figure 6.17. This can be easily understood by examining the transient echo signal. This signal follows the following relation:

$$S_{HDPE}\left(\tau, t_w, \tau'\right) \propto \left| P_{3PE}^{(3)}\left(\tau, t_w, \tau'\right) \right|^2 \tag{6.12}$$

Differentiating this for a polarization determined by some correlation function $M'(t)$ made up of a fast part $M'_{fast}(t_{23})$ and some slow SOBO modes contributing to $M'_{slow}(t_{23})$, as in

$$M'(t) = (1-a)M'_{fast}(t) + a\,M'_{slow}(t)\,, \tag{6.13}$$

will yield its maximum position t_{max} as was shown in section 3.7. At long coherence times this gives for the maximum position:

$$\left(\frac{\partial t_{max}}{\partial \tau}\right) = M'_{slow}\left(t_w\right)\,. \tag{6.14}$$

And therefore, in a first order approximation, the linear dependence of the maximum position on the inverse correlation time can be expressed as:

$$t_{max} = \tau - \frac{\Lambda_i}{\Delta_i^2}\,. \tag{6.15}$$

This shows that any other but a linear temperature dependence of the diffusive solvent mode parameters does not lead to an adequate description of the experimental results. It also reinforces the connection between the 3PEPS and the HDPE results, as changing the parameters of the strongly-overdamped modes to match, for instance, the peakshift data will also change the transient echo maximum position.

Whereas the temperature dependence of the parameters of the above modes are in accordance with the physical interpretation of the associated relaxation processes, the temperature dependence of the amplitude of the fastest intramolecular GCD mode does not follow naturally from the interpretation that this mode arises from ultrafast dephasing of the vibronic manifold. In studies of liquid dynamics in the femtosecond time domain, the solvent relaxation decays are divided into slow diffusive components and a fast inertial contribution. The latter component is not necessarily viscosity dependent. Here the amplitude of the ultrafast GCD of the correlation function was taken to vary exponentially with temperature through the characteristic time τ_0. This functional dependence was chosen on purely phenomenological grounds and also for its simplicity. However the experimental data can also be described with other non-linear functional dependencies with sufficient accuracy.

Summarizing the discussion on the temperature dependent parameters, all the BO parameters that vary with temperature, do so in a manner that is consistent with the physical origin of the modes that they describe. However, the additional variation of the decay time of the fastest mode is required to match all simulation with all experiments consistently.

Upon comparing the time-integrated and the time-resolved photon echo experiments, the fact that the temperature dependence of 3PEPS data at 210 fs shows no evidence of the phase change at 150 K, whereas the HDPE results at the same waiting time do show this transition, is surprising. This is highly unexpected as both experiments are essentially sensitive to the same physical processes and therefore should yield comparable information. Furthermore, the EPS experiment is usually considered as a quick and simple means of obtaining the system dynamics. However, it completely fails to reveal the fundamental structural rearrangement that takes place during the glass transition that is clearly seen in the HDPE experiment at this particular waiting time.

This paradoxical situation can be understood by comparing the analytical expressions for both signals. Here we assume the same bimodal correlation function as used above in equation (3.17). After a Taylor expansion around t_w the relation between the slow part of the correlation function $M'_{slow}(t_w)$ that is sensitive to diffusive solvent dynamics and the echo peakshift function $t_{max}(t_w)$ is expressed as:

$$aM'_{slow}(t_w) = \frac{\Delta\sqrt{\pi}\, t_{max}(t_w)}{1+2\Delta^2 t_{max}^2(t_w)} .$$

(6.16)

Assuming that the high-temperature limit applies and that $\Delta^2 t_{max}^2(t_w) \ll 1$ this can be rewritten as

$$t_{max}(t_w) = \frac{a\, M_{slow}(t_w)}{\Delta\sqrt{\pi}}$$

(6.17)

From here we derive the sensitivity of the EPS position to the balance between fast (homogeneous) and slow (inhomogeneous) modes, i.e. the parameter a:

$$\frac{\delta t_{max}(t_w)}{\delta a} = \frac{M_{slow}(t_w)}{\Delta\sqrt{\pi}} .$$

(6.18)

For the HDPE experiment, the position of the maximum of the time-resolved echo signal with respect to the coherence time $t'_{max}(\tau)$ can be expressed as:

$$t'_{max}(\tau) = M'_{slow}(t_w)\tau - \frac{1-a}{a}\int_0^{t_{max}} M'_{fast}(t_w)\, dt .$$

(6.19)

Similarly to equation (6.18), it follows that:

$$\frac{\delta t'_{max}(\tau)}{\delta a} = \frac{\int_0^\infty M_{fast}(t_w)\, dt}{a^2} ,$$

(6.20)

which serves as a handy indicator of the ratio between the fast and the slow modes.

Now we use equations (6.18) and (6.20) to estimate sensitivity of the 3PEPS and HDPE experiments to the balance between homogeneous and inhomogeneous contributions to the line broadening. Let us suppose that $M'_{slow}(t_w)$ is close to unity as it is the case for waiting times of $t_w = 210$ fs, and $\Delta = 0.05$ PHz (see Table 6.1). Then equation (6.18) yields:

$$\frac{\delta t_{max}}{\delta a} = 10 \text{ fs} \tag{6.21}$$

The integral over the fast mode that enters equation (6.20), can be estimated as approximately equal to the correlation time, i.e. ≥ 100 fs at the temperatures around the glass transition, which results in

$$\frac{\delta t'_{max}}{\delta a} = \frac{100}{a^2} \text{ fs} . \tag{6.22}$$

That is at least a decimal order of magnitude larger than equation (6.21). Therefore, changes in the ratio between the fast and the slow parts of the correlation function do have a much more profound impact on the time resolved HDPE signal as compared to the echo peakshift position. An additional consideration here is that the EPS depends on the amplitude of the environmental fluctuations Δ while the HDPE does not. The absorption spectrum narrows with the decrease of temperature, see Figure 6.1.a, adding to the 3PEPS the systematic temperature offset that masks the dynamics relevant information. In contrast, the HDPE experiment is free of such complications.

The fact that the 3PEPS is directly proportional to the ratio between the fast and slow parts of the correlation function can be used to strengthen the argument that the amplitude of the fast Gaussian mode has a strong temperature dependence. Below the glass temperature, the slow part of the correlation function is close to unity $M'(t_w) \approx 1$ at waiting times of $t_w = 210$ fs because the solvent motion is frozen, the damping of the 150 cm^{-1} vibrational mode is moderate, and not temperature-dependent any longer. Therefore, the 3PEPS function reflects mostly the balance between the relative amplitudes of the fast and slow part of the correlation function (never mind the ~25% changes in the absorption spectrum width).

6.4 Conclusions

In this chapter the effects of temperature on solvation dynamics were studied. The solvent, a glass-forming liquid, was cooled down from room temperature down to 3 K, a temperature range that includes the glass transition of this liquid at 150 K . The solvation dynamics were

studied by measuring the optical dephasing of a coherently excited ensemble of chromophores.

Temperature dependent optical dephasing in condensed matter has been studied several times before by others, but never over a temperature range this wide nor a range including a phase transition. For this reason, in these studies the results could be interpreted by either implicitly or explicitly assuming a SD that was temperature independent. Contrary to the experiments reported here, these studies used time integrated techniques like 2PE, 3PE and 3PEPS to measure the optical polarisation. In this chapter the echo signal was heterodyned using a local oscillator pulse in order to get a better insight in the ratio between fast and slow contributions to the optical dephasing. It is shown that it is not possible to do this with time integrated techniques only.

The 3PEPS results at a waiting time of 210 fs do not show signs of the glass transition because the solvent modes are too slow to have a noticeable effect on the peakshift at that time. This underlines the importance of time resolving the echo signal with a heterodyning field. In the HDPE results at the same waiting time, the glass transition is clearly discernible. This underlines the strengths of this technique; the heterodyned data allow for a much better separation of the contributions of the various modes. The HDPE technique can reveal dynamics that would have gone unnoticed in a time-integrated experiment.

The solvation dynamics of DTTCI in a PD/EtOH mixture can only be described with a temperature dependent SD. This is especially true above the glass transition temperature. The slowing down of molecular motion with decreasing temperature is clearly reflected in the characteristics of the corresponding MBO description. Even below the glass transition, when all solvent motion has vanished the SD is somewhat temperature dependent to make the behaviour of the inertial ultrafast contributions in the MBO-model reflect the experimental behaviour of the optical dephasing.

The description of the ultrafast mode was changed from the Gaussian character used by De Boeij *et al.* to a Gaussian correlation decay that is associated with a SD that linearly goes to zero at small wavelengths. The SD has to approach zero at the shortest wavelengths in this manner in order to have a description that yields reasonable polarisation decays.

Having modelled the correlation function by means of one fast mode, three intramolecular underdamped and four strongly damped solvent modes it is possible to simulate all the experiments, including absorption and emission profiles, at all temperatures with a reasonable degree of accuracy. This was done using a limited and closed set of BO-parameters that vary with temperature in a way that can be reasonably expected considering the physics involved.

From all this it can be concluded that especially time-resolved optical techniques are powerful tools in studying the ins and outs of solvation dynamics. Here it was shown that a

PD/EtOH mixture shows large aberrations from Arrhenius behaviour, and can therefore be considered a fragile liquid. The difficulty in studying solvation dynamics through optical dephasing lies in the precise characterisation of all the contributions to the correlation decay and the subsequent separation of intramolecular modes and solvent modes. The photon echo experiments are also inherently ensemble experiments and therefore not sensitive to the non-ergodic aspects of the glass transition and the solvation dynamics of the super-cooled liquid.

Chapter 7

2D Correlation Spectroscopy

In this chapter the principles of two dimensional (2D) Fourier transform spectroscopy are introduced and applied to the heterodyne detetected photon echo (HDPE) data set of the previous chapter. Visualizing the echo signal along two frequency axis, ω_1 and ω_3, instead of the time resolved representation, is called 2D Fourier transform spectroscopy or correlation spectroscopy. It is shown that even for an ensemble of chromophores that can be described as independent two-level systems representing the data along two correlated frequency axes is feasible and more instructive than the corresponding representation in the time-domain. The 2D peak shapes in the frequency domain yield more intuitive qualitative clues about the evolution of the individual microscopic environments. A new quantitative method for the interpretation of these spectra that is simple and straightforward is derived and applied to the correlation spectra.

7.1 Introduction

In the previous chapter the HDPE data were presented as they were collected. From the resulting time-domain representation of the data, all information regarding the correlation function can be assessed. This evaluation was made by fitting the transient echo profiles with Gaussians and observing the position of the transient echo maximum. However, it is not the only way to read the qualities and deduce the quantities of the correlation function. In nuclear magnetic resonance (NMR) [294,295] and in infrared (IR) spectroscopy [296-302] the data sets are usually represented in the frequency domain that is essentially the

double Fourier transformation (FT) of data along the τ and τ' axis. This allows for easy visual identification of coupled resonance modes by identifying cross-peaks. Furthermore, since the 2D peak shapes are sensitive to the system – bath interactions [303-311], the line shapes are suitable for estimation of the times scales of the bath dynamics that some optical mode (or nuclear spin) is subject to [312]. 2D Fourier transform (FT) electronic spectra can reveal the fluctuations of the electronic energy gap in the same way that 2D NMR follows spins in the so-called COSY (COrrelation SpectroscopY) and NOESY (Nuclear Overhauser Effect SpectroscopY) experiments [313,314].

The main differences between femtosecond optics experiments and pulsed NMR experiments are the sample size and the pulse length. The sample thickness to wave length ratio in optical experiments is ~ 100, whereas it is $\sim 1/100$ in NMR. This allows in the optical case for separation of different contributions to the signal field, by choosing the proper phase matched excitation geometry. Additionally, the pulses used in NMR contain millions of cycles of the electric field, whereas femtosecond pulses often contain just a few oscillations. And during the short optical pulse, nuclei of the system under study are basically captured motionless instead of being motionally averaged.

On the other hand, the dynamics in 2D femtosecond experiments are more complicated than the spin dynamics in 2D NMR. Unlike NMR experiments, the optical experiments can not be generally interpreted in the Bloch framework [55,148,152,153,164,170,177]. Also, in the optical IR domain the separation between coupled resonances is on the order of or sometimes even smaller than the line broadening. This complicates the interpretation of
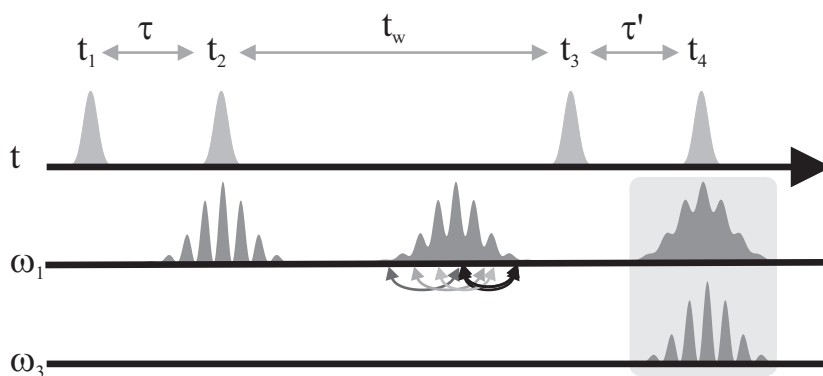
Figure 7.1. Conceptual representation of 2D correlation spectroscopy. The frequency grating created by the first two pulses is overlapped with the grating created by the next two pulses. Due to spectral diffusion the ω_1 grating is washed away during waiting time t_w, diminishing the correlation between the two pairs.

these optical 2D IR spectra with respect to their NMR counterparts. Furthermore, it is challenging to create precise optical $\frac{1}{2}\pi$ optical femtosecond pulses and therefore the femtosecond 2D experiments are usually carried out in the weak pulse limit.

Correlation spectroscopy can be best understood in terms of the grating scattering in frequency space as introduced in Section 3.4 [315]. In a three-pulse echo (3PE) experiment the first pulse creates some population in the excited state of a set of optical two-level systems by coherent excitation, see the upper part of Figure 7.1. A second pulse has the same effect on this ensemble of chromophores and the interference of both excitations leads to a frequency grating in both ground and excited state. The echo signal is then the delayed scattering of a third pulse on this grating after it has freely propagated for some waiting time t_w. In the heterodyne detected photon echo (HDPE) experiment this signal is subsequently mixed with a local oscillator pulse to effectively time-resolve the echo.
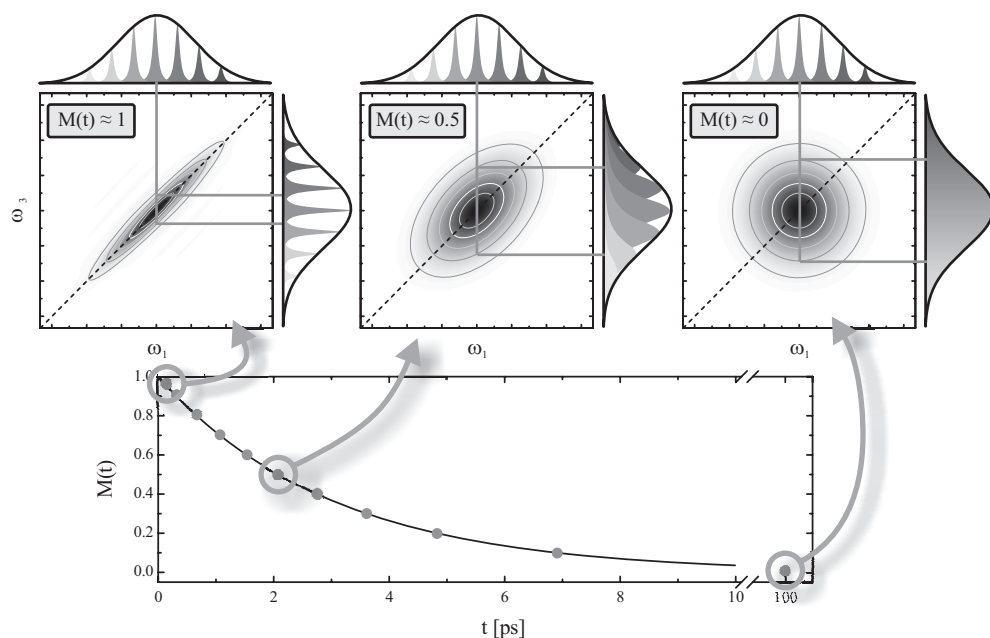
Figure 7.2. As the correlation function $M(t)$ decays the frequency grating written by the first pulse pair is washed out. The second frequency grating can then not be completely matched to second frequency grating anymore and this results in less elliptical and more circular correlation spectra. The exponentially decaying function $M(t)$ is also used as a model correlation function in the simulations of the time-resolved echo plots depicted in Figure 7.3.

Another way of looking at the HDPE is as an experiment in which two frequency gratings, created by two pulse pairs, are correlated to each other. This is illustrated in the lower two diagrams of Figure 7.1. Pulses 1 and 2 create a frequency grating that is overlapped by the modulation caused by pulse 3 and 4. The amount of overlap is determined by the extent of memory loss and dissipation in the period t_w between the two pulse pairs and it sets the properties of the resulting heterodyne.

Interpretation of the 2D correlation spectrum (CS) is illustrated in Figure 7.2. At short waiting times no memory loss has occurred as the transition frequencies of all chromophores are perfectly static (the case of inhomogeneous broadening). In other words, the chromophores excited with a certain frequency ω_1 retain ("remember") this frequency during the whole waiting time period. Therefore the resulting peak shape will be an almost straight diagonal line along $\omega_1 = \omega_3$. At the other extreme, a complete memory loss will have occurred when the two gratings are overlapped (the case of totally homogeneous broadening). In this limit, all frequencies on the axis associated with the first pulse pair (ω_1) can be correlated to all frequencies on the axis associated with the second pulse pair (ω_3). Therefore the resulting 2D peak shape will be circular. In any intermediate case the peak shape has an elliptic shape. The eccentricity of this ellipse is therefore a measure of the frequency – frequency correlation function associated with the system's transition.

The fact that the diagonal elongation can serve as indication of the ratio between system homogeneity and inhomogeneity has been known for at least a decade. This idea is based on the so-called "projection slice theorem" that links the diagonal Bloch echo, i.e. the light emitted at $\tau' = \tau$, with the anti-diagonal elongation of the CS [316-318]. Amazingly enough, to the best of our knowledge no quantitative relationship between the eccentricity and correlation function has been established so far despite a fair amount of attention to this issue. For instance, the first attempt to numerical characterization was undertaken by Okumura *et al.* [308] who suggested that the ratio between the two frequency slices along the diagonal and anti-diagonal axes of the CS be the measure for the correlation function. In doing so, the authors were only able to distinguish between the two extreme case of pure inhomogeneous and purely homogeneous line broadening. The retrieval of the exact value of the correlation function in intermediate cases proved impossible using this method.

In a further paper by Tokmakoff [319] this issue was elaborated on. The author, following de Boeij *et al.* [177], observed on the limitations of the method conventionally used in nonlinear optical spectroscopy, which is to define a model, calculate the experimental observables, and iteratively adjust the model parameters by comparing the experiment and model calculations. There is little flexibility in this approach to assessing whether the model is appropriate for the system, particularly in the case of phenomenological models. A single experimental observable assigned to the multidimensional pattern that intuitively gives in-

sight into the dynamics of the system would allow for a more direct interpretation of experimental results. An example of such a parameter is, for instance, an echo-peak shift function employed in Chapter 6. Ellipticity of CS could provide precisely such an opportunity as well. Unfortunately, the relationship between the ellipticity of the CS was only presented on a qualitative level.

The most developed theoretical approach to the 2D CS was given by Jonas *et al.* [307,312,315]. In these papers the main emphasis was put at extremely short waiting times as most of the system inhomogeneity was vanished within the first 100 fs. The interpretation of experimental data did involve some detailed analysis, including propagation and corresponding pulse-distortion effects. The rapid loss of the phase memory was most probably connected to the unlucky choice of the chromophore, the dye IR144, which is known for its extremely fast intramolecular dynamics. The selection of the DTTCI dye as was done in the previous Chapter, should allow for obtaining diagonally elongated 2D CS at much longer picosecond delays even at room temperature.

In a similar treatment, Kwac and Cho [320] considered both 2D transient dichroism (that has been discussed above) and 2D transient birefringence (i.e. refractive index modulation). The main emphasis was put on the connection between the correlation function and the slant of the tangential line separating the positive and negative contours in these spectra, that is, the birefringence for optical 2-level systems and dichroism for 3-level systems. It was shown that the correlation function is directly related to the slant of the line separating the positive and negative parts of the spectra. In this manner the authors reproduced the correlation function of a fluctuating transition frequency even though the changes in the slant between both regions were rather small. It should be pointed out, however, that the slant for a 3-level system inherently involves the correlation between the lower and upper transitions that is not necessarily perfect because of the potential anharmonicity. On the other hand, the transient birefringence pattern used for a 2-level system, is more difficult to deal with experimentally as it spans a broader frequency range and does not allow for independent data validation by calculating the so-called marginals (*vide infra*). Interestingly, the ellipticity of the dichroic 2D spectra in 2-level systems largely escaped attention as a possibility for deriving $M(t)$. In addition, the pump-probe configuration [296,299,301] that was considered, inherently excludes derivation of any dynamics at short times.

Finally, Brixter *et al.* [321] have reported on 2D correlation spectra that were used to study excitation transfer in photosynthetic systems. The emphasis in this work was on the position of off-diagonal peaks in the CS, since these are indicative of excitation transfer. The authors were able to accurately model population transfer as a function of time using a simple Frenkel exciton Hamiltonian by analyzing the spectra. It is worth pointing out that the main focus of the present Chapter is not with cross-peaks since these only appear when

the optical transition would be coupled to some other nearby near resonance mode, which is clearly not the case here.

In this Chapter the heterodyne detected photon echo experiments in the time-domain, as presented in Chapter 6, are presented in the frequency domain , i.e. as 2D correlation spectra. It is demonstrated how the 2D Fourier transformation can be carried out, several pitfalls in this process are pointed out and the ways to circumvent them are described. The main result of the chapter is a novel and elegant method for measuring the value of the correlation function $M(t)$ by assessing the eccentricity of the CS elliptic shape. The method is essentially based on measuring the eccentricity ε of the 2D spectrum, and calculating the correlation function value as $M(t_w) = \varepsilon^2/(2 - \varepsilon^2)$. This manner of measuring the dephasing though the eccentricity of the spectra can be intuitively grasped while at the same time it yields quantitative results.

7.2 Theory

The CS is directly related to the 2D time resolved 3PE signal by a double Fourier transformation:

$$S(\omega_3, \omega_1, t_w) \propto \mathrm{Re} \int_0^\infty d\tau' \int_0^\infty d\tau \, S(\tau', \tau, t_w) \exp\left[i\omega_1 \tau + i\omega_3 \tau' \right] \ . \tag{7.1}$$

Here $S(\tau', \tau, t_w)$ is the complete expression for the time resolved 3PE signal.

In order to further demonstrate the principles of obtaining the correlation function from the correlation spectra it is supposed that the high temperature limit (HTL) applies, $k_B T \gg \hbar\Lambda$, to simplify the analysis. When the HTL is valid only one correlation function needs to be considered since in that case $M'(t) = M''(t) \equiv M(t)$. Furthermore it is assumed that the system is characterized by some simple exponentially decaying correlation function $M(t)$. If this function is nearly constant on the time scale of τ and τ' the line shape function can be approximated by a second order Taylor expansion of equation (3.55). This limit, where $M(t) \approx 1$ during the coherence time, is called the diffusion limit. At short times the line broadening function can be approximated as:

$$g(t) \cong \frac{\Delta^2}{2} t^2 \ . \tag{7.2}$$

At longer waiting times the expansion of the function becomes:

$$g(t + t_w) \cong g(t_w) + \Delta^2 t \int_0^{t_w} M(t') \, dt' + \frac{\Delta^2}{2} t^2 M(t_w) \ . \tag{7.3}$$

By calculating the response functions for the rephasing and non-rephasing Liouville pathways the following expression for the echo and virtual signals is found:

$$S\left(\tau',\tau,t_w\right) \propto \exp\left[-\frac{\Delta^2}{2}\left(\tau'^2+\tau^2 \mp 2\,\tau\,\tau'M\left(t_w\right)\right) - i\omega_{eg}\left(\tau' \mp \tau\right)\right] \times$$
$$\left[1 + \exp\left[-i2\lambda\tau'\left(1-M\left(t_w\right)\right)\right]\right]. \tag{7.4}$$

The expression for the correlation spectrum that follows from this echo signal is far more complicated in the case of a non zero Stokes shift, $\lambda \neq 0$, then when the term that includes the reorganization energy λ can be disregarded. That is precisely this case that is, for the sake of clarity, discussed in this section. The former, more general, case is discussed and compared to the situation where $\lambda = 0$ in Appendix 7.6

Setting the Stokes shift to zero yields the following expressions for the echo signals:

$$S\left(\tau',\tau,t_w\right) \propto \exp\left[-\frac{\Delta^2}{2}\left(\tau'^2+\tau^2 \mp 2\,\tau\,\tau'M\left(t_w\right)\right) - i\omega_{eg}\left(\tau' \mp \tau\right)\right]. \tag{7.5}$$

Now, in order to discuss the CS of these two signals this expression needs to be Fourier transformed along both the τ axis and the τ' axis. First the transformation along τ of the expression for the echo signal yields:

$$S\left(\omega_1,\tau',t_w\right) \propto \int_0^\infty d\tau \exp\left[i\omega_1\tau\right]\exp\left[-\frac{\Delta^2}{2}\left(\tau'^2+\tau^2 - 2\,\tau\,\tau'M\left(t_w\right)\right) - i\omega_{eg}\left(\tau' - \tau\right)\right]. \tag{7.6}$$

In order to be able to interpret the spectra intuitively, it is important to separate the purely absorptive contributions to the signal form the dispersive parts. Dealing with only the absorptive part of the signal allows a more intuitive interpretation of 2D patterns. Furthermore, it can be directly compared with pump-probe experiments and absorption spectra, thus providing an independent opportunity for calibration of the results (*vide infra*).

A 2D CS with only absorptive line shapes is obtained by adding the 2D spectra of the echo and the virtual echo [303,322]. The individual rephasing and non-rephasing 2D spectra show a distorted line shape due to the so-called "phase-twist". This twist arises because the 2D FT of a signal evolving with a complex phase in two time periods leads to a combination of absorptive and dispersive features. When the two signals are added in equal weights, the dispersive parts cancel out.

The virtual echo experiment samples the conjugate frequencies with respect to the regular echo experiment and the signal is given by:

$$S\left(\omega_1,\tau',t_w\right) \propto \int_{-\infty}^0 d\tau \exp\left[i\omega_1\tau\right]\exp\left[-\frac{\Delta^2}{2}\left(\tau'^2+\tau^2 + 2\,\tau\,\tau'M\left(t_w\right)\right) - i\omega_{eg}\left(\tau' + \tau\right)\right]. \tag{7.7}$$

These signals are measured in the phase matched directions. The only difference between the two experiments, is the time ordering of the first two pulses. The sum of the signals stemming from both the rephasing and non-rephasing pathways is then:

$$S\left(\omega_1, \tau', t_w\right) \propto \int_{-\infty}^{\infty} d\tau \, \exp\left[i\omega_1\tau\right] \exp\left[-\frac{\Delta^2}{2}\left(\tau'^2 + \tau^2 - 2\tau\tau'M\left(t_w\right)\right) - i\omega_{eg}\left(\tau' - \tau\right)\right]. \qquad (7.8)$$

After a couple of straightforward steps the Fourier transform along the τ' axis can also be taken. This yields the real part of the 2D spectra that corresponds to the absorption
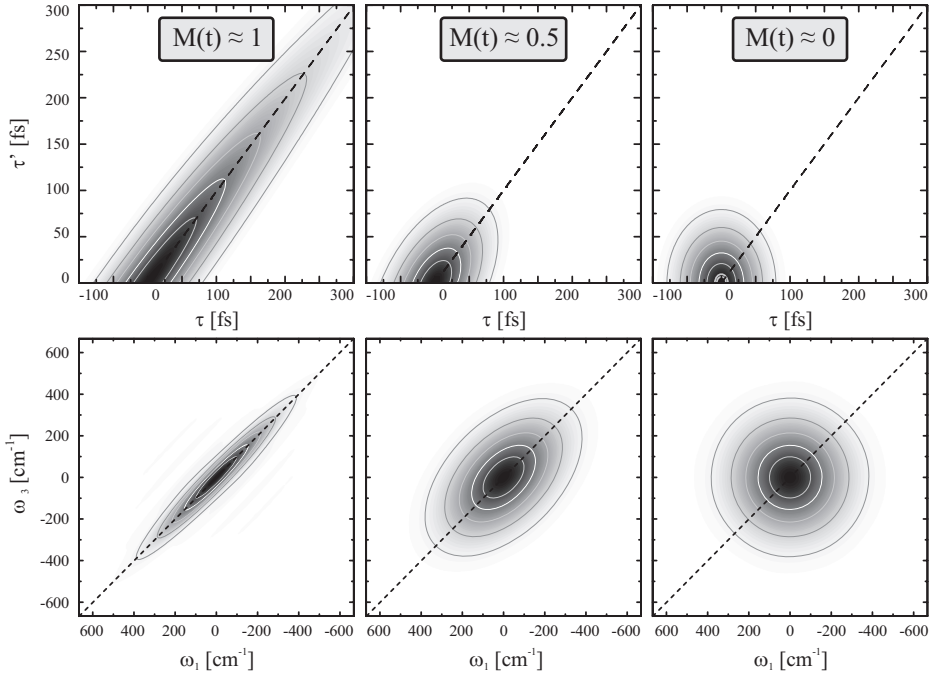
Figure 7.3. Comparison of time-domain and frequency-domain spectra for three stages of dephasing: the static regime, yielding strongly elliptic spectra, the intermediate case and the limit of fast fluctuations, yielding circular spectra. The time-resolved spectra were calculated using the correlation function shown in Figure 7.2 and the CS where retrieved by Fourier transforming these data sets. In turn the correlation function can be retrieved by measuring the eccentricity of the CS that results from these Fourier transformations. The grey dots in the bottom graph of Figure 7.2 are calculated from the major axes of the corresponding CS using equation (7.15) and they match perfectly with the original values of $M\left(t\right)$.

changes:

$$S\left(\omega_1, t_w, \omega_3\right) \propto \exp\left[-\frac{\left(\omega_1 + \omega_{eg}\right)^2}{2\Delta^2}\right] \times$$

$$\int_0^\infty d\tau' \exp\left[-\frac{\Delta^2}{2}\tau'^2\left(1 - M^2\left(t_w\right)\right) + i\left(\omega_3 - \omega_{eg} + \left(\omega_1 + \omega_{eg}\right)M\left(t_w\right)\right)\tau'\right].$$

(7.9)

This in turn leads to the final expression for the 2D CS:

$$S\left(-\omega_1, t_w, \omega_3\right) \propto$$

$$\exp\left[-\frac{\left(\omega_3 - \omega_{eg}\right)^2}{2\Delta^2\left(1 - M^2\left(t_w\right)\right)} - \frac{\left(\omega_1 - \omega_{eg}\right)^2}{2\Delta^2\left(1 - M^2\left(t_w\right)\right)} + \frac{2\left(\omega_3 - \omega_{eg}\right)\left(\omega_1 - \omega_{eg}\right)M\left(t_w\right)}{2\Delta^2\left(1 - M^2\left(t_w\right)\right)}\right].$$

(7.10)

The expression in the argument of the exponent shows that the expected peak shape, or contour shape for a set signal intensity $S\left(\omega_3, -\omega_1\right) = const$, is elliptical.

The eccentricity of the spectra can be used as a measure of the correlation function. The 2D conic section pattern described by the argument in equation (7.10) can be rewritten as:

$$\left(\omega_3 - \omega_{eg}\right)^2 + \left(\omega_1 - \omega_{eg}\right)^2 - 2M\left(t_w\right)\left(\omega_3 - \omega_{eg}\right)\left(\omega_1 - \omega_{eg}\right) =$$

$$-2\Delta^2\left(1 - M^2\left(t_w\right)\right)\ln\left[S\left(\omega_3, \omega_1, t_w\right)\right]$$

(7.11)

The elliptical spectra are oriented along the $\omega_1 = \omega_3$ diagonal axis. Therefore a coordinate rotation is applied to the above expression. Rotating by an angel γ yields:

$$\left(\omega_3 - \omega_{eg}\right)^2\left(1 + M\left(t_w\right)\sin\left[2\gamma\right]\right) + \left(\omega_1 - \omega_{eg}\right)^2\left(1 - M\left(t_w\right)\sin\left[2\gamma\right]\right) +$$

$$2M\left(t_w\right)\left(\omega_3 - \omega_{eg}\right)\left(\omega_1 - \omega_{eg}\right)\cos\left[2\gamma\right] = -2\Delta^2\left(1 - M^2\left(t_w\right)\right)\ln\left[S\left(\omega_3, \omega_1, t_w\right)\right]$$

(7.12)

The cross term vanishes if the system is rotated by $45°$ along the coordinates $\{\omega_1, \omega_3\}$ and $\gamma = \pi/4$. Now the major axis of the ellipse is aligned with the ω_3-axis. The ellipse axes are

$$a = \eta\sqrt{1 + M\left(t_w\right)} \text{ and } b = \eta\sqrt{1 - M\left(t_w\right)}.$$

(7.13)

The axis length along the $\omega_1 = \omega_3$ direction is indicated by a and b is the axis length along the orthogonal to that direction. The normalization factor η depends on the signal level. The ellipse eccentricity is defined in terms of the ellipse axis-lengths:

$$\varepsilon = \sqrt{1 - \left(\frac{b}{a}\right)^2} = \sqrt{1 - \frac{1 - M\left(t_w\right)}{1 + M\left(t_w\right)}} = \sqrt{\frac{2M\left(t_w\right)}{1 + M\left(t_w\right)}}.$$

(7.14)

Subsequently, the correlation function can then be rewritten as:

$$M(T) = \frac{\varepsilon^2}{2 - \varepsilon^2} = \frac{a^2 - b^2}{a^2 + b^2}.$$

(7.15)

This fits with the quantitative introduction given above. For very homogeneously broadened absorption spectra, when $M(t) \simeq 0$, the correlation spectra are circular and therefore the eccentricity is very small: $\varepsilon \simeq 0$. In the opposite inhomogeneous case, when the contours are extremely elliptical, then $M(t) \simeq 1$ and $\varepsilon \rightarrow 1$.

In Figure 7.3 the effects of the system – bath fluctuations on the CS shape are illustrated with both the time-domain and the frequency-domain spectra. It shows that at long times, when the correlation function is nearly completely decayed, $M(t) \approx 0$, the two frequency gratings cannot be correlated anymore. The system is homogenous and the CS has a circular shape. At the other extreme, at times short times when $M(t) \approx 1$ the system is still inhomogeneous. The correlation between both gratings is still large and the resulting frequency-domain spectrum has an elliptical shape stretched along the $\omega_1 = \omega_3$ axis.

7.3 Practical Issues

In order to separate the conjugate rephasing and non-rephasing experiments when processing the experimental time-domain data, the echo signal $S_R(\omega_3, \tau, t_w)$ for $\tau > 0$, and the virtual echo signal $S_{NR}(\omega_3, \tau, t_w)$ for $\tau < 0$, are Fourier transformed independently along the τ'-axis. The two Fourier integrals are

$$S_R(\omega_3, \tau, t_w) \propto \int_{-\infty}^{\infty} d\tau' \, S(\tau', \tau > 0, t_w) \cos\left[\omega_3 \tau' + \omega_{eg} \tau\right] \tag{7.16}$$

and

$$S_{NR}(\omega_3, \tau, t_w) \propto \int_{-\infty}^{\infty} d\tau' \, S(\tau', \tau < 0, t_w) \cos\left[\omega_3 \tau' + \omega_{eg} \tau\right]. \tag{7.17}$$

These two integrals provide the two contributions that can be added up to give rise to a spectrum with only purely absorptive features.

There are two practical issues to consider when analyzing the experimental results. The first concerns the next step that is performed in the analysis of the experimental results. This is the cosine Fourier transformation along the τ-axis. The scanning step in the HDPE experiments along the τ-axis is typically 2 to 5 fs. Therefore, as there is no interferometric scanning over this axis, the ω_{eg} frequency is not automatically recorded and has to be introduced artificially into the transformation in the equations (7.16) and (7.17).

As can be seen in the full expression of $P^{(3)}(\tau, t_w, \tau')$ in equation (3.40), the contributions from $R_A(t_1, t_2, t_3)$ and $R_B(t_1, t_2, t_3)$, resulting from the rephasing Liouville pathways A and B (see Figure 3.3), to the third-order polarization have conjugate frequencies with respect to the contributions from the non-rephasing parts $R_C(t_1, t_2, t_3)$ and $R_D(t_1, t_2, t_3)$. If these two contributions are Fourier transformed individually, the peaks in the spectral representation appear in the conjugate quadrants $(\mp\omega_1 \pm \omega_3)$ and $(\pm\omega_1 \mp \omega_3)$ of the Fourier plane respectively [303,322].

However, if the ω_{eg} frequency is not introduced artificially in this case, the traces resulting from the transformations in the ω_1 and $-\omega_1$ quadrants of the Fourier plane overlap, which is confusing. So some arbitrary finite value is assigned to ω_{eg} in these two equations and the FT is performed yielding:

$$\tilde{S}(\omega_3, \omega_1, t_w) \propto \int_{-\infty}^{\infty} d\tau \, \mathrm{Re}\left[S_R(\omega_3, \tau, t_w) + S_{NR}(\omega_3, \tau, t_w) \right] \cos\left[\omega_1 \tau \right]. \tag{7.18}$$

After this, the artificially added frequency ω_{eg} needs to be removed again to shift ω_1 back to zero:

$$S(\omega_3, \omega_1, t_w) = \tilde{S}(\omega_3, \omega_1 - \omega_{eg}, t_w). \tag{7.19}$$

The principle is illustrated in Figure 7.4 for three artificial values of ω_{eg}. If this frequency is large enough the two peaks are completely separated after the second Fourier transformation step and the signal, which is the sum of the rephasing and non-rephasing contributions, can be analyzed after subtracting ω_{eg} again.

The second issue concerns the equal weighing of the absorptive and dispersive parts of
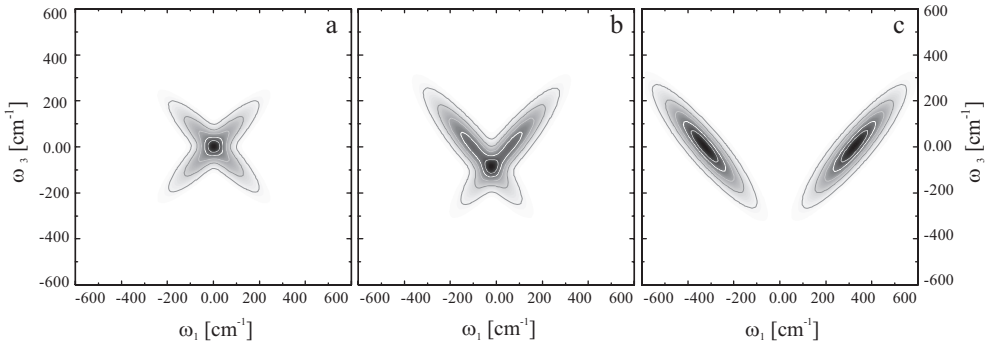

Figure 7.4. CS peak shapes obtained by: a) not adding an artificial ω_{eg} frequency, resulting in full overlap of the peaks in the ω_1 and $-\omega_1$ quadrants of the Fourier plane, b) adding a small ω_{eg}, resulting in partial overlap, c) adding a sufficiently large ω_{eg} to achieve full separation of both parts of the CS.

the signal. If these two contributions are unequally weighted, the spectra have a mixed-phase character. This is reflected by tilted 2D shapes. Small experimental uncertainties in the timing of the excitation pulses can lead to unequal weighing of the rephasing and non-rephasing pathways. Equations (7.16) and (7.17) show that if the zero along the τ-axis that is used in the analysis is not coincident with the actual zero-time, this leads to overestimating either the rephasing or non-rephasing signal.

This is demonstrated in Figure 7.5. The time resolved spectrum in the middle panel of Figure 7.3, $M(t) = 0.5$, is reproduced in the spectral representation with the timing used in the separation of S_R and S_{NR} deliberately misplaced compared to the origin of the τ-axis. The left panel was calculated with a -5 fs offset, the middle panel is the correct CS, and the right panel was calculated wit a 5 fs offset. The left and right spectra have a mixed-phase character. The spectra do not have purely absorptive features, but also contain contributions form the dispersive part of the response function. This results in spectra that have contours that are tilted off the diagonal axes, the so-called phase twist. The amount of phase twist can be quantified by comparing the marginals of the spectra, which is the signal integrated along either axis. This is done in the bottom panels of Figure 7.5. It is clear that in the left and right panel these marginals have strongly differing shapes, and when the timing is right they are identical.

Some degree of phase twist can be inherent to a 2D CS. For example, in multilevel vibrational systems the number of rephasing and non-rephasing Liouville pathways is not the same. This asymmetry results in cross peaks that are tilted with respect to the diagonal peaks in 2D IR vibrational correlation spectroscopy [297,298,300,301].

However, spectra of independent two level systems do not exhibit this inherent asymmetry. Therefore, as a check of the pulse timing when processing experimental time-resolved data, it is possible to compare the marginals of the resulting spectrum. Integrating equation (7.10) along for instance the ω_1 axis yields:

$$S_{mg}(\omega_3) \propto \int d\omega_1 \, S(\omega_3, \omega_1, t_w) = \exp\left[-\frac{(\omega_3 - \omega_{eg})^2}{2\Delta^2}\right]. \tag{7.20}$$

This has no dependence on the correlation function and is equal, as expected, to the absorption spectrum:

$$S_{abs}(\omega) \propto \mathrm{Re}\left[\int dt \exp\left[i(\omega - \omega_{eg})\,t - g(t)\right]\right] = \exp\left[-\frac{(\omega - \omega_{eg})^2}{2\Delta^2}\right]. \tag{7.21}$$

Since both marginals should have the same absorptive shape, they can be used to check if the separation between the dispersive imaginary part of the response function and the absorptive real part is complete. To allow for the experimental uncertainty of the exact values of the times τ and τ' small adjustments, within 5 fs, of both times are allowed. By comparing both marginals until the best coincidence is reached, the exact pulse timing is retrieved. This procedure can also be used to account – at least in part – for the effects of finite pulse durations.

On a final note: no triangular or other filtering has been applied in the Fourier transformations, as it was found to affect the low temperature data where the inhomogeneity is strong and because the baseline was subtracted from the time dependent data in the first place.
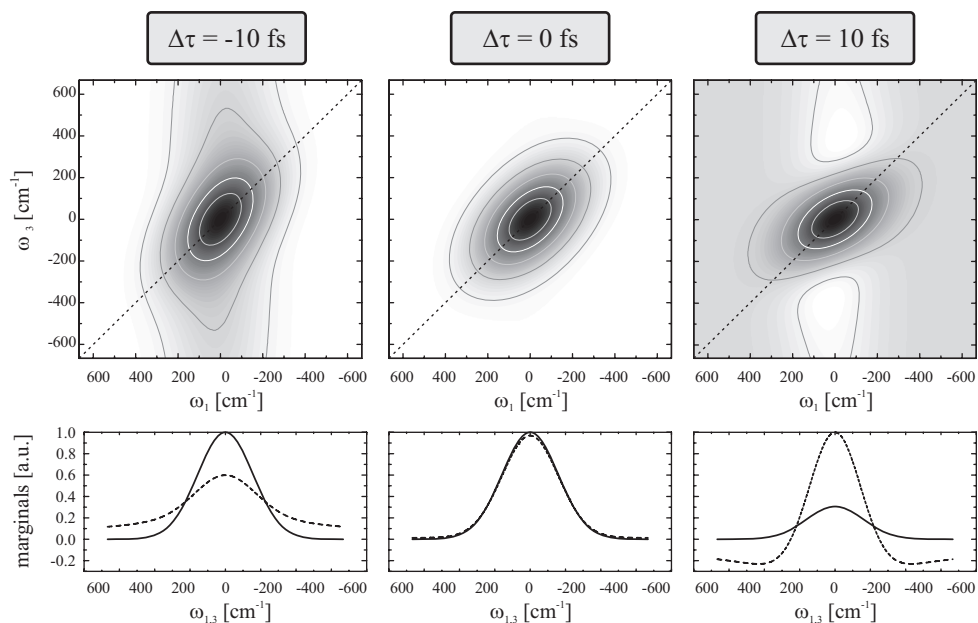
Figure 7.5. The effects of unequal balancing of the rephasing and non-rephasing pathways due to uncertainties in the pulse timings to the shape of a CS. The top panels show the phase twisted spectra with an experimental off-set of the coherence time τ. The bottom panels show the marginals of these spectra. The marginals along the ω_3 axis are indicated by a dashed line.

7.4 Results

Figure 7.6 shows a model correlation function (solid curve) for which the corresponding 2D spectra (insets) were calculated using the complete expressions as in Chapter 6. The values of the correlation function at these times, derived according to equation (7.15), are indicated by the black circles. Obviously, equation (7.15) produces excellent results (with the exception of short times) which fully justify the assumptions made upon its derivation.

In the more general case with the Stokes shift included, the equilateral contours turn into a sum of two ellipses with their centers shifted along the ω_3-axis by the momentarily value of the Stokes shift (Figure 7.6, the upper right inset). Interestingly enough, equation (7.15) again produces acceptable results (open circles). The largest deviations appear at intermediate times, but the error does never exceed 5%. The reason for that is that at short times the Stokes shift has not developed yet, while for the long times the CS – although elongated –
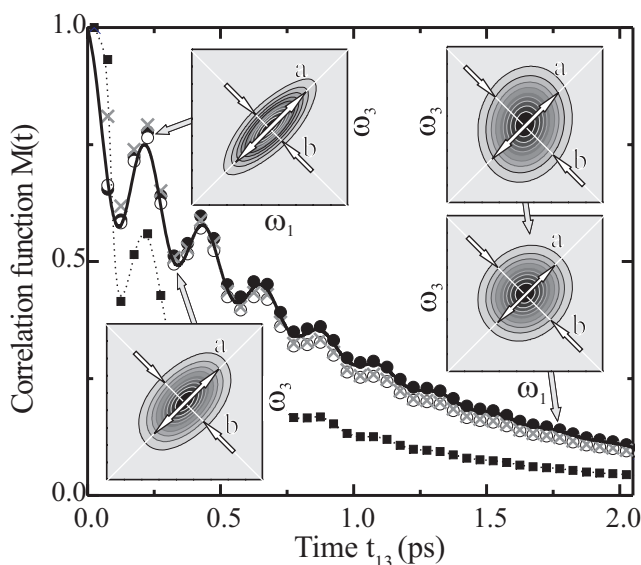
Figure 7.6. Full scale calculations of correlation spectra, based on a realistic correlation function $M(t)$ (solid line). The data points indicate the value of $M(t)$ recalculated form the shape of the spectra using equation (7.15) with no Stokes shift (solid circles), with Stokes shift (open symbols), for finite pulses with the spectrum equal to the system absorption before (black squares) and after normalization (crosses). The latter points shows that this method yields accurate results as the crosses coincide perfectly with the original correlation function.

still possesses equal cross-section along the diagonal and antidiagonal directions.

Finally, in the case of finite pulse durations, when the excitation spectrum does not overlap the complete absorption spectrum, equation (7.15) consistently generates underestimated values (Figure 7.6, squares). This originates from the fact that the ω_1 and ω_3-projections of the CS are related to a product of the pulse spectrum and inhomogeneous and homogeneous contributions to the absorption spectrum, respectively. As the inhomogeneous contribution exceeds the homogeneous one, the length of the a-axes is depreciated which results in lower values of $M(t)$. However, after normalization of the CS along both axes to the pulse spectrum, know in NMR as deconvolution [323], the correct values of the correlation function are retrieved (Figure 7.6, crosses). In time-domain experiments finite pulse duration effects would indeed require deconvolution of the time-resolved signal with the temporal pulse profile. In practice this is much more difficult to accomplish then the above normalization procedure, illustrating the advantages of the frequency domain representation.

Figure 7.7 shows the experimental correlation spectra at several waiting times at 300 K. This is essentially the same data set as in Figure 6.6. The increasing homogeneity of the system with time is clearly visible. The elliptical peak shape at a waiting time of 215 fs indicates substantial inhomogeneity as the waiting time is still too short for any major dephasing to have taken place. Only the fast intramolecular mode and the inertial solvent mode contribute to the width of the ellipse at this time. The 215 fs waiting time is also the first recurrence of the main slow vibrational mode. At this time the coherently excited wave packet returns to its initial position, adding to the inhomogeneous character of the system. At 310 fs this wave packet is at the far point of its oscillation period. This can be seen by the circular character of the corresponding CS. Subsequently when it rephases for the second time at 420 fs, most of the inhomogeneity is returned again, as is obvious form the shape of this CS.

At 1 ps, the slow modes that make up the wave packet are completely decayed and the homogeneous character of the CS is evident. Finally, at 100 ps the peak shape is nearly circular indicating that the correlation function nearly completely decayed and the transition is homogeneously broadened.

As it was described in the previous section, the marginals of the 2D spectra, i.e. the respective projections along the ω_1 / ω_3 axis, serve as independent checks of data validity. In Figure 7.8 the product of the excitation spectrum and the absorption spectrum is compared to the marginals along both axes of the experimental and the simulated CS. The marginals of the spectra reflect the absorption spectrum very well.
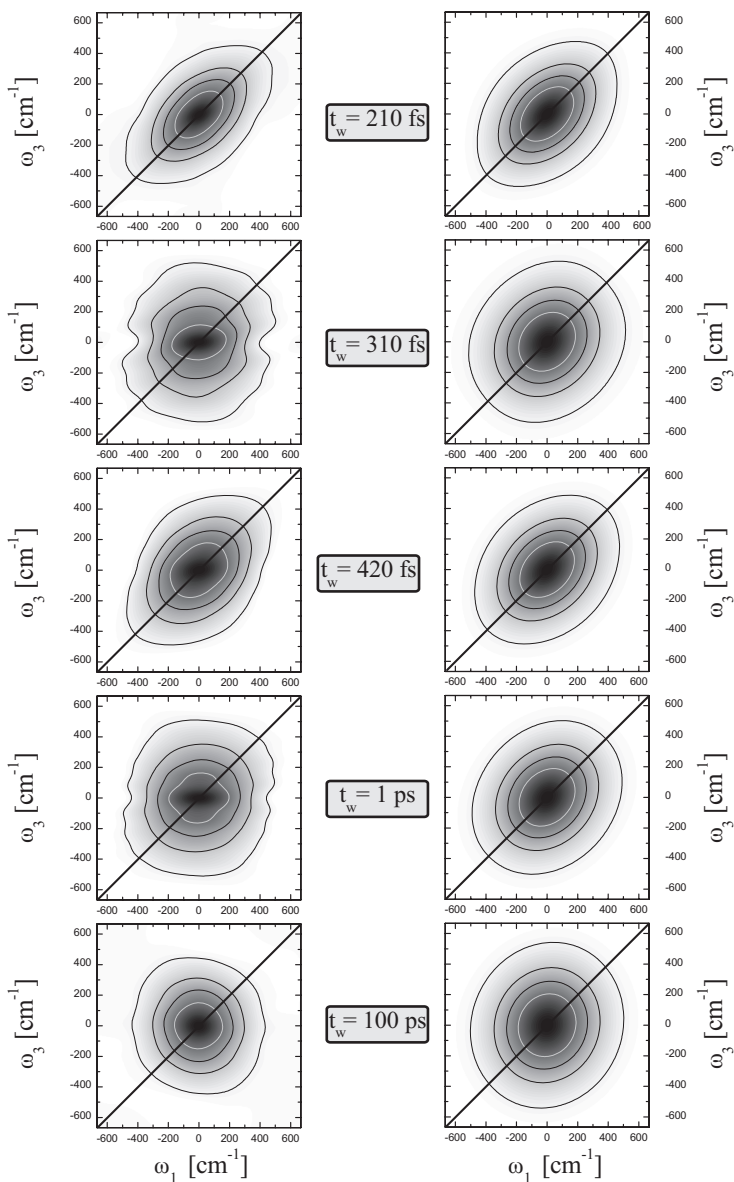
Figure 7.7. The correlation spectra of DTTCI in an EtOH/PD mixture at 300 K at various waiting times t_w. The panels on the left show the experimental data and the right hand panels depict the corresponding simulations. The dephasing trend is clearly visible from the changing shape of the contours of the spectra.
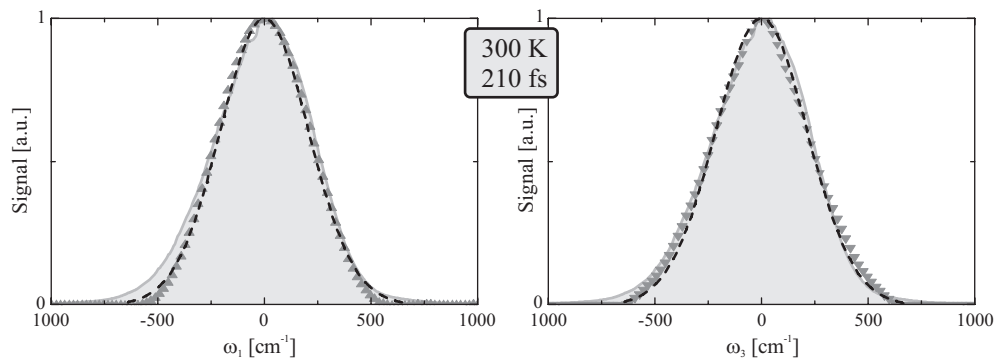
Figure 7.8. The marginals of both the experimental CS (triangles) and the simulated CS (dashed line) at a waiting time of 215 fs and at 300K compare well to each other and to the product of the excitation pulse spectrum and the absorption spectrum at room temperature (gray curve). The pulse spectrum and the absorption spectrum that were used to generate this product are depicted in Chapter 4.

Only if the excitation pulses have a perfectly Fourier transform limited temporal profile on the part of their spectral bandwidth that overlaps with the chromophores absorption spectrum the marginals will be as wide as this product.

A similar trend as in the waiting time dependent data is discernible in the temperature dependent data presented in Figure 7.9. All data are taken for a waiting time $t_w = 210$ fs where the effects of the intramolecular vibrational modes are minimal. This series of plots brings out the strengths of the frequency domain representation. Details of the system's line broadening can be observed at a glance. The diagonal axes of the various plots for example clearly show that the absorption spectrum narrows with decreasing temperature. At the same time the shortening of the length of the diagonal cross section of the plots at lower temperatures is greatly surpassed by the shrinking of the anti-diagonal axes. Whereas at room temperature the spectra still have a considerable width along the anti-diagonal direction, at 3 K this width is nearly completely determined by the finite pulse length. This illustrates in an intuitive way the transformation from a somewhat homogeneously broadened optical transition to a overwhelmingly inhomogeneously broadened spectrum.

The above qualitative analysis was quantified by measuring the eccentricity of the spectral contours. The contour at half the maximum signal intensity was selected and fitted to a generic parametric equation of an ellipse:
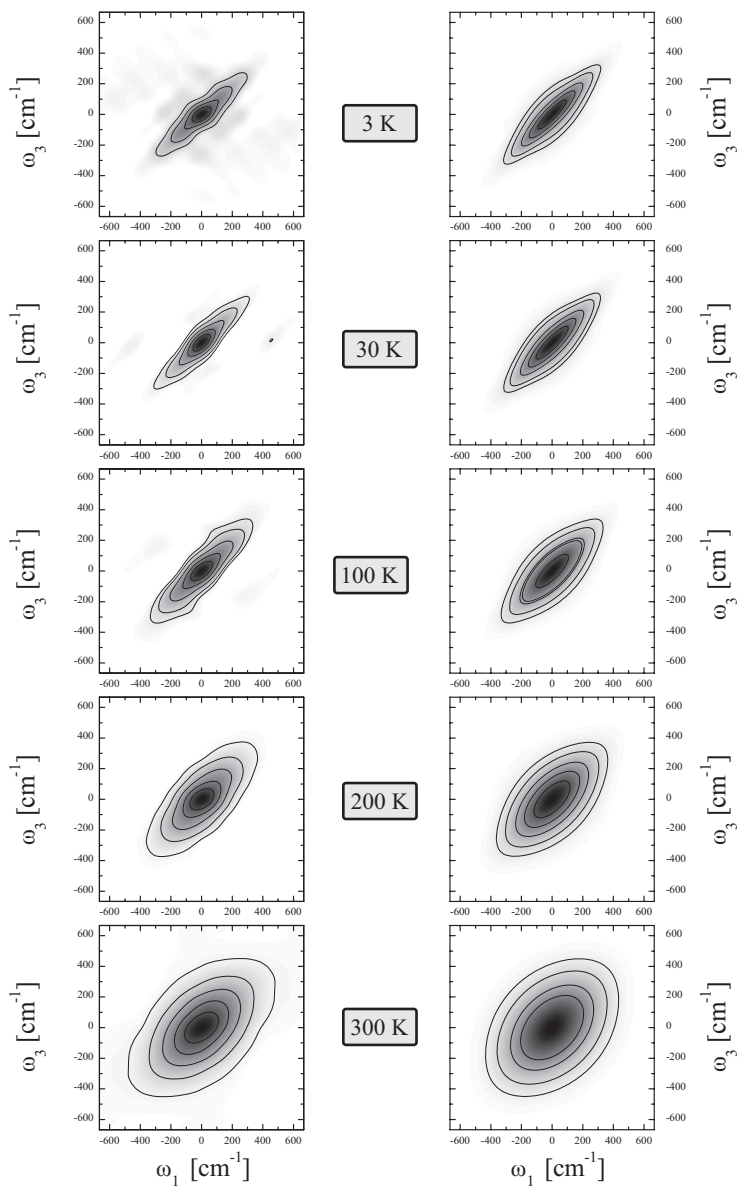
Figure 7.9. The correlation spectra of DTTCI in an EtOH/PD mixture at a waiting time $t_w = 210\ fs$ at various temperatures. The left hand panels show the experimental data and the right hand panels the simulations. The low temperature spectra exhibit strong inhomogeneous character as is reflected by the elliptic shape of the spectra.

$$\frac{\left(\boldsymbol{\omega}_C \cdot \boldsymbol{\omega}_\varphi\right)^2}{a^2} + \frac{\boldsymbol{\omega}_C \cdot \boldsymbol{\omega}_C - \left(\boldsymbol{\omega}_C \cdot \boldsymbol{\omega}_\varphi\right)^2}{b^2} = 1 \,. \tag{7.22}$$

Here $\boldsymbol{\omega}_C = \left\{\omega_1^0, \omega_3^0\right\}$ indicates the centre point of the curve and $\boldsymbol{\omega}_\varphi = \left\{\cos[\varphi], \sin[\varphi]\right\}$ sets the angle φ of the axes of the ellipse. The length of the axes is set by parameters a and b. All parameters were set to vary freely in the fitting procedure. When the best fit to the data
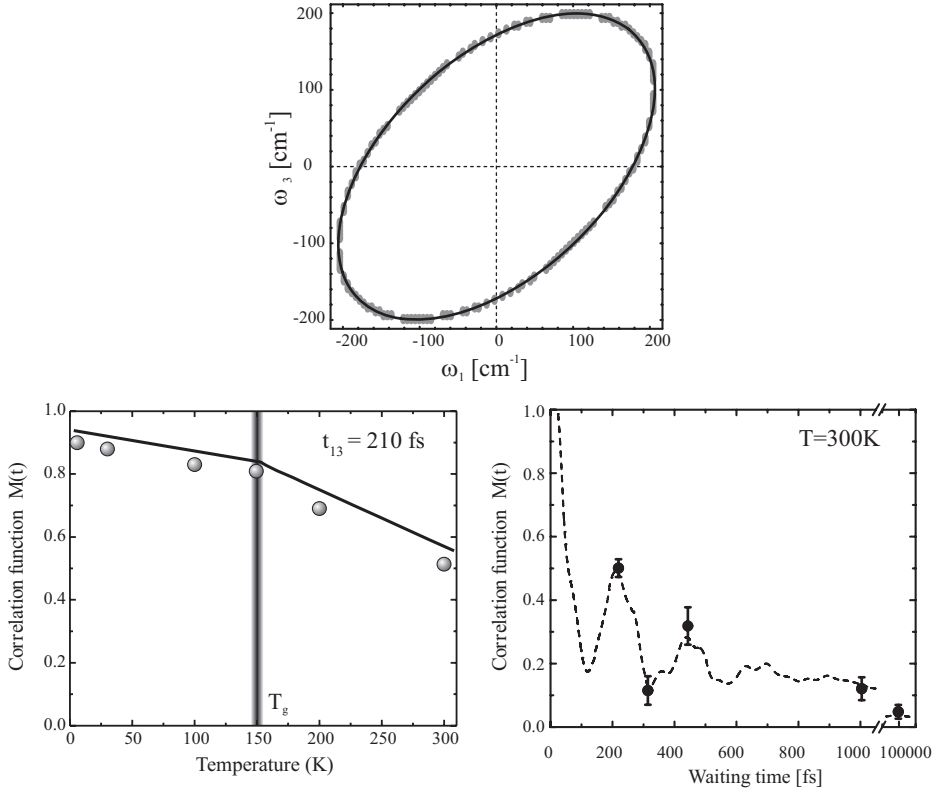
Figure 7.10. The top panel show a typical fit of the ellipse in equation (7.22) to a contour of a CS. This fit (solid line) is to the contour at FWHM of the CS at t_w = 210 fs and 300 K (grey dots). The relative length of the axes of the ellipse are set by the correlation function $M(t)$. The lower panels show the correlation function values for several temperatures at t_w = 210 fs and for several waiting times at 300 K as deduced from the eccentricity of the correlation spectra's of Figures 7.7 and 7.9. The dashed curves show the correlation function $M(t)$ as established in Chapter 6.

was determined for a given set of parameters, the value of the correlation function $M(t)$ was determined using equation (7.15).

Figure 7.10 shows the values of $M(t)$ established from the Figures 7.7 and 7.9. These are compared to the correlation functions as determined from the experiments in Chapter 6. The correspondence between the values as determined through the ellipticity of the ellipse with the previously determined correlation function is excellent.

The retrieval procedure does not seem to be affected by deviations of the 2D CS from a perfect ellipse, which are especially evident at low temperatures Figure 7.9. These distortions are due to side-band features that originate from the most prominent 150 cm^{-1} vibrational mode. This mode is not eluded by the homogeneous broadening that becomes less prominent with the temperature decrease. Note that the steady-state absorption spectrum (Figure 6.6.a) provides no evidence for the existence of such a mode even at 3K.

7.5 Conclusions

In this chapter the time-resolved photon echo data as measured through HDPE experiments is presented in the frequency domain in the same way this is commonly done in NMR and FT IR experiments. This representation is shown to yield more intuitive clues about the dynamics of the system under study than the time domain.

The conversion from the time to the frequency domain involves a straightforward 2D Fourier transformation. By adding the echo signal at negative delays to that at positive times the absorptive part of the signal was retrieved. The absorptive part is much easier to interpret than the dispersive counterpart because an independent calibration of the CS can be performed by comparing the marginals of the CS to the absorption spectrum or to pump-probe spectra. Also by comparing both marginals to each other the precise experimental timing of the excitation pulses can be fine tuned. By equalizing both marginals, spectra can be produced that exhibit no phase twist, i.e. no unequal weighing of the rephasing and non-rephasing parts of the polarization.

It was also shown that there is no need for interferometric scanning of the two delay times τ and τ' in the case of a 2-level system. Even if the carrier frequency of the heterodyne is not recorded along both axes it is still possible to perform the Fourier transformation to obtain a 2D CS.

Next, a novel, simple and quantitative method is presented for measuring the value of the correlation function $M(t)$ by assessing the eccentricity of the CS elliptic shape. The lengths of the major and minor axis of the spectral ellipse are related to the correlation function through a very simple relationship. Strongly inhomogeneous systems exhibit

sharply elliptical spectra whereas homogeneous systems exhibit circular spectra. Therefore the dephasing in the system at a certain time and temperature can be assessed by comparing the both axes. Even though Stokes shifted stimulated emission can potentially complicate the interpretation of the eccentricity of the spectra somewhat, this equation yields accurate quantitative results. More importantly the eccentricity of a spectral elliptic shape can be estimated intuitively and at a glance, thus yielding a clear visual clue about the dynamics of the solvent. The determination of the degree of correlation through this method is independent of the signal intensity. This greatly enhances the accuracy of this method.

2D correlation spectroscopic techniques are sensitive to the same type of dynamics as their time resolved counterparts. Therefore, it is not surprising that correlation spectra derived from HDPE data sets contain no additional information with respect to the time resolved spectra. They do, however, yield a constructive and insightful means of representing the data. The CS allows for an intuitive inspection of the character of the solvent dynamics the system is subject to. Therefore, the arguments given above suggest that it is reasonable to expect that the 2D correlation spectroscopy will find broad application in the study of solvent dynamics. Furthermore, a number of extensions of the proposed idea that are applicable to different systems can be foreseen.

The proposed method can easily be transferred to the pump-probe 2D spectroscopy that might be more practical for systems with slow dynamics [296]. Here the strategy should be the following: first, one takes the diagonal scan with $\omega_1 = \omega_3$, and second, the anti-diagonal scan, that is with $\omega_1 = -\omega_3$. The width of the former contour yields the diagonal length a while width of the latter trace provides the anti-diagonal length b. The correlation function is subsequently calculated according to equation (7.15). This strategy offers a quick and simple way of obtaining the correlation function since only two frequency – frequency scans need to be recorded. However, one should keep in mind that the time resolution in this experiment is somehow compromised.

The established connection between the CS eccentricity and correlation function can also be extended into 3-level systems. This is useful for adequate modeling of, for instance, electronic structure in molecular aggregates or IR vibrational transitions. In this case, along with the *auto*correlation function of the lower transition, the *cross*correlation function of the lower and higher transition is derived directly from a CS. This paves the way to the direct experimental verification of the validity of the linear response approximation that is implicitly used throughout non-linear spectroscopy, i.e. that dynamics at the ground and excited states are identical. As also explained in Chapter 3, this premise implies that both states propagate over time in an identical fashion. Furthermore, such cross correlations can be particularly useful for studying the through-bond correlations such as the symmet-

ric/asymmetric stretching modes in water [324] and through-space correlations of the process of energy transfer in light-harvesting proteins [321] and molecular wires [325].

7.6 Appendix

The complete expression for the correlation spectrum, including a Stokes-shift, is more complicated than the expressions introduced in section 7.2. Including a reorganization energy in the calculation of the response functions for the rephasing and non-rephasing Liouville pathways yields the following expression for the echo and virtual:

$$S(\tau, t_w, \tau') \propto \exp\left[-\frac{\Delta^2}{2}\left(\tau'^2 + \tau^2 \mp 2\tau\tau' M(t_w)\right) - i\omega_{eg}\left(\tau \mp \tau'\right)\right] \times$$
$$\left[1 + \exp\left[-i2\lambda\tau'\left(1 - M(t_w)\right)\right]\right]. \tag{7.23}$$

This expression is first Fourier transformed along the coherence time τ axis:

$$S(\omega_1, t_w, \tau') \propto \int d\tau \exp[i\omega_1\tau] \exp\left[-\frac{\Delta^2}{2}\left(\tau'^2 + \tau^2 \mp 2\tau\tau' M(t_w)\right) - i\omega_{eg}\left(\tau' \mp \tau\right)\right] \times$$
$$\left[1 + \exp\left[-i2\lambda\tau'\left(1 - M(t_w)\right)\right]\right]. \tag{7.24}$$

This can be rewritten as

$$S(\omega_1, t_w, \tau') \propto \exp\left[\frac{\left(i\left(\omega_1 \pm \omega_{eg}\right) \pm \Delta^2\tau' M(t_w)\right)^2}{2\Delta^2} - \frac{\Delta^2\tau'^2}{2} - i\omega_{eg}\tau'\right] \times$$
$$\left[1 + \exp\left[-i2\lambda\tau'\left(1 - M(t_w)\right)\right]\right], \tag{7.25}$$

and subsequently as

$$S(\omega_1, t_w, \tau') \propto \left[1 + \exp\left[-i2\lambda\tau'\left(1 - M(t_w)\right)\right]\right] \times$$
$$\exp\left[-\frac{\left(\omega_1 \pm \omega_{eg}\right)^2}{2\Delta^2} \pm i\left(\omega_1 \pm \omega_{eg}\right)\tau' M(t_w) - \frac{\Delta^2\tau'^2}{2}\left(1 - M^2(t_w)\right) - i\omega_{eg}\tau'\right]. \tag{7.26}$$

Next, the Fourier transformation along the second coherence time, τ', is performed:

$$\text{Re}\big[S(\omega_1, t_w, \omega_3) \big] \propto \exp\left[-\frac{(\omega_1 - \omega_{eg})^2}{2\Delta^2} \right] \int d\tau' \, \exp\big[i(\omega_3 - \omega_{eg})\tau' \big] \times$$

$$\Big[1 + \exp\big[-i2\lambda\tau'(1 - M(t_w)) \big] \Big] \exp\left[\pm i(\omega_1 - \omega_{eg})\tau' M(t_w) - \frac{\Delta^2 \tau'^2}{2}(1 - M^2(t_w)) \right]. \tag{7.27}$$

Here the rephasing and the non-rephasing contributions are already combined to generate the expression for the absorptive part of the signal. Only the positive frequencies are retained. This can be rewritten as:

$$\text{Re}\big[S(\omega_1, t_w, \omega_3) \big] \propto \exp\left[-\frac{(\omega_1 - \omega_{eg})^2}{2\Delta^2} - \frac{\big[(\omega_3 - \omega_{eg}) + M(t_w)(\omega_1 - \omega_{eg}) \big]^2}{2\Delta^2(1 - M^2(t_w))} \right] +$$

$$\exp\left[-\frac{(\omega_1 - \omega_{eg})^2}{2\Delta^2} - \frac{\big[(\omega_3 - \omega_{eg} - 2\lambda(1 - M(t_w))) + M(t_w)(\omega_1 - \omega_{eg}) \big]^2}{2\Delta^2(1 - M^2(t_w))} \right], \tag{7.28}$$

and then as:

$$\text{Re}\big[S(\omega_1, t_w, \omega_3) \big] \propto \exp\left[-\frac{\tilde{\omega}_1^2 + \tilde{\omega}_3^2 - 2M(t_w)\tilde{\omega}_1 \tilde{\omega}_3}{2\Delta^2(1 - M^2(t_w))} \right] +$$

$$\exp\left[-\frac{\tilde{\omega}_1^2 + \big(\tilde{\omega}_3 - 2\lambda(1 - M(t_w))\big)^2 - 2M(t_w)\big(\tilde{\omega}_3 - 2\lambda(1 - M(t_w))\big)\tilde{\omega}_1}{2\Delta^2(1 - M^2(t_w))} \right], \tag{7.29}$$

with $\tilde{\omega}_i = (\omega_i - \omega_{eg})$. The signal is therefore represented by two, possibly overlapping, ellipses. This can be seen by looking at the marginals. The projection onto the ω_1-axis by integration over excitation frequency ω_3 gives

$$\text{Re}\big[S(\omega_1, t_w) \big] = \int d\omega_3 \, \text{Re}\big[S(\omega_1, t_w, \omega_3) \big]$$

$$= \exp\left[-\frac{\tilde{\omega}_1^2}{2\Delta^2} \right]. \tag{7.30}$$

The other marginal is found after a projection onto the ω_3-axis by integration over excitation frequency ω_1:

$$\text{Re}\big[S(t_w, \omega_3) \big] = \int d\omega_1 \, \text{Re}\big[S(\omega_1, t_w, \omega_3) \big]$$

$$= \exp\left[-\frac{\tilde{\omega}_3^2}{2\Delta^2} \right] + \exp\left[-\frac{(\tilde{\omega}_3 - 2\lambda(1 - M(t_w)))^2}{2\Delta^2} \right]. \tag{7.31}$$

This marginal is characterized by an absorption profile as the other marginal plus a transient emission profile. For long waiting times, when $M(t_w) \approx 0$, the emission is Stokes-shifted to $\tilde{\omega}_3 - 2\lambda$, as expected.

For intermediate waiting times it is instructive to shift the excitation frequency ω_3 to the position in between the absorption and the transient emission, $\omega_3 \rightarrow \omega_3 + \lambda(1 - M(T))$. This gives:

$$\text{Re}\left[S(\omega_1, t_w, \omega_3)\right] \propto$$

$$\exp\left[-\frac{\tilde{\omega}_1^2 + \left(\tilde{\omega}_3 + \lambda\left(1 - M(t_w)\right)\right)^2 - 2\tilde{\omega}_1 M(t_w)\left(\tilde{\omega}_3 + \lambda\left(1 - M(t_w)\right)\right)}{2\Delta^2\left(1 - M^2(t_w)\right)}\right] + $$

$$\exp\left[-\frac{\tilde{\omega}_1^2 + \left(\tilde{\omega}_3 - \lambda\left(1 - M(t_w)\right)\right)^2 - 2\tilde{\omega}_1 M(t_w)\left(\tilde{\omega}_3 - \lambda\left(1 - M(t_w)\right)\right)}{2\Delta^2\left(1 - M^2(t_w)\right)}\right]. \tag{7.32}$$

First, for the sake of argument, the hypothetical case of zero Stokes shift, when $\lambda = 0$, is considered. Then signal reads as conic section:

$$\text{Re}\left[S(\omega_1, T, \omega_3)\right] \propto \exp\left[-\frac{\tilde{\omega}_1^2 + \tilde{\omega}_3^2 - 2\tilde{\omega}_1\tilde{\omega}_3 M(t_w)}{2\Delta^2\left(1 - M^2(t_w)\right)}\right]. \tag{7.33}$$

Its equilateral contours are ellipses tilted by $45°$:

$$\tilde{\omega}_1^2 + \tilde{\omega}_3^2 - 2\tilde{\omega}_1\tilde{\omega}_3 M(t_w) \propto -2\Delta^2\left(1 - M^2(t_w)\right) \cdot \ln\left[\text{Re}\left[S(\omega_1, t_w, \omega_3)\right]\right]. \tag{7.34}$$

The ellipse axes are $a = \eta\sqrt{1 + M(T)}$ along the $\omega_1 = \omega_3$ direction, and $b = \eta\sqrt{1 - M(T)}$ along the orthogonal to $\omega_1 = \omega_3$ direction. Here η is a normalization factor that depends on the signal level. The correlation function can now be readily calculated as:

$$M(T) = \frac{a^2 - b^2}{a^2 + b^2} = \frac{\varepsilon^2}{2 - \varepsilon^2}, \tag{7.35}$$

Where, as before in section 7.2, ε is the ellipse eccentricity.

In the more general case of $\lambda \neq 0$ the equilateral contours are not simple ellipses any longer as follows from equation (7.32) because the appearance of the spectrally shifted emission. In this case in fact, the signal can be represented by a sum of two ellipses with their respective centres shifted by the value of the momentarily Stokes shift.

The above proposed scenario however, can still be applied in this case to equation (7.32). This approach then still gives the right result regarding to the value of the correlation function. To demonstrate this, we apply a $45°$ axis rotation to equation (7.32). This implies that $\tilde{\omega}_1' = \frac{1}{\sqrt{2}}\left(\tilde{\omega}_1 + \tilde{\omega}_3\right)$ and $\tilde{\omega}_3' = \frac{1}{\sqrt{2}}\left(\tilde{\omega}_1 - \tilde{\omega}_3\right)$. This substitution yields:

$$\mathrm{Re}\Big[S\big(\omega_1,t_w,\omega_3\big)\Big] \propto \exp\left[-\frac{\left[\tilde{\omega}_1'+\frac{\lambda}{\sqrt{2}}\big(1-M\big(t_w\big)\big)\right]^2}{2\Delta^2\big(1+M\big(t_w\big)\big)}-\frac{\left[\tilde{\omega}_3'-\frac{\lambda}{\sqrt{2}}\big(1-M\big(t_w\big)\big)\right]^2}{2\Delta^2\big(1-M\big(t_w\big)\big)}\right]$$

$$+\exp\left[-\frac{\left[\tilde{\omega}_1'-\frac{\lambda}{\sqrt{2}}\big(1-M\big(t_w\big)\big)\right]^2}{2\Delta^2\big(1+M\big(t_w\big)\big)}-\frac{\left[\tilde{\omega}_3'+\frac{\lambda}{\sqrt{2}}\big(1-M\big(t_w\big)\big)\right]^2}{2\Delta^2\big(1-M\big(t_w\big)\big)}\right].$$

(7.36)

Here the irrelevant normalization factor of $\exp[-\big(\lambda^2/2\big)\big(1-M\big(t_w\big)\big)^2]$ was omitted.

Next the axes lengths are calculated along the new coordinates and it is shown that equation (7.35) is still valid. The axes at a given signal level $\mathrm{Re}\Big[S^0\big(\omega_1,\tau',\omega_3\big)\Big]$ can be calculated from the following equations:

$$\mathrm{Re}\Big[S^0\big(\omega_1,t_w,\omega_3\big)\Big] = \exp\left[-\frac{\lambda^2}{4\Delta^2}\big(1-M\big(t_w\big)\big)\right]\times$$

$$\left(\exp\left[-\frac{\left[a+\frac{\lambda}{\sqrt{2}}\big(1-M\big(t_w\big)\big)\right]^2}{2\Delta^2\big(1+M\big(t_w\big)\big)}\right]+\exp\left[-\frac{\left[a-\frac{\lambda}{\sqrt{2}}\big(1-M\big(t_w\big)\big)\right]^2}{2\Delta^2\big(1+M\big(t_w\big)\big)}\right]\right),$$

(7.37)

and

$$\mathrm{Re}\Big[S^0\big(\omega_1,T,\omega_3\big)\Big] = \exp\left[-\frac{\lambda^2}{4\Delta^2}\frac{\big(1-M\big(t_w\big)\big)^2}{\big(1+M\big(t_w\big)\big)}\right]\times$$

$$\left(\exp\left[-\frac{\left[b-\frac{\lambda}{\sqrt{2}}\big(1-M\big(t_w\big)\big)\right]^2}{2\Delta^2\big(1-M\big(t_w\big)\big)}\right]+\exp\left[-\frac{\left[b+\frac{\lambda}{\sqrt{2}}\big(1-M\big(t_w\big)\big)\right]^2}{2\Delta^2\big(1-M\big(t_w\big)\big)}\right]\right).$$

(7.38)

This can be approximated as:

$$a \approx \eta\big(1+M\big(t_w\big)\big)\left[1+\frac{\lambda^2}{4\Delta^2}\big(1-M\big(t_w\big)\big)^3\right],$$

(7.39)

and also

$$b \approx \eta\left(1 - M\left(t_w\right)\right)\left[1 + \frac{\lambda^2}{4\Delta^2}\left(1 - M\left(t_w\right)\right)\right]. \qquad (7.40)$$

This can be combined as:

$$\frac{a^2 - b^2}{a^2 + b^2} \approx M\left(t_w\right)\left[1 - \frac{\lambda^2}{2\Delta^2}\left(1 - M\left(t_w\right)\right)^2\right]. \qquad (7.41)$$

This resembles the expression for the case that $\lambda = 0$, and it is actually nearly equal to the correlation function with a high degree of accuracy, considering the fact that the largest deviations occur at the point where $M\left(t_w\right) = 0.25$. For typical widths of absorption spectra and typical reorganization energies the last term in equation (7.41) is quite small:

$$\frac{\lambda^2}{2\Delta^2}\left(1 - M\left(t_w\right)\right)^2 \leq 0.1. \qquad (7.42)$$

The reason that the Stokes shift perturbs the effectiveness of equation (7.35) very little, is that the Stokes shift is connected to the transition broadening via the fluctuation-dissipation theorem [55,125]. At short waiting times when the system is primarily inhomogeneously broadened, the Stokes shift has not been developed yet. Therefore, the 2D contour is not substantially distorted. At long waiting times, the Stokes shift is fully realized but the system has also lost the phase memory. As the cuts are taken along the diagonal and anti-diagonal axes the ω_3 elongation is fully compensated for. The worst-case scenario is realized in the intermediate situation, namely when $M\left(t\right) = 0.25$; however, even here the deviations never exceed 5%, which is an acceptable accuracy.

Samenvatting

Glas maken is één van die technologieën waar de mensheid al lang gebruikt van maakt. Al zo'n vijf duizend jaar om precies te zijn. Dus je zou denken dat we inmiddels wel bijna alles weten wat er over glazen te weten valt. Nou, dat valt tegen. Zeker wanneer je de kennis die we hebben van de fysica van kristallen vergelijkt met die van glazen.

Het verschil tussen glazen en kristallen is dat de deeltjes waaruit deze substanties zijn opgebouwd, de moleculen, in een glas niet, zoals in een kristal, netjes geordend in een rooster zitten, juist volkomen wanordelijk door elkaar heen. Als je een willekeurige vloeistof langzaam afkoelt, zal die bij een bepaalde temperatuur bevriezen. Er vormen zich dan, als het vriespunt bereikt is, kristallen. Maar wanneer je de vloeistof snel afkoelt, kun je voorbij dit vriespunt komen zonder dat zich kristallen vormen. Dan heb je een zogenaamde supergekoelde vloeistof. De moleculen in deze vloeistof bewegen een stuk langzamer dan bij een hogere temperatuur. En als je nog verder afkoelt, bewegen ze zelfs bijna helemaal niet meer. De vloeistof vloeit dan niet meer maar is, net als een kristal, vast geworden. Bij die temperatuur, de 'glastemperatuur', heeft zich dan een glas gevormd. Een glas is dus niet per sé een materiaal waar je doorheen kan kijken, zoals een vensterruit of theeglas, mocht je dat denken. Een glas is eigenlijk een toestand, zoals hierboven uitgelegd. Van elke vloeistof is wel een glasvorm te maken. De glazen die bestudeerd worden in dit boekje zijn bijvoorbeeld gemaakt van eenvoudige vormen van alcohol.

Het gebrek aan orde in zo'n glas is één van de redenen dat fysici niet zoveel met glazen aankunnen. Omdat kristallen, in tegenstelling tot glazen, een grote interne symmetrie hebben, helpt dit bij het begrijpen van wat er op atomair en moleculair niveau allemaal gebeurt. En van daaruit kun je dan allerlei dagelijkse eigenschappen van kristallen verklaren, zoals de vorm, kleur, warmtegeleiding, hardheid, enzovoort.

Voor glazen is dit veel lastiger vanwege het ontbreken van die symmetrie. Toch, als je om je heen kijkt in de kamer waar je nu zit, of misschien in de aula van het Academiegebouw waar je nu zit te wachten op het "Hora Finita", zijn de meeste vaste stoffen die je ziet wanordelijk van aard. Hout, steen, beton, de meeste metalen, plastics worden allemaal eerder door wanorde dan door orde gekenmerkt. Dus alleen al om die reden zou je verwachten dat er veel wetenschappelijke aandacht uit zo gaan naar glazen en andere wanordelijke materialen, ook wel amorfe stoffen genoemd. Toch is dat (nog) niet het geval.

Bijna de hele vaste stof fysica is gewijd aan de kristallen. Dat komt omdat ze zo goed te bestuderen zijn vanwege de interne symmetrie. En daardoor is zelfs het ´broodje aap´ ver-

haal ontstaan dat glazen helemaal geen vorm van vaste stof zijn, maar in wezen heel strope-
rige vloeistoffen. En dat je dit zou kunen zien aan de gekleurde stukjes glas die al honder-
den jaren in gebrandschilderde ramen van kathedralen zitten. Want die zouden aan de on-
derkant wat dikker zijn dan aan de bovenkant omdat ze langzaam zouden uitvloeien.
Nonsens. Er bestaat geen enkel wetenschappelijk bewijs dat die stukjes aan de onderkant
dikker zijn. Er zijn wel variaties in doorsnee, maar dat komt omdat ze vroeger niet zo goed
een glas konden maken met een uniforme dikte. Glazen, dus ook de ramen van kathedralen,
zijn gewoon vaste stoffen.

Het bestuderen van de microscopische eigenschappen van amorfe stoffen wordt dus be-
moeilijkt door het ontbreken van symmetrie, en er is minder wetenschappelijke aandacht
dan glazen zouden verdienen. Maar dat wil niet zeggen dat er geen fysische modellen be-
staan om glazen te beschrijven. Er bestaan er zelfs een heleboel. Voor elk temperatuurge-
biedje (ruim boven de glastemperatuur, vlak boven de glastemperatuur, net onder de glas-
temperatuur, enz.), bestaat tenminste één fysische benadering. En meestal zijn het er meer.
In mijn hoofdstukken 1 en 2 geef ik een hele korte introductie op een aantal van de meest
gebruikte benaderingen.

Het is ook de moeite waard om zoveel benaderingen te hebben. Glazen hebben funda-
menteel andere eigenschappen dan vloeistoffen, zonder dat er op moleculair niveau een
enorme structuurverandering plaats vindt bij de overgang van een vloeistof naar een glas en
omgekeerd. Het is niet eens een plotselinge overgang, zoals bij smelten en koken, maar een
geleidelijke. Dit laatste is iets waar bijvoorbeeld glasblazers gebruik van maken. Als glas
niet eerst zacht zou worden als het verwarmd wordt, maar direct vloeibaar, zouden we geen
bierglazen hebben maar bierkruiken. Grote veranderingen in de eigenschappen van materia-
len die niet gepaard gaan met grote structuurveranderingen komen in de natuur nauwelijks
voor. Dit gegeven alleen, maakt glazen en de glasovergang wetenschappelijk dus al interes-
sant. Helaas ontbreekt op dit moment nog een duidelijk overkoepelend benadering die gla-
zen en de glasovergang adequaat kan beschrijven. Het is maar de vraag of die er ooit komt.

In mijn onderzoek heb ik me niet bezig gehouden met alle mogelijke modellen en alle
mogelijke omstandigheden. Ik heb mij geconcentreerd op twee modellen die toegepast
worden in twee extreme omstandigheden. Die modellen heb ik getest op hun effectiviteit en
de toepasbaarheid buiten het nauwe temperatuur gebied waar ze doorgaans worden gebruikt
in mijn vakgebied van de niet lineaire optica.

Het ene uiterste is de extreem lage temperatuur dicht bij het absolute nulpunt, de laagste
temperatuur die mogelijk is. Daar geldt het TLS model, dat de wanordelijkheid van glazen
als uitgangspunt neemt. Het andere uiterste, de hoge temperatuur waar het glas vloeistof is
geworden, is het domein van het MBO model. Denk bij hoge temperatuur in het geval van
mijn alcohol glazen aan kamertemperatuur. Dit MBO model is succesvol toegepast om

vloeistof dynamica te beschrijven, maar het zou op zich bij lagere temperatuur ook toegepast moeten kunnen worden. Deze twee modellen worden uiteengezet in hoofdstuk 2.

De techniek die gebruikt is om deze modellen te testen is die van de foton echo's. Dit is een techniek die voor de buitenstaander vaak lastig te doorgronden is. Maar laten we het proberen. Stel je lost een kleurstof op in een vloeistof. Neem bijvoorbeeld de vloeistof op de kaft van dit boekje. Die is blauw gemaakt. Als je dat zou willen kwantificeren zou je een absorptie spectrum moeten opnemen van die vloeistof. Je kijkt dan naar welke kleuren licht, en daarmee bedoelen wij spectroscopisten welke frequenties van het licht, door de vloeistof heen komen en welke geabsorbeerd worden door de kleurstof. In de vloeistof op de kaft komen de blauwe kleuren, de hoge frequenties, mooi door, en worden de rode kleuren, de lage frequenties, geabsorbeerd. In figuur 1.3 zie je drie van dat soort absorptiespectra.

Het punt is nu dat de individuele kleurstofmoleculen, als je dat zou kunnen meten, een absorptiespectrum hebben dat veel nauwer is dan de brede band die alle kleurstofmoleculen samen vormen. Dat komt omdat door de wanorde in glazen en vloeistoffen alle kleurstofmoleculen een andere omgeving hebben en daarom allemaal een net iets andere kleur (resonantie frequentie) krijgen. De breedte van het totale absorptiespectrum is daarom een indicatie voor de mate van wanorde in de vloeistof.

Dat laatste is op zich al interessante informatie. Maar we willen meer. De structuur van de omgeving van alle kleurstofmoleculen verandert continu. Dit gebeurt super snel in een warme vloeistof en super langzaam in koud glas. Maar de gemiddelde absorptiefrequentie van de kleurstof blijft hetzelfde en de totale mate wanorde ook. Dus aan het absorptiespectrum verandert niets. Maar als je nu een aantal kleurstof moleculen (een subset) apart zou zetten die allemaal precies dezelfde frequentie hebben bij het begin van je experiment, en ze daarna in de tijd zou volgen, dan zou je wel een verandering zien. Dit is geïllustreerd door de donkere bogen in de drie spectra in figuur 1.3. Met het verstrijken van de tijd spreiden de kleurstofmoleculen van de subset zich uit over het hele spectrum, totdat de subset dezelfde vorm heeft gekregen als het absorptiespectrum zelf. In vloeistoffen gaat dit heel erg snel, omdat de omgevingen van de kleurstofmoleculen heel snel veranderen en in glazen gaat dit dus heel langzaam. De snelheid waarmee de subset van vorm verandert, zegt dus iets over de dynamica in de vloeistof of het glas dat bestudeerd wordt. En dat is precies wat we willen weten.

Deze uitzaksnelheid meten we met de eerder genoemde foton echo's. Zo'n echo is een lichtflitsje dat ontstaat nadat de kleurstof eerst is blootgesteld aan drie zelfgemaakte lichtpulsjes. Door de tijd tussen de pulsjes te veranderen wordt de foton echo sterker of zwakker. In figuur 1.4 is dat schematisch weergegeven. De uitzaksnelheid wordt door spectroscopisten 'defaseringstijd' genoemd en wordt weergegeven met het symbool T_2. Dit symbool komt dan ook vaak terug in de tekst van mijn proefschrift. Als je precies wilt we-

ten hoe het werkt, kun je de tekst onder figuur 1.4 doorlezen, en, als je niet bang bent voor een formule of twee, lees dan hoofdstuk 3. In dit hoofdstuk wordt de theorie van dit soort spectroscopie van begin tot eind behandeld, en ook de manier waarop die theorie ingrijpt op de twee glas- en vloeistof modellen die getest worden.

Om de lichtpulsjes voor foton echo´s te maken is een flinke hoeveelheid optische apparatuur nodig. Met name lasers. De details hiervan worden behandeld in hoofdstuk 4. Om de experimenten goed te doen moet je rekening houden met allerlei subtiele effecten die je resultaten danig kunnen verstoren. Eén van die effecten, een soort ongewild warmte effect, heeft een flink aantal van mijn collega's over de hele wereld een aantal jaren bezig gehouden. In dit deel van mijn proefschrift, maak ik aan alle onduidelijkheid op dat gebied een einde.

In hoofdstuk 5 wordt het TLS-model getest. Dit model was altijd erg succesvol in het kwalitatief beschrijven van diverse eigenschappen van koude glazen. Denk bijvoorbeeld aan de warmtegeleiding, de warmtecapaciteit of ook de geluidssnelheid. Het uitgangspunt hierbij was dat de interne wanorde samen met de lage temperatuur zorgen voor een soort achtergrond van ruis van waaruit de bovenstaande eigenschappen konden worden verklaard. Dit klinkt een beetje abstract, maat geloof me, het is een elegant model.

Ook de defasering van kleurstofmoleculen in het glas kon hiermee kwalitatief beschreven worden. Helaas waren er kwantitatief wel altijd wat problemen. Om die te verhelpen is het model in de loop der tijd aangepast met een aantal extra parameters, matsfactoren, om model en experiment precies met elkaar in overeenstemming te brengen. Mijn stelling in hoofdstuk 5 is dat je die parameters helemaal niet nodig hebt. Als je de wiskunde netter doet, zoals iemand anders suggereerde, en ongewenste experimentele effecten uitsluit dan kun je ook zonder die parameters je onderzoeksdata prima verklaren. Op één punt na. In het allereerste begin van het experiment is de inzaksnelheid veel hoger dan je zou mogen verwachten aan de hand van het model. Dit is echter een beperking van het model. Er zijn een aantal redenen bekend waarom dit effect gemeten wordt, en die worden niet meegenomen in het TLS-model. Het zou dus een idee zijn in de toekomst daar wel rekening mee te houden. Voor het overige behandel ik een aantal punten betreffende de vorm van de foton echo's en de tijdsduur waarover je ze kan meten – de zogemaande populatie dimensie – die van wat minder van belang zijn.

In hoofdstuk 6 komt dan het MBO-model aan de orde. Dit model neemt wel de effecten mee die zorgen voor de snelle defasering in het begin. Als foton echo's worden gemeten voor verschillende temperaturen, dan blijkt het MBO-model de resultaten niet zonder meer te kunnen verklaren. Het model behandelt de effecten die de omgeving op de kleurstofmoleculen heeft als zogenaamde 'harmonische oscillatoren'. Dat is dezelfde methode waarmee je een slinger van een uurwerk kunt beschrijven of een gewichtje aan een veer. Dit is een

verstandige keuze, want de harmonische oscillator wordt al sinds Christiaan Huygens in detail begrepen. En de wiskunde die hiervoor in het model nodig is, is relatief eenvoudig.

Je hebt een stuk of acht oscillatoren nodig om het samenspel van kleurstof en omgeving goed te kunnen beschrijven. Het zou mooi zijn als het niet nodig is de parameters van deze oscillatoren te veranderen als de je naar andere temperaturen gaat. Helaas, bij lagere temperaturen verandert het karakter van deze oscillatoren aanzienlijk. Ik laat in dit hoofdstuk zien hoe die veranderingen bijna allemaal gerelateerd kunnen worden aan de veranderingen in de dynamica van de vloeistof die (uiteindelijk) in een glas verandert. Dus met een paar aanpassingen, die min of meer voortvloeien uit bestaande glasvormingstheorie, kun je de experimenten toch prima beschrijven. Alleen het snelle begin van de defasering levert weer problemen op, net als in het vorige hoofdstuk. Het lijkt er dus op dat de fysische oorzaak dat het snelle begin veroorzaakt anders in elkaar steekt dan algemeen aangenomen wordt. Concluderend blijkt het MBO-model over een flink temperatuursgebied toe te passen, mits rekening gehouden wordt met de fysische oorsprong van de oscillatoren.

Omdat een deel van het werk in dit hoofdstuk zich concentreert op de verhouding tussen het snelle begin en de langzame staart van de defasering, besteed ik een deel van de tekst aan de manier waarop je dit het beste kunt meten. Niet alle foton echo technieken doen dat namelijk even goed. Het blijkt het beste te werken als je de echo overlapt met een extra lichtpulsje, en vervolgens de interferentie van die twee meet. Aan het einde van het hoofdstuk bespreek ik waarom dit zo is.

Bij gebruik van bovenstaande interferentie methode, heb je uiteindelijk vier lichtpulsen nodig, namelijk twee paren van twee pulsen die elkaar snel opvolgen. Dit maakt het mogelijk, mede omdat je uiteindelijk een interferentiepatroon meet, om de experimentele data niet zoals gebruikelijk weer te geven langs twee tijdassen, maar langs twee frequentieassen. De tijdassen worden gevormd door de tijdsduur tussen de pulsen in beide paren en zijn één op één te relateren aan de twee frequentie assen. Dit laatste is een fundamenteel fysisch gegeven. In hoofdstuk 7 laat ik zien hoe dit transformeren naar frequentieassen moet.

Het weergeven van deze data langs twee frequentieassen heeft als voordeel dat het interpreteren van de data veel makkelijker wordt. In hoofdstuk 6 was daar nog een gecompliceerde numerieke methode voor nodig. In hoofdstuk 7 wordt een extreem simpele, maar toch nauwkeurige methode gegeven, waarmee je ook de defasering ook uitstekend kwantitatief kunt meten. Dit is niet de eerste keer dat foto echo data langs twee frequentieassen wordt weergegeven, integendeel, in een aantal andere vormen van spectroscopie gebeurt dit standaard, maar het is wel voor het eerst dat deze eenvoudige en overzichtelijke interpretatie methode gebruikt wordt. Na al het uitzoekwerk in hoofdstuk 5 en 6 is deze nieuwe methode één van de belangrijkste vondsten die in dit werk gepresenteerd worden.

Bibliography

[1]   S.R.Elliot, *"Physics of Amorphous Materials"*. Longman Higher Education, Essex, 1990.
[2]   P.W.Anderson, B.I.Halperin, C.M.Varma, *"Anomalous low-temperature thermal properties of glasses and spin glasses"*, Philos. Mag. **25**, 1 (1972).
[3]   C.A.Angell, J.M.Sare, E.J.Sare, *"Glass-Transition Temperatures for Simple Molecular Liquids and Their Binary-Solutions"*, J. Phys. Chem. **82** (24), 2622-9 (1978).
[4]   R.A.Jones, *"Soft Condensed Matter"*. Oxford University Press, New York, 2002.
[5]   H.Rawson, *"Properties and Applications of Glass"*. Elsevier, Amsterdam, 1985.
[6]   H.Rawson, *"Glasses and Their Applications"*. IOM Communications, Leeds, 1991.
[7]   C.Lilyquist, R.H.Brill, *"Studies in Early Egyptian Glass"*. Metropolitan Museum of Art, New York, 2000.
[8]   L.Oppenheim, R.H.Brill *et al.*, *"Glass and Glassmaking in Ancient Mesopotamia"*. Corning Museum Of Glass Press, Corning, 1970.
[9]   D.F.Grose, R.Mandle, R.C.Hobbs, *"Early Ancient Glass"*. Hudson Hills Press, Manchester, 1989.
[10]   C.Kittel, *"Introduction to Solid State Physics"*. Wiley, New York, 1986.
[11]   S.J.Hawkes, *"Glass doesn't flow and doesn't crystallize and it isn't a liquid"*, J. Chem. Educ. **77** (7), 846-8 (2000).
[12]   Y.M.Stokes, *"Flowing windowpanes: fact or fiction?"*, Proc. R. Soc. London, Ser. A **455** (1987), 2751-6 (1999).
[13]   R.C.Plumb, *"Antique windowpanes and the flow of supercooled liquids"*, J. Chem. Educ. **66** (12), 994-6 (1989).
[14]   J.T.Fourkas, *"Science in a state of transition"*, Chem. Ind. (16), 644-8 (1998).
[15]   R.Zallen, *"The Physics of Amorphous Solids"*. John Wiley & Sons, New York, 1998.
[16]   M.R.Carpenter, D.B.Davies, A.J.Matheson, *"Measurement of the glass-transition temperature of simple liquids"*, J. Chem. Phys. **46**, 2451 (1967).
[17]   G.Rosen, J.Avissar *et al.*, *"Centrifuge melt spinning"*, J. Phys. E: Sci. Instrum. **20** (5), 571-4 (1987).
[18]   C.A.Angell, *"The viscous-liquid-glassy-solid problem"*, Supercooled Liquids **676**, 14-26 (1997).
[19]   C.A.Angell, *"The nature of glassforming liquids, the origin of superionics and 'tight' vs. 'loose' glassy conductors"*, Solid State Ionics **105** (1-4), 15-24 (1998).
[20]   C.A.Angell, *"Formation of glasses from liquids and biopolymers"*, Science **267** (5206), 1924-35 (1995).
[21]   H.Weintraub, *"Through the glass lightly"*, Science **267** (5204), 1609-18 (1995).
[22]   P.W.Anderson, *"Basic Notions of Condensed Matter Physics "*. Westview Press, Reading, MA, USA, 1997.
[23]   C.A.Angell, *"Ten questions on glassformers, and a real space 'excitations' model with some answers on fragility and phase transitions"*, J. Phys. : Condens. Matter **12** (29), 6463-75 (2000).
[24]   W.Kauzmann, *"The Nature of the Glassy State and the Behavior of Liquids at Low Temperatures"*, Chem. Rev. **43** (2), 219-56 (1948).
[25]   J.H.Gibbs, E.A.DiMarzio, *"The nature of the glass transition and the glassy state"*, J. Chem. Phys. **28** (3), 373-83 (1958).
[26]   F.H.Stillinger, *"Supercooled liquids, glass transitions, and the kauzmann paradox."*, J. Chem. Phys. **88** (12), 7818-25 (1988).
[27]   G.S.Fulcher, *"Analysis of recent measurements of the viscosity of glasses"*, J. Am. Ceram. Soc. **8**, 339-55 (1925).
[28]   H.Vogel, *"The law of the relation between the viscosity of liquids and the temperature"*, Physik. Z. **22**, 645-6 (1921).
[29]   H.Frauenfelder, A.R.Bishop *et al.*, *"Landscape paradigms in physics and biology (spec. issue)"*, Physica D **107** (2-4) (1997).
[30]   S.Sastry, *"The relationship between fragility, configurational entropy and the potential energy landscape of glass-forming liquids"*, Nature **409** (6817), 164-7 (2001).
[31]   S.Sastry, P.G.Debenedetti, F.H.Stillinger, *"Signatures of distinct dynamical regimes in the energy landscape of a glass-forming liquid"*, Nature **393** (6685), 554-7 (1998).
[32]   U.Bengtzelius, W.Götze, A.Sjölander, *"Dynamics of supercooled liquids and the glass-transition"*, J. Phys. C: Sol. St. Phys. **17** (33), 5915-34 (1984).
[33]   W.Götze, L.Sjögren, *"Relaxation processes in supercooled liquids."*, Rep. Prog. Phys. **55** (3), 241-376 (1992).
[34]   W.Götze, *"Recent tests of the mode-coupling theory for glassy dynamics"*, J. Phys. : Condens. Matter **11** (10A), A1-A45 (1999).
[35]   E.Leutheusser, *"Dynamical model of the liquid-glass transition"*, Phys. Rev. A **29** (5), 2765-73 (1984).
[36]   G.Adam, J.H.Gibbs, *"On temperature dependence of cooperative relaxation properties in glass-forming liquids"*, J. Chem. Phys. **43** (1), 139 (1965).
[37]   C.A.Angell, K.L.Ngai *et al.*, *"Relaxation in glassforming liquids and amorphous solids"*, J. Appl. Phys. **88** (6), 3113-57 (2000).
[38]   F.H.Stillinger, T.A.Weber, *"Packing structures and transitions in liquids and solids"*, Science **225** (4666), 983-9 (1984).

[39]   W.A.Phillips, *"Tunneling states in amorphous solids"*, J. Low Temp. Phys. **7**, 351 (1972).
[40]   W.A.Phillips, *"Amorphous solids: low-temperature properties."*. Springer-Verlag, Berlin, 1981.
[41]   R.C.Zeller, R.O.Pohl, *"Thermal conductivity and specific heat of noncrystalline solids"*, Phys. Rev. B: Condens. Matter **4**, 2029 (1971).
[42]   S.Hunklinger, M.von Schickfus, *"Amorphous Solids: low-temperature properties."*. Springer-Verlag, Berlin, 1981.
[43]   H.P.H.Thijssen, R.van den Berg, S.Völker, *"Thermal broadening of optical homogeneous linewidths in organic glasses and polymers studied via photochemical holeburning"*, Chem. Phys. Lett. **97**, 295 (1983).
[44]   H.C.Meijers *"Spectral Diffusion in Amorphous Solids"* , PhD Thesis, Rijksuniversiteit Groningen (1994)
[45]   D.Thorn Leeson *"Exploring Protein Energy Landscapes"* , PhD Thesis, Rijksuniversiteit Groningen (1997)
[46]   E.Rossler, V.N.Novikov, A.P.Sokolov, *"Toward a general description of the dynamics of glass formers"*, Phase Transitions **63** (1-4), 201-33 (1997).
[47]   J.Gapinski, W.Steffen *et al.*, *"Spectrum of fast dynamics in glass forming liquids: Does the "knee" exist?"*, J. Chem. Phys. **110** (5), 2312-5 (1999).
[48]   A.J.Kovacs, J.J.Aklonis *et al.*, *"Isobaric volume and enthalpy recovery of glasses .2. A transparent multiparameter theory"*, J. Polym. Sci. , Part B: Polym. Phys. **34** (15), 2467-532 (1996).
[49]   O.S.Narayana, *"Model of structural relaxation in glass"*, J. Am. Ceram. Soc. **54** (10), 491 (1971).
[50]   A.Q.Tool, *"Relation between inelastic deformability and thermal expansion of glass in its annealing range"*, J. Am. Ceram. Soc. **29** (9), 240-53 (1946).
[51]   A.Q.Tool, *"Viscosity and the extraordinary heat effects in glass"*, J. Res. NIST **37** (2), 73-90 (1946).
[52]   R.W.Boyd, *"Nonlinear Optics"*. Boston, MA [etc.] : Academic Press, 1992.
[53]   M.D.Levenson, S.S.Kano, *"Introduction to nonlinear laser spectroscopy"*. Academic press, Boston, Mass., 1988.
[54]   Y.R.Shen, *"The principles of nonlinear optics"*. Wiley & Sons, New York, 1984.
[55]   S.Mukamel, *"Principles of nonlinear optical spectroscopy"*. New York, NY, [etc.] : Oxford University Press, 1995.
[56]   H.Sillescu, *"Heterogeneity at the glass transition: a review"*, J. Non-Cryst. Solids **243** (2-3), 81-108 (1999).
[57]   M.D.Ediger, *"Supercooled liquids and glasses"*, J. Phys. Chem. **100** (31), 13200-12 (1996).
[58]   F.Stickel, E.W.Fischer, R.Richert, *"Dynamics of glass-forming liquids .1. Temperature-derivative analysis of dielectric-relaxation data"*, J. Chem. Phys. **102** (15), 6251-7 (1995).
[59]   F.Stickel, E.W.Fischer, R.Richert, *"Dynamics of glass-forming liquids .2. Detailed comparison of dielectric relaxation, dc-conductivity, and viscosity data"*, J. Chem. Phys. **104** (5), 2043-55 (1996).
[60]   C.Hansen, F.Stickel *et al.*, *"Dynamics of glass-forming liquids .3. Comparing the dielectric alpha- and beta-relaxation of 1-propanol and o-terphenyl"*, J. Chem. Phys. **107** (4), 1086-93 (1997).
[61]   H.Wendt, R.Richert, *"Heterogeneous relaxation patterns in supercooled liquids studied by solvation dynamics"*, Phys. Rev. E **61** (2), 1722-8 (2000).
[62]   H.Z.Cummins, G.Li *et al.*, *"Dynamics of supercooled liquids and glasses: Comparison of experiments with theoretical predictions"*, Z. Naturforsch. , B: Chem. Sci. **103** (3-4), 501-19 (1997).
[63]   J.H.Kristensen, I.Farnan, *"Measurement of molecular motion in solids by nuclear magnetic resonance spectroscopy of half-integer quadrupole nuclei"*, J. Chem. Phys. **114** (21), 9608-24 (2001).
[64]   S.Sen, J.F.Stebbins, *"Heterogeneous NO3- ion dynamics near the glass transition in the fragile ionic glass former Ca0.4K0.6(NO3)(1.4): A N-15 NMR study"*, Phys. Rev. Lett. **78** (18), 3495-8 (1997).
[65]   N.O.Birge, P.K.Dixon, N.Menon, *"Specific heat spectroscopy: Origins, status and applications of the 3 omega method"*, Thermochim. Acta **305**, 51-66 (1997).
[66]   D.Turnbull, M.H.Cohen, *"Free-volume model of amorphous phase - glass transition"*, J. Chem. Phys. **34** (1), 120-& (1961).
[67]   D.Turnbull, M.H.Cohen, *"Molecular transport in liquids and glasses"*, J. Chem. Phys. **31**, 1164-9 (1959).
[68]   D.Turnbull, M.H.Cohen, *"On free-volume model of liquid-glass transition"*, J. Chem. Phys. **52** (6), 3038-& (1970).
[69]   M.H.Cohen, G.S.Grest, *"Liquid-Glass Transition, A Free-Volume Approach"*, Phys. Rev. B **20** (3), 1077-98 (1979).
[70]   M.H.Cohen, G.S.Grest, *"A New Free-Volume Theory Of The Glass-Transition"*, Annals of the New York Academy of Sciences **371** (OCT), 199-209 (1981).
[71]   C.Hansen, F.Stickel *et al.*, *"Dynamics of glass-forming liquids. IV. True activated behavior above 2 GHz in the dielectric alpha-relaxation of organic liquids"*, J. Chem. Phys. **108** (15), 6408-15 (1998).
[72]   F.Stickel, E.W.Fischer *et al.*, *"Anomalies in the scaling of the dielectric alpha-relaxation - reply"*, Phys. Rev. Lett. **73** (21), 2936 (1994).
[73]   P.G.Debenedetti, *"Metastable Liquids"*. Princeton University Press, Princeton, NJ, 1996.
[74]   P.G.Debenedetti, F.H.Stillinger, *"Supercooled liquids and the glass transition"*, Nature **410** (6825), 259-67 (2001).
[75]   J.Laherrere, D.Sornette, *"Stretched exponential distributions in nature and economy: "fat tails" with characteristic scales"*, Eur. Phys. J. B. **2**, 525 (1998).
[76]   K.L.Ngai, *"Correlation between the secondary beta-relaxation time at T-g and the Kohlrausch exponent of the primary alpha-relaxation"*, Physica A **261** (1-2), 36-50 (1998).
[77]   L.Piché, R.Maynard *et al.*, *"Anomalous sound-velocity in vitreous silica at very low-temperatures"*, Phys. Rev. Lett. **32** (25), 1426-9 (1974).
[78]   M.T.Loponen, R.C.Dynes *et al.*, *"Observation of time-dependent specific heat in amorphous SiO₂"*, Phys. Rev. Lett. **45**, 457 (1980).

Bibliography

[79] M.Meissner, K.Spitzmann, *"Experimental evidence on time-dependent specific heat in vitreous silica"*, Phys. Rev. Lett. **46**, 265 (1981).

[80] B.Golding, J.E.Graebner, *"Phonon echoes in glass"*, Phys. Rev. Lett. **37**, 852 (1976).

[81] J.Jäckle, *"On the ultrasonic attenuation in glasses at low temperatures. (Localized states in amorphous insulators)"*, Z. Phys. A **257**, 212 (1972).

[82] B.Golding, J.E.Graebner *et al.*, *"Nonlinear phonon propagation in fused silica below 1 K"*, Phys. Rev. Lett. **30**, 223 (1973).

[83] S.Hunklinger, W.Arnold, S.Stein, *"Anomalous ultrasonic attenuation in vitreous silica at low temperatures"*, Phys. Lett. A **45A** (4), 311-2 (1973).

[84] J.L.Black, *"Relationship between the time dependent specific heat and the ultrasonic properties of glasses at low temperatures"*, Phys. Rev. B: Condens. Matter **17** (6), 2740-61 (1978).

[85] R.Maynard, R.Rammal, R.Suchail, *"Spectral diffusion decay of spontaneous echoes in disordered systems"*, J. Phys. Lett. **41** (12), L291-L294 (1980).

[86] P.Hu, L.R.Walker, *"Spectral-diffusion decay in echo experiments"*, Phys. Rev. B: Condens. Matter **18** (3), 1300-5 (1978).

[87] R.J.Silbey, J.M.A.Koedijk, S.Völker, *"Time and temperature dependence of optical linewidths in glasses at low temperature: spectral diffusion"*, J. Chem. Phys. **105** (3), 901-9 (1996).

[88] Y.S.Bai, M.D.Fayer, *"A new approach to the nonlinear spectroscopic investigation of dynamics in complex solids: theory and experiments"*, Comm. Cond. Mat. Phys. **14** (6), 343-64 (1989).

[89] L.R.Narashimhan, K.A.Littau *et al.*, *"Probing organic glasses at low temperature with variable time scale optical dephasing measurements"*, Chem. Rev. **90** (3), 439 (1990).

[90] H.C.Meijers, D.A.Wiersma, *"Low temperature dynamics in amorphous solids: A photon echo study"*, J. Chem. Phys. **101** (8), 6927 (1994).

[91] J.M.A.Koedijk, R.Wannemacher *et al.*, *"Spectral diffusion in organic glasses: Time dependence of spectral holes"*, J. Phys. Chem. **100** (51), 19945 (1996).

[92] P.M.Selzer, D.L.Huber *et al.*, *"Anomalous fluorescence linewidth behaviour in $Eu^{3+-\ doped\ silicate\ glass}$"*, Phys. Rev. Lett. **36**, 813 (1976).

[93] R.M.Shelby, *"Measurement of optical homogeneous linewidths in a glass with picosecond accumulated photon echoes"*, Opt. Lett. **8**, 88 (1983).

[94] J.M.Hayes, R.P.Stout, G.J.Small, *"Holeburning, softon-phonon scattering and ultrafast dephasing of impurity electronic transitions in glasses"*, J. Chem. Phys. **74**, 4266 (1981).

[95] Y.S.Bai, M.D.Fayer, *"Effects of spectral diffusion in incoherent photon-echo experiments"*, Phys. Rev. B: Condens. Matter **37** (17), 10440-3 (1988).

[96] Y.S.Bai, M.D.Fayer, *"Optical dephasing in glasses: theoretical comparison of the incoherent photon echo, accumulated grating echo, and two-pulse photon echo experiments"*, Chem. Phys. **128** (1), 135-55 (1988).

[97] T.L.Reinecke, *"Fluorescence linewidths in glasses"*, Sol. St. Comm. **32** (11), 1103 (1979).

[98] M.M.Broer, B.Golding *et al.*, *"Low-temperature optical dephasing of rare-earth ions in inorganic glasses"*, Phys. Rev. B: Condens. Matter **33** (6), 4160-5 (1986).

[99] D.L.Huber, M.M.Broer, B.Golding, *"Low-temperature optical dephasing of rare-earth ions in glass"*, Phys. Rev. Lett. **52** (25), 2281-4 (1984).

[100] D.L.Huber, M.M.Broer, B.Golding, *"Theories of homogeneous optical linewidths of impurities in glasses"*, Phys. Rev. B: Condens. Matter **33** (10), 7297 (1986).

[101] D.Zimdars, M.D.Fayer, *"Electronic spectral diffusion in glasses: the influence of coupling to the medium on experimental observables"*, J. Chem. Phys. **104**, 3865 (1996).

[102] A.Suarez, R.J.Silbey, *"Low-temperature dynamics in glasses and the stochastic sudden-jump model"*, Chem. Phys. Lett. **218** (5-6), 445-53 (1994).

[103] P.Hu, L.R.Walker, *"Spectral diffusion in glasses at low temperatures"*, Sol. St. Comm. **24** (12), 813-6 (1977).

[104] E.Geva, J.L.Skinner, *"Theory of photon echoes and hole burning in low temperature glasses: How good are the standard approximations?"*, J. Chem. Phys. **107** (19), 7630 (1997).

[105] S.Gasiorowicz, *"Quantum Physics"*. John Wiley & Sons, New York, 1974.

[106] S.Hunklinger, M.Schmidt, *"An explanation of the anomalous temperature dependence of optical linewidths in glasses"*, Z. Phys. B **54** (2), 93-7 (1984).

[107] A.Heuer, R.J.Silbey, *"Tunneling in real structural glasses: a universal theory"*, Phys. Rev. B: Condens. Matter **49** (2), 1441-4 (1994).

[108] A.Heuer, R.J.Silbey, *"Microscopic description of tunneling systems in a structural model glass"*, Phys. Rev. Lett. **70** (25), 3911-4 (1993).

[109] A.Heuer, R.J.Silbey, *"Low-temperature anomalies of glasses: What can we learn from computer simulations?"*, Physica B **219-220**, 255-7 (1996).

[110] A.Heuer, R.J.Silbey, *"Collective dynamics in glasses and its relation to the low-temperature anomalies"*, Phys. Rev. B: Condens. Matter **53** (2), 609-19 (1996).

[111] P.Reineker, K.Kassner, *"Optical spectroscopy of glasses"*. Reidel Publishing Company, Dordrecht, 1986.

[112] J.L.Black, B.I.Halperin, *"Spectral diffusion, phonon echoes, and saturation recovery in glasses at low temperatures"*, Phys. Rev. B: Condens. Matter **16** (6), 2879-95 (1977).

188

[113]   C.K.Chan, S.O.Sari, *"Tunable dye laser pulse converter for production of picosecond pulses"*, Appl. Phys. Lett. **25** (7), 403-6 (1974).

[114]   Y.S.Bai, M.D.Fayer, *"Time scales and optical dephasing measurements: investigation of dynamics in complex systems"*, Phys. Rev. B: Condens. Matter **39** (15), 11066-84 (1989).

[115]   D.R.Reichman, R.J.Silbey, *"On the relaxation of a two-level system: beyond the weak-coupling approximation"*, J. Chem. Phys. **104** (4), 1506-18 (1996).

[116]   J.R.Klauder, P.W.Anderson, *"Spectral diffusion in spin resonance experiments"*, Phys. Rev. **125**, 912 (1962).

[117]   L.R.Narashimhan, K.A.Littau *et al.*, *"Low-temperature glass dynamics probed by optical dephasing measurements"*, J. Lumin. **45** (1-6), 49-53 (1990).

[118]   A.V.Naumov, Y.G.Vainer, *"Minimal distance between chromophore and two-level systems in amorphous solids: effect on photon echo and single molecule spectroscopy data"*, J. Lumin. **98** (1-4), 63-74 (2002).

[119]   W.Pflueg, F.-L.H.Brown, R.J.Silbey, *"Variance and width of absorption lines of single molecules in low temperature glasses"*, J. Chem. Phys. **108** (16), 6876-83 (1998).

[120]   H.A.Kramers, *"Brownian motion in a field of force and the diffusion model of chemical reactions"*, Physica **7** (4), 284-304 (1940).

[121]   E.A.Carter, J.T.Hynes, *"Solvation dynamics for an ion-pair in a polar-solvent - time-dependent fluorescence and photochemical charge-transfer"*, J. Chem. Phys. **94** (9), 5961-79 (1991).

[122]   R.Jimenez, G.R.Fleming *et al.*, *"Femtosecond solvation dynamics of water"*, Nature **369** (6480), 471-3 (1994).

[123]   M.Maroncelli, G.R.Fleming, *"Computer-simulation of the dynamics of aqueous solvation"*, J. Chem. Phys. **89** (8), 5044-69 (1988).

[124]   M.Maroncelli, G.R.Fleming, *"Comparison of time-resolved fluorescence stokes shift measurements to a molecular theory of solvation dynamics"*, J. Chem. Phys. **89** (2), 875-81 (1988).

[125]   R.Kubo, M.Toda, N.Hashitsume, *"Statistical physics"*. Springer, Berlin, 985.

[126]   L.Onsager, *"Reciprocal Relations in Irreversible Processes. I."*, Phys. Rev. **37** (4), 405-26 (1931).

[127]   L.Onsager, *"Reciprocal Relations in Irreversible Processes. II."*, Phys. Rev. **38** (12), 2265-79 (1932).

[128]   T.Keyes, *"Instantaneous normal mode approach to liquid state dynamics"*, J. Phys. Chem. A **101** (16), 2921-30 (1997).

[129]   M.Cho, G.R.Fleming *et al.*, *"Instantaneous normal-mode analysis of liquid water"*, J. Chem. Phys. **100** (9), 6672-83 (1994).

[130]   M.Buchner, B.M.Ladanyi, R.M.Stratt, *"The Short-Time Dynamics of Molecular Liquids - Instantaneous-Normal-Mode Theory"*, J. Chem. Phys. **97** (11), 8522-35 (1992).

[131]   T.M.Wu, R.F.Loring, *"Phonons in Liquids - A Random-Walk Approach"*, J. Chem. Phys. **97** (11), 8568-75 (1992).

[132]   T.Keyes, J.T.Fourkas, *"Instantaneous normal mode theory of more complicated correlation functions: Third- and fifth-order optical response"*, J. Chem. Phys. **112** (1), 287-93 (2000).

[133]   G.Seeley, T.Keyes, *"Normal-Mode Analysis of Liquid-State Dynamics"*, J. Chem. Phys. **91** (9), 5581-6 (1989).

[134]   Y.G.Vainer, M.A.Kol'chenko *et al.*, *"Optical dephasing in doped organic glasses over a wide (0.35-100 K) temperature range: Solid toluene doped with Zn-octaethylporphine"*, J. Chem. Phys. **116** (20), 8959-65 (2002).

[135]   S.J.Zilker, D.Haarer *et al.*, *"Temperature-dependent line broadening of chromophores in amorphous solids: Differences between single-molecule spectroscopy and photon echo results"*, J. Lumin. **76**, 157-60 (1998).

[136]   J.T.Fourkas, M.Berg, *"Temperature-dependent ultrafast solvation dynamics in a completely nonpolar system"*, J. Chem. Phys. **98** (10), 7773-85 (1993).

[137]   U.Zurcher, T.Keyes, *"Configurational entropy and collective modes in normal and supercooled liquids"*, Phys. Rev. E **60** (2), 2065-70 (1999).

[138]   D.R.Reichman, G.A.Voth, *"Self-consistent harmonic theory of solvation in glassy systems: Classical solvation"*, J. Chem. Phys. **112** (7), 3267-79 (2000).

[139]   D.R.Reichman, G.A.Voth, *"Self-consistent harmonic theory of solvation in glassy systems: Quantum solvation"*, J. Chem. Phys. **112** (7), 3280-4 (2000).

[140]   R.Zwanzig, *"On the Relation Between Self-Diffusion and Viscosity of Liquids"*, J. Chem. Phys. **79** (9), 4507-8 (1983).

[141]   R.van Zon, J.Schofield, *"Mode-coupling theory for multiple-point and multiple-time correlation functions"*, Phys. Rev. E **6501** (1), art-011106 (2002).

[142]   W.X.Li, T.Keyes, *"Instantaneous normal mode theory of diffusion and the potential energy landscape: Application to supercooled liquid CS2"*, J. Chem. Phys. **111** (12), 5503-13 (1999).

[143]   D.D.Brace, S.D.Gottke *et al.*, *"Orientational dynamics of the glass forming liquid, dibutylphthalate: Time domain experiments and comparison to mode coupling theory"*, J. Chem. Phys. **116** (4), 1598-606 (2002).

[144]   J.S.Ma, D.VandenBout, M.Berg, *"Application of mode-coupling theory to solvation dynamics"*, Phys. Rev. E **54** (3), 2786-96 (1996).

[145]   E.T.J.Nibbering *"Femtosecond Optical Dynamics in Liquids"* , PhD Thesis, Rijks univeristeit Groningen (1993)

[146]   Y.J.Yan, S.Mukamel, *"Rate theories, dephasing processes, and nonlinear optical-line shapes"*, J. Phys. Chem. **93** (19), 6991-6 (1989).

[147]   Y.J.Yan, S.Mukamel, *"Semiclassical dynamics in liouville space - application to molecular electronic spectroscopy"*, J. Chem. Phys. **88** (9), 5735-48 (1988).

[148]   W.P.de Boeij *"Ultrafast solvation dynamics explored by nonlinear optical spectroscopy"* , PhD Thesis, Rijksuniversiteit Groningen (1997)

Bibliography

[149]   Y.Nagasawa, S.A.Passino, J.Taiha, G.R.Fleming, in Post Conference Ed.Ultrafast.Phenomena.1996., pp 369-370,*"Femtosecond 3 pulse stimulated photon echo peak shift measurements of organic polymer glass from room temperature to 30 K"*, (1996)

[150]   Y.Nagasawa, Y.Y.Jae, G.R.Fleming, *"Solute-solvent interaction dynamics studied by photon echo spectroscopies in polymer glasses"*, J. Chem. Phys. **109** (14), 6175-83 (1998).

[151]   C.J.Bardeen, G.Cerullo, C.V.Shank, in Post Conference Ed.Ultrafast.Phenomena., pp 365-366,*"Temperature-dependent electronic dephasing of molecules in polymers measured by femtosecond three pulse photon echoes"*, (1996)

[152]   S.Mukamel, R.F.Loring, *"Nonlinear response function for time-domain and frequency-domain four-wave mixing"*, J. Opt. Soc. Am. B **3** (4), 595-606 (1986).

[153]   R.F.Loring, S.Mukamel, *"Unified theory of photon echoes: the passage from inhomogeneous to homogeneous line broadening"*, Chem. Phys. Lett. **114** (4), 426-9 (1985).

[154]   Allen,L. & Eberly,J.H. *"Optical Resonances and Two-Level Atoms."* (1975). Wiley, New York.
         Ref Type: Generic

[155]   J.A.Armstrong, N.Bloembergen *et al.*, *"Interactions between Light Waves in a Nonlinear Dielectric"*, Phys. Rev. **127** (6), 1918-39 (1962).

[156]   N.Bloembergen, H.Lotem, R.T.Lynch, *"Lineshapes in coherent resonant Raman scattering"*, Indian J. Pure Appl. Phys **16**, 151 (1978).

[157]   N.Bloembergen, *"Nonlinear Optics"*. World Scientific Publishing Company, 1996.

[158]   K.Duppen *"Nonlinear optical investigations of vibrational dynamics in solids"* , PhD Thesis, Rijksuniversiteit Groningen (1985)

[159]   S.Mukamel, E.Hanamura, *"Four-wave mixing using partially coherent fields in systems with spatial correlations"*, PHYSICAL REVIEW. A **33** (2), 1099-108 (1986).

[160]   T.Petrosky, I.Prigogine, *"The Liouville space extension of quantum mechanics"*, Adv. Chem. Phys **99**, 1-120 (1997).

[161]   R.P.Feynman, F.L.Vernon, R.W.Hellwarth, *"Geometrical Representation of the Schr odinger Equation for Solving Maser Problems"*, J. Appl. Phys. **28**, 49 (1957).

[162]   S.Mukamel, E.Hanamura, *"Four-wave mixing using partially coherent fields in systems with spatial correlations"*, PHYSICAL REVIEW. A **33** (2), 1099-108 (1986).

[163]   Y.Tanimura, S.Mukamel, *"Real-time path-integral approach to quantum coherence and dephasing in nonadiabatic transitions and nonlinear optical response"*, Phys. Rev. E **47** (1), 118-36 (1993).

[164]   R.F.Loring, J.Y.Yi, S.Mukamel, *"Time-resolved fluorescence and hole-burning line shapes of solvated molecules: longitudinal dielectric relaxation and vibrational dynamics"*, J. Chem. Phys. **87** (10), 5840-57 (1987).

[165]   T.K.Yee, T.K.Gustafson, *"Diagrammatic analysis of the density operator for nonlinear optical calculations: Pulsed and cw responses"*, Phys. Rev. A **18** (4), 1597-617 (1978).

[166]   E.T.J.Nibbering, D.A.Wiersma, K.Duppen, *"Ultrafast nonlinear spectroscopy with chirped optical pulses"*, Phys. Rev. Lett. **68** (4), 514 (1992).

[167]   E.T.J.Nibbering, D.A.Wiersma, K.Duppen, *"Femtosecond non-Markovian optical dynamics in solution"*, Phys. Rev. Lett. **66** (19), 2464 (1991).

[168]   S.de Silvestri, A.M.Weiner *et al.*, *"Femtosecond dephasing studies of dye molecules in a polymer host"*, Chem. Phys. Lett. **112** (3 195-9) (1984).

[169]   A.M.Weiner, S.de Silvestri, E.P.Ippen, *"Three-pulse scattering for femtosecond dephasing studies: theory and experiment"*, J. Opt. Soc. Am. B **2** (4 645-62) (1985).

[170]   W.P.de Boeij, M.S.Pshenichnikov, D.A.Wiersma, *"Ultrafast solvation dynamics explored by femtosecond photon echo spectroscopies"*, Annu. Rev. Phys. Chem. **49**, 99-123 (1998).

[171]   W.P.de Boeij, M.S.Pshenichnikov, D.A.Wiersma, *"On the relation between the echo-peak shift and Brownian-oscillator correlation function"*, Chem. Phys. Lett. **253** (1-2 53-60) (1996).

[172]   G.R.Fleming, M.H.Cho, *"Chromophore-solvent dynamics"*, Annu. Rev. Phys. Chem. **47**, 109-34 (1996).

[173]   M.H.Cho, J.Y.Yu *et al.*, *"The integrated photon echo and solvation dynamics"*, J. Phys. Chem. **100** (29), 11944-53 (1996).

[174]   M.Cho, N.F.Scherer *et al.*, *"Photon echoes and related four-wave-mixing spectroscopies using phase-locked pulses"*, J. Chem. Phys. **96** (8), 5618-29 (1992).

[175]   W.P.de Boeij, M.S.Pshenichnikov, D.A.Wiersma, *"Heterodyne-detected stimulated photon echo: applications to optical dynamics in solution"*, J. Chem. Phys. **233** (2-3), 287-309 (1998).

[176]   Wiersma,D.A., de Boeij,W.P. & Pshenichnikov,M.S., pp. 194-195 (Opt. Soc. America, Washington, DC, USA,1996).

[177]   W.P.de Boeij, M.S.Pshenichnikov, D.A.Wiersma, *"System-bath correlation function probed by conventional and time-gated stimulated photon echo"*, J. Phys. Chem. **100** (29 11806-23) (1996).

[178]   J.B.W.Morsink, W.H.Hesselink, D.A.Wiersma, *"Photon echoes stimulated from long lived ordered populations in multi level systems. The effect of intersystem crossing and optical branching"*, Chem. Phys. **71**, 289 (1982).

[179]   M.Berg, C.A.Walsh *et al.*, *"Dynamics in low temperature glasses; Theory and experiments on optical dephasing, spectral diffusion, and hydrogen tunneling"*, J. Chem. Phys. **88** (3), 1564-87 (1988).

[180]   M.Berg, C.A.Walsh *et al.*, *"Picosecond photon echo and optical hole burning studies of chromophores in organic glasses"*, J. Lumin. **38** (1-6), 9-14 (1987).

[181]   P.Hu, S.R.Hartmann, *"Theory of spectral diffusion decay using an uncorrelated sudden-jump model"*, Phys. Rev. B: Condens. Matter **9** (1), 1-13 (1974).

[182] W.O.Putikka, D.L.Huber, *"Optical linewidths and photon-echo decays of impurities in glasses"*, Phys. Rev. B: Condens. Matter **36** (6), 3436-41 (1987).

[183] D.L.Huber, W.O.Putikka, *"Homogeneous linewidths and photon echo decay rates of rare earth and transition metal impurities in glasses"*, J. Lumin. **40-41**, 567-8 (1988).

[184] D.Thorn Leeson, O.Berg, D.A.Wiersma, *"Low-temperature protein dynamics studied by the long-lived stimulated photon echo."*, J. Phys. Chem. **98** (14), 3913 (1994).

[185] H.C.Meijers, D.A.Wiersma, *"Glass dynamics probed by the long lived stimulated photon echo"*, Phys. Rev. Lett. **68**, 381 (1992).

[186] I.D.Abella, N.A.Kurnit, S.R.Hartmann, *"Photon Echoes"*, Phys. Rev. **141** (1), 391-406 (1966).

[187] W.H.Hesselink *"Picosecond dephasing and relaxation in molecular mixed crystals"* , PhD Thesis, Rijksuniversiteit Groningen (1980)

[188] C.K.Chan, S.O.Sari, R.E.Foster, *"Pulse properties of the tunable dye laser pulse convertor"*, J. Appl. Phys. **47** (3), 1139-41 (1976).

[189] R.Wallenstein, T.W.Hänsch, *"Powerful dye laser oscillator-amplifier system for high resolution spectroscopy"*, Optics Communications **14** (3), 353-7 (1975).

[190] S.M.Curry, R.Cubeddu, T.W.Hänsch, *"Intensity stabilization of dye laser radiation by saturated amplification"*, Appl. Phys. **1** (3), 153-9 (1973).

[191] L.R.Milgram, *"The Colours of Life"*. Oxford University Press, Oxford, 1997.

[192] A.T.Gradyushko, M.P.Tsvirko, *"Probabilities of intercombination transitions in porphyrin and metalloporphyrin molecules"*, Opt. Spektrosk. **31**, 291 (1971).

[193] A.T.Gradyushko, A.N.Sevchenko *et al.*, *"Energetics of photophysical processes in chlorophyll-like molecules"*, Photochem. Photobiol. **11**, 387 (1970).

[194] I.Y.Chan, W.G.van Dorp *et al.*, *"The lowest triplet state of Zn porphin"*, Mol. Phys. **22**, 741 (1971).

[195] R.M.Shelby, R.M.MacFarlane, *"Population holeburning using a triplet reservoir : S1-S0 transition of zn-porphin in n-octane"*, Chem. Phys. Lett. **64**, 545 (1979).

[196] P.J.van der Zaag, J.P.Galaup, S.Völker, *"In search of spectral diffusion in glasses; a time resolved transient holeburning study of porphins in polyethylene"*, Chem. Phys. Lett. **166**, 263 (1990).

[197] F.J.Bermejo, G.J.Cuello *et al.*, *"Disorder effects on glassy dynamics: Separation of orientational and positional correlations"*, Physica A **241** (1), 883 (1997).

[198] M.A.Miller, M.Jimenez-Ruiz *et al.*, *"Comparison of the structural and orientational dynamics in ethanol"*, Phys. Rev. B: Condens. Matter **57** (22), R13977 (1998).

[199] C.Talon, M.A.Ramos *et al.*, *"Low-temperature specific heat and glassy dynamics of a polymorphic molecular solid"*, Phys. Rev. B: Condens. Matter **58** (2), 745 (1998).

[200] M.A.Ramos, S.Vieira *et al.*, *"Quantitative Assessment of the Effects of Orientational and Positional Disorder on Glassy Dynamics"*, Phys. Rev. Lett. **78** (1), 82 (1997).

[201] W.H.Press, *"Numerical recipes in Pascal: the art of scientific computing"*. Cambridge University Press, Cambridge, 1989.

[202] A.Gabrielli, M.A.Munoz, L.Pietronero, *"A simple model of slow relaxation dynamics"*, J. Phys. IV **8**, 105 (1998).

[203] D.L.Huber, *"Dynamical model for stretched exponential relaxation in solids"*, Phys. Rev. E: Stat. Phys. , Plasmas, Fluids **53** (6), 6544-6 (1996).

[204] H.C.Meijers, D.A.Wiersma, *"Spectral diffusion in glasses: a photon echo study of zincporphin in ethanol"*, Chem. Phys. Lett. **181**, 312 (1991).

[205] S.J.Zilker, D.Haarer, *"Line broadening in a polymer glass as investigated by stimulated photon echo spectroscopy: Spectral diffusion versus heating effects"*, Chem. Phys. **220** (Issue 1-2), 167 (1997).

[206] P.Neu, R.J.Silbey *et al.*, *"Nonequilibrium spectral diffusion due to laser heating in stimulated-photon-echo spectroscopy of low-temperature glasses"*, Phys. Rev. B: Condens. Matter **56** (18), 11571-8 (1997).

[207] A.Schonle, S.W.Hell, *"Heating by absorption in the focus of an objective lens"*, Opt. Lett. **23** (5), 325-7 (1998).

[208] R.B.Stephens, G.S.Cieloszyk, G.L.Salinger, *"Thermal conductivity and specific heat of non-crystalline solids"*, Phys. Lett. A **38A** (3), 215 (1971).

[209] R.Jankowiak, J.M.Hayes, G.J.Small, *"Low temperature specific heat of glasses: temperature and time dependence"*, Phys. Rev. B: Condens. Matter **38**, 2084 (1988).

[210] C.C.Yu, A.J.Legget, *"Low teperature properties of amorphous materials : through a glass darkly"*, Comm. Cond. Mat. Phys. **14**, 231 (1988).

[211] A.Rundquist, C.Durfee *et al.*, *"Ultrafast laser and amplifier sources"*, Appl. Phys. B **65** (2), 161-74 (1997).

[212] Y.G.Basov, *"Femtosecond radiation pulses from solid-state lasers"*, J. Opt. Technol. **64** (1), 3-14 (1997).

[213] P.M.W.French, *"The generation of ultrashort laser-pulses"*, Rep. Prog. Phys. **58** (2), 169-262 (1995).

[214] J.R.Lincoln, M.J.P.Dymott, A.I.Ferguson, *"Femtosecond pulses from an all-solid-state kerr-lens mode- locked CrLiSaf laser"*, Opt. Lett. **19** (16), 1210-2 (1994).

[215] C.Spielmann, P.F.Curley *et al.*, *"Ultrabroadband femtosecond lasers"*, IEEE J. Quantum Electron. **30** (4), 1100-14 (1994).

[216] T.Brabec, F.Krausz, *"Intense few-cycle laser fields: frontiers of nonlinear optics"*, Rev. Mod. Phys. **72** (2), 545-91 (2000).

[217] F.Krausz, M.E.Fermann *et al.*, *"Femtosecond solid-state lasers"*, IEEE J. Quantum Electron. **28** (10), 2097-122 (1992).

Bibliography

[218] D.E.Spence, P.N.Kean, W.Sibbett, *"60-fsec pulse generation from a self-mode-locked Ti-sapphire laser"*, Opt. Lett. **16** (1), 42-4 (1991).

[219] J.P.Likforman, G.Grillon *et al.*, *"Generation of 27 fs pulses of 70-kw peak power at 80 mhz repetition rate using a cw self-pulsing Ti-sapphire laser"*, Appl. Phys. Lett. **58** (19), 2061-3 (1991).

[220] M.T.Asaki, C.P.Huang *et al.*, *"Generation of 11-fs pulses from a self-mode-locked Ti-sapphire laser"*, Opt. Lett. **18** (12), 977-9 (1993).

[221] C.P.Huang, M.T.Asaki *et al.*, *"17-fs pulses from a self-mode-locked Ti-sapphire laser"*, Opt. Lett. **17** (18), 1289-91 (1992).

[222] A.Baltuska, Z.Wei *et al.*, *"All-solid-state cavity-dumped sub-5-fs laser"*, Appl. Phys. B **65** (2), 175-88 (1997).

[223] A.Baltuska *"Hydrated electron dynamics explored with 5-fs optical pulses"* , PhD Thesis, Rijksuniversiteit Groningen (2000)

[224] A.A.Angelutz, D.P.Krindach *et al.*, *"Kerr lens modulation processes in femtosecond Ti: sapphire laser"*, Proceedings of SPIE **2095**, 73 (2003).

[225] S.J.Zilker, J.Friebel *et al.*, *"Investigation of low-temperature line broadening mechanisms in organic amorphous solids with photon echo, hole-burning, and single-molecule spectroscopy"*, Chem. Phys. Lett. **289** (5-6), 553-8 (1998).

[226] S.J.Zilker, L.Kador *et al.*, *"Comparison of photon echo, hole burning, and single molecule spectroscopy data on low-temperature dynamics of organic amorphous solids"*, J. Chem. Phys. **109** (16), 6780-90 (1998).

[227] F.T.H.den Hartog, M.P.Bakker *et al.*, *"Long-time spectral diffusion induced by short-time energy transfer in doped glasses: concentration-, wavelength- and temperature dependence of spectral holes"*, Chem. Phys. Lett. **297**, 313 (1998).

[228] K.Lazonder, K.Duppen, D.A.Wiersma, *"Ethanol glass dynamics: Logarithmic line broadening and optically induced dephasing"*, J. Phys. Chem. B **104** (27), 6468-77 (2000).

[229] J.Müller, D.Haarer *et al.*, *"Investigation of spectral diffusion in PMMA on timescales from 10(-5) to 10(4) seconds via transient and photophysical hole burning"*, Chem. Phys. **237** (3), 483 (1998).

[230] O.V.Khodykin, J.Müller *et al.*, *"Anomalous spectral diffusion in polymer glasses"*, Europhys. Lett. **44** (1), 68 (1998).

[231] K.Fritsch, J.Friedrich, B.M.Kharlamov, *"Nonequilibrium phenomena in spectral diffusion physics of organic glasses"*, J. Chem. Phys. **105** (5), 1798 (1996).

[232] G.Hannig, H.Maier *et al.*, *"Interacting tunneling states: A hole-burning study of spectral diffusion"*, Mol. Cryst. Liq. Cryst. **291**, 11 (1996).

[233] H.Maier, D.Haarer, *"Non-logarithmic spectral diffusion dynamics Evidence for interactions between tunneling centers"*, J. Lumin. **4**, 413 (1997).

[234] H.Maier, B.M.Kharlamov, D.Haarer, *"Two-level system dynamics in the long-time limit: a power-law time dependence"*, Phys. Rev. Lett. **76** (12), 2085 (1996).

[235] H.Maier, D.Haarer, *"Equilibrium and nonequilibrium tunneling dynamics and spectral diffusion in the millikelvin regime"*, J. Lumin. **64**, 87 (1995).

[236] P.Neu, R.J.Silbey *et al.*, *"Nonlogarithmic spectral diffusion in proteins and glasses"*, J. Lumin. **76-77**, 619-22 (1998).

[237] A.V.Naumov, Y.G.Vainer, S.J.Zilker, *"Nonexponential two-pulse photon echo decay in amorphous solids at low temperatures"*, J. Lumin. **86** (3-4), 273-8 (2000).

[238] J.F.Berret, *"How universal are the low-temperature acoustic properties of glasses?"*, Zeitschrift f++r Physik. B, Condensed matter **70** (1), 65-72 (1988).

[239] E.Geva, J.L.Skinner, *"Two-pulse photon echoes from zinc-meso-tetraphenylporphine/polymethylmethacrylate are not consistent with the tunneling two-level system model"*, J. Chem. Phys. **108** (20), 8485-8 (1998).

[240] A.Criado, M.Jimenez-Ruiz *et al.*, *"Role of low-frequency vibrations on sound propagation in glasses at intermediate temperature"*, Phys. Rev. B **61** (13), 8778-83 (2000).

[241] B.Jackson, R.J.Silbey, *"Theoretical description of photochemical holeburning in soft glasses"*, Chem. Phys. Lett. **99**, 331 (1983).

[242] A.Elschner, L.R.Narashimhan, M.D.Fayer, *"High temperature optical dephasing mechanism for dye molecules in PMMA glass"*, Chem. Phys. Lett. **171**, 19 (1990).

[243] G.K.Liu, R.L.Cone, *"Laser-induced instantaneous spectral diffusion in Tb/sup 3+/ compounds as observed in photon-echo experiments"*, Phys. Rev. B: Condens. Matter **41** (10), 6193 (1990).

[244] S.Kröll, E.Y.Xu, R.Kachru, *"Influence of excited-state Pr/sup 3+/ on the relaxation of the Pr/sup 3+/:YAlO/sub 3/ /sup 3/H/sub 4/-/sup 1/D/sub 2/ transition"*, Phys. Rev. B: Condens. Matter **44** (1), 30 (1991).

[245] S.Kröll, E.Y.Xu *et al.*, *"Intensity-dependent photon-echo relaxation in rare-earth-doped crystals"*, Phys. Rev. B: Condens. Matter **41** (16), 11568 (1990).

[246] A.V.Naumov, Y.G.Vainer, *"Modified model of photon echoes in low-temperature glasses: Effect of minimal distance between two-level systems and chromophore"*, J. Phys. Chem. B **107** (9), 2054-60 (2003).

[247] A.V.Naumov, Y.G.Vainer, *"Minimal distance between chromophore and two-level systems in amorphous solids: effect on photon echo and single molecule spectroscopy data"*, J. Lumin. **98** (1-4), 63-74 (2002).

[248] E.Geva, J.L.Skinner, *"Theory of single-molecule optical line-shape distributions in low-temperature glasses"*, J. Phys. Chem. B **101** (44), 8920-32 (1997).

[249] D.L.Huber, *"Diffusion of optical excitation at finite temperatures"*, J. Chem. Phys. **78** (5), 2530-2 (1983).

[250] W.E.Moerner, M.Orrit, *"Illuminating single molecules in condensed matter"*, Science **283** (5408), 1670-+ (1999).

[251] P.Tamarat, A.Maali *et al.*, *"Ten years of single-molecule spectroscopy"*, J. Phys. Chem. A **104** (1), 1-16 (2000).

192

[252]   J.Tittel, R.Kettner *et al.*, *"Spectral diffusion in an amorphous polymer probed by single molecule spectroscopy"*, J. Lumin. **64**, 1 (1995).

[253]   B.Kozankiewicz, J.Bernard, M.Orrit, *"Single molecule lines and spectral hole burning of terrylene in different matrices"*, J. Chem. Phys. **101** (11), 9377 (1994).

[254]   A.M.Boiron, P.Tamarat *et al.*, *"Are the spectral trails of single molecules consistent with the standard two-level system model of glasses at low temperatures?"*, Chem. Phys. **247** (1), 119 (1999).

[255]   M.Orrit, J.Bernard *et al.*, *"Optical spectroscopy of single molecules in solids"*, Prog. Opt. **35**, 61-144 (1996).

[256]   E.Geva, J.L.Skinner, *"Optical line shapes of single molecules in glasses: Temperature and scan-time dependence"*, J. Chem. Phys. **109** (12), 4920-6 (1998).

[257]   E.Geva, J.L.Skinner, *"Single molecule spectral trajectories in low-temperature glasses"*, Chem. Phys. Lett. **287** (1-2), 125-30 (1998).

[258]   J.L.Skinner, E.Geva, *"Single-molecule spectroscopy, photon echoes, and hole burning in low-temperature glasses"*, J. Lumin. **76-77**, 270-3 (1998).

[259]   M.Orrit, J.Bernard *et al.*, *"Stark effect on single molecules in a polymer matrix"*, Chem. Phys. Lett. **196** (6), 595 (1992).

[260]   M.Vachaa, L.Yi *et al.*, *"Inhomogeneous and single molecule line broadening of terrylene in a series of crystalline n-alkanes"*, J. Chem. Phys. **106** (20), 8324 (1997).

[261]   Y.G.Vainer, M.A.Kol'chenko *et al.*, *"Photon echoes in doped organic amorphous systems over a wide (0.35-50 K) temperature range"*, J. Lumin. **86** (3-4), 265-72 (2000).

[262]   C.J.Bardeen, G.Cerullo, C.V.Shank, *"Temperature-dependent electronic dephasing of molecules in polymers in the range 30 to 300 K"*, Chem. Phys. Lett. **280** (1-2), 127-33 (1997).

[263]   Y.Nagasawa, Y.Y.Jae *et al.*, *"Excited state dynamics of chromophores in glasses and in photosynthetic proteins"*, Faraday Discussions (108 23-34) (1997).

[264]   N.V.Gruzdev, E.G.Sil'kis *et al.*, *"Photon-echo study of ultrafast dephasing in amorphous solids in wide temperature region with incoherent light"*, J. Phys. IV **1** (C7), 439-42 (1991).

[265]   N.V.Gruzdev, E.G.Sil'kis *et al.*, *"Ultrafast dephasing of Resorufin in d-ethanol glass from 1.7 to 40 K studied by incoherent photon echo"*, J. Opt. Soc. Am. B **9** (6), 941-5 (1992).

[266]   N.V.Gruzdev, Y.G.Vainer, *"Nanosecond spectral diffusion and optical dephasing in organic glasses over a wide temperature range: incoherent photon echo study of resorufin in D- and D/sub 6/-ethanol"*, J. Lumin. **56** (1-6), 181-96 (1993).

[267]   Y.G.Vainer, N.V.Gruzdev, *"Dynamics of organic amorphous media at low temperatures: an incoherent photon echo study of resorufin in ethanol-d and -d/sub 6/ at 1.7-35 K. II. Analysis of results"*, Opt. Spectrosc. **76** (2), 232-40 (1994).

[268]   W.P.de Boeij, M.S.Pshenichnikov, D.A.Wiersma, *"Ultrafast solvation dynamics explored by femtosecond photon echo spectroscopies"*, Annu. Rev. Phys. Chem. **49**, 99-123 (1998).

[269]   de Boeij,W.P., Pshenichnikov,M.S. & Wiersma,D.A., pp. 404-405 (Opt. Soc. America, Washington, DC, USA,1996).

[270]   W.P.de Boeij, M.S.Pshenichnikov, D.A.Wiersma, *"Mode suppression in the non-Markovian limit by time-gated stimulated photon echo"*, J. Chem. Phys. **105** (8 2953-60) (1996).

[271]   S.J.Rosenthal, R.Jimenez *et al.*, *"Solvation dynamics in methanol - experimental and molecular-dynamics simulation studies"*, J. Mol. Liq. **60** (1-3), 25-56 (1994).

[272]   N.Nandi, S.Roy, B.Bagchi, *"Ultrafast solvation dynamics in water - isotope effects and comparison with experimental results"*, J. Chem. Phys. **102** (3), 1390-7 (1995).

[273]   S.Yoshioka, Y.Miyake *et al.*, *"Temperature dependence of low-frequency responses in various kinds of liquids"*, J. Lumin. **94**, 771-4 (2001).

[274]   S.Kinoshita, Y.Kai *et al.*, *"Femtosecond optical Kerr effect measurement on initial process of liquid dynamics"*, J. Lumin. **87-9**, 706-8 (2000).

[275]   Y.Watanabe, S.Kinoshita, *"Frequency-domain four-wave mixing spectroscopy in disordered materials"*, J. Lumin. **87-9**, 895-7 (2000).

[276]   S.Kinoshita, Y.Kai, Y.Watanabe, *"Origin of initial rise process of ultrafast exponential response in liquids"*, Chem. Phys. Lett. **301** (1-2), 183-8 (1999).

[277]   J.Wiedersich, T.Blochowicz *et al.*, *"Fast and slow relaxation processes in glasses"*, J. Phys. : Condens. Matter **11** (10A), A147-A156 (1999).

[278]   J.Wiedersich, N.V.Surovtsev, E.Rossler, *"A comprehensive light scattering study of the glass former toluene"*, J. Chem. Phys. **113** (3), 1143-53 (2000).

[279]   Y.Gu, A.Widom, P.M.Champion, *"Spectral line shapes of damped quantum oscillators: Applications to biomolecules"*, The Journal of chemical physics **100** (4), 2547-60 (1994).

[280]   D.W.Oxtoby, *"Vibrational Relaxation in Liquids"*, Annu. Rev. Phys. Chem. **32** (1), 77-101 (1981).

[281]   V.B.Nemtsov, I.I.Fedchenia *et al.*, *"Density dependence of vibrational energy relaxation rates in supercritical solution: a hydrodynamic model"*, Phys. Rev. E. Stat. Phys. Plasmas. Fluids Relat Interdiscip. Topics. **60** (4 Pt A), 3814-22 (1999).

[282]   D.R.Greig, G.C.Joy III, D.F.Shriver, *"Temperature dependent Raman spectra of the ordered and disordered phases of Ag[sub 2]HgI[sub 4] and Cu[sub 2]HgI[sub 4]"*, The Journal of chemical physics **67** (7), 3189-93 (1977).

[283]   A.Tokmakoff, B.Sauter, M.D.Fayer, *"Temperature-dependent vibrational relaxation in polyatomic liquids: Picosecond infrared pump--probe experiments"*, The Journal of chemical physics **100** (12), 9035-43 (1994).

[284]   D.J.Myers, M.Shigeiwa *et al.*, *"Temperature and density dependent solute vibrational relaxation in supercritical fluoroform"*, The Journal of chemical physics **115** (10), 4689-95 (2001).

Bibliography

[285]   T.J.Kang, J.W.Yu, M.Berg, *"Rapid Solvation of A Nonpolar Solute Measured by Ultrafast Transient Holeburning"*, Chem. Phys. Lett. **174** (5), 476-80 (1990).

[286]   J.W.Yu, T.J.Kang, M.Berg, *"Subpicosecond Relaxation of Solvent Perturbations of Nonpolar Electronic States Measured by Transient Hole Burning"*, J. Chem. Phys. **94** (9), 5787-95 (1991).

[287]   J.Ma, D.V.Bout, M.Berg, *"Transient Hole-Burning of S-Tetrazine in Propylene Carbonate - A Comparison of Mechanical and Dielectric Theories of Solvation"*, J. Chem. Phys. **103** (21), 9146-60 (1995).

[288]   J.Ma, J.T.Fourkas *et al.*, *"Multiple time scales in the nonpolar solvation dynamics of supercooled liquids"*, Supercooled Liquids **676**, 199-211 (1997).

[289]   M.A.Berg, Y.H.Zhang *et al.*, *"Inertial and diffusive dynamics of a nonpolar solute"*, Abstr. Am. Chem. Soc. **220**, U195 (2000).

[290]   Y.H.Zhang, M.A.Berg, *"Ultrafast dichroism spectroscopy of anthracene in solution. III. Nonpolar solvation dynamics in benzyl alcohol"*, J. Chem. Phys. **115** (9), 4231-8 (2001).

[291]   Y.H.Zhang, M.A.Berg, *"Ultrafast dichroism spectroscopy of anthracene in solution. II. Solvation dynamics from a one-dimensional experiment"*, J. Chem. Phys. **115** (9), 4223-30 (2001).

[292]   Y.H.Zhang, M.I.Sluch *et al.*, *"Ultrafast dichroism spectroscopy of anthracene in solution. I. Inertial versus diffusive rotation in benzyl alcohol"*, J. Chem. Phys. **115** (9), 4212-22 (2001).

[293]   Y.H.Zhang, J.W.Jiang, M.A.Berg, *"Ultrafast dichroism spectroscopy of anthracene in solution. IV. Merging of inertial and diffusive motions in toluene"*, J. Chem. Phys. **118** (16), 7534-43 (2003).

[294]   A.G.Palmer, J.Williams, A.McDermott, *"Nuclear magnetic resonance studies of biopolymer dynamics"*, J. Phys. Chem. **100** (31), 13293-310 (1996).

[295]   W.P.Aue, E.Bartholdi, R.R.Ernst, *"2-Dimensional Spectroscopy - Application to Nuclear Magnetic-Resonance"*, J. Chem. Phys. **64** (5), 2229-46 (1976).

[296]   S.Woutersen, P.Hamm, *"Nonlinear two-dimensional vibrational spectroscopy of peptides"*, J. Phys. : Condens. Matter **14** (39), R1035-R1062 (2002).

[297]   N.H.Ge, M.T.Zanni, R.M.Hochrasser, *"Effects of vibrational frequency correlations on two-dimensional infrared spectra"*, J. Phys. Chem. A **106** (6), 962-72 (2002).

[298]   M.T.Zanni, R.M.Hochrasser, *"Two-dimensional infrared spectroscopy: a promising new method for the time resolution of structures"*, Current Opinion in Structural Biology **11** (5), 516-22 (2001).

[299]   S.Woutersen, Y.G.Mu *et al.*, *"Subpicosecond conformational dynamics of small peptides probed by two-dimensional vibrational spectroscopy"*, PNAS **98** (20), 11254-8 (2001).

[300]   M.C.Asplund, M.T.Zanni, R.M.Hochrasser, *"Two-dimensional infrared spectroscopy of peptides by phase-controlled femtosecond vibrational photon echoes"*, PNAS **97** (15), 8219-24 (2000).

[301]   P.Hamm, M.Lim *et al.*, *"The two-dimensional IR nonlinear spectroscopy of a cyclic penta-peptide in relation to its three-dimensional structure"*, PNAS **96** (5), 2036-41 (1999).

[302]   A.Tokmakoff, M.J.Lang *et al.*, *"Two-dimensional Raman spectroscopy of vibrational interactions in liquids"*, Phys. Rev. Lett. **79** (14), 2702-5 (1997).

[303]   M.Khalil, N.Demirdoven, A.Tokmakoff, *"Coherent 2D IR spectroscopy: Molecular structure and dynamics in solution"*, J. Phys. Chem. A **107** (27), 5258-79 (2003).

[304]   J.T.Fourkas, *"Higher-order optical correlation spectroscopy in liquids"*, Annu. Rev. Phys. Chem. **53**, 17-40 (2002).

[305]   M.H.Cho, *"Nonlinear response functions for the three-dimensional spectroscopies"*, J. Chem. Phys. **115** (10), 4424-37 (2001).

[306]   J.D.Hybl, Y.Christophe, D.M.Jonas, *"Peak shapes in femtosecond 2D correlation spectroscopy"*, Chem. Phys. **266** (2-3), 295-309 (2001).

[307]   S.M.G.Faeder, D.M.Jonas, *"Two-dimensional electronic correlation and relaxation spectra: Theory and model calculations"*, J. Phys. Chem. A **103** (49), 10489-505 (1999).

[308]   K.Okumura, A.Tokmakoff, Y.Tanimura, *"Two-dimensional line-shape analysis of photon-echo signal"*, Chem. Phys. Lett. **314** (5-6), 488-95 (1999).

[309]   J.D.Hybl, A.W.Albrecht *et al.*, *"Two-dimensional electronic spectroscopy"*, Chem. Phys. Lett. **297** (3-4), 307-13 (1998).

[310]   L.Lepetit, M.Joffre, *"Two-dimensional nonlinear optics using Fourier-transform spectral interferometry"*, Opt. Lett. **21** (8), 564-6 (1996).

[311]   J.T.Fourkas, H.Kawashima, K.A.Nelson, *"Theory of Nonlinear-Optical Experiments with Harmonic-Oscillators"*, J. Chem. Phys. **103** (11), 4393-407 (1995).

[312]   J.D.Hybl, A.A.Ferro, D.M.Jonas, *"Two-dimensional Fourier transform electronic spectroscopy"*, J. Chem. Phys. **115** (14), 6606-22 (2001).

[313]   C.M.Cheatum, A.Tokmakoff, J.Knoester, *"Signatures of beta-sheet secondary structures in linear and two-dimensional infrared spectroscopy"*, J. Chem. Phys. **120** (17), 8201-15 (2004).

[314]   N.Demirdoven, C.M.Cheatum *et al.*, *"Two-dimensional infrared spectroscopy of antiparallel beta-sheet secondary structure"*, J. Am. Chem. Soc. **126** (25), 7981-90 (2004).

[315]   D.M.Jonas, *"Two-dimensional femtosecond spectroscopy"*, Annu. Rev. Phys. Chem. **54**, 425-63 (2003).

[316]   J.D.Hybl, A.Yu *et al.*, *"Polar Solvation Dynamics in the Femtosecond Evolution of Two-Dimensional Fourier Transform Spectra"*, J. Phys. Chem. A **106** (34), 7651-4 (2002).

[317]   R.R.Ernst, G.Bodenhausen, A.Wokaun, *"Nuclear Magnetic Resonance in One and Two Dimensions"*. Oxford University Press, Oxford, 1987.

194

[318]   K.F.Everitt, E.Geva, J.L.Skinner, *"Determining the solvation correlation function from three-pulse photon echoes in liquids"*, The Journal of chemical physics **114** (3), 1326-35 (2001).

[319]   A.Tokmakoff, *"Two-Dimensional Line Shapes Derived from Coherent Third-Order Nonlinear Spectroscopy"*, J. Phys. Chem. A **104** (18), 4247-55 (2000).

[320]   K.Kwac, M.H.Cho, *"Molecular dynamics simulation study of N-methylacetamide in water. II. Two-dimensional infrared pump-probe spectra"*, J. Chem. Phys. **119** (4), 2256-63 (2003).

[321]   T.Brixner, J.Stenger *et al.*, *"Two-dimensional spectroscopy of electronic couplings in photosynthesis"*, Nature **434** (7033), 625-8 (2005).

[322]   M.Khalil, N.Demirdoven, A.Tokmakoff, *"Obtaining absorptive line shapes in two-dimensional infrared vibrational correlation spectra"*, Phys. Rev. Lett. **90** (4) (2003).

[323]   R.R.Ernst, G.Bodenhausen, A.Wokaun, *"Principles of nuclear magnetic resonance in one and two dimensions"*. Oxford University Press, Oxford, 1990.

[324]   M.L.Cowan, B.D.Bruner *et al.*, *"Ultrafast memory loss and energy redistribution in the hydrogen bond network of liquid H2O"*, Nature **434** (7030), 199-202 (2005).

[325]   P.Tinnefeld, M.Heilemann, M.Sauer, *"Design of molecular photonic wires based on multistep electronic excitation transfer"*, Chemphyschem. **6** (2), 217-22 (2005).